

CHARACTERIZING THE INFLUENCE OF PROCESS  
VARIABLES IN LASER CLADDING AL-20WT%Si ONTO AN  
ALUMINIUM SUBSTRATE

---

LOUIS GEORGE VON WIELLIGH

# COPYRIGHT STATEMENT

The copy of this dissertation has been supplied on condition that anyone who consults it is understood to recognise that its copyright rests with the Nelson Mandela Metropolitan University and that no quotation from the dissertation and no information derived from it, may be published without the Nelson Mandela Metropolitan Universities prior consent.

CHARACTERIZING THE INFLUENCE OF PROCESS  
VARIABLES IN LASER CLADDING AL-20WT%Si ONTO AN  
ALUMINIUM SUBSTRATE

By

**LOUIS GEORGE VON WIELLIGH**

Dissertation submitted in fulfilment of the full requirements for the degree of

**MAGISTER TECHNOLOGIAE: ENGINEERING: MECHANICAL**

In the faculty of Engineering, The built environment and Information  
Technology at the Nelson Mandela Metropolitan University

January 2008

**Promoters**

Prof D.G Hattingh

Dr A Els-Botes

# AUTHOR'S DECLARATION

I hereby declare that the work done in this dissertation is my own, unaided work. All sources used or referred to have been documented and recognized. I further declare that this dissertation has not been previously submitted in full or partial fulfillment of the requirements for an equivalent or higher qualification at any other educational institution.

.....

Author's signature

Date: .....

# ACKNOWLEDGEMENTS

This dissertation could never have been completed without the guidance, support and encouragement of several individuals, companies and institutions.

First and foremost I would like to thank my family for their belief in me, continued support and encouragement in everything I do. With such a foundation one could only succeed. Secondly I would like to thank my promoters Prof D.G Hattingh and Dr A Els-Botes for their guidance, valuable time, support and input throughout the duration of the research project. A special thank you to Mrs Lucinda Lindsey, the office manager at ACTS, for always being available to assist with anything and everything, keeping the wheels turning.

I would also like to thank and acknowledge the support of several institutions, companies and individuals. The National Laser Centre at the CSIR for sponsoring the laser beam time and the Al-Si powder for the project and making their equipment available. I would especially like to mention Mr Herman Burger and Mr Corney van Rooyen from the National Laser Centre for the introduction they gave me to laser cladding, their assistance, guidance and interest in the research project, it was sincerely appreciated. To Mr Tony Paterson from AFSA for organizing the aluminium required for the project, Hulamin Pty Ltd and Mr Pieter du Plessis for sponsoring the

aluminium plate and Dr Jacques Pietersen at the NMMU for his assistance with the statistical analysis of the data. In addition I would like to thank the NRF and Rolls Royce, who awarded me the Rolls Royce IAE scholarship, for their financial support.

Lastly I would like to thank all the people in and around the Manufacturing Technology Research Centre and the Automotive Component Technology Station for creating a pleasant working environment conducive to research.

# ABSTRACT

The research investigated the application of continuous coaxial laser cladding by powder injection as a surface treatment or coating process. The investigation aimed to establish the relationship between a change in the main laser cladding process variables and the geometry and characteristics of an Al-20wt%Si single pass clad layer formed on an Al 1370-F substrate using a Nd:YAG laser. The main process variables considered were: laser power, laser scanning velocity and the powder feed rate.

The relationship between a change in the main laser cladding process variables and the geometry and characteristics of the clad layer was established by statistically analysing the variation in the process response with a change in the main laser cladding process variables. The process variables were varied based on a full-factorial, experimentally optimized test matrix.

The clad geometry which is mainly defined by: the clad height, width, clad aspect ratio, depth of alloy penetration, and the clad root angle/wetting angle was investigated. In addition to the clad geometry several clad characteristics were investigated such as the dilution of the clad layer in the substrate material, the Vickers microhardness and microstructure of the clad cross-section, the powder efficiency of the process and the amount of visible defects.

The study successfully established the relationship between the main laser cladding process variables and the clad geometry and characteristics. The secondary objective of establishing a suitable processing window by considering the relationship mentioned above was only partially met since it is believed that further refinement of the experimental cladding test setup and therefore also the experimental variable test levels is required.



# TABLE OF CONTENTS

<b>List of figures</b>	<b>VII</b>
<b>List of tables</b>	<b>XIV</b>
<b>Glossary of terms</b>	<b>XVII</b>
<b>1. SCOPE OF THE INVESTIGATION.....</b>	<b>1</b>
1.1 Introduction.....	1
1.2 Laser cladding as a surface treatment/coating process .....	1
1.2.1 Comparison between laser cladding and competing techniques .....	4
1.2.2 Coaxial laser cladding by powder injection.....	4
1.3 Problem statement .....	6
1.3.1 Sub-problems .....	6
1.4 Hypothesis.....	7
1.5 Delimitations .....	8
1.6 Significance of the research .....	10
1.6.1 Towards the Nelson Mandela Metropolitan University (NMMU).....	10
1.6.2 Towards the development of the process and South African industry .....	11
1.7 Research path .....	10
1.8 Analysis of the test samples.....	13
<b>2. INTRODUCTION TO LASER CLADDING.....</b>	<b>14</b>
2.1 Laser material interaction .....	14
2.1.1 Introduction.....	14
2.1.2 Laser absorption in metals .....	14
2.1.3 The effect of laser and material properties on adsorption .....	18
2.2 Laser cladding timeline.....	29
2.3 Major application areas .....	32
2.3.1 Coatings .....	32
2.3.2 Repair and refurbishment.....	34

2.3.3 Rapid prototyping and tooling.....	35
2.4 Laser cladding equipment .....	36
2.4.1 The laser source.....	36
2.4.2 Fibre optic beam delivery .....	48
2.4.3 The processing head.....	54
2.4.4 The powder delivery system.....	56
2.5 Laser cladding in relation to other laser surface treatments.....	69
2.6 Laser cladding methods .....	71
2.6.1 Pre-deposition laser cladding .....	71
2.6.2 One step laser cladding with wire feeding.....	75
2.6.3 One step laser cladding with powder injection .....	77
2.7 Laser cladding process variables .....	79
2.8 Laser cladding process models.....	81
2.9 Energy distribution in laser cladding with powder injection .....	82
2.10 Single pass clad geometry .....	88
2.11 The clad root angle or wetting angle .....	91
2.12 Aspect ratio .....	92
2.13 Dilution .....	93
2.14 Powder efficiency .....	94
2.15 The effect of process variables on the clad geometry and characteristics .....	99
2.16 Microstructural development .....	100
2.16.1 The Al-Si binary system.....	100
2.16.2 Factors influencing microstructural development .....	105
2.16.3 The solidification front velocity and temperature gradient .....	107
2.16.4 Reported microstructures of laser processed Al-Si alloys.....	109
<b>3. OPTIMIZATION OF THE EXPERIMENTAL SETUP .....</b>	<b>115</b>
3.1 Introduction.....	115
3.2 Test sample.....	116
3.2.1 Sample material composition .....	116
3.2.2 Sample geometry .....	116
3.2.3 Sample surface preparation .....	116
3.2.4 Evaluation of the sample surface roughness.....	118
3.3 Powder/alloy addition .....	122

---

3.4	Laser beam profiling.....	123
3.4.1	Introduction.....	123
3.4.2	Objective: Laser beam profiling.....	125
3.4.3	Setup and test procedure: Laser beam profiling.....	126
3.4.4	Results: Laser beam profiling.....	130
3.4.5	Discussion: Laser beam profile.....	134
3.5	Determining the main process variables test levels.....	135
3.5.1	Introduction.....	135
3.5.2	Objective: Variable test level tests.....	135
3.5.3	Experimental test setup: Establishing the variable test levels.....	136
3.5.4	Experimental test procedure: Establishing the variable test levels.....	140
3.5.5	Experimental test matrix: Establishing the variable test levels.....	140
3.5.6	Test results: Establishing the variable test levels.....	143
3.5.7	Discussion: Process variable test levels.....	146
3.6	Analysis of the coaxial nozzle.....	147
3.6.1	Introduction.....	147
3.6.2	Objective: Coaxial nozzle tests.....	147
3.6.3	Experimental test setup: Coaxial nozzle tests.....	148
3.6.4	Experimental test procedure: Coaxial nozzle tests.....	149
3.6.5	Experimental test matrix: Coaxial nozzle tests.....	150
3.6.6	Test results: Coaxial nozzle tests.....	150
3.6.7	Discussion: Cold stream powder profile.....	154
3.7	Determining the optimum gas flow rate.....	156
3.7.1	Introduction.....	156
3.7.2	Objective: Optimization of the gas flow rate.....	156
3.7.3	Experimental test setup: Optimization of the carrier gas flow rate.....	156
3.7.4	Experimental test procedure: Optimization of the carrier gas flow rate.....	156
3.7.5	Test matrix: Optimization of the carrier gas flow rate.....	157
3.7.6	Test results: Carrier gas flow rate tests.....	158
3.7.7	Discussion: Optimization of the carrier gas flow rate.....	159
3.8	Analysis of the GTV PF 2/2 powder feeder.....	160
3.8.1	Introduction.....	160
3.8.2	Objective: Investigation of the powder feed unit.....	160
3.8.3	Experimental test setup: Investigation of the powder feed unit.....	161
3.8.4	Experimental test procedure: Investigation of the powder feed unit.....	162

3.8.5	Experimental test matrix: Investigation of the powder feed unit .....	163
3.8.6	Test results: Investigation of the powder feed unit .....	165
3.8.7	Discussion: Investigation of the powder feed unit .....	168
3.9	Alignment of the coaxial nozzle .....	169
3.9.1	Introduction.....	169
3.9.2	Objective: Alignment verification tests.....	171
3.9.3	Experimental test setup: Alignment verification tests .....	171
3.9.4	Experimental alignment verification procedure.....	174
3.9.5	Experimental nozzle stand-off distance verification procedure .....	176
3.9.6	Experimental alignment verification test matrix .....	179
3.9.7	Test results: Experimental alignment verification tests.....	179
3.9.8	Discussion: Experimental alignment verification tests.....	180
3.10	Cladding test matrix.....	181
3.10.1	Introduction.....	181
3.10.2	Objective of the final experimental cladding test matrix .....	181
3.10.3	Experimental test setup .....	181
3.10.4	Experimental test procedure.....	183
3.10.5	Final experimental test matrix.....	183
<b>4.</b>	<b>LASER CLADDING PROCESS RESPONSE.....</b>	<b>185</b>
4.1	Introduction.....	185
4.2	The effect of the main process variables on the clad geometry .....	186
4.2.1	Clad height .....	186
4.2.2	Clad width.....	187
4.2.3	Width of the melt pool.....	189
4.2.4	Alloy penetration depth .....	190
4.2.5	Clad area above the substrate surface.....	192
4.2.6	Clad area below the substrate surface.....	194
4.2.7	The clad root angle.....	196
4.2.8	The clad aspect ratio .....	198
4.3	The effect of the main process variables on clad characteristics .....	201
4.3.1	Dilution.....	201
4.3.2	Powder efficiency .....	205

---

4.4 Vickers microhardness .....	208
4.4.1 Statistical analysis of vickers microhardness tests.....	210
4.5 Microstructural development .....	216
4.5.1 Introduction.....	216
4.5.2 General microstructures observed .....	216
4.5.3 General phases observed .....	220
4.5.4 Microstructural scale and variation.....	220
4.5.5 Variation in the size and volume fraction of the silicon particles .....	224
4.5.6 Solidification rate .....	226
4.5.7 Solidification direction.....	229
4.5.8 Relationship between microstructure, hardness & clad characteristics.....	233
4.6 Defect population .....	234
4.7 Combined process variables .....	238
<b>5. FINAL CONCLUSIONS AND FUTURE WORK.....</b>	<b>241</b>
5.1 Introduction.....	241
5.2 The process response.....	241
5.2.1 Clad height .....	243
5.2.2 Clad width .....	244
5.2.3 The clad aspect ratio .....	245
5.2.4 Alloy penetration depth .....	247
5.2.5 Dilution.....	251
5.2.6 Powder efficiency .....	253
5.2.7 Vickers microhardness and microstructure of the clad layer.....	258
5.2.8 General observations regarding the shape of the clad cross-section....	262
5.3 Processing window.....	266
5.4 Future work .....	267
<b>REFERENCE LIST.....</b>	<b>269</b>
<b>APPENDIX A.....</b>	<b>274</b>
<b>APPENDIX B.....</b>	<b>279</b>

**APPENDIX C.....283**  
**APPENDIX D.....286**  
**APPENDIX E.....289**

## LIST OF FIGURES

Figure 1.1:	Principle of coaxial laser cladding by powder injection using a continuous coaxial nozzle.	6
Figure 1.2:	Flow diagram indicating the intended research path.	12
Figure 1.3:	Schematic indicating the various aspects of the single clad layer that was investigated.	13
Figure 2.1:	Incident radiation on an optically smooth surface.	16
Figure 2.2:	The relationship between reflectivity and wavelength for various materials.	20
Figure 2.3:	(a) p-polarized ray; (b) s-polarized ray	22
Figure 2.4:	Variation in the reflectivity of steel to polarized 1060 nm radiation.	23
Figure 2.5:	The effect of temperature on the reflectivity of various metals exposed to 1.06 $\mu\text{m}$ radiation.	24
Figure 2.6:	Multiple reflections of laser light incident on an optically rough surface.	26
Figure 2.7:	Interference phenomena as a result of an oxide layer on the surface of a metal.	27
Figure 2.8:	Absorption as a function of the oxide layer thickness on steel for 1.06 $\mu\text{m}$ radiation.	28
Figure 2.9:	Energy levels for neodymium indicating why an Nd:YAG laser is considered to be a four level laser.	41
Figure 2.10:	Comparison of the spectral match between optical excitation using flash lamps and laser diodes with the peak Nd:YAG absorption band at 808 nm.	42
Figure 2.11:	Principle of a diode pumped Nd:YAG Rofin DY series laser.	43
Figure 2.12:	Schematic illustrating the various parameters of a propagating beam.	47
Figure 2.13:	The principle of light transmission through step and graded index fibres.	52

Figure 2.14:	Schematic illustrating the re-collimation and focusing of the laser beam as it exits from the optical fibre.	54
Figure 2.15:	The principle of a volumetric powder feed unit using a powder feed disc.	58
Figure 2.16:	Principle of off-axis cladding.	60
Figure 2.17:	Principle of two different off-axis cladding methods. Figure 2.17(a) illustrates dragging injection. Figure 2.17(b) illustrates stinging injection .	61
Figure 2.18:	Simplified schematic of the exit of a continuous coaxial nozzle .	63
Figure 2.19:	The influence of nozzle slit size on the diameter of the powder stream at its focus position.	64
Figure 2.20:	The influence of powder particle size on the diameter of the powder stream at its focus.	64
Figure 2.21:	A discontinuous or three-way coaxial nozzle.	67
Figure 2.22:	Schematic illustrating the difference between laser dispersing, alloying and cladding in terms of composition and dilution in the base material.	70
Figure 2.23:	The principle of pre-deposition laser cladding.	72
Figure 2.24:	a) Illustrates how the molten coating contracts when irradiated by the laser source. (b) Illustrates how contraction exposes the substrate increasing dilution in the adjacent coating.	75
Figure 2.25:	One step laser cladding with wire feeding.	76
Figure 2.26:	One step coaxial laser cladding by powder injection using a three-way coaxial nozzle.	77
Figure 2.27:	Process variables that influence the laser cladding process and quantitative outputs.	80
Figure 2.28:	a) Assumed cross-section of the clad on the substrate. (b) Homogeneous distribution of powder particles over the laser beam diameter on the substrate.	85
Figure 2.29:	Dimensions that define the typical single pass clad cross-section.	88
Figure 2.30:	Laser cladding cross-sections with its associated dilution, wetting angle and interfacial free energy.	89



Figure 2.31:	The change in the clad-cross section with an increase in the powder feed rate and a relatively fixed width determined by the laser beam diameter on the substrate surface.	91
Figure 2.32:	Inter-run porosity between adjacent clad layers forming a coating.	91
Figure 2.33:	Calculated laser power required to melt the substrate and the powder particles as a function of the particle velocity for coaxial cladding.	98
Figure 2.34:	Undercooling due to a high solidification rate.	103
Figure 2.35:	Change in microstructure due to a change in the solidification rate.	103
Figure 2.36:	Coupled growth regions in an asymmetric hypothetical phase diagram.	104
Figure 2.37:	Schematic illustrating the relationship between $V_s$ and $V_{sf}$ .	107
Figure 2.38:	The calculated solidification conditions in laser surface re-melting at two different scanning velocities. Figure 2.38 (a) represents the change in the temperature gradient and Figure 2.38 (b) the change in the solidification rate with respect to the depth from the free surface (d).	109
Figure 2.39:	A SEM micrograph of a five branched silicon crystal surrounded by $\alpha$ -aluminium halos with inter-dendritic eutectic.	110
Figure 2.40:	An optical micrograph of an Al 40wt%Si FGC produced at $P = 3000$ W and $v_s = 26.7$ mm/s. Micrographs A, B and C indicate the variation in both size and volume fraction of the silicon particles at the top (A), middle (B) and bottom (C) of the clad layer.	111
Figure 3.1:	Surface reflectivity before and after wire brushing. Original test sample at the top, wire brushed sample below.	117
Figure 3.2:	Sample surface preparation steps.	117
Figure 3.3:	Sub-division of the traversing length of the detector.	120
Figure 3.4:	Test setup for evaluating the test sample Ra values.	120
Figure 3.5:	Gas atomized spherical Al-Si20wt% particles.	122
Figure 3.6:	Microstructure of the Al-20wt%Si powder particles.	123

Figure 3.7:	(a) Beam profile measurement in a focussed laser beam. (b) The working principle of the rotating hollow needle with detector on a feed slide. The smallest possible traversing step size is 12.5 $\mu\text{m}$ .	125
Figure 3.8:	Laser beam profiling setup, indicating the reference plane (a) and the distance from it to the top surface (b) of the UFF100 laserscope. Also indicated is the sign convention used for the z-axis.	126
Figure 3.9:	Schematic indicating the position the UFF100 needle recess and various scan positions.	129
Figure 3.10:	Caustic diagram indicating the beam profile or beam diameter with respect to each scanning position along the z-axis. ( $w$ =beam radius).	132
Figure 3.11:	Cladding setup to determine the various process variable test level settings.	136
Figure 3.12:	Test sample holder.	138
Figure 3.13:	Robot working sequence.	139
Figure 3.14:	Experimental test setup for the cold stream analysis of the powder flow from a coaxial nozzle.	148
Figure 3.15:	The variation in the powder stream profile with a change in the powder feed rate and carrier gas flow rate.	151
Figure 3.16:	Measurements taken from the digital images for the visual analysis of the coaxial nozzle.	153
Figure 3.17:	Experimental test setup for determining the relationship between the powder disc speed and the powder mass flow rate in grams/second .	161
Figure 3.18:	Graph representing the powder mass flow rate versus the powder disc rotational speed for each of the test sequences.	165
Figure 3.19:	Nozzle height and alignment adaptor fitted to the bottom of the processing head.	170
Figure 3.20:	Alignment verification test setup.	171
Figure 3.21:	Illustrates the three-axis alignment test jig clamped to the work surface with the coaxial nozzle and nozzle height and alignment adaptor positioned over the test target.	173

Figure 3.22:	Visual inspection of the alignment between the coaxial nozzle work axis and the alignment test jig work axis (centre of the conical nozzle) representing the beam propagation axis.	175
Figure 3.23:	(a) Powder streams from a three-way coaxial nozzle impacting on a conical surface. (b) Schematic illustrating the change in the deflection angle of a powder particle with a change in the nozzle stand-off distance.	178
Figure 4.1:	Relationship between the calculated clad root angle and aspect ratio.	200
Figure 4.2:	Contour plot indicating the dependence of dilution on the relationship between the change in the clad area above and below the substrate at the various test levels.	204
Figure 4.3:	Decrease in the clad area below the substrate with an increase in the laser scanning velocity.	205
Figure 4.4:	Position of indentations on the clad cross-section making up the hardness profile of the clad layer.	209
Figure 4.5:	Typical vickers microhardness profile observed.	209
Figure 4.6:	Histogram representing the number of maximum microhardness indentations relative to their position from the edge of the free surface of the clad cross-section.	212
Figure 4.7:	Fitted line plot indicating the relationship between $HV_{\max}$ and dilution.	213
Figure 4.8:	SEM micrographs of the five main types of microstructures observed.	218
Figure 4.9:	Featureless, transitional zone at the bottom of clad layer at the clad-substrate interface.	219
Figure 4.10:	SEM micrographs of the main phases observed.	220
Figure 4.11:	Influence of an increase in the main process variables test level on the clad microstructure.	224
Figure 4.12:	Microstructural transition/scale variation on either side of the solidification front.	227
Figure 4.13:	Measurements to determine the variation in both the solidification front angle and the velocity of the solidification front across the height of the longitudinal clad cross-section.	228
Figure 4.14:	Variation in the dendrite growth direction across the clad height	230

---

Figure 4.15:	Banding observed in a longitudinal section through the centreline of the clad layer.	232
Figure 4.16:	Change in the growth orientation of the dendritic structure, re-orientating itself towards the moving laser beam.	232
Figure 4.17:	Relationship between the maximum microhardness of the clad cross-section and the type of microstructure that developed upon solidification.	233
Figure 4.18:	Powder particles adhering to the substrate surface at the root of the clad layer not actually forming part of the clad layer itself.	236
Figure 4.19:	False build-up defect at the sides of the clad cross-section.	237
Figure 5.1:	Relationship between the clad height and the combined process parameter CP1.	244
Figure 5.2:	Contour plot indicating the relationship between the clad characteristics: dilution; the calculated clad root angle, and the clad aspect ratio.	246
Figure 5.3:	Relationship between the clad aspect ratio and the combined process parameter CP6.	247
Figure 5.4:	Relationship between the depth of alloy penetration and the modified combined process parameter CP2*.	249
Figure 5.5:	SEM micrograph indicating the resemblance between the laser beam intensity profile and the profile of the clad area below the substrate.	250
Figure 5.6:	Relationship between the level of dilution and the combined process parameter CP6.	253
Figure 5.7:	The three powder streams from the three-way coaxial nozzle impacting on the substrate surface.	256
Figure 5.8:	The change in the powder concentration of the powder stream with an increase in the powder feed rate under cold stream flow conditions. The powder mass flow rate in A=0.627 g/min; B= .134 g/min; C= 1.634 g/min, and D=2.180 g/min.	257
Figure 5.9:	Relationship between the maximum hardness and dilution of the clad layer.	259
Figure 5.10:	Influence of an increase in the main process variables test level on the clad microstructure.	261

Figure 5.11:	Increase in the ratio between the powder stream diameter to the laser beam diameter on the substrate surface with an increase in the powder mass flow rate.	264
Figure 5.12:	Lateral spread of the clad layer beyond the melt-substrate interface.	265
Figure 5.13:	A) Working below the beam focus. (B) Working above the beam focus.	268

## LIST OF TABLES

Table 1.1	Comparison between selected properties of laser cladding and some competing coating techniques.	4
Table 2.1	The influence of laser and material properties on the absorptivity of a metal surface.	18
Table 2.2	A summary of the reflectivity and absorptivity of various non-ferrous metals at different wavelengths of an Nd: YLF laser.	20
Table 2.3	Reflectivity of the same material prepared with various surface roughness exposed to a CO <sub>2</sub> laser with a normal angle of incidence.	25
Table 2.4	Comparison between laser cladding and other coating techniques.	33
Table 2.5	Typical wall plug efficiencies for industrial lasers. The wall plug efficiency is the percentage of the optical energy extracted from the system compared to the electrical energy input into the system.	38
Table 2.6	Several TEM modes with Gaussian energy intensity distributions.	46
Table 2.7	Various models describing the cladding process.	82
Table 2.8	A summary of the effect of an increase in the various process variables on the clad geometry and its properties.	99
Table 3.1	Average wt% from the chemical composition test on the Al-1370 F substrate.	116
Table 3.2	Test settings used for arithmetic mean roughness (Ra) evaluation according to DIN standards.	120
Table 3.3	Summary of the arithmetical mean surface roughness values.	121
Table 3.4	Results from laser beam profiling tests.	131
Table 3.5	Comparison of the laser beam intensity profile at its focus and at the experimental cladding position.	133
Table 3.6	Random test variable levels tested during the setup tests.	142
Table 3.7	Tabulated results from the setup test matrix.	144

Table 3.8	Main process variable test level settings established based on the results of the setup test matrix.	146
Table 3.9	Experimental test matrix for the visual analysis tests of the coaxial nozzle.	150
Table 3.10	Tabulated measurement results from the visual analysis of the coaxial nozzle.	153
Table 3.11	Experimental test matrix for determining the optimum carrier gas volume flow rate.	157
Table 3.12	Tabulated test results from the experimental test matrix indicating the depression of the clad centre when considering the clad profile on the substrate surface.	159
Table 3.13	Test matrix indicating the test settings used to determine the powder mass flow rate at various powder disc speeds and the consistency of powder delivery.	164
Table 3.14	Test results from the four test sequences indicating the mass of powder caught in the test beaker in 300 seconds.	166
Table 3.15	Tabulated calculation results for the mass of powder delivered per 300 seconds and powder mass flow rate per second for each test level setting of the powder disc speed.	167
Table 3.16	Tabulated results from the experimental test procedure to verify the nozzle stand off distance.	177
Table 3.17	Variable settings for random tests to confirm alignment.	179
Table 3.18	Test results from the alignment verification tests.	180
Table 3.19	Main process variable test levels for the final experimental cladding test matrix.	184
Table 4.1	The mean clad height for each process variable test level.	186
Table 4.2	The mean clad width for each process variable test level.	187
Table 4.3	The mean width of the melt pool for each process variable test level.	189
Table 4.4	The mean depth of alloy penetration for each process variable test level.	190
Table 4.5	The mean clad area above the substrate for each process variable test level.	192

Table 4.6	The mean clad area below the substrate for each process variable test level.	195
Table 4.7	The mean root angle for each process variable test level.	197
Table 4.8	The mean clad aspect ratio for each process variable test level.	199
Table 4.9	The mean dilution (Geometrical test method) for each process variable test level.	202
Table 4.10	The mean dilution (Area ratio test method) for each process variable test level.	202
Table 4.11	The mean powder efficiency for each process variable test level.	206
Table 4.12	The change in the mean, maximum microhardness of the clad cross-section.	211
Table 4.13	The change in the mean, minimum hardness of the clad cross-section.	215
Table 4.14	SEM micrographs of sample C014 and sample C057 indicating a typical reduction in the microstructural scale, and variation in the type of microstructure, respectively.	222
Table 4.15	SEM micrographs indicating a general increase in both the volume fraction and size of the Si particles, from the bottom of the clad layer to the top of the clad layer.	226
Table 4.16	Tabulated measurement results of the variation in the solidification front angle.	228
Table 4.17	Examples of the influence of directional and iso-directional heat extraction on the shape of the dendritic structure.	231
Table 4.18	Some of the typical defects observed in the clad layers from the experimental test matrix.	235
Table 4.19	Correlation between combined process parameters and individual clad characteristics. Where: R is the correlation coefficient, a and b are constants in the linear relation: $Q = a + b.CP$ .	238
Table 4.20	Results of the correlation between the final test matrix results and known combined process parameters.	239
Table 5.1	Summary of the observed effect of an increase in the test level of the main process variables on the clad geometry and characteristics.	243



## GLOSSARY OF TERMS

### A

**Active medium:** Collection of species capable of undergoing stimulated emission at a given wavelength. Normally used to describe the type of laser.

**Alloy:** An alloy is a metal comprised of two or more elements, at least one of which is metallic.

### B

**Beam:** A collection of rays that may be parallel, convergent or divergent.

**Beam diameter:** The diameter of an aperture in a plane perpendicular to the beam axis that contains a given fraction of the total beam power. The points are commonly defined as the positions at which the intensity has fallen to  $1/e$  (0.368), or  $1/e^2$  (0.135) of the peak level.

**Beam waist:** The location of the minimum beam diameter or beam width.

**Beer-Lambert law:** The absorptance of a beam of collimated monochromatic radiation in a homogenous isotropic medium is proportional to the absorption path length and to the concentration of the absorbing species.

**Brewster angle:** The angle of incidence at which polarized light in a given plane undergoes no loss through reflection.

### C

**Carrier gas:** An inert or semi-inert gas such as argon or helium acting as the conveying medium for the powder particles suspended in it.

**Co-deposition:** Refers to a cladding process in which the coating material (either in wire or powder form) and laser beam is simultaneously applied to the substrate material.

**Collimation:** The process of making light rays as parallel as possible such that they have low divergence.

**Continuous wave (CW) operation:** The continuous emission mode of a laser, in which radiation is emitted continuously over a time greater than 0.25 s.

**Cooling rate:** The average slope of the time-temperature curve taken over a specified time and temperature interval.

## D

**Dendrite:** A crystal with a treelike branching pattern. It is most evident in cast metals, slowly cooled through the solidification range.

**Depth of focus:** The distance over which the beam diameter does not vary by more than the specified fraction of the focused beam diameter, e.g. 5% or the  $\sqrt{2}$ .

**Dilution:** Refers to the composition of the alloy addition which is altered after mixing with the substrate material.

**Divergence:** Angle of beam spread measured in radians.

## F

**Flashlamp:** A gas-filled lamp that is excited by an electrical pulse to produce a short, bright flash of light. Used for optical pumping of the active medium in a laser.

**Focal length:** The distance between the center of an optical device and the point on the optical axis to which parallel rays of light are brought to focus. It is assigned a negative value if the rays diverge from an apparent source behind the optical device.

## H

**HAZ:** The heat affected zone describes the region adjacent to the fusion zone in the base material that has experienced a thermal transformation, without melting, caused by the heat conducted from the clad layer.

**Hypereutectic alloy:** In an alloy system exhibiting a eutectic, any alloy whose composition has excess of alloying element compared with the eutectic composition and whose equilibrium microstructure contains some eutectic structure.

**Hypoeutectic alloy:** In an alloy system exhibiting a eutectic, any alloy whose composition has an excess of base metal compared to the eutectic composition and whose equilibrium microstructure contains some eutectic structure.

## L

**Laser:** Acronym for light amplification by stimulated emission of radiation.

**Laser efficiency:** The quotient of the total power in the laser beam and the total input power to the laser. Often referred to as the wall plug efficiency.

**Liquidus:** In a phase diagram, the locus of points representing the temperatures at which components begin to freeze during cooling or finish melting during heating.

## M

**Macrostructure:** The structure of metals as revealed by macroscopic examination of the etched surface of a polished specimen.

**Mass flow rate:** The mass of powder which passes through a given unit area per unit time.

**Metastable:** A non-equilibrium condition under which a state can exist for a limited time.

**Microstructure:** Microstructure refers to the microscopic description of the individual constituents of a material. The length scale is 100 - 1micrometer.

**Mode (Longitudinal):** The electric field distribution within an optical cavity in the direction of the propagating laser beam.

**Mode (Traverse):** The electric field distribution within an optical cavity perpendicular to the direction of the propagating laser beam.

**N**

**Nd:YAG laser:** A solid state laser in which the active gain medium is the neodymium-doped crystal yttrium aluminum garnet.

**Nucleation:** Initiation of a phase transformation at discrete sites, the new phase growing from the nuclei.

**Numerical model:** Models that are designated by or expressed in numbers.

**P**

**Phase:** A physically distinct homogenous body of matter. In physics, the solid, liquid and gas states are referred to as phases. In materials science, the definition is extended to describe a region in a material with a distinct crystal structure, a single composition, and constant physical and chemical properties.

**Polarization:** The orientation of the plane containing the oscillation of the electric field of an electromagnetic wave.

**Power density:** The quotient of the beam power and the cross-sectional area of the beam.

**Porosity:** Imperfections in the form of coarse (>0.5 mm diameter) or fine (<0.5 mm diameter) holes in a solid material.

**Powder efficiency:** Powder efficiency is used to quantify the ratio between the total mass of powder supplied to the melt pool and the actual amount of powder used for the formation of the clad layer as a percentage.

**Preferred orientation:** A condition of a polycrystalline aggregate in which the crystal orientations are not random, but tend to align in a specific direction in the bulk material that is completely related to the direction of working.

**Pre-placed:** Refers to a cladding process in which the coating material, whether in plate, foil, wire or powder form, is placed or spread on the substrate material prior to the application of the laser beam.

**Process variables:** The material properties, beam characteristics and processing conditions that may be varied during laser material processing.

## R

**Recalescence:** The increase in temperature that occurs after undercooling, because the rate of liberation of heat during transformation of a material exceeds the rate of dissipation of heat.

**Repeatability:** The variation in measurements taken by a single person or instrument on the same item and under the same conditions. A measurement may be said to be repeatable when this variation is smaller than some agreed limit.

## S

**Shielding gas:** An inert or semi-inert gas such as argon/helium that is used to protect the weld/fusion zone area from atmospheric attack.

**Solid state:** Used to denote that the active medium of a laser is in the solid form.

**Statistics:** A branch of applied mathematics concerned with the collection and interpretation of quantitative data and the use of probability theory to estimate population parameters.

**Substrate:** The base material on which the coating material, alloy addition or cladding layer is fused to form the clad layer through the interaction with the laser beam.

**Species:** An ion, molecule or atom in which a laser transition occurs.

**Supercooling:** Cooling to a temperature below that of an equilibrium phase transformation without the transformation taking place. Also referred to as undercooling.

**T**

**Tribology:** Deals with the interaction of surfaces in relative motion and its associated reactions such as friction and wear.

**V**

**Volumetric:** Relates to a measurement by volume

**Volumetric/Volume flow rate:** The volumetric flow rate, also volume flow rate and rate of fluid flow, is the volume of fluid which passes through a unit area per unit time.

**W**

**Wavelength:** The minimum distance between points at which the electric vector of an electromagnetic wave has the same value. Measured along the direction of propagation of the wave, and it is equal to the velocity divided by the frequency.

**Wear:** Gradual removal of material from a surface. Several wear mechanisms exist namely abrasive wear (caused by harder particles), adhesive wear (adhesion of minute contact points that pulls material from surface), oxidation and other chemical reactions or diffusion.

**Working distance:** The distance between the surface of a specimen being processed and the optical centre of the focusing lens in the case of the processing head.

# 1 Scope of the investigation

## 1.1 Introduction

In this chapter a brief introduction to the laser cladding process is given as applied in this investigation. The benefits of laser cladding are highlighted and a comparison between laser cladding and competing processes are given. Subsequent to the process introduction the objectives of the investigation is stated, the research path to be followed and aspects that would be focused on during the analysis of the test samples that would ultimately test the hypothesis.

## 1.2 Laser cladding as a surface treatment/coating process

The focus of this investigation is on the application of laser cladding technology as a surface treatment/coating process. Therefore, for this investigation, the laser cladding process can be defined as a surface treatment process in which a suitable coating material, with the desired properties, is fused onto the surface of a substrate material through the interaction with a laser beam in order to improve the surface properties of the substrate material.

The cladding process is characterized by low and highly localized energy input and a small heat affected zone in order to produce a coating with superior service properties; a strong fusion bond with the substrate material;

low dilution of the alloy addition in the substrate material, and minimal distortion of the part or component.

These characteristics of the laser cladding process offer several advantages over conventional coating processes. Using laser cladding a very small or specific area can be coated with a high degree of accuracy/precision. The low and localized energy input allows the process to be applied near thin walls and used on temperature sensitive parts without any pre-or post treatments. Lower dilution compared to other coating processes such as tungsten inert gas; high velocity oxy-fuel; plasma sprayed; plasma arc or gas arc surface welding means that a thinner coating can be applied while still producing a coating with all the superior properties of the material addition. The lower energy input into the base material and the application of thinner coatings result in very little distortion of the part/component, which leads to a significant reduction in post treatment machining.

The high solidification and cooling rates of the cladding process produces a more homogenous distribution of the elements within the coating and results in finer microstructures and/or metastable phases. The result is a coating with superior wear and corrosion properties compared to competing processes. In addition the quality of a laser clad coating is generally high; with very little porosity; few imperfections, and a strong fusion bond with the substrate.



The process can be automated since the laser beam can be manipulated easily and in a flexible manner. The laser beam can also be directed into inaccessible locations. Another advantage is that laser cladding is a non-contact process and therefore there is no tool wear or mechanical forces acting on the work piece.

The main disadvantage of the laser cladding process is the high investment; operating, and maintenance cost of the laser cladding equipment and the relative unfamiliarity of laser based material processing. According to *Ion* the capital cost of laser cladding equipment is several orders of magnitude higher than conventional equipment and the learning curve required to understand the process and equipment is knowledge intensive (1). Laser cladding would generally only be considered for niche applications; in cases where sufficient volumes are to be processed, or where it would add sufficient value to make it economically feasible. (1)

Other disadvantages include the lack of quality control and standards and procedures for laser cladding. *Toyserkani et al* remarked the following: “Standard specifications for cladding procedures have not yet been developed. Laser processing facilities therefore draw up their own Cladding Procedure Specification which contains the relevant parameters and allowable ranges that are to be used for clads (2).”

### 1.2.1 Comparison between laser cladding and competing techniques

Table 1.1 illustrates some of the previously mentioned advantages of the laser cladding process and compares it to other conventional coating processes. Where: LC-Laser cladding; SMA-Shielded metal arc; MIG-Metal inert gas; SA- Submerged arc; TIG-tungsten inert gas, PS-Plasma spraying, HVOF-High velocity oxy-fuel and PA-Plasma arc.

Process	Thickness (mm)	Deposition rate (kg/h)	Distortion	Precision	Dilution (%)	Integrity
LC	0.2-2.0	0.2-7	Low	High	1-5	High
SMA	1.6-10	0.5-2.5	Medium	Low	15-25	High
MIG	1-6	2.3-11	Medium	Low	15-20	High
SA	2-10	5-25	High	Low	10-50	High
TIG	0.5-3.0	0.5-3.5	High	Medium	10-20	Medium
PS	0.1-0.2	0.5-7	Low	Medium	5-30	Low
Flame	0.8-2.0	0.45-2.7	High	Low	1-10	Medium
HVOF	0.3-1.5	1-5	Low	Low	Low	Medium
PA	1-5	2.5-6.6	Medium	Medium	Medium	Medium

Table 1.1: Comparison between selected properties of laser cladding and some competing coating techniques.

### 1.2.2 Coaxial laser cladding by powder injection

Several laser cladding techniques exist. The most prominent and widely researched technique is co-deposition coaxial laser cladding with powder injection due to its omni-directional processing ability and high powder efficiency.

In co-deposition coaxial laser cladding the material addition in the form of powder is transported in a carrier gas; usually argon; helium, or nitrogen, and delivered via the nozzle coaxial with the laser beam propagation axis. As the laser beam passes through the powder cloud a certain percentage of the laser energy is absorbed while a certain percentage is reflected from the powder cloud, reducing its intensity and changing the energy distribution of the laser beam on the substrate surface (3). The remaining energy from the laser beam, not absorbed or reflected by the powder cloud, is absorbed or reflected by the substrate surface creating a very shallow melt pool into which the powder particles are blown.

Surface tension gradients are the main driving force for fluid flow within the melt pool causing the powder particles to be mixed rapidly within the melt pool. As the laser source moves away rapid solidification takes place resulting in the formation of the clad layer.

Additional shielding gas via the nozzle can also be applied if oxidation is a concern. In the case of continuous coaxial nozzles, shielding gas is generally always used and referred to as the shaping gas as it is used to shape the powder stream as it exits from the nozzle in addition to acting as an oxidation inhibitor. The principle of coaxial laser cladding is illustrated in Figure 1.1.

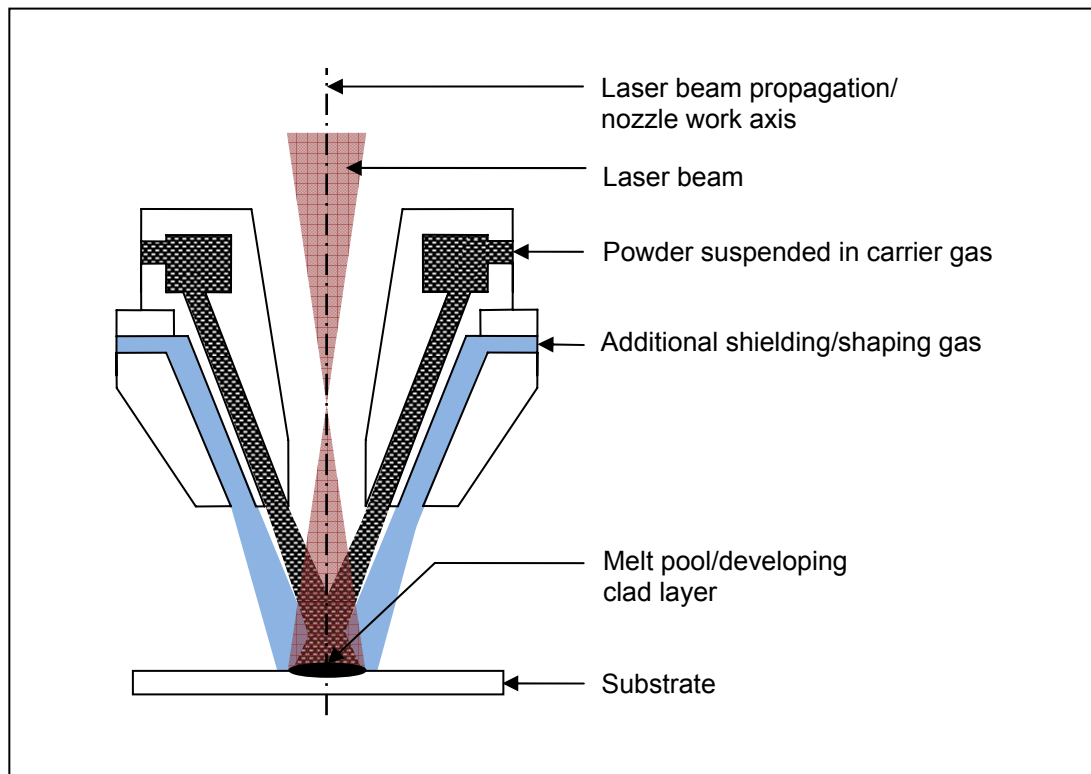


Figure 1.1: Principle of coaxial laser cladding by powder injection using a continuous coaxial nozzle.

### 1.3 Problem statement

To establish the relationship between the main laser cladding process variables and the geometry and characteristics of a single pass clad layer on a light metal substrate.

#### 1.3.1 Sub-problems

In order to realize the objective of this investigation several key areas needed to be addressed which are listed as sub-problems below:

#### **1.3.1.1 Sub-problem one**

Determine the underlying laser cladding process theory. Although the word theory is used the emphasis is not as much on the physical laws that govern the laser cladding process but rather the behaviour of the laser cladding process in response to certain process inputs.

#### **1.3.1.2 Sub-problem two**

Determine the components that form part of a typical cladding platform in order to establish an experimental cladding test setup that could be used for the investigation of the laser cladding process.

#### **1.3.1.3 Sub-problem three**

Develop an experimental test matrix that would enable the evaluation and interpretation of the effect of a change in the main process variables on the clad geometry and characteristics.

### **1.4 Hypothesis**

A definite relationship exists between the main laser cladding process variables and the geometry of a single pass clad layer and by establishing this relationship a probable processing window could be established for the application of a specific coating material on a specific light metal substrate using a Nd:YAG laser with a principle wavelength of 1064 nm.

## 1.5 Delimitations

The following delimitations were identified based on the available test setup:

- It is commonly accepted that the best intensity profile for laser cladding is a homogenous intensity profile. It has been established that the output of the 4 kW Rofin, fiber delivered Nd:YAG laser at the National Laser Center has a top hat intensity profile that is relatively homogenous at its focus. However cladding is seldom carried out at the focus position and it is thus to be expected that the intensity profile would not be ideally homogenous.
- Selection of whether cladding is carried out above or below the waist diameter and the spot diameter of the laser beam on the substrate will be dictated by the focus lenses and nozzles that are available.
- The effects of the geometry and volume of the substrate material on the formation of a single pass clad layer will not be considered.
- The investigation of the effect of the main process variables on the clad geometry and properties can only be evaluated by considering single pass clad layers. Therefore the bond strength between the clad layer and the substrate would not be evaluated or quantified since current ASTM test methods require a coating with overlapping clad tracks for the evaluation of bond strength. In order to produce a coating a proper clad overlap needs to be determined and the main process variable test levels needs to be refined. Therefore it will be assumed that if a proper fusion bond exists between the clad layer

and the substrate a satisfactory bond is achieved.

- It was initially envisaged that the laser cladding investigation would be carried out in two separate stages. In the first stage of the investigation an experimental test matrix would be tested in order to establish the basic cladding set-up and to determine the boundary conditions of the main cladding test variables. Based on the analysis of the test results of the first stage a final cladding test setup and experimental test matrix were to be tested to test the hypothesis. However, due to limited beam time available at the National Laser Center both stages of the investigation will be compressed into a four day session in which the necessary tests will be carried out in order to complete the cladding platform set-up; establish the boundary conditions for the main process variables, and test a test matrix that would provide the necessary outcomes. It is therefore considered that several set-up conditions that could have been optimized would not be.
- It was not possible to examine the clad cross-sections to better interpret results from the set-up tests. This was mainly due to time constraints but also due to the ready availability of the necessary equipment. Therefore interpretation of the results of the cladding set-up test matrix was limited to the visual inspection of the clad layer on the substrate.

- The boundary conditions of the laser cladding test setup had to be selected such that it posed no risk of damage to the expensive test equipment. This was not necessarily a limitation, but it did not allow the proper investigation of the upper and lower boundary conditions of the cladding process.

## **1.6 Significance of the research**

It is envisaged that the research would contribute towards the following:

### **1.6.1 Towards the Nelson Mandela Metropolitan University (NMMU)**

- The establishment of laser material processing as a viable research field.
- It would provide the NMMU with sufficient, basic knowledge, of the requirements for the integration of its Nd:YAG laser cell into a functional laser cladding platform aimed towards further research of the laser cladding process. The NMMU would thus establish itself as the first tertiary institution in South Africa with the capability to research the process, and the second research institution in South Africa next to the National Laser Centre.
- The platform will not only allow the NMMU to investigate the field of laser cladding but also open up several other research fields closely related to the cladding process such as rapid prototyping/direct metal casting.



### **1.6.2 Towards the development of the process and South African industry**

- The research would contribute towards increasing the “knowledge data base” for the coating of light metals. This would increase the data available for the development and improvement of more accurate numerical process models; statistical relations; control methods; standards; quality control, and the overall improvement of the laser cladding process efficiency.
- The research could contribute towards establishing/strengthening the support structure and knowledge base for future laser cladding applications in the South African industry.

## **1.7 Research path**

A flow diagram of the intended research path is shown in Figure 1.2. The research path consists of four different phases. The outcome of each phase is summarized in a separate chapter. Under each chapter heading a few key focus areas are highlighted for quick reference. Not all the focus areas are covered in the chapters, especially when considering the focus areas mentioned under the heading, chapter two. It was believed that it would not be of any benefit to the investigation to describe the decision making process in such detail.

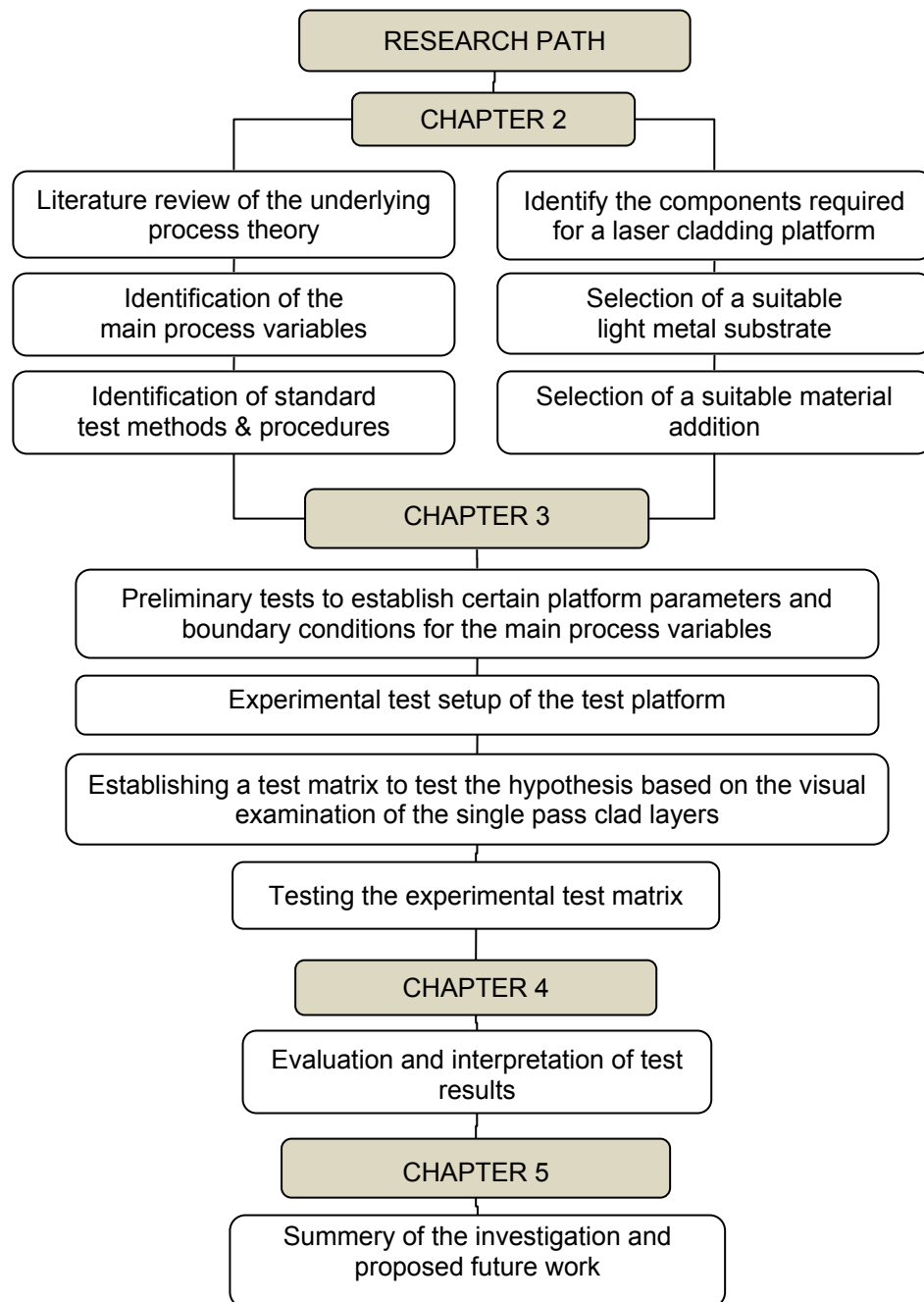


Figure 1.2: Flow diagram indicating the intended research path.

## 1.8 Analysis of the test samples

Figure 1.3 indicates the various clad geometries and characteristics considered for the investigation of the effect of the main process variables on the process response. All tests or measurements will be done in accordance with ASTM standards where applicable.

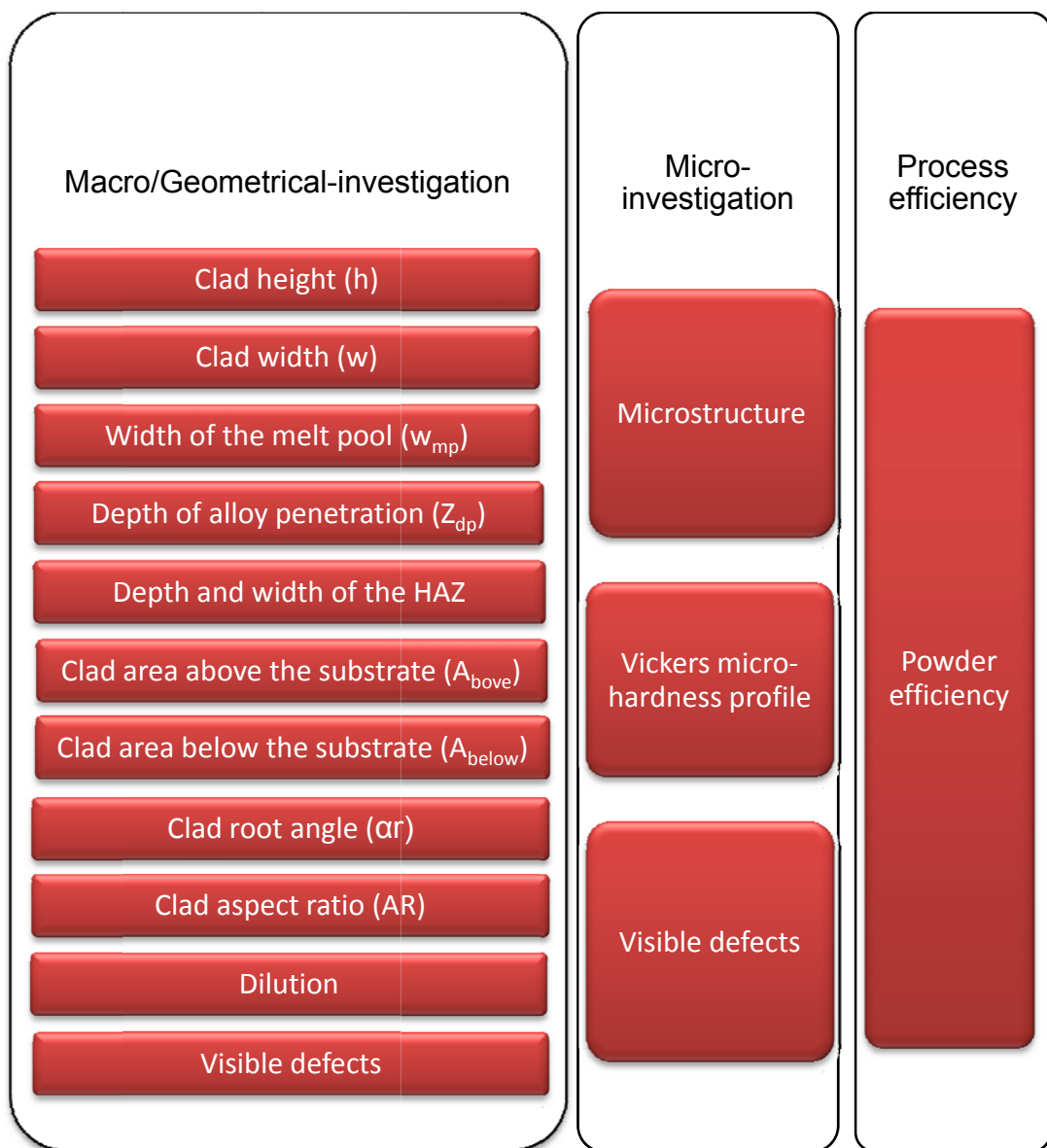


Figure 1.3: Schematic indicating the various aspects of the single pass clad layer that was investigated.

## 2 Introduction to laser cladding

### 2.1 Laser material interaction

#### 2.1.1 Introduction

A key part of laser material processing is a fundamental understanding of laser-material interaction. It allows the engineer to determine the capabilities and limitations of a specific material processing application. In addition it assists the engineer to estimate the optimal processing parameters and conditions. Laser material interaction can be considered by treating light as a particle or wave. In this investigation light will be treated as a wave.

#### 2.1.2 Laser absorption in metals

When laser radiation incident on a material reaches the surface of that material, a fraction will be reflected at the surface and a fraction is absorbed and penetrates into the material. Depending on whether the material is a weak or strong absorber and on the material thickness some radiation will be transmitted through the material (4).

The fraction of the radiation reflected off the material surface is called the reflectivity ( $\rho$ ), the fraction absorbed by the material surface is called the absorptivity ( $\alpha$ ) and the fraction that is transmitted through the material is called the transmissivity ( $\tau$ ) of the material. The definitions of these dimensionless ratios are defined below:

$$(\rho) = \frac{\text{Radiation reflected from material surface}}{\text{Radiation incident on material surface}} \quad (0 \leq \rho \leq 1) \quad (2.1)$$

$$(\alpha) = \frac{\text{Radiation absorbed by material}}{\text{Radiation incident on material surface}} \quad (0 \leq \alpha \leq 1) \quad (2.2)$$

$$(\tau) = \frac{\text{Radiation transmitted through material}}{\text{Radiation incident on material surface}} \quad (0 \leq \tau \leq 1) \quad (2.3)$$

In order to satisfy the first law of thermodynamics the sum of the absorbed, reflected and transmitted radiation must be equal to the incident radiation.

Therefore it can be stated that:

$$1 = \rho + \alpha + \tau \quad (2.4)$$

At this stage it is important to distinguish between two different material types. Materials that do not transmit any radiation ( $\tau = 0$ ) and materials that do ( $\tau \neq 0$ ). These materials are called opaque and semi-transparent materials respectively. Metals and alloys are opaque at visible and infrared wavelengths, except in the case of extremely thin films. For opaque surfaces,  $\tau = 0$  and therefore equation 2.4 can be re-written as (5):

$$1 = \rho + \alpha \quad (2.5)$$

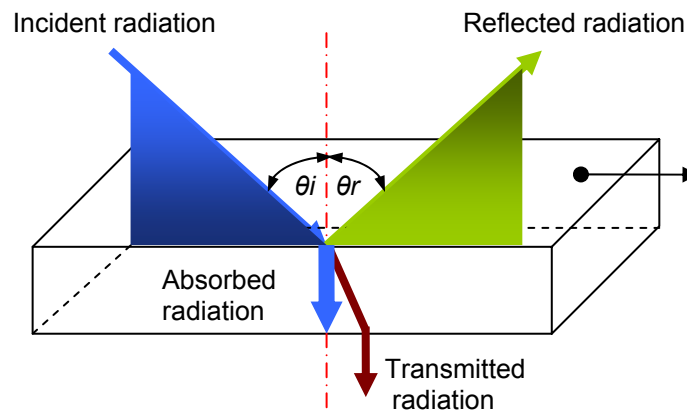


Figure 2.1: Incident radiation on an optically smooth surface.

In metals radiation is absorbed by the electrons in the upper  $10^{-6}$  to  $10^{-5}$  cm of the metal surface. Metals therefore have typical electromagnetic skin depths. The electromagnetic skin depth or absorption length is defined as the depth from the surface where the intensity of radiation has exponentially decreased to  $1/e^2$  from its original value (1). **Bergstrom** remarked that the intensity of an electromagnetic wave is proportional to the square of its amplitude. Its intensity decreases with distance as it passes through an absorbing medium, and could be described according to **Beer Lambert's law** for homogeneous media:

$$I(z) = I_0 \cdot e^{-\alpha z} \quad (2.6)$$

Where  $I_z$  is the intensity at some depth,  $z$ ,  $I_0$  the intensity of the incident radiation and,  $\alpha$  the absorption coefficient (6).

The absorption coefficient describes the attenuation of the incident radiation with depth as it propagates into a material, and depends on the material type, radiation wavelength, and intensity (1) (7).

The manner in which radiation is absorbed is explained by **Steen**. When electromagnetic radiation passes over a small bound charged particle, the particle is set into motion or accelerated by the force exerted on it by the electrical field. Forced vibration of the particle is initiated if the frequency of the radiation does not correspond to the natural resonant frequency of the particle. Since the force induced by the electrical field is very small it is the interaction between photons and electrons which are either bound or free that are considered in this discussion (The process of photons being absorbed by electrons is known as the inverse Bremsstrahlung effect.). As the electrons vibrate it will either re-radiate in all directions or it would be restrained by the lattice phonons. If the electrons are restrained the phonons will cause the structure to vibrate. This vibration is transmitted through the structure by normal diffusion type processes due to the linking of molecules in the structure. The vibration of the structure results in heat generation. If sufficient energy is absorbed melting will occur. Melting occurs when the vibrations become so intense that the molecular bonds are stretched to such an extent that they are no longer able to exhibit any mechanical strength. Heat flow can be described by Fourier's law of heat conduction. (7)

### 2.1.3 The effect of laser and material properties on adsorption

In order to optimize laser material processing it is necessary to couple as much of the incident energy from the laser beam to the work surface. The efficiency with which the energy from the laser can be coupled to the work surface is dependent on the absorptivity ( $\alpha$ ) of the material to the incident radiation. It is thus important to understand what factors influence the absorptivity of a material. (6)

In his investigation, **Bergstrom** identified several laser beam and material properties that influence absorptivity as summarized Table 2.1 (6):

Laser beam properties	Material properties
<ul style="list-style-type: none"> <li>• Intensity</li> </ul>	<ul style="list-style-type: none"> <li>• Composition</li> </ul>
<ul style="list-style-type: none"> <li>• Wavelength</li> </ul>	<ul style="list-style-type: none"> <li>• Temperature</li> </ul>
<ul style="list-style-type: none"> <li>• Angle of incidence</li> </ul>	<ul style="list-style-type: none"> <li>• Surface roughness</li> </ul>
<ul style="list-style-type: none"> <li>• Polarization, p or s</li> </ul>	<ul style="list-style-type: none"> <li>• Surface and bulk defects and impurities</li> </ul>

Table 2.1: The influence of laser and material properties on the absorptivity of a metal surface (6).

Sections 2.1.3.1 to 2.1.3.7 consider the individual effect of each of the properties listed in Table 2.1 on the absorption of laser radiation by a material surface.



### 2.1.3.1 Intensity

According to the *Laser Institute of America (LIA)*, at low intensities the laser beam is almost completely reflected from a reflective material.

As the laser beam intensity increases reflectivity will decrease until eventually adsorption is enough to cause surface melting (4).

### 2.1.3.2 Wavelength and composition

For metals absorption generally, increases with a decrease in the wavelength of the incident radiation (8) as seen in Figure 2.2. The *LIA* remarked that all metals have high reflectivity at long infrared wavelengths. At wavelengths longer than 5  $\mu\text{m}$ , the reflectivity of the material surface is strongly dependent on electrical conductivity.

The *LIA* states that highly conductive metals have the highest values of infrared reflectivity. Therefore the reflectivity of copper is higher than that of aluminium which in turn is higher than that of iron alloys (4). This observation corresponds with the results from an investigation of *Bergstrom et al* on the absorptance of metallic alloys to Nd:YAG and Nd:YLF laser light, summarized in Table 2.2.

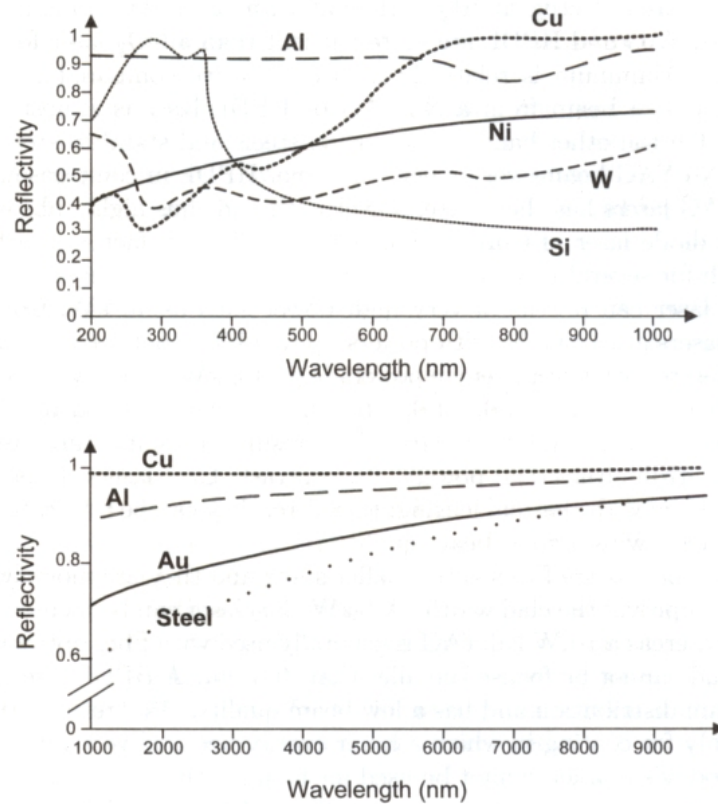


Figure 2.2: The relationship between reflectivity and wavelength for various materials (2).

Material	$\lambda = 1053 \text{ nm}$		$\lambda = 527 \text{ nm}$	
	$\alpha$ (%)	$p$ (%)	$\alpha$ (%)	$P$ (%)
Al 1050-A	16	84	32	68
Al 5251-NS4	24	76	48	52
Al 6082-T6	24	76	39	61
Cu (C106/Cu7n37)	6	94	58	42
Brass (CZ108/Cu DHP)	12	88	38	62
Zinc coated steel	64	36	47	53

Table 2.2: A summary of the reflectivity and absorptivity of various non-ferrous metals at different wavelengths of an Nd: YLF laser (9).

The high reflectivity of metals at long infrared wavelengths and the variation in reflectivity with material composition therefore have an important practical effect on the choice of laser for a specific laser material processing application (4). The high reflectivity of wavelengths near 10  $\mu\text{m}$  means that CO<sub>2</sub> lasers, with a wavelength of 10.6  $\mu\text{m}$ , for example, may experience problems performing certain functions unless the laser power is very high. As previously mentioned the *LIA* stated that this is especially true for conductive metals such as aluminium and copper for which reflectivity is very high at the CO<sub>2</sub> laser wavelength. In such a case it might be better to use an Nd:YAG laser, with a wavelength of 1.064  $\mu\text{m}$  for which reflectivity is lower. The *LIA* further remarked that for ferrous metals, conductivity is not that high and therefore reflectivity would be lower. In the case of ferrous metals there may be enough initial absorption to break down the surface of the metal and increase coupling above its initial value (4).

The typical values for the absorption of different metals at different wavelengths vary significantly in literature. Most values are for chemically pure metals with smooth polished surfaces at room temperature. However, it is still useful for comparison; as an estimate, and for establishing adsorption trends.

### **2.1.3.3 Angle of incidence and polarization**

Reflectivity varies with both polarization and the angle of incidence.

Electromagnetic radiation transports energy through empty space in

oscillating electric and magnetic fields at right angles to each other and the direction of propagation.

Polarization characterizes the relationship between the plane of oscillation of the electrical field and the direction of propagation. Generally only the electrical field is considered since it is the most important when considering laser material interaction (1). If the plane of polarization is in the plane of incidence, the ray is said to be *p*-polarized. If the ray has its plane of polarization at right angles to the plane of incidence it is said to be *s*-polarized.

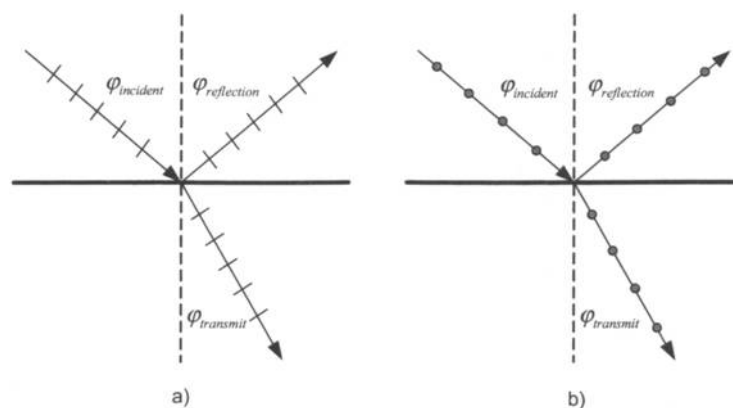


Figure 2.3: (a) *p*-polarized ray; (b) *s*-polarized ray (2)

The variation in the reflectivity of a steel surface exposed to *s*- and *p*-polarized 1060 nm radiation and various angles of incidence is clearly noticeable in Figure 2.4.

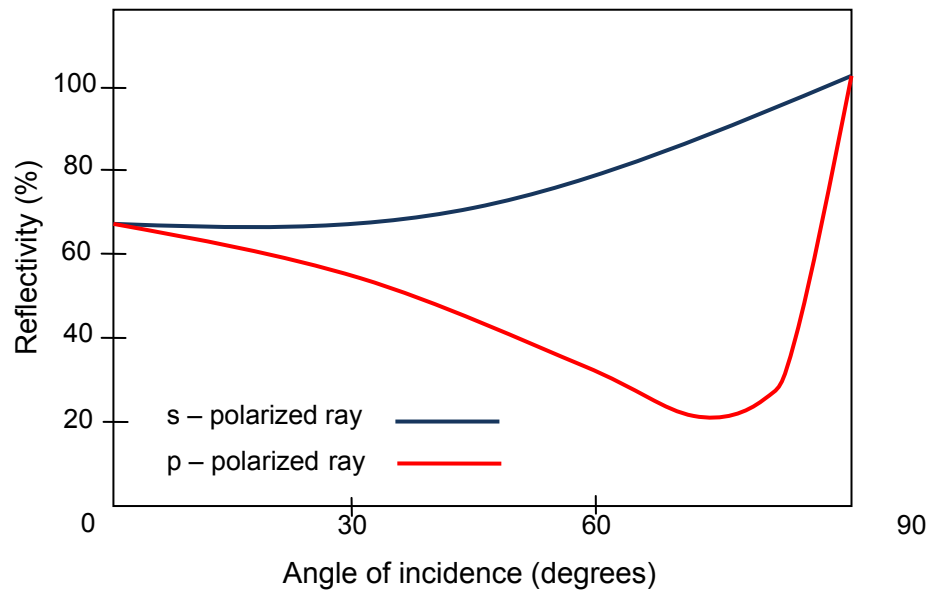


Figure 2.4: Variation in the reflectivity of steel to polarized 1060 nm radiation (7).

The reflectivity of optically smooth metal surfaces can be estimated using Fresnel's relations for directional reflectivity. The angle of incidence where maximum absorption occurs is called the Brewster angle (7) (1).

The laser used for this investigation however is a fibre-delivered Nd:YAG laser. Any polarization that might have existed is destroyed and the beam exiting from a multimode fibre is generally randomly polarized. Thus there is no relationship between the planes formed by the electric field vectors of the individual waves making up the wave train (4). Due to this fact the angle of incidence and polarization will not be discussed in more detail for this investigation.

### 2.1.3.4 The effect of temperature

The variation of absorption with temperature is an important factor in understanding the dynamic behaviour of laser material processing (6). **Steen** remarks that reflectivity decreases with an increase in temperature resulting in a corresponding increase in absorption (7).

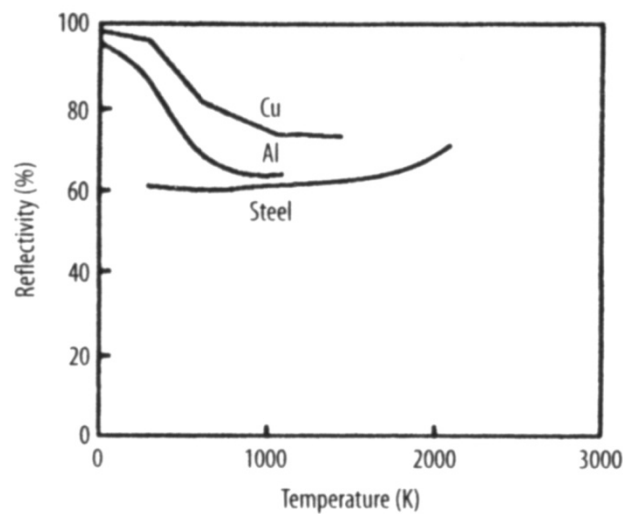


Figure 2.5: The effect of temperature on the reflectivity of various metals exposed to 1.06  $\mu\text{m}$  radiation. (7)

**Stromberger et al** states that the effect of temperature on absorptivity can usually be successfully modelled as a linear function where absorptivity increases with an increase in temperature except around the melting point of a metal. As the material undergoes a solid-liquid phase change, the number of electrons increases simultaneously with metal density and DC resistivity. The result is a significant step-like increase in absorptivity which could be in the order of 100-200% according to **Stromberg et al**. **Stromberg et al** however also mentioned that evidence of unusually high, as well as low, absorptivity at the melting point could be found in literature (8).

According to the *LIA* an increase in the temperature of a solid is always accompanied by an exponential increase in free electrons which results in increased absorption and heating (4).

### 2.1.3.5 The effect of the material surface roughness

Surface roughness could have a significant effect on the absorption of a material at a specific wavelength (7) (6). A surface is optically smooth or perceived as being flat if its surface roughness is much smaller than the wavelength of the laser. Reflection from an optically smooth surface is specular in nature. A surface would appear rough to incident laser radiation when its surface roughness is much larger than the wavelength of the laser. In the case of an optically rough surface, reflection would be diffuse in nature (4).

In general the surface of a material becomes less reflective as its surface roughness increases and reflection becomes more diffuse in nature (4) as indicated by Table 2.3.

Surface roughness	Reflectivity (%)		
	Direct	Diffuse	Total
Sandpaper roughened (1 $\mu$ m)	90	2.7	92.7
Sandblasted (19 $\mu$ m)	17.3	14.5	31.8
Sandblasted (50 $\mu$ m)	1.8	20	21.8

Table 2.3: Reflectivity of the same material prepared with various surface roughness exposed to a CO<sub>2</sub> laser with a normal angle of incidence (7).

This can be attributed to the possibility of multiple reflections off local peaks and valleys of a rough surface before leaving the surface in a non-specular direction, increasing absorption of the incident light. **Steen** stated that there may also be some “stimulated absorption” due to beam interference with sideways reflected beams (7).

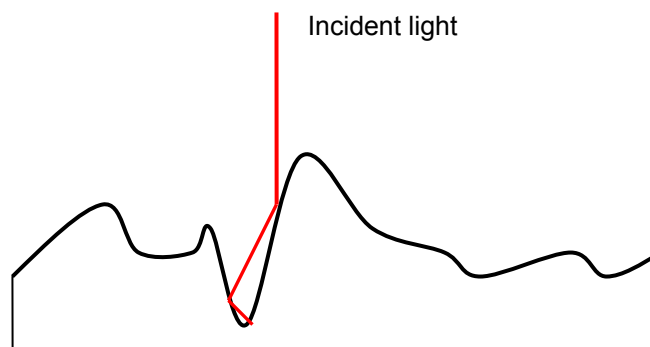


Figure 2.6: Multiple reflections of laser light incident on an optically rough surface (7).

However **Bergstrom** states that not all roughness geometries lead to an increase in absorption. **Bergstrom** remarks that this was observed in a study by **Matsuyama et al** wherein it was showed that peak absorptivity decreased using an asymmetric triangulated surface model (6).

#### 2.1.3.6 The effect of oxide films on the material surface

Oxide layers can cause an increase in the adsorption of a material surface by as much as an order of magnitude. The influence of the oxide layer on adsorption however is coupled to the thickness of the oxide layer and the wavelength of the laser (6).



For example a thin oxide layer on aluminium, up to 100 angstroms in thickness, will significantly increase absorption at wavelengths lower than 1.5  $\mu\text{m}$ . This is however not true for thicker oxide layers (4).

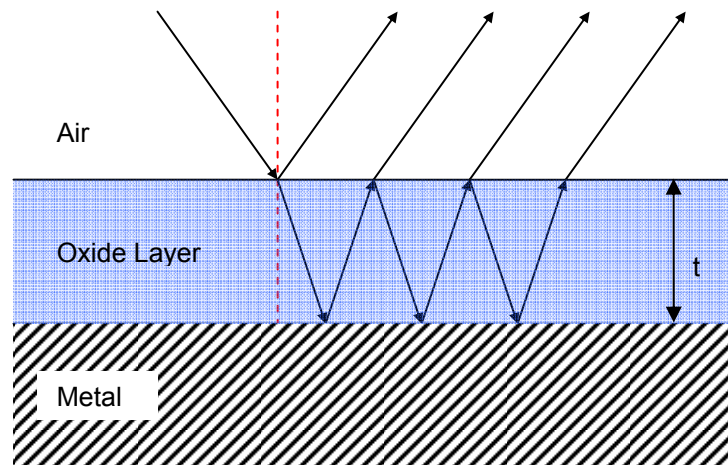


Figure 2.7: Interference phenomena as a result of an oxide layer on the surface of a metal (8).

Increased absorption due to an oxide layer is mainly due to interference phenomena inside the oxide layer. Figure 2.7 shows radiation incident on an oxide layer which is partly reflected and partly absorbed by the metal surface, and partly reflected back again at the oxide-atmosphere boundary (6).

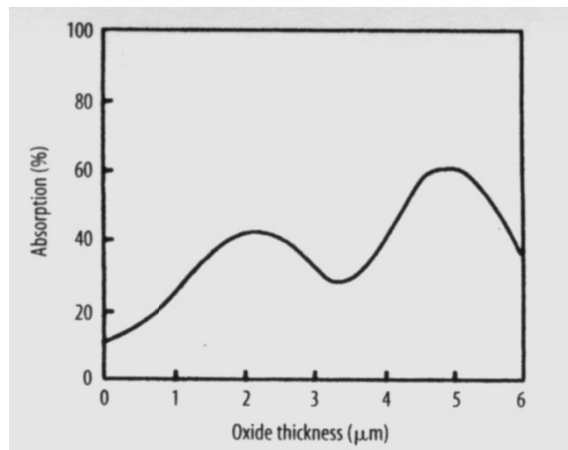


Figure 2.8: Absorption as a function of the oxide layer thickness on steel for 1.06  $\mu\text{m}$  radiation (7).

To accurately determine the effect of oxidation in laser material processing is difficult as the rate of oxidation is coupled to temperature, and therefore oxidation effects are likely to change during laser material processing.

### 2.1.3.7 The effect of surface films and material imperfections

Thin surface layers/films can form on the material surface as a result of a chemical reaction, adsorption of lubricants such as grease and water, or the gathering of electrostatics such as dust particles (4). **Bergstrom** remarks that these surface films/ impurities on or in the material surface could possibly increase the absorption of radiation. For example, electrostatics such as dust particles or abrasive particles left behind by polishing, of different sizes and shapes, could lead to enhanced local absorptivity. Their effect is largely determined by their composition and absorption properties with respect to the laser wavelength being used. Another example is an increase in local absorptivity due to material defects such as cracks, pores and grooves (6).

## 2.2 Laser cladding timeline

The first laser, a ruby laser, was developed by Dr Theodore Maiman in the 1960s. It was a scientific breakthrough that proved to provide the answer to a multitude of scientific and engineering problems.

Laser material processing rapidly developed in the 1970s as a result of the continued improvement in both laser power and efficiency. In particular the development of high power gas lasers, such as CO<sub>2</sub> lasers, in 1975, made laser cutting, welding and hardening a reality. In the late 1970's a pre-placed laser cladding method was used to determine the feasibility of applying dense ceramic cladding on metallic work pieces by Gnanamuthu at Rockwell International Corporation in Thousand Oaks, California.

During this same period several research groups around the world started research projects developing equipment and systems for the development and improvement of the laser cladding process. One of these groups which contributed significantly to the development of laser cladding technology was under the leadership of W M Steen from the Imperial College at the University of London, England, who later moved to the University of Liverpool. Together with Vijitha Weersinghe, Steen introduced laser cladding by powder injection to academia and conducted several investigations to evaluate and develop the process. Another research group, led by Jyoti Mazumber, at the University of Illinois in the United States of America, in the 1980s contributed several fundamental principles of the process.

This research group not only investigated process mechanisms and developed models for the process but they also applied the technology to a variety of metals and ceramics to investigate their ability to be clad and its potential as wear and corrosion resistant layers.

The unique features of the laser cladding process became more apparent and in the 1980s industry started to take notice. Laser cladding was identified as a process with a significant edge over conventional processes used for the application of wear and corrosion resistant layers.

The earliest reported use, in 1981, of laser cladding by industry was the hardfacing of Nimonic turbine blade interlock shrouds for the RB 211 jet engine at Rolls -Royce. Pratt and Whitney, in 1983, used pre-placed laser cladding for hardfacing their nickel-based turbines in JT8 and JT9 engines. Hardfacing of turbine blade shroud tips and z-notches using laser cladding became a technology used by various leading engine manufacturers such as General Electric, Pratt & Whitney, Allied Signal, Rolls - Royce, Allison, Solar and MTU. As a result, several companies such as Avco Everett Metalworking Lasers Inc and United Technologies Industrial Lasers Inc were established in the late 1980s to deal with the for metal coating and repair needs of industry in both North America and Europe.

In the automotive industry several automotive manufacturers in Asia and Europe such as Fiat, Toyota and Mercedes Benz used laser cladding technology for coating engine valve seats.

In the 1980s laser cladding was also widely considered as a technology that could benefit the component repair market. Several different companies and research groups such as Huffman Corporation (USA), Gorham Technologies (USA), Starrag (Switzerland), Sultzer (The Netherlands) and SIFCO Turbine Components (Ireland), to name a few, utilized laser cladding for the repair of turbine blades. Laser cladding was also successfully used for the re-building and coating of the H-dimension of worn turbine vanes, the tip of turbine blades and turbine bolts.

In 1986 a process called stereo lithography, which used ultra-violet lasers to selectively cure photo polymer materials, was patented as a new process for prototyping complex parts. In 1988 the first commercial stereo lithography machine was sold - creating a new industry named rapid prototyping. However most of these systems used polymers and photopolymers. Industry required a new process that could rapidly fabricate metallic prototypes that could be used directly in real machines in order to reduce design time and manufacturing cost. Thus in the 1990s, in response to industry demands, laser cladding technology used for rapid prototyping or layered manufacturing started to receive a great deal of attention and continues to be explored today by various research groups under a variety of names.

According to *Toyserkani et al*, industry and research groups are beginning to recognize the flexibility and potential of laser cladding technology and continue to invest in its development (2).

## **2.3 Major application areas**

### **2.3.1 Coatings**

Coating involves the deposition of thin wear, corrosion or chemical resistant layers on the surface of a substrate material. These coatings can also be used as thermal barrier coatings. The surface properties of the substrate material are altered by the coating material, exhibiting properties that could generally not be achieved through the use of the substrate material alone (2). It thus becomes possible to use a relatively inexpensive base material resulting in significant material cost savings (10).

The majority of published papers relates to metallic coatings in the aerospace, medical and automotive industries. Some of the important material groups used as coating material include titanium based alloys, nickel based alloys, super-alloys, iron-based alloys, aluminium-based alloys and cobalt-based alloys (2).

*Toyserkani et al* remarks that although laser cladding has the potential to be utilized in various metal coating industries, its application is limited due to its overall high cost and low processing speeds. However, with the development of new lasers such as high power diode and fibre lasers, the improvement of

laser efficiency, and the reduction in the cost of new lasers, laser cladding has the potential to be widely accepted by major industries (2).

**Toyserkani et al** also remarks that the leading metallic coating market for laser cladding is in the aerospace industry, more specifically in the coating of commercial aircraft gas turbines. Based on the information released by Gorham Technologies the world original equipment market for coatings used in the commercial gas turbine sector is estimated to be approximately \$460 million per annum (2).

Table 2.4 contains a comparison of some important features of competing coating technologies/methods, as listed by **Toyserkani et al**.

Feature	Laser cladding	Welding	Thermal spraying	Physical vapour deposition
Bond strength	High	High	Moderate	Low
Dilution	Low	High	Zero	Zero
Coating materials	Metals and ceramics	Metals	Metals and ceramics	Metals and ceramics
Coating thickness	50 $\mu\text{m}$ -2 mm	1 – several mm	50 $\mu\text{m}$ -several mm	0.05-10 $\mu\text{m}$
Repeatability	Moderate to high	Moderate	Moderate	High
Heat affected zone	Low	High	High	Very low
Controllability	Moderate to high	Low	Moderate	Moderate to high
Cost	High	Low to moderate	Moderate	High

Table 2.4: Comparison between laser cladding and other coating techniques (2).

Based on Table 2.4, laser cladding offers some significant advantages in that it creates a strong metallurgical bond with the substrate; with low dilution, and a small heat affected zone.

### **2.3.2 Repair and refurbishment**

Repair and refurbishment of high value components such as moulds, dies, turbine blades and military components is another major application area for laser cladding. Laser cladding can be used to “rescue” high value components which are over machined due to design or machining process errors. Conventional methods use welding technology, but these methods are usually destructive due to the high process temperatures and large heat-affected zones across the repair area. This leads to poor mechanical quality, cracks, porosity and very short component life. Laser cladding on the other hand can provide permanent structural repair and refurbishment on many alloys, including alloys such as aluminium which are considered un-weldable by conventional methods.

A good example is the repair of advanced gas turbine engines. These gas turbine engines are fitted with single crystal directionally solidified components in order to achieve higher thermal efficiencies. It is in the manufacturing and repair of these components that laser cladding is considered as a critical/essential technology due to its small heat-affected zone, the control over the depth of the heat-affected zone, high solidification rates, lower dilution and increased cleanliness. **Toyserkani et al** remarks



that in some cases such as oriented airfoil castings that are highly susceptible to recrystallization when exposed to intense heat during conventional processes, it is recognized as the only repair technology (2).

It is well known that the size of the refurbishment and repair market is immense but there seems to be no concrete data that defines its size, according to *Toyserkani et al.* However, *Toyserkani et al* states that considering that the global market for the repair of aircraft engine turbines and compressor blades, used in civil and military applications is estimated to be about \$1.2 billion per annum the potential marked seems enormous (2).

### **2.3.3 Rapid prototyping and tooling**

A relatively new application area for laser cladding is the rapid prototyping and rapid tooling markets which involve the manufacturing of complex components or tools (2).

#### **2.3.3.1 Rapid prototyping**

According to *Toyserkani et al* laser cladding technology has the potential to address the current gap in the market. A survey by the National Center for Manufacturing Science indicated that laser cladding could potentially reduce the time of die production by 40%, if the process is controllable over the dimensions of the product. In the production of surgical tools it has been reported that laser cladding can reduce the amount of production steps from 62 to 7.

In addition, laser cladding also has the potential to produce functionally graded materials. This ability makes it especially suitable for aerospace applications where a light component is required with a hard surface (2).

### **2.3.3.2 Rapid tooling**

In the case of rapid tooling, manufacturers are looking for technologies that are able to produce high value tools and components with high integrity, high density and good surface quality at low manufacturing costs and short manufacturing times. Production of these tools and components such as cutting tools, dies and moulds have traditionally been manufactured by highly skilled tool and mould makers using CNC and electrical discharge machining. Applications of rapid tooling categorized per sector in North America are: consumer products (25%); automotive (24%); business machines (11%); medical (8%); aerospace (8%); government (5%) and the rest 8% (2).

## **2.4 Laser cladding equipment**

### **2.4.1 The laser source**

A laser basically consists of an optical cavity at which ends two mirrors are placed parallel with each other to form an optical oscillator. The optical oscillator is a chamber in which the light oscillates back and forth between the two mirrors, along the optical axis and through the active medium. The active medium is placed between the two mirrors and is responsible for the amplification of the light oscillations through the process of stimulated

emission. In order to activate the active medium, some form of energy input is required. Thus any laser system usually has some sort of pumping system.

This may be a DC or RF power supply in the case of CO<sub>2</sub>, excimer and He-Ne lasers, flash lamps or diodes in the case of the Nd:YAG laser, or it might even be through some chemical reaction such as in an iodine laser. In order to extract useful energy from the oscillating system one of the mirrors is partially reflective allowing some of the light to emerge from the optical cavity as a laser beam. The other mirror is totally reflective. The design of the optical cavity usually centres around the length of the optical cavity and the shape of the mirrors (7).

#### **2.4.1.1 Laser classification**

Lasers can be classified according to their:

- active medium used (Gas, solid, liquid);
- output power (mW, W, kW);
- wavelength (Infrared, visible or ultraviolet);
- operational mode (Continuous wave, pulsed or both);
- application (Cutting, welding, cladding, micromachining etc.)

The active medium is the most widely used method to classify lasers as it is the active medium that determines the principle characteristics of the laser beam (1).

### 2.4.1.2 Suitable lasers for laser material processing

Due to the high power requirements for laser material processing only a few lasers are widely used in laser material processing. These lasers are summarized below:

- CO<sub>2</sub> lasers;
- Nd:YAG Lasers;
- Nd:Glass lasers;
- High power diode lasers (HPDL);
- Excimer lasers;
- Fiber lasers (7).

Laser type	Wavelength ( $\mu\text{m}$ )	Quantum efficiency (%)	Wall plug efficiency (%)
Carbon dioxide	10.6	45	12
Carbon monoxide	5.4	100	19
Nd:YAG	1.06	40	4
Nd:Glass	1.06	40	2
Nd:YAG (Diode pumped)	1.06	40	8-12
Diode GaAs	0.75-0.87	$\approx 80$	50
Diode Gap	0.54	$\approx 80$	50
Excimer KrF	0.248	$\approx 80$	0.5-2

Table 2.5: Typical wall plug efficiencies for industrial lasers. The wall plug efficiency is the percentage of the optical energy extracted from the system compared to the electrical energy input into the system (7).

### 2.4.1.3 The Nd:YAG laser

**Koechber et al** remarks that the Nd:YAG laser is by far the most commonly used solid state laser for material processing. The active/gain medium in an Nd:YAG laser consists of a solid host material, yttrium aluminium garnet ( $\text{Y}_3\text{Al}_5\text{O}_{12}$ ) doped with rare earth ions neodymium ( $\text{Nd}^{3+}$ ) that take the place of yttrium ions [ $\text{Y}^{3+}$ ] in the garnet lattice. The host material is a synthetic crystal with a garnet-like structure which has several unique properties that makes it suitable for laser operation. The YAG host is stable, mechanically robust, physically hard, optically isotropic, and transparent from below 300 nm to beyond 4  $\mu\text{m}$  and more importantly has good thermal stability and a high thermal conductivity. In addition the cubic structure of YAG crystals tends to favour a narrow fluorescent line width that results in a high gain and low threshold for laser operation (11) (12).

The YAG crystal is generally doped with between 0.2 and 1.4%  $\text{Nd}^{3+}$  by weight for use in laser gain applications. This produces an efficient, four-level, Nd:YAG laser gain medium which can be used for both continuous wave (CW) or pulsed operation. Generally the  $\text{Nd}^{3+}$  concentration for a pulsed laser is  $\pm 1.2\%$ . For high power CW industrial applications an  $\text{Nd}^{3+}$  concentration of between 0.4 and 1% is generally recommended with the optimum concentration around 0.8%. The power of the laser system is limited by the steady state temperature and thermal gradient of the laser gain material.

Thus the maximum continuous wave power depends on:

- The volume of the laser gain component;
- Optimizing the doping concentration according to the system cooling efficiency; and,
- The spectral characteristics of the excitation radiation (11).

The maximum power that can be extracted from a Nd:YAG rod is currently  $\pm 400\text{W}/100\text{ mm}$  before serious distortion due to thermal lensing occurs or even cracking of the rod itself (7). Thus for multi-kilowatt Nd:YAG lasers, several rods are arranged in series to produce the high output powers required for laser material processing (13). Nd:YAG crystals are usually produced in rod or slab form for high beam quality. Rods range from about 8-10 mm in diameter and are up to 220 mm in length with several possible end configurations (11).

As mentioned before an Nd:YAG laser is a four-level system in which laser light is generated through the transition between different energy levels of the neodymium ion. This concept is illustrated in Figure 2.9. Species are optically excited from the ground state to the upper pump or absorption bands ( $E_2$ ). Optical excitation is followed by the rapid non-radiative decay to a lower energy level called the upper laser level or metastable state ( $E_3$ ).

Laser transition or energy emission in the form of radiation occurs between the upper laser level ( $E_3$ ) and the lower laser level or terminal state ( $E_4$ ). This transition is associated with a specific quantity of energy and a specific wavelength. Laser transition is followed by rapid relaxation from the terminal state to the ground state ( $E_1$ ) (1).

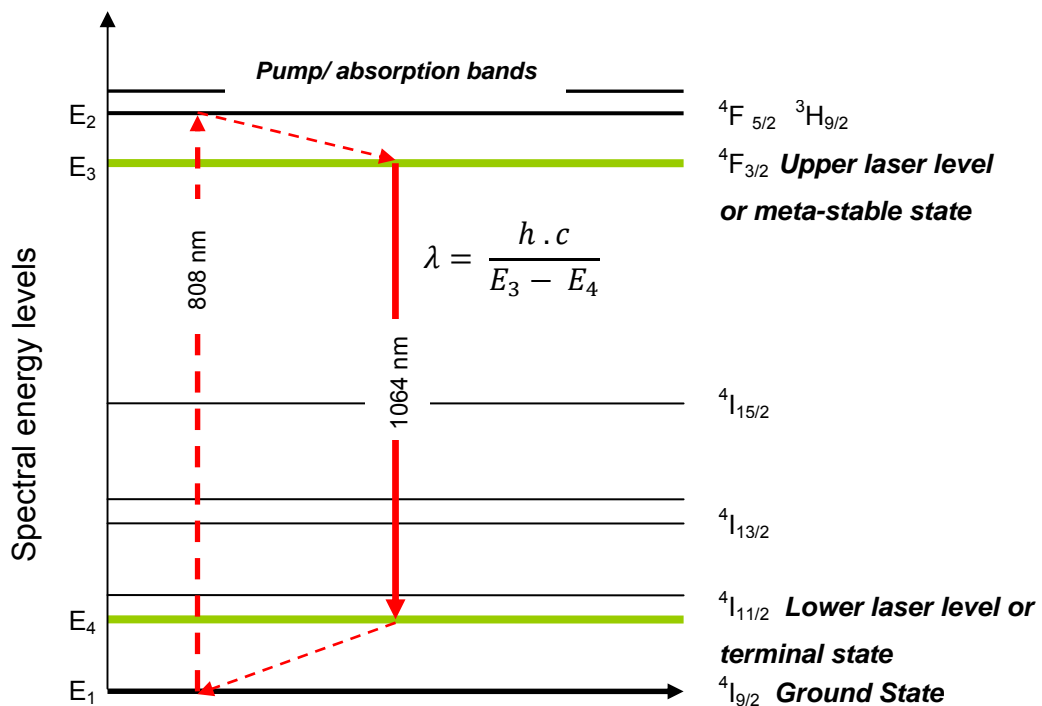


Figure 2.9: Energy levels for neodymium indicating why an Nd:YAG laser is considered to be a four level laser (4) (1).

Optical excitation in pulsed lasers occurs by using krypton flash lamps; in high power continuous lasers through krypton arc lamps and more recently excitation occurs by using laser diodes. The electrical efficiency of an Nd:YAG laser is  $\pm 3\%$  when excitation occurs using gas discharge lamps, however with excitation using diode lasers the overall efficiency increases to  $\pm 10\%$ .

The increase in efficiency is due to the good spectral match between diode laser emission and the Nd:YAG absorption bands. AlGaAs diode lasers emit a narrow band of wavelengths which could be adjusted by varying the Al content so that it falls exactly in the most efficient pumping region for neodymium ions, the 808 nm absorption band.

The improvement in the spectral match results in lower thermal loading on the Nd:YAG crystal which leads to an improvement in beam quality, increase in possible laser output power, and pulse repetition frequency (13).

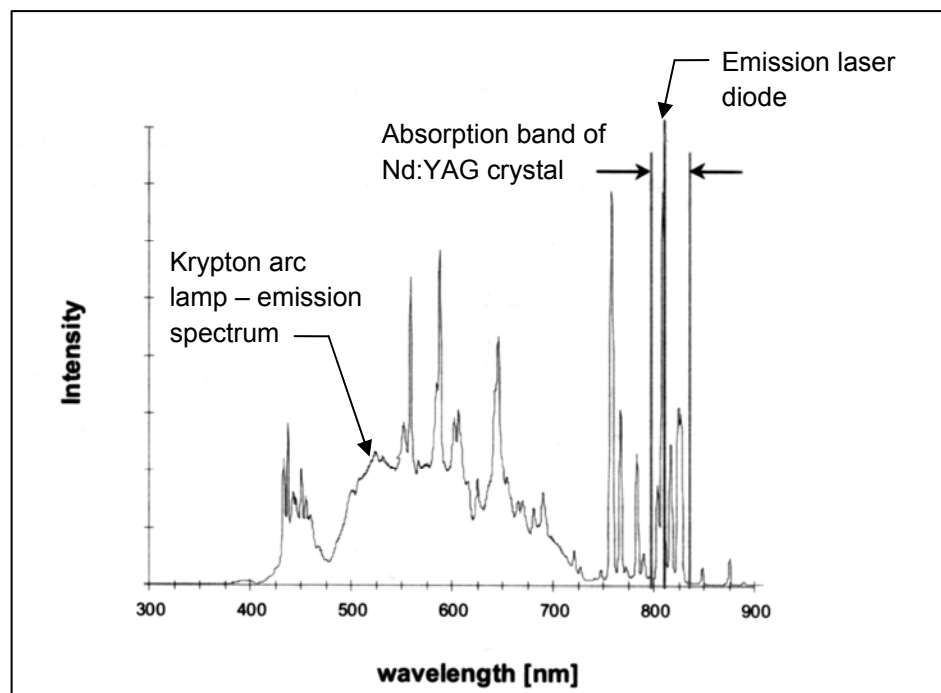
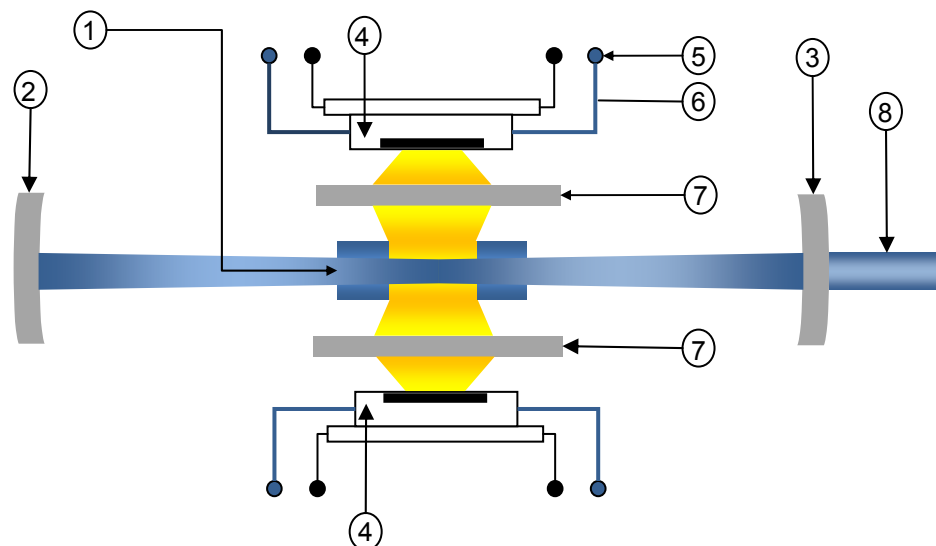


Figure 2.10: Comparison of the spectral match between optical excitation using flash lamps and laser diodes with the peak Nd:YAG absorption band at 808 nm (13).



The principle Nd:YAG emission wavelength is 1064.14 nm at which the index of refraction ( $n$ ) is 1.8169 and the reflectance ( $R$ ) is 0.0841. If used in combination with non-linear optical components, the wavelength can easily be frequency-doubled to produce an output wavelength of 532 nm (7) (11) (12).

The major advantages of an Nd:YAG laser is the ability of the laser beam to be transmitted to the work surface through an optical fibre and the higher absorption of the Nd:YAG laser wavelength by metals compared to CO<sub>2</sub> lasers, making it suitable for processing highly reflective materials such as copper and aluminium (13).



- |   |                      |
|---|----------------------|
| 1. Active medium - Nd:YAG crystal           | 5. Electrical supply |
| 2. Totally reflective rear mirror           | 6. Cooling           |
| 3. Partially reflective out coupling mirror | 7. Collimating optic |
| 4. AlGaAs diode arrays                      | 8. Laser beam        |

Figure 2.11: Principle of a diode-pumped Nd:YAG Rofin DY series laser (13).

#### 2.4.1.4 Laser beam properties

##### Wavelength

The wavelength of a laser is mainly dependent on the active medium used and the geometry of the optical cavity. The laser cavity acts as an optical oscillator in which standing electromagnetic waves are set up whose properties are defined by the geometry of the optical cavity (7).

In order for light in the optical cavity to be amplified it must have a wavelength that satisfies the standing wave condition (1). The standing wave condition states that if that distance is equal to an integral multiple of the lasing wavelength, the waves will add in amplitude by constructive interference. However if the optical cavity is not an exact multiple of the lasing wavelength, destructive interference will occur that will destroy laser action (14).

In general with the exception of tuneable lasers, such as dye lasers, the optical cavity of a laser is designed to produce monochromatic light which effectively has a single wavelength, for example, an Nd:YAG laser has a wavelength of 1064 nm (7) (1). In practice however, an industrial laser operates in a very narrow band of wavelength around a central peak (1).

## **Coherence**

Coherent radiation consists of waves travelling with the same wavelength; amplitude, and wave front. Coherency is thus a measure of the degree to which light waves are in phase in both space and time (1).

Time coherence implies the possibility of predicting the phase and amplitude of a wave after a given time interval between the initial and final observation. If the prediction can be repeated at some later time, coherence of a magnitude equal to the intervals between predictions is said to exist. A wave is spatially coherent if there is a constant phase difference between any two chosen points on the wave front.

## **Transverse electromagnetic/spatial mode**

A laser cavity is an optical oscillator in which longitudinal standing electromagnetic waves are set up that is defined by the geometry of the cavity. Through the interference of these standing waves with each other transverse standing waves emerge from the cavity as the mode structure of the beam (7). The transverse electromagnetic mode (TEM) describes the beam intensity with position in a plane perpendicular to the direction of beam propagation (1).


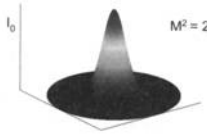








TEM	Cross-section	Distribution
TEM <sub>00</sub>		
TEM <sub>10</sub>		
TEM <sub>11</sub>		
TEM <sub>01</sub>		
TEM <sub>01*</sub>		

Table 2.6: Several TEM modes with Gaussian energy intensity distributions (2).

## Divergence

Divergence is a measure of the increase in the beam diameter as it propagates from the laser source. One of the significant advantages of lasers is its low divergence which allows it to propagate over long distances without a significant change in the beam diameter. A low divergence also implies that a laser can be focused to extremely small diameters. The divergence of a laser beam is generally determined by measuring the beam diameter at various positions with a beam profiler.

### Beam waist

The beam waist refers to the minimum diameter of the beam (Refer to Figure 2.12). The beam waist generally lies within the optical cavity. However if the beam is focused using a focusing lens it forms a new waist diameter. The beam converges to and from the new waist diameter with a far-field divergence of  $\Theta_1$  (13).

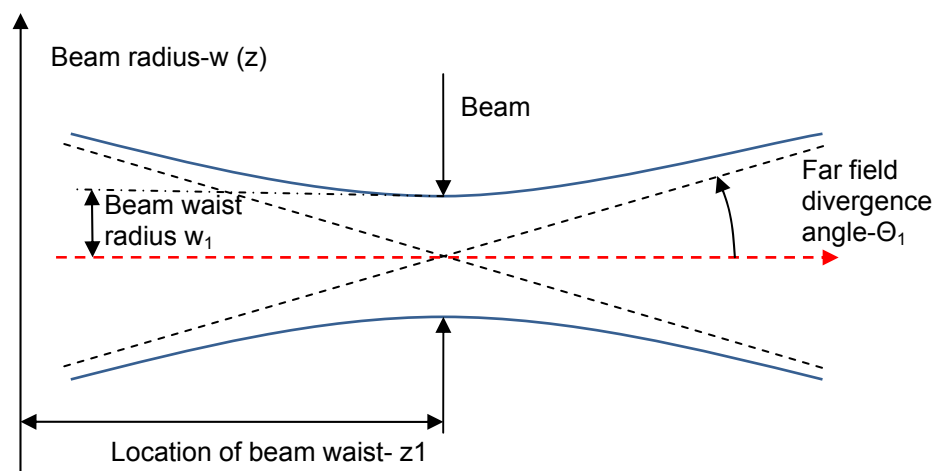


Figure 2.12: Schematic illustrating the various parameters of a propagating beam (13).

### Focused spot size

A laser beam has the ability to be focused to a very small spot size. The diameter of the focused spot size is directly proportional to the wavelength of the beam and inversely proportional to the numerical aperture of the objective lens (1).

## 2.4.2 Fibre optic beam delivery

### 2.4.2.1 The fibre optic cable

The fibre optic core is generally made from extremely pure silica in which impurities, such as transition metal ions, copper, iron, cobalt or hydroxyl, are kept below one part per billion. Pure silica fibres can be produced inexpensively with a high degree of reliability (7).

Bulk transmission efficiencies greater than 99% is possible for Nd:YAG lasers with a wavelength of 1064 nm due to pure silica's excellent transmissive properties for wavelengths between 400 and 1200 nm.

Generally fibre optics are not very efficient in the ultraviolet range below 400 nm as the absorption of silica increases with a decreasing wavelength and would be destroyed by carbon dioxide lasers with a wavelength of 10 600 nm (4). The most common step index fibres have a core diameter of between 0.3 and 1 mm. Fibres with smaller core diameters are difficult to use because of the high power density that the fibre end will be exposed to, and the difficulty of coupling the laser beam into the core (1). The damage threshold of silica fibres is in the order of  $1-5 \times 10^9 \text{ W/cm}^2$ . For safe operation the power density should be 10% less than the damage threshold (1). To reduce the power density on the fibre end, a fibre with a bigger core could be used but then the focus- ability of the laser beam would be compromised. The smallest focused diameter of a multimode fibre is generally equal to the fibre core diameter (7). Fibres with a core diameter bigger than 1 mm are not

recommended due the loss of flexibility and the subsequent introduction of bending losses (1).

#### **2.4.2.2 Transmission losses**

The total losses for a fibre optic delivery system are generally  $\pm 10-15\%$ .

Total losses consists of reflective losses of  $\pm 3-5\%$  at each end of the fibre at the in- and output coupling optics, internal losses of  $\pm 1\%$  in the fibre itself and reflective losses due to the cover slide that provides some protection for the fibre optic output face due to back reflection from the work piece (4) (1).

#### **2.4.2.3 Single mode versus multimode fibres**

##### **Single mode fibres (4)**

Single mode fibres are suitable for transporting light from lasers with a fundamental mode beam (Typically a Gaussian profile with a uniform, coherent phase front). Suitable laser sources are Ar-Ion, high quality Nd:YAG lasers, high quality amplifiers or single mode fibre lasers. Single mode fibres have small core diameters and require strict optical conditions to be met for power coupling in and out of the fibre.

Normal single mode fibres are not designed to preserve the polarization of the optical cavity of the laser. However, if the state of polarization is important, expensive, polarization, preserving single mode fibres can be used.

**Multimode fibres (4)**

According to the *LIA* multimode fibres are the workhorse for transporting high power laser beams from the visible to near infrared. A major advantage of multimode fibres is the simplified coupling optics that can be used due to larger fibre core diameters, and the ability to accept optically incoherent and multiphase wave fronts.

Multimode fibres cannot preserve the polarization of the optical cavity, instead it is scrambled into randomly polarized multiple spatial modes resembling a typical laser speckle pattern. This characteristic of multimode fibres does not affect material processing significantly. For most laser material processing applications the polarization of the laser beam is not important.

The major disadvantage of multimode fibres is the reduction in the intensity of the laser beam due to its bigger core diameters. Another possible disadvantage is broadening of laser pulses in the nano-second and smaller range. Pulse broadening simply means that an optical ray that enters the fibre at a steep angle will be delayed in arrival at the other end when compared to a ray travelling collinear to the fibre core axis.



#### **2.4.2.4 Fibres for Nd:YAG laser beams transmission**

There are basically two main types of optical fibres suitable for Nd:YAG lasers, namely:

##### **Step index fibres (7) (1)**

In a step index fibre the light follows a zigzag path down the fibre until the rays homogeneously fill the core. The output beam has the same diameter as the fibre core and has an intensity profile which is essentially flat topped.

Step index fibres are generally the fibre chosen for laser material processing since the output beam properties are sufficient for most laser material processing applications, and less expensive than graded index fibres.

##### **Graded index fibres (7) (1)**

In a graded index fibre the refractive index parabolically decreases from the middle of the fibre core towards the edge. The ray is transmitted through the fibre in an undulating manner and, due to the parabolic variation of the refractive index of the fibre, the path length of all rays are virtually equal for any angle of propagation. This means that the fibre is able to retain some of the original beam input mode structure.

Graded index fibres produce beams that are more intense. This could be an advantage in certain processes, for instance in welding highly reflective materials where the penetration depth is important.

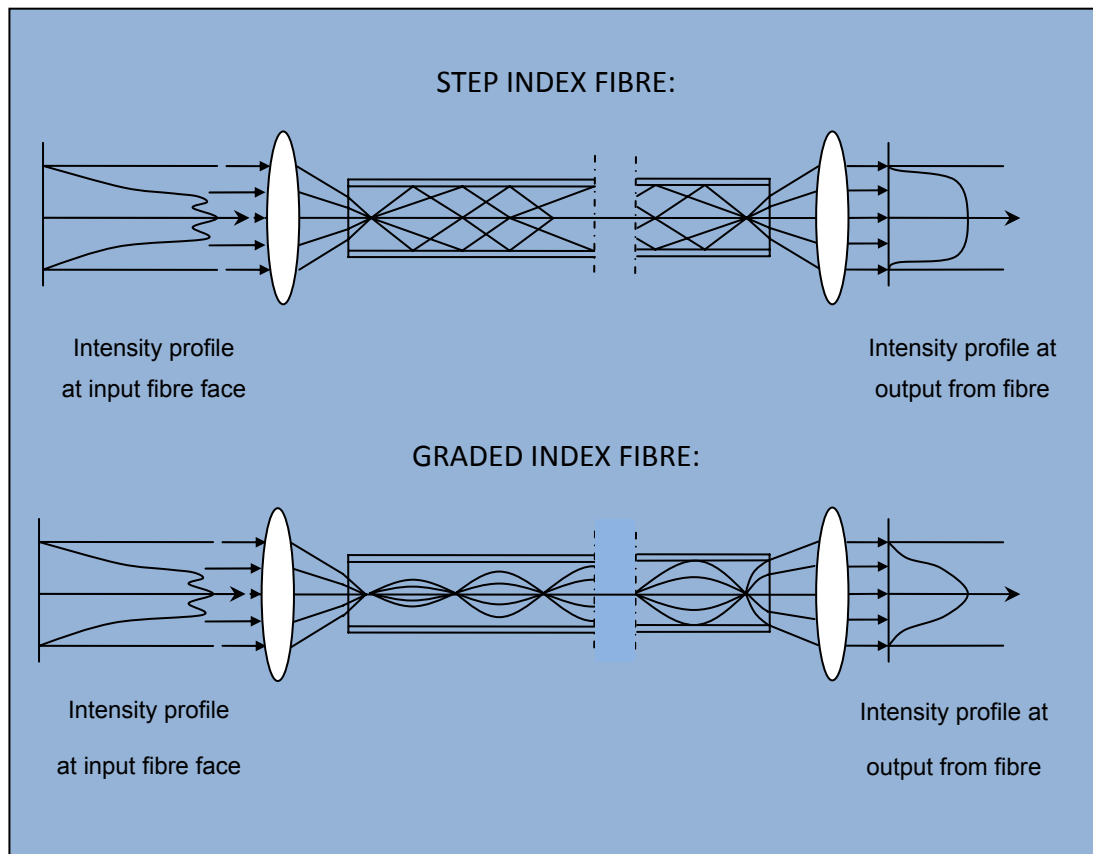


Figure 2.13: The principle of light transmission through step and graded index fibres (13).

#### 2.4.2.5 Advantages and disadvantages of fibre optic beam delivery

Fibre optic beam delivery offers several advantages over conventional beam delivery due to its ability to transmit the laser beam safely to a work surface over long distances; around curves, and to multiple workstations.

The compact size of the fibre and focusing modules provides for easy mounting on a robot system allowing flexible three-dimensional movements and manipulation around a fixed work piece (4). Conventional mirror based beam delivery systems on the other hand require complex motion systems when large multi-axis work envelope stations are used. In addition they

require elaborate beam alignment procedures and are susceptible to contamination and power absorption (1).

Robotic systems are generally not as accurate as fixed beam, moving work piece or multi-axis fixed work piece systems, but is sometimes the best choice when the required process accuracy is not very high, such as in welding applications (4). With the accuracy and repeatability of robots increasing, robot-controlled fibre optic beam delivery systems are becoming more common (1).

Both conventional and fibre optic beam delivery can be used with robots but fibre optic beam delivery is much less complex. Conventional optics for robot operations is very expensive when compared to fibre optics. This means that laser sources for material processing are limited to excimer, Nd:YAG, high power diode and fibre lasers when robot operation is preferred (1). It is important to note that for all Nd:YAG lasers the beam divergence changes with average power output. Thus when conventional optics are used, the spot size varies directly with the divergence angle and gets bigger as the average laser power increases. However in the case of fibre optic beam delivery the fibre core diameter and the focal length of the final focus lens determines the spot diameter and is independent of the average laser power (4).

### 2.4.3 The processing head

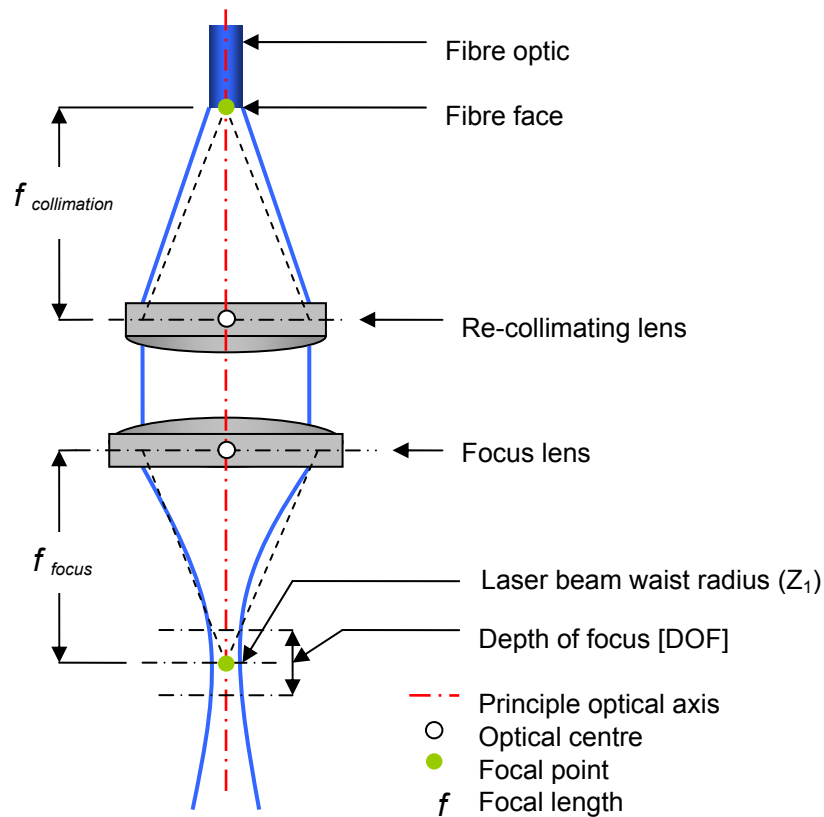


Figure 2.14: Schematic illustrating the re-collimation and focusing of the laser beam as it exits from the optical fibre.

The collimator and processing head contains the out-coupling optics that generally consists of a collimating lens, located in the collimator, and a focusing lens located in the processing head.

The purpose of the collimator- processing head assembly is to re-collimate the laser beam as it exits from the fibre optic and to focus it to the desired diameter. (Refer to Figure 2.14)

As the laser beam exits the processing head it converges to a new beam waist and diverges away from it beyond the beam waist. The minimum diameter to which the beam can be focused is equal to the diameter of the fibre since the focused spot size is simply the product of the fibre diameter and the ratio of the focal length of the focus lens to the focal length of the re-collimating lens. See equation 2.7 below:

$$w_1 = 0.5 \cdot \left[ \phi_f \cdot \left( \frac{f_f}{f_c} \right) \right] \quad (2.7)$$

Where  $w_1$  is the new beam waist radius/focused spot radius,  $\phi_f$  the diameter of the optical fibre,  $f_f$  and  $f_c$  the focal lengths of the focusing and re-collimating lens respectively (15).

A suitable focusing lens should be selected with care, taking into consideration several factors such as: the equipment used in combination with it; the desired beam diameter on the substrate surface; the safe operational distance from the work surface, and the mean power density in the focus of the laser beam for example.

**Schneider** states that the mean power density in the focus of the laser beam can be reduced by either decreasing the laser power or by increasing the focused spot size/new beam waist.

**Schneider** further states that decreasing the laser power should not be considered, since a certain amount of power is required to melt and heat the substrate. **Schneider** instead suggests that a focal lens with a larger focal length should be used. This has the added advantage of increasing the distance between the lens and the work surface reducing the risk of powder particles damaging the lens during laser cladding (10).

#### **2.4.4 The powder delivery system**

The powder delivery system which includes all the components responsible for delivering, controlling and shaping the powder stream plays an important role in the cladding process and clad quality. Section 2.4.4.1 to 2.4.4.3 briefly discusses each of the components that make up the powder delivery system.

##### **2.4.4.1 The powder feeder**

Consistent, accurate, non-pulsating and reproducible powder delivery by the powder feeder is the foundation for successful cladding. A wide variety of powder feeders are available in industry and can be categorized based on their principle of operation. For example gravity-based, mechanical or screw type, fluidized bed or vibrating powder feeders. Some powder feeders combine some of these principles into a single unit (2). **Schneider** states that the development of new powder feeders is directed towards mass flow rate control instead of volumetric feed rate control as well as instantaneous flow variation (10).

The GTV PF 2/2 powder feeder, used in this investigation is a volumetric powder feed unit using a rotating disc similar to the Sulzer Metco TWIN-10-compact. The principle of volumetric powder feeding is explained with the aid of Figure 2.15.

The volume of powder delivered by a powder feeder, based on the principle of volumetric feed rate control, is a function of the predetermined powder deposition volume and the rotational speed of the powder feed disc. Powder is conveyed from the gas tight powder hopper which is at a slight overpressure into the annular groove, of fixed width and depth, in the powder feed disc. The spreader distributes the powder at a defined height across the width of the groove (The width and height of powder deposition is determined by the shape of the spreader unit). The powder is carried through the holder for the suction part out of the annular groove into the anti-static hose and conveyed towards the powder nozzle (16).

A carrier gas is used to convey the powder particles to the nozzle through the anti-static hose. The carrier gas, usually argon, helium or nitrogen, not only conveys the powder but also helps to protect the melt pool from the negative effects of oxidation (10). Argon is the most commonly used carrier gas for Nd:YAG laser applications due to its excellent shielding properties derived from its inert chemistry and the fact that it is heavier than air. In addition it is less expensive than Helium (17).

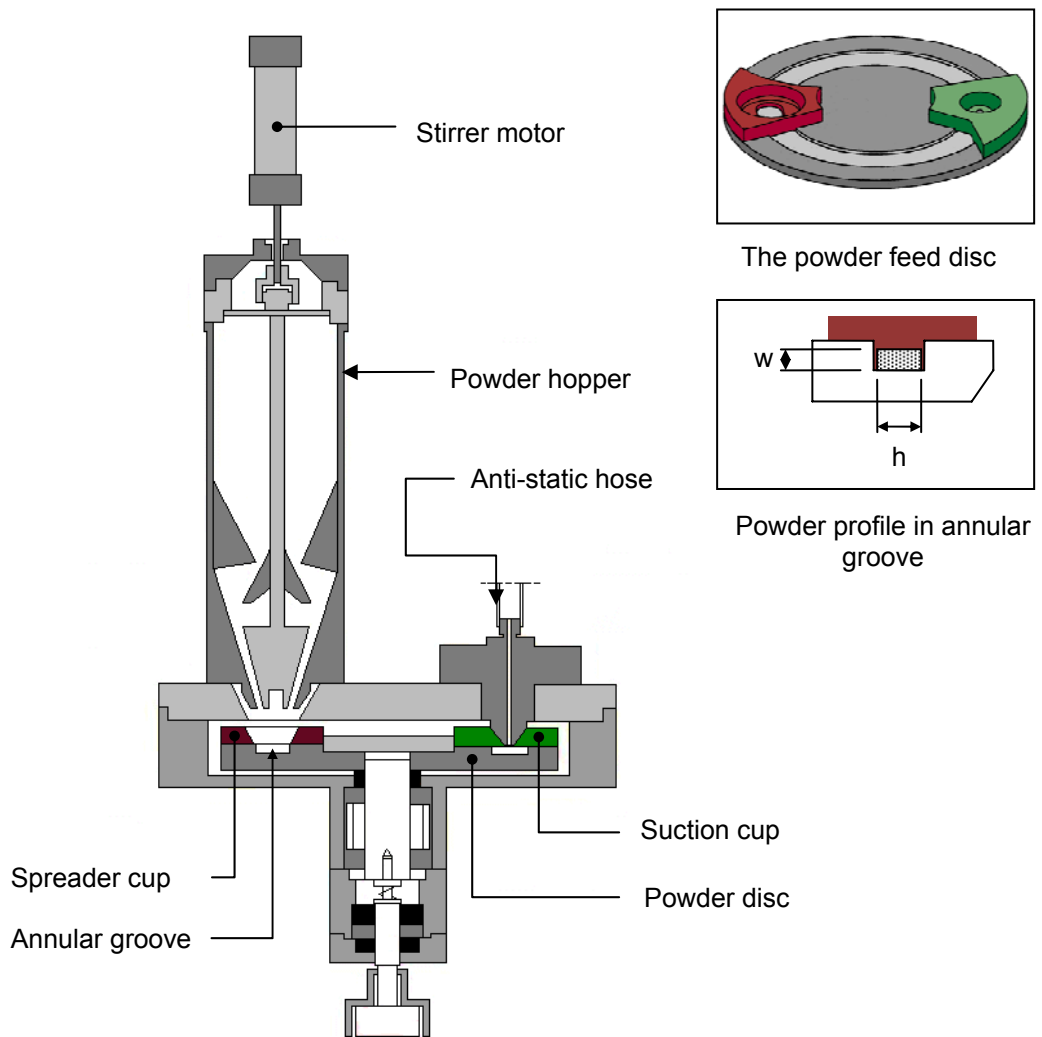


Figure 2.15: The principle of a volumetric powder feed unit using a powder feed disc (16).

The GTV PF 2/2 powder feeder has three controllable inputs: the rotational speed of the powder feed disc; the carrier gas flow rate, and the carrier gas pressure which is fixed and set according to the manufacturer's specifications. Thus of the remaining two variables the rotational speed of the powder feed disc determines the powder mass flow rate and the carrier gas flow rate the powder particle speed exiting the nozzle. According to **Sulzer**



**Metco** the carrier gas setting is independent of the powder flow, and it can be adjusted to convey powders over long distances.

#### **2.4.4.2 The powder splitter**

As its name suggests, the function of the powder splitter is simply to accurately split a single powder stream from the powder feed unit into a number of, generally three, powder streams. The powder splitter is generally located near the nozzle.

#### **2.4.4.3 Powder delivery nozzles**

The nozzle is responsible for shaping and directing the powder stream into the shallow melt pool created on the substrate surface. It forms a critical part of the powder delivery system and knowledge of the nozzle apex angle, the powder focus position, the powder stream diameter at its focus and the velocity of the powder particles are crucial. Together these parameters determine the interaction phenomena between the laser beam, powder particles, carrier gas and the melt pool (2).

Nozzles can be divided into two categories, depending on the orientation of the nozzle work axis relative to the optical axis of the laser beam.

For off-axis nozzles, the nozzle work axis lies at an angle relative to the optical axis of the laser beam while for coaxial nozzles the work axis and optical axis coincide.

The three nozzle types that will be described are the most commonly used nozzles for laser cladding by powder injection and cover most applications encountered in industry. There are however applications that requires specific solutions, such as in the case of cladding cylinder bores in engine blocks. Not only is access restricted but the clad surface is in a plane perpendicular to the cylinder axis. This requires the use of special optics and nozzles or the integration of the two (18).

#### 2.4.4.4 The off-axis nozzle

In powder injection with an off-axis nozzle the nozzle is positioned lateral to the laser beam. The nozzle's position is defined by the angle,  $\theta$ , between the nozzle work axis and the substrate and the stand-off distance ( $l_s$ ) between the nozzle tip and the substrate as indicated by Figure 2.16.

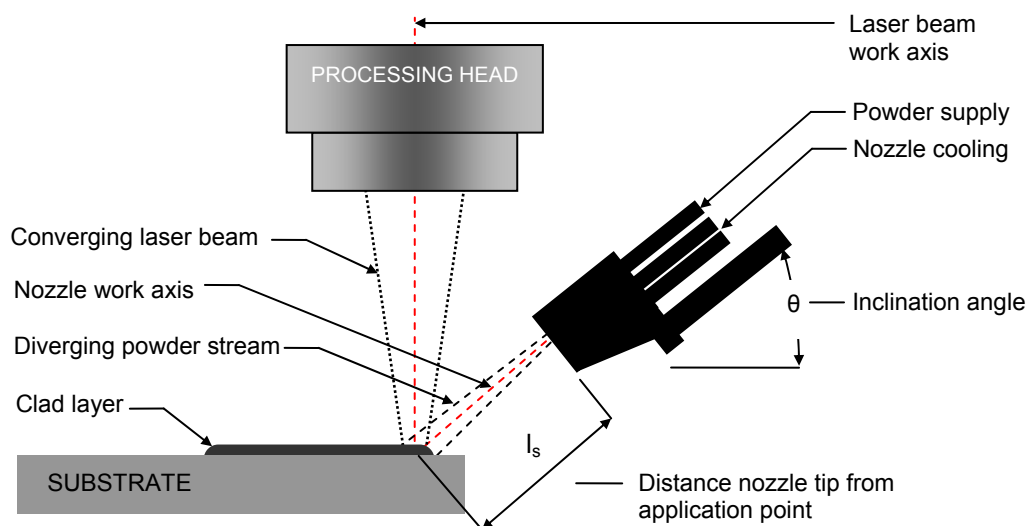


Figure 2.16: Principle of off-axis cladding (18).

There are two different methods of powder injection. In dragging injection, substrate movement is in the same direction as the powder particle flow direction. In stinging injection, the direction of powder particle flow is in the opposite direction relative to the direction of substrate movement. (Refer to Figure 2.17)

Higher powder efficiencies can be achieved using the dragging injection method as more powder is blown directly into the melt pool, as compared to the stinging injection method.

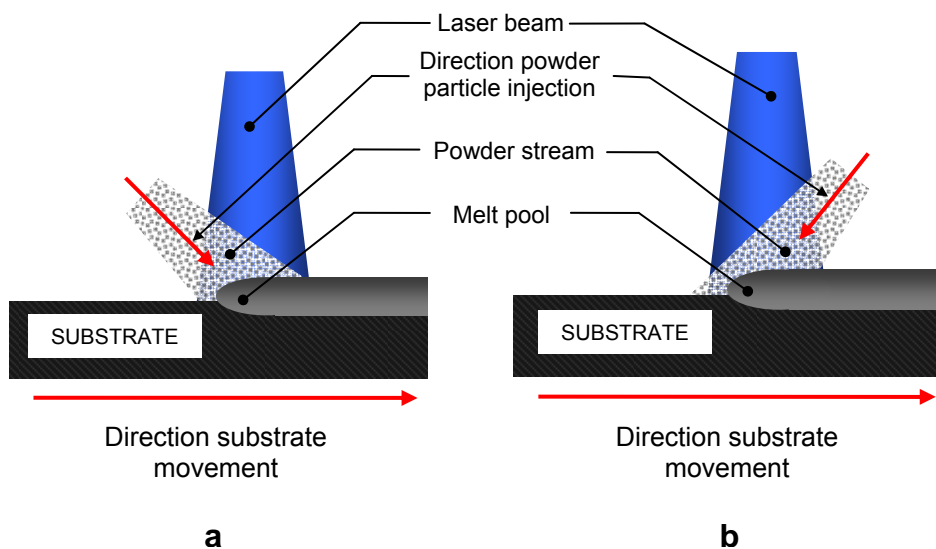


Figure 2.17: Principle of two different off-axis cladding methods. Figure 2.17(a) illustrates dragging injection. Figure 2.17(b) illustrates stinging injection (19)

Since the powder stream diverges as it leaves the nozzle *Weisheit et al* states that the stand-off distance should be as small as possible in order to achieve high powder efficiencies. Typical stand-off distances mentioned

range between 8 and 12 mm. In addition **Weisheit et al** states that an increase in the angle,  $\theta$  (Refer to Figure 2.16), leads to an improvement in powder efficiency due to a reduction in the projected cross-sectional area of the powder stream on the substrate surface (18) (19).

#### **2.4.4.5 Coaxial nozzle types**

##### **Continuous coaxial nozzles (CCN) (18)**

A continuous coaxial nozzle produces a converging-diverging powder stream cone, around and coaxial with the laser beam. Powder fed from the powder feed unit is split into three identical powder streams by a powder splitter. The individual powder streams are fed into a ring-shaped expansion chamber inside the nozzle. Inside the expansion chamber a homogenous powder cloud is formed, which is fed into a cone-shaped slit shaping the powder cloud into a hollow cone around the laser beam. The cone converges to and diverges from its focus point. Continuous cladding for long periods of time requires the nozzle to be cooled. This is generally done by a separate water cooling circuit as the collimator; processing head and nozzle are often made from different materials.

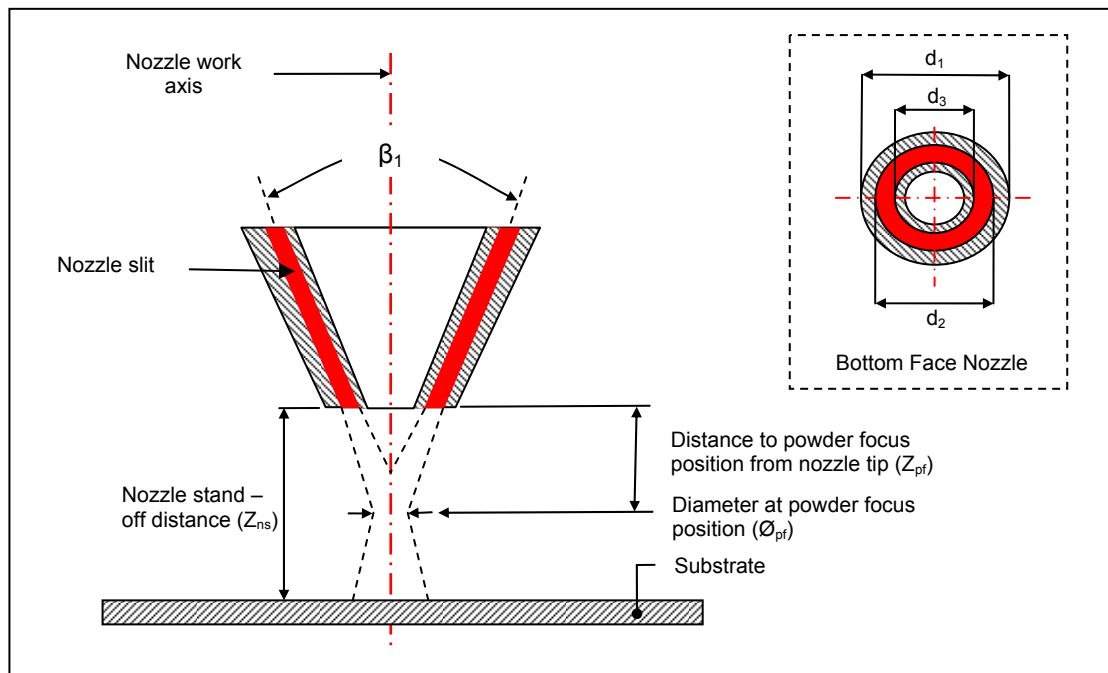
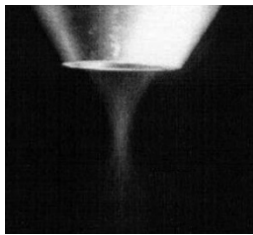


Figure 2.18: Simplified schematic of the exit of a continuous coaxial nozzle.

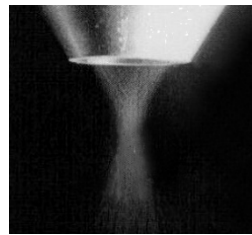
**Weisheit et al** mentions several factors that influence the formation of the powder stream from a continuous coaxial nozzle and how these factors relate to the cladding process. A brief summary is given below: (Refer to Figure 2.18)

- *The apex angle ( $\beta$ )* – The apex angle is the main factor that determines the geometry of the hollow powder cone, the position of the powder focus point relative to the nozzle tip ( $Z_{pf}$ ) and diameter of the focused powder stream ( $\varnothing_{pf}$ );
- *The nozzle slit size* – An increase in the nozzle slit size causes a significant increase in the diameter of the focused powder stream; (Refer to Figure 2.19)

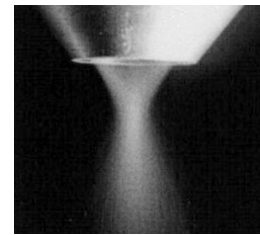
- *The powder feed rate ( $m_p$ )* – An increase in the powder feed rate causes an increase in the diameter of the focused powder stream;
- *The powder particle size* – A reduction in particle size results in a smaller diameter at the powder focus. (Refer to Figure 2.20)



Slit size: 0.7 mm  
 $Z_{pf} \approx 11$  mm  
 $\varnothing_{pf} \approx 2$  mm

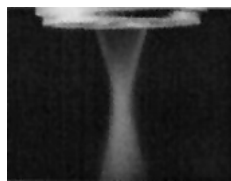


Slit size: 1.4 mm  
 $Z_{pf} \approx 11$  mm  
 $\varnothing_{pf} \approx 2.7$  mm

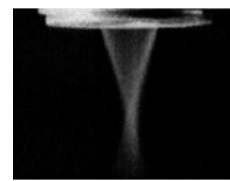


Slit size: 2.1 mm  
 $Z_{pf} \approx 11$  mm  
 $\varnothing_{pf} \approx 3.5$  mm

Figure 2.19: The influence of nozzle slit size on the diameter of the powder stream at its focus position. From experiments carried out by **Weisheit et al** with a Fe-based powder with a particle size of  $-150+50$   $\mu\text{m}$  (18).



Particle size:  $-90 + 45$   $\mu\text{m}$   
 $\varnothing_{pf} \approx 1.8$  mm



Particle size:  $-45 + 22$   $\mu\text{m}$   
 $\varnothing_{pf} \approx 1.5$  mm

Figure 2.20: The influence of powder particle size on the diameter of the powder stream at its focus (18).

**Weisheit et al** states that the typical powder focus diameter of a continuous coaxial nozzle is  $\pm 1-3$  mm. In their investigation the ratio between the laser beam diameter on the substrate surface (2.8 mm) and the powder focus diameter ( $\pm 1.8$  mm) was determined to be 0.67. The highest powder efficiency achieved was 50 % which could be improved if a smaller ratio is used.

**Weisheit et al** further remarks that with all other variables being fixed the highest powder efficiency is achieved when the distance between the nozzle tip and the powder focus position ( $Z_{pf}$ ) is equal to the nozzle stand-off distance ( $Z_{ns}$ ).

**Weisheit et al** also remarked on the importance of the tilt angle of the nozzle. It was determined experimentally that at a tilt angle larger than  $20^\circ$  the powder distribution in the expansion chamber becomes subject to the effects of gravity influencing the homogenous nature of powder delivery, thus affecting the quality of the clad layer.

### **Discontinuous coaxial or three-way nozzle (18)**

In a discontinuous nozzle, three individual nozzles,  $120^\circ$  apart, create three individual powder streams distributed around the laser beam, forming a powder stream focus. (Refer to Figure 2.21)

Unlike in the case of continuous coaxial nozzles, the powder for a discontinuous coaxial nozzle is conveyed directly from the powder splitter to the three individual nozzles through anti-static tubing. According to **Weisheit et al** the factors that influence the geometry of the powder stream for a discontinuous coaxial nozzle is essentially the same as that of a continuous coaxial nozzle except that it is the diameter of the individual nozzles that affect the diameter of the powder stream at its focus and not a nozzle slit.

According to **Weisheit et al** the highest powder efficiency is again achieved if  $Z_{ns} = Z_{pf}$ . However compared to the continuous nozzle the powder efficiency decreases much more significantly when  $Z_{ns}$  is smaller or larger than  $Z_p$  due to the divergence of the individual powder streams. The typical focused core diameter of the powder stream for a three-way nozzle is slightly bigger and lies in the region of 2.5 to 4 mm. It is not as sensitive to being tilted as the continuous nozzle. At a tilt angle of between 0-45° the powder stream is only slightly affected. Discontinuous coaxial nozzles have also been successfully used with a tilt angle up to 90°.



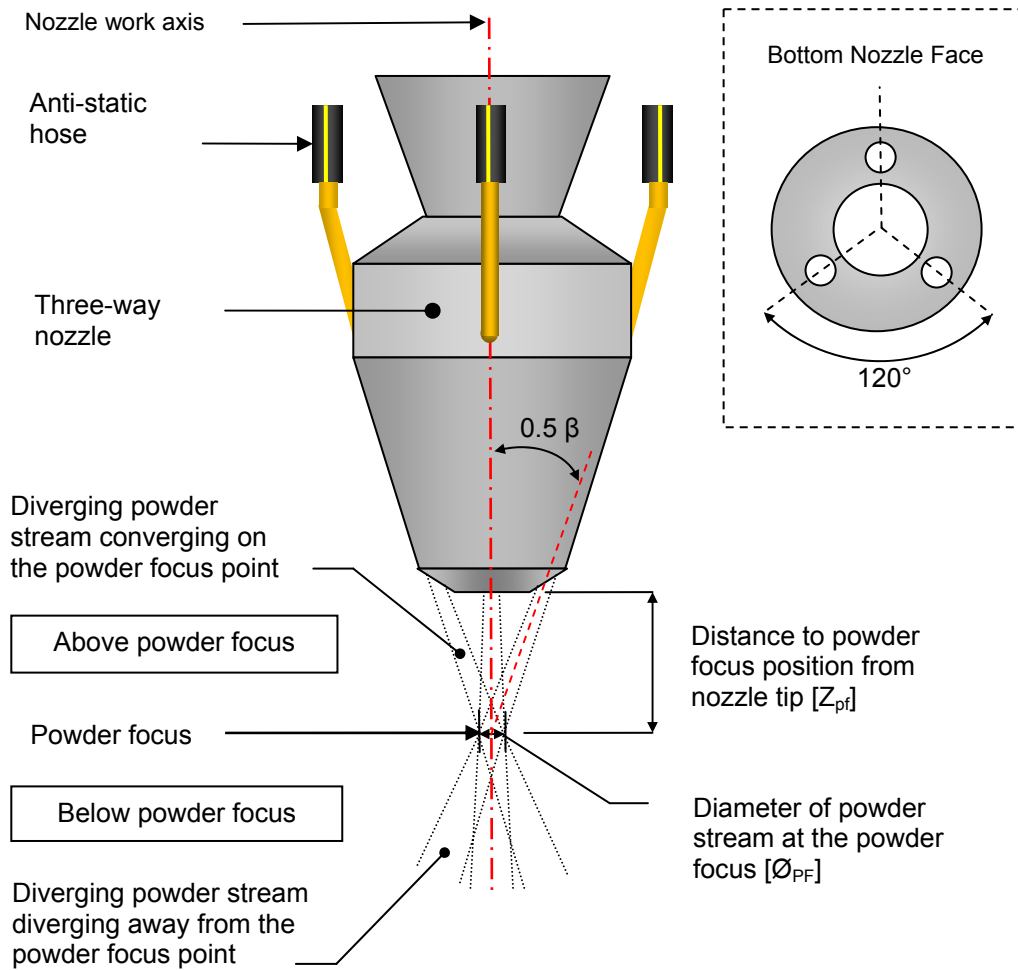


Figure 2.21: A discontinuous or three-way coaxial nozzle.

### Comparison between the three different nozzle types

Off-axis nozzles are mainly used for 2D applications due to the different local cladding conditions produced, depending on the direction in which the substrate moves relative to the powder particle flow direction. When the powder stream is delivered coaxial with the laser beam, all directions of substrate movement are in a plane perpendicular to the powder flow direction which makes coaxial cladding independent of the cladding direction. Thus it

is possible to produce similar clad tracks that are independent from the direction of substrate movement (20). It is this ability that makes coaxial nozzles more suitable for 3D cladding applications (18) (20).

In some applications access is restricted such as in the reconditioning of bearing surfaces on big crankshafts for truck, ship or power plant engines. In such applications the narrow shape and relatively small size of the off-axis powder nozzle provide easier access to the cladding surface (18).

Continuous coaxial nozzles produce a smaller powder focus diameter than discontinuous coaxial nozzles which makes it suitable for applications that require small clad tracks such as in the reconditioning of engine seals and aerofoil tips in turbine engines (18).

The advantage of discontinuous coaxial nozzles is the ability to tilt the nozzle work axis. This ability increases its potential for 3D cladding applications when compared to continuous coaxial nozzles which are sensitive to gravitational effects. Discontinuous coaxial nozzles are thus more suitable for the repair or modification of forming and casting tools for example (18).

## **2.5 Laser cladding in relation to other laser surface treatments**

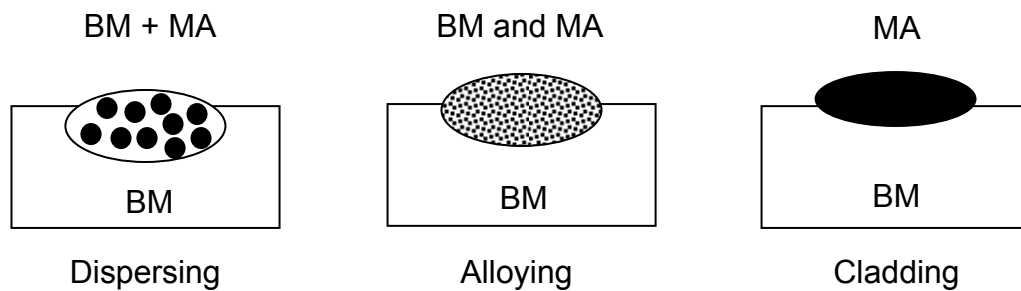
Laser cladding is closely related to two other laser surface treatment processes namely: laser alloying and laser dispersing. Laser cladding, alloying and dispersing can be distinguished from other surface treatment processes in that an additional material with a different composition to that of the base material is added to the base material to form a new surface layer with the desired properties. Other laser surface treatment processes such as laser transformation hardening and surface re-melting are based on a microstructural change in the base material surface itself without any material addition being added to alter the surface properties of the material (10).

All three processes, laser cladding, alloying and dispersing involve the formation of a melt pool on the substrate surface to which a material addition is added. The distinction between laser cladding, alloying and dispersing is the degree of mixing between the material addition and the base material and the depth of the penetration in the base material (10) (2).

Laser dispersing involves extensive substrate melting. The material additions which are generally hard, wear-resistant particles, such as carbides are added to the melt pool. The high solidification rates and short interaction times between the material addition and substrate avoids significant melting of the material addition. The resultant composition consists of the material addition plus the substrate material (21) (10).

Laser alloying involves substantial surface melting, but less than in laser dispersing. Dilution of the material addition in the substrate material is extensive. The composition of the resulting surface layer is a homogeneous or near-homogeneous mixture of the material addition and the substrate material due to extensive intermixing (21).

In laser cladding, surface melting and the dilution of the material addition in the substrate is kept to a minimum. The composition of the resultant surface layer is therefore mostly the same as that of the material addition (2).



BM: Base material MA: Material addition

Figure 2.22: Schematic illustrating the difference between laser dispersing, alloying and cladding in terms of composition and dilution in the base material (10).

## 2.6 Laser cladding methods

Laser cladding methods can be divided into two main categories based on the amount of processing steps involved in the cladding process, namely:

1. Pre-deposition laser cladding;
2. Co-deposition laser cladding (10) (2).

### 2.6.1 Pre-deposition laser cladding

Pre-deposition laser cladding is one of the simplest cladding methods and one of the most common techniques used in early investigations (1) (10).

Pre-deposition laser cladding is a two step process in which the material addition is pre-deposited onto the substrate before irradiating it with a laser source. The coating material/material addition may be in the form of dry powder, wire, strip, foil, sheet, tape, mat or slurry. The most common pre-deposition process is cladding with pre-placed powder. The powder is often mixed with an organic binder, forming a powder paste (1).

The first step in pre-deposition cladding involves the deposition of the coating material/material addition onto the substrate material. The second processing step involves scanning the material addition with a laser source. Heat input from the laser beam generates a melt pool on the surface of the material addition, which is initially thermally isolated from the substrate. Through continued heat input the melt pool propagates first to the interface between the material addition and the substrate and then into the substrate itself.

The amount of heat input has to be carefully controlled to ensure a good metallurgical bond between the coating material and the substrate, and to prevent excessive melting of the substrate that would increase dilution of the material addition (10) (1) (7) (2). (Refer to Figure 2.23)

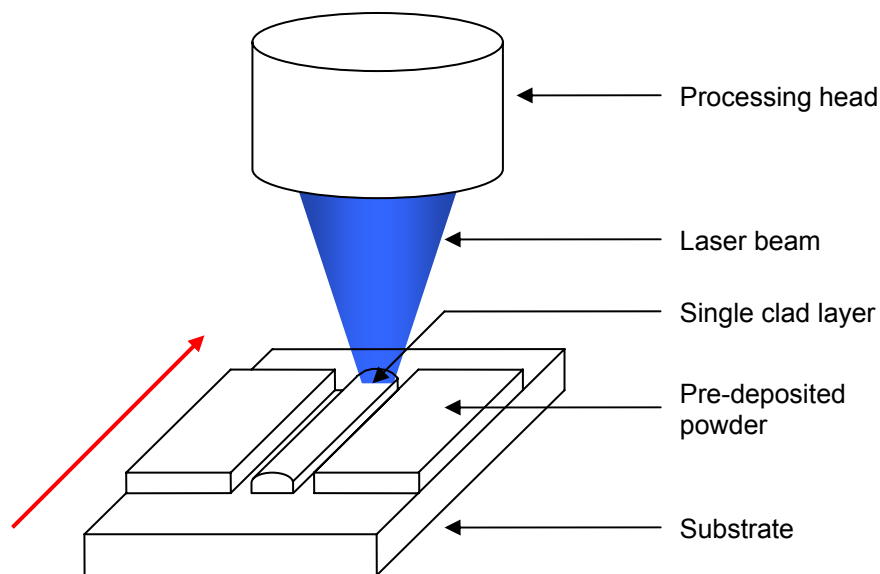


Figure 2.23: The principle of pre-deposition laser cladding. The red arrow indicates the scanning direction of the laser beam (10).

#### 2.6.1.1 Disadvantages of pre-deposition laser cladding

- Requires a high energy input;
- It is extremely difficult to achieve a good fusion bond without high dilution;
- Part complexity is limited;
- Powder is easily blown away by the shielding gas, which makes the effective prevention of oxidation difficult;

- It is difficult to achieve a uniform bed thickness of the pre-deposited material addition;
- An *in situ* change in the composition of the material addition is not possible (1) (7).

Several processing methods have been developed to overcome some of these disadvantages. Dry powder is often mixed with an organic (1) or chemical (10) binder to form a powder paste, ensuring that it sticks to the substrate and preventing it from being blown away by the shielding gas employed. A suitable binder should be chosen with care as these binders generally evaporate during processing, possibly leading to porosity and other defects in the clad layer (1) (10).

The material addition may be pre-deposited by a suitable thermal spray process, in which case the laser beam is used to re-melt the material addition. This method results in a sound metallurgical bond with the substrate, refined grain structures and reduces porosity. The commercial application of such a process is however limited due to the fact that it involves two separate processing steps (1).

A uniform and controllable depth of alloy paste can be pre-deposited onto the substrate ahead of the scanning laser source by employing readily locatable mats that spread the paste evenly over the substrate. Few material additions are available in this form, which reduces its application potential (1). Material

addition in chip or foil form may be pre-placed in the desired locations on the substrate material. These types of material addition can readily be applied to contoured shapes and the amount of material is easily controlled. They melt readily, forming a good bond with the substrate and porosity is generally avoided.

However as with powder pastes, material additions in chip or foil form is not available in a wide variety of alloys and the efficiency of energy usage is normally lower than in the case of co-deposition powder feeding (1).

Pre-deposition laser cladding is most suitable for producing single clad tracks and cladding flat surfaces. It is possible to produce clad tracks adjacent to each other forming a coating, but it generally results in increased dilution.

The reason for this is illustrated in Figure 2.24. As the laser beam is scanned across the pre-deposited material addition, the material addition starts to melt. The width of the melt is closely related to the width of the laser beam on the substrate. As the beam leaves the area the molten material starts to cool down and contract due to surface tensions. Owing to the contraction of the molten material addition the surface of the substrate directly adjacent to the clad track, is no longer covered with the pre-deposited material addition anymore.

As the laser scans the surface of the material addition adjacent to the first track, and a portion of the first clad track to form the second track, the area



not covered with the material addition, exposed during the formation of the first clad track, is exposed to direct laser radiation. This area thus experiences excessive heating resulting in an increase in dilution (10).

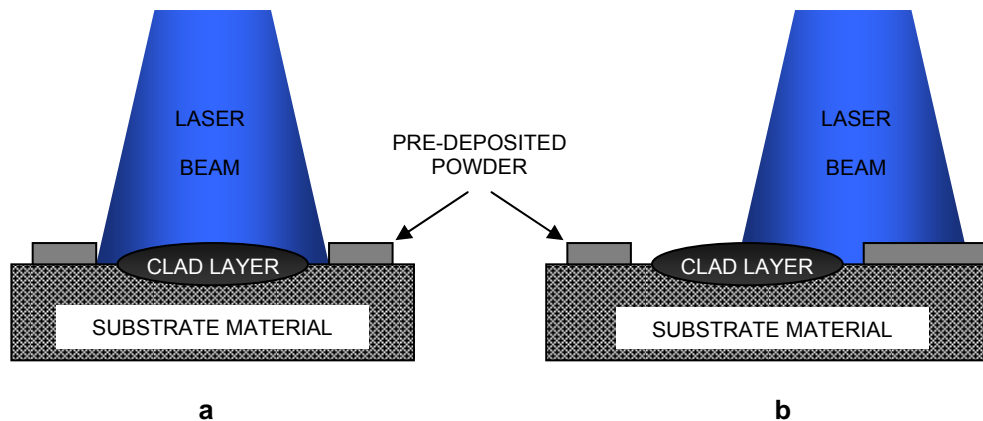


Figure 2.24: (a) Illustrates how the molten coating contracts when irradiated by the laser source. (b) Illustrates how contraction exposes the substrate increasing dilution in the adjacent coating.

In general, it could be said that the major disadvantage of pre-deposition laser cladding is that it requires two processing steps; thus the industrial application thereof is limited when considering economical constraints.

### 2.6.2 One step laser cladding with wire feeding

In one step wire feed laser cladding the material addition is delivered to the substrate in the form of wire. The wire is fed into the interaction area/melt pool under laser irradiation forming a coating with a good fusion bond with the substrate (19).

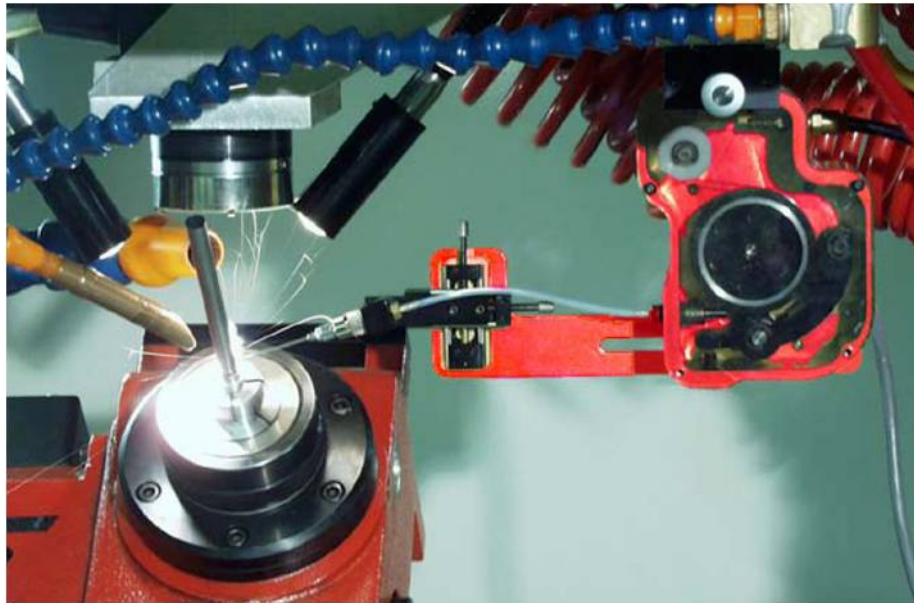


Figure 2.25: One step laser cladding with wire feeding (22).

The advantages of wire feed laser cladding are a relatively clean working environment when compared with the powder delivery method and almost 100% efficient use of the material addition which is less expensive than powder additions. There are however also several disadvantages. Coupling between the wire and the laser is less efficient than in the powder delivery method (21). The wire creates a shadowing effect, reducing coupling between the laser beam and the substrate. Therefore either the laser power needs to be increased or the wire preheated (21). In addition wire feeding requires accurate control of the wire feed rate and precise positioning of the wire which is in contact with and should not disturb the melt pool (10). This makes dilution difficult to control (19). Another major disadvantage is the availability of the various cladding alloys in wire form (1) (19).

### 2.6.3 One step laser cladding with powder injection

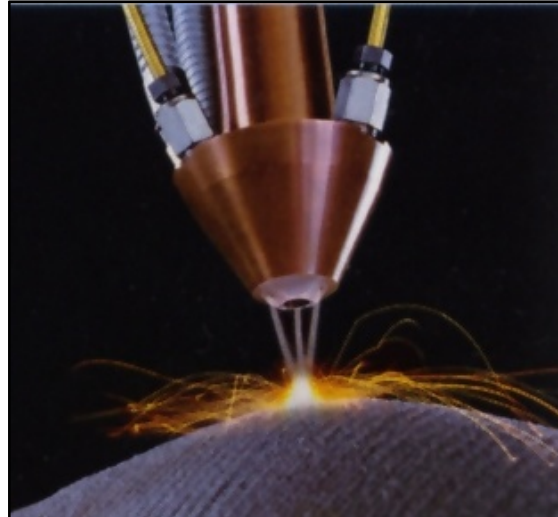


Figure 2.26: One step coaxial laser cladding by powder injection using a three-way nozzle (23).

Laser cladding by powder injection is the most common laser cladding method used. It is one of the few cladding techniques which has a well defined heated region, a fusion bond with low dilution and is easily adaptable to automatic processing (7).

In coaxial one step laser cladding by powder injection the powder is delivered coaxially with the laser beam. As the laser beam passes through the powder particles a certain percentage of the laser energy will be absorbed while a certain percentage will be reflected by the powder particles reducing the intensity and changing the energy distribution of the laser beam on the substrate surface (3).

**Schneider** states that laser power attenuation by the powder particles increases linearly with an increase in the powder mass flow rate but that an increase in laser power does not result in a corresponding increase in laser power attenuation (10).

Reported laser power attenuation values range between 1-9 % of the total laser power for off- axis laser cladding. A percentage of laser power attenuation is due to absorption while the majority seems to be due to reflection off the powder particles (24) (10).

The remaining energy from the laser beam, not absorbed or reflected by the powder cloud, is absorbed or reflected by the substrate surface creating a very shallow melt pool into which the powder particles are blown. Surface tension gradients are the main driving force for fluid flow within the melt pool causing the powder particles to be mixed rapidly within the melt pool (2).

**Schneider** remarks that an investigation by **Picasso** showed that convection is an important factor to consider in explaining the temperature and velocity fields within the melt pool. **Schneider** thus states that the shape of the melt pool is governed by convective flow which is mainly driven by surface tension gradients induced by temperature differences on the surface due to absorption of energy from the laser beam (10). As the laser source moves away rapid solidification takes place resulting in the formation of the clad layer.

## 2.7 Laser cladding process variables

According to *Oliveira et al* an accurate description of the laser cladding process is complicated by the amount of process parameters involved, physical phenomena and by multiple interactions taking place during the cladding process (20)(Refer to Figure 2.27).

Physical phenomena include mass and heat transfer, melt pool dynamics, phase transformations etcetera. Interactions include the interaction between the laser beam and powder stream, laser beam and substrate, powder stream and melt pool, powder stream and un-melted substrate etcetera (20) (10) (2).

The main process variables that influence the operational cladding process window are laser power ( $P$ ), the laser scanning velocity ( $v_s$ ), the powder feed rate ( $m_p$ ) and the carrier gas volume flow rate ( $v_g$ ) (20).

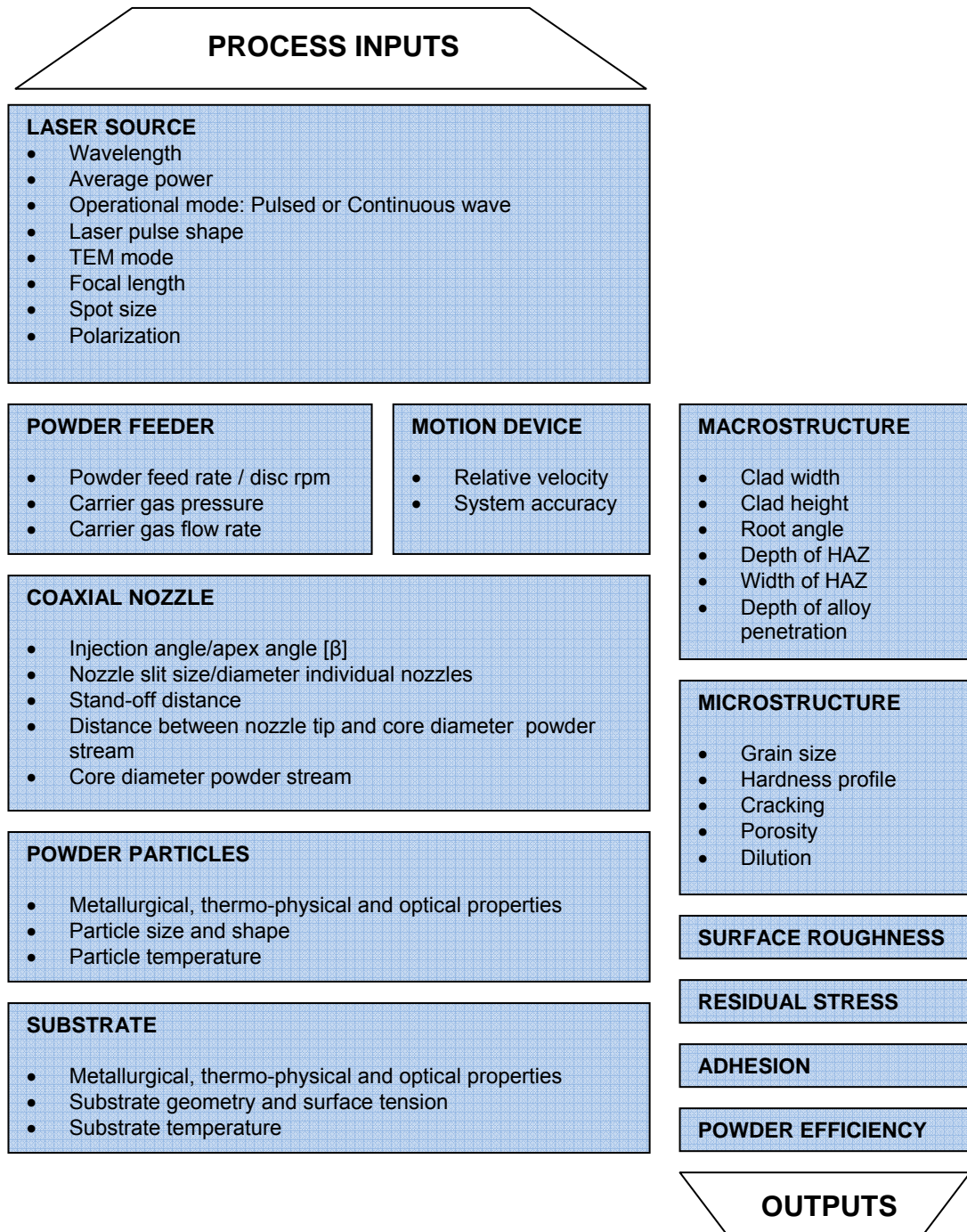


Figure 2.27: Process variables that influence the laser cladding process and quantitative outputs (2) (10).

## 2.8 Laser cladding process models

*Toyserkani et al* states that models based on physical laws contribute to the better understanding of the cladding process and a precise model can support the required experimental research to develop laser cladding.

*Toyserkani et al* continues by listing several steady state and dynamic models developed by researchers summarized in Table 2.7 after which several of these models are discussed in more detail. One such model is the lumped model which is useful in gaining an understanding of the energy distribution within the cladding process and will be discussed in more detail in section 2.9.

Researchers and date	Model description
<i>Chande et al. 1985</i>	<i>Numerical model to obtain convective diffusion of matter in the melt pool.</i>
<i>Kar et al. 1987</i>	<i>Analytical model to obtain a diffusion model for extended solid solution</i>
<i>Hoadley et al. 1992</i>	<i>Numerical model to obtain the temperature field in a longitudinal clad track</i>
<i>Lemoine et al. 1993</i>	<i>Analytical model to determine powder efficiency.</i>
<i>Picasso et al. 1994</i>	<i>Numerical model to obtain clad geometry and melt pool temperature</i>
<i>Picasso et al. 1994</i>	<i>Numerical model to determine fluid motion and melt pool shape</i>
<i>Jouvard et al. 1997</i>	<i>Analytical model to obtain critical energies for Nd:YAG laser cladding</i>
<i>Colaco et al. 1996</i>	<i>Geometrical analysis to obtain clad heights and powder efficiency</i>
<i>Romer et al. 1997</i>	<i>Analytical model to obtain the temperature of the melt pool</i>
<i>Kaplan et al. 1997</i>	<i>Numerical model to obtain powder particle temperature, melting limits and melt pool cross-section</i>

*Table continued*

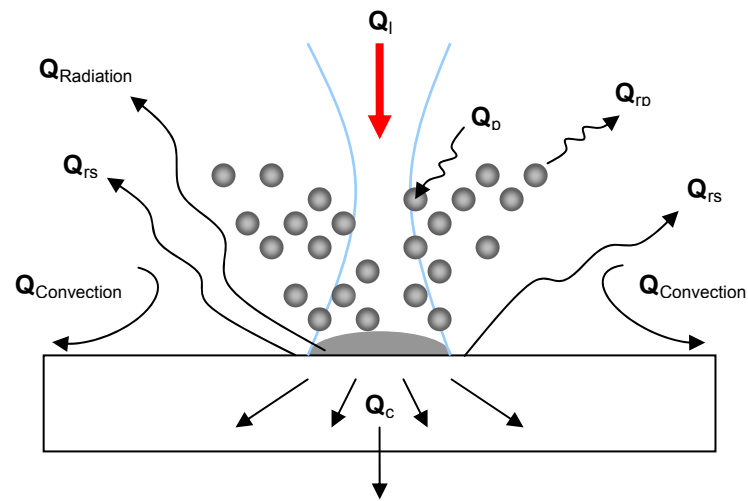
<b>Frenk et al. 1997</b>	<i>Analytical model to obtain the total power absorbed by the melt pool</i>
<b>Lin et al. 1998</b>	<i>Numerical model to determine the powder catchment efficiency</i>
<b>Bamberger et al. 1998</b>	<i>Analytical model to obtain the depth of the clad and melt pool temperature</i>
<b>Romer et al. 1990</b>	<i>Stochastic model to determine the melt pool temperature</i>
<b>Kim et al. 2000</b>	<i>Numerical model to determine the melt pool shape and dilution</i>
<b>Toyserkani et al. 2002</b>	<i>Neural network and stochastic models to determine the clad height</i>
<b>Toyserkani et al. 2003</b>	<i>Numerical model to obtain the clad bead geometry</i>
<b>Zhao et al. 2003</b>	<i>Numerical model to obtain dilution and the melt pool temperature</i>
<b>Labudovic et al. 2003</b>	<i>Numerical model to obtain dimensions of fusion, residual stress and transient temperature profiles.</i>

Table 2.7: Various models describing the cladding process (2).

## 2.9 Energy distribution in laser cladding with powder injection

In order to describe the distribution of energy in the laser cladding process consider the energy balance of the cladding process at the hand of a lumped model as described by **Toyserkani et al.** In a lumped model time is the only independent variable which allows for the use of simple differential equations as opposed to partial differential equations. The energy balance can be expressed by the equation below:





$$Q_c = Q_l - Q_{rs} - Q_L + Q_p(\eta - 1) - Q_{rp} - Q_{radiation} - Q_{convection} \quad (2.8)$$

Where  $Q_c$  is the total energy absorbed by the substrate (J),  $Q_l$  is the laser energy (J),  $Q_{rs}$  is the reflected energy from the substrate,  $Q_L$  is the latent energy of fusion (J),  $\eta$  is the powder efficiency,  $Q_p$  is the absorbed power by the powder particles (J),  $Q_{rp}$  is the reflected energy from the powder particles (J) and  $Q_{radiation}$  and  $Q_{convection}$  is the energy loss due to radiation and convection (J) respectively.

The laser energy input is given by:

$$Q_l = A_l \cdot P_l \cdot t_i = \pi \cdot r_l^2 \cdot P_l \cdot t_i \quad (2.9)$$

Where  $A_i$  is the area of the laser beam spot on the substrate ( $m^2$ ),  $r_i$  is the beam spot radius on the substrate (m),  $P_i$  is the average laser power (W) and  $t_i$  the interaction time (s) between the substrate and the laser beam expressed as:

$$t_i = \frac{2 \cdot r_i}{U} \quad (2.10)$$

Where  $U$  is the laser scanning velocity (m/s).

The reflected energy from the substrate is given by the expression:

$$Q_{rs} = (1 - \beta_w) \cdot (Q_l - Q_p) \quad (2.11)$$

Where  $\beta_w$  is the absorption coefficient of the substrate.

The latent energy of fusion is expressed by:

$$Q_L = L_f \cdot \rho \cdot V \quad (2.12)$$

Where  $L_f$  is the latent heat of fusion (J/kg),  $\rho$  the average density of the clad area ( $kg/m^3$ ) and  $V$  is the volume of the melt pool including the clad area ( $m^3$ ). In order to calculate the volume it is assumed that the clad layer can be represented by a cylinder as indicated in Figure 2.28 (a) where the width of the clad and the length of the melt pool is assumed to be equal to the laser beam diameter on the substrate.

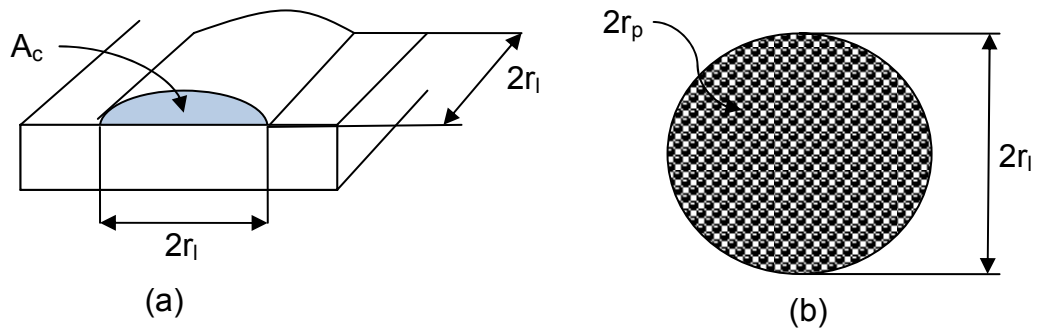


Figure 2.28: (a) Assumed cross-section of the clad on the substrate. (b) Homogeneous distribution of powder particles over the laser beam diameter on the substrate (2).

Assuming that the dilution is negligible which if the process is optimized would be a reasonable assumption the volume of the melt pool is given by the expression:

$$V = 2r_l \cdot A_c = 2r_l \cdot \left( \frac{m}{\rho_p \cdot U} \right) \cdot \eta \quad (2.13)$$

Where  $A_c$  is the cross sectional area ( $m^2$ ) of the melt pool and  $\rho_p$  is the particle density ( $kg/m^3$ ). The powder efficiency ( $\eta$ ) in a lumped model is assumed to be equal to the ratio of the laser beam ( $2.r_l$ ) and the powder stream diameter ( $2.r_p$ ) on the substrate. Thus:

$$\eta = 2 \cdot \left( \frac{r_l}{r_p} \right) \quad (2.14)$$

In order to derive an equation for the absorption of energy by the powder particles a homogeneous distribution of powder particles is assumed over the cross section of the laser beam diameter on the substrate in a lumped model.

The number of powder particles ( $n$ ) in the laser beam area is calculated using the expression:

$$n = \frac{3 \cdot m \cdot t_i}{4 \cdot \rho_p \cdot r_p} \quad (2.15)$$

The overall area in the laser beam cross section taken up by the powder particles is called the attenuated area ( $m^2$ ),  $A_{at}$  and is calculated from the expression:

$$A_{at} = n \cdot \pi \cdot r_p^2 = \frac{3 \cdot m \cdot t_i}{4 \cdot \rho_p \cdot r_p} \quad (2.16)$$

The energy absorbed by the powder particles can then be obtained from the expression:

$$Q_p = Q_l \cdot \left( \frac{A_{at}}{A_l} \right) = \frac{3 \cdot Q_l \cdot m \cdot t_i}{4 \pi \cdot \rho_p \cdot r_p \cdot r_l^2} \quad (2.17)$$

The energy reflected by the powder particles is given by the expression:

$$Q_{rp} = (1 - \beta_p) \cdot Q_p \quad (2.18)$$

The energy lost through radiation by the substrate surface is given by:

$$Q_{radiation} = A_l \cdot \varepsilon_t \cdot \sigma \cdot (T^4 - T_o^4) \quad (2.19)$$

Where  $\varepsilon_t$  is the emissivity of the substrate surface,  $\sigma$  is the **Stefan-Boltzman** constant ( $\text{W/m}^2 \cdot \text{K}^4$ ),  $T$  is the melt pool temperature (K) and  $T_0$  is the ambient temperature (K).

The convective loss assuming a concentrated heating area corresponding to the laser beam area is given by the expression:

$$Q_{convection} = A_l \cdot h_c \cdot (T - T_0) \quad (2.20)$$

Where,  $h_c$  is the heat convection coefficient ( $\text{W/m}^2 \cdot \text{K}$ ). **Toyserkani et al** remarks that calculating  $h_c$  can be difficult but two researchers, **Goldak** and **Yang** suggested an experimental expression that is given below:

$$h_c = 24.1 \times 10^{-4} \cdot \varepsilon_t \cdot T^{1.61} \quad (2.21)$$

**Toyserkani et al** states that this equation introduces a non-linear term into the final energy balance which can however be ignored for simplification of the final differential equation. Finally the energy absorbed by the substrate surface,  $Q_c$ , can be given in integral form as being:

$$Q_c = \rho \cdot c_p \int_{V_s} T(x, y, z, t_i) \cdot d.V_s \quad (2.22)$$

Where  $V_s$  is the heat effected volume ( $\text{m}^3$ ) in Cartesian co-ordinates ( $x, y, z$ ) and  $\rho$  is the average density of the clad region ( $\text{kg/m}^3$ ).

**Toyserkani et al** states that substitution of the various equations into the energy balance equation leads to an equation for  $Q_c$ , which, when substituted into the equation 2.22, leads to a lumped differential equation that represents a lumped model of the laser cladding process. The differential equation can be solved by different numerical approaches (2).

## 2.10 Single pass clad geometry

The geometry of a single pass clad cross-section is usually defined by the clad height ( $h$ ), width ( $w$ ), depth of clad penetration into the substrate ( $Z_{pd}$ ) and the root angle ( $\theta_r$ ) also referred to as the wetting angle in text (20) (2).

(Refer to Figure 2.29)

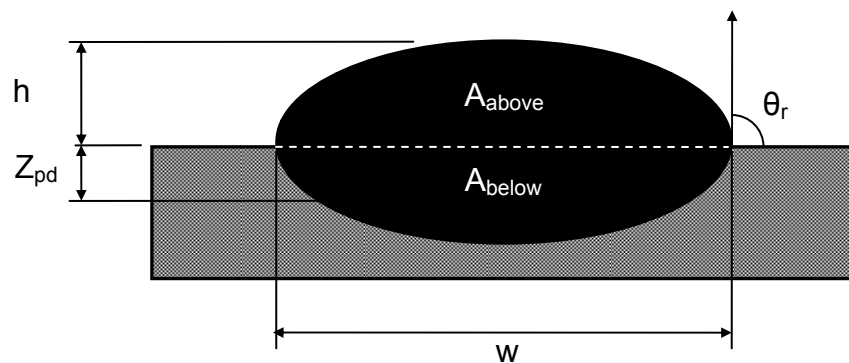


Figure 2.29: Dimensions that define the typical single pass clad cross-section (10) (2).

**Toyserkani et al** and **Steen** state that there are three basic single pass clad geometries that can develop during the laser cladding process (2) (7). (Refer to Figure 2.30)

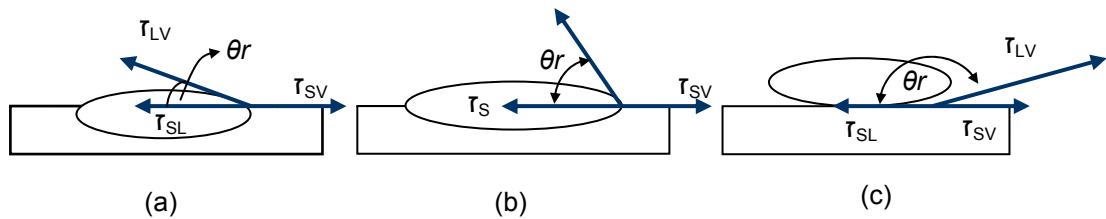


Figure 2.30: Laser cladding cross-sections with its associated dilution, wetting angle and interfacial free energy (2).

**Toyserkani et al** goes further to explain the dependence of the resultant clad geometries in Figure 2.30 on the amount of dilution, the wetting angle ( $\theta_r$ ) and the surface tension ( $\tau$ )/interfacial free energies. Three interfacial energies are considered: solid-liquid ( $\tau_{SL}$ ), solid-vapour ( $\tau_{SV}$ ) and liquid-vapour free interfacial energy ( $\tau_{LV}$ ). **Toyserkani et al** states that the balance between the three free interfacial energies governs the shape of the clad cross-section. The energy balance can be expressed as:

$$\gamma_{SV} - \gamma_{SL} = \gamma_{LV} \cdot \cos\theta_r \quad (2.23)$$

**Toyserkani et al** states that the liquid will wet the substrate as  $\cos\theta_f$  approaches 1 or if  $\tau_{SV} - \tau_{SL} > \tau_{LV}$  which relates to Figure 2.30 (b). He further mentions that a large positive spreading factor ( $S = \tau_{SV} - \tau_{SL} - \tau_{LV}$ ) causes spreading while a low number causes non-wetting such as in Figure 2.30 (c) (2).

**Gedda** agrees with **Toyserkani et al** that for a liquid droplet on a solid surface, the contact angle is determined by the various surface tensions associated with the liquid, the solid and the air. **Gedda** states that the contact angle remains the same if more liquid is added to the droplet but that the contact area between the droplet and the solid increases. **Gedda** however states that the contact angle in laser cladding is not determined by the surface tension of the liquid, although surface tension varies due to temperature differences. According to **Gedda** the effect of surface tensions is negligible compared to the effect of the laser beam diameter on the substrate. **Gedda** states that the laser beam diameter on the substrate more or less fixes the width of the melt-substrate interface which means that the melt cannot spread laterally. Therefore **Gedda** states that since the melt cannot spread laterally, the clad cross-section will assume a shape which forms part of a circle. The circle is intersected by a chord of more or less fixed width represented by the melt-substrate surface interface. **Gedda** thus concludes that the cross section of a single pass clad layer is largely determined by the laser beam diameter on the substrate and the volume of the clad track per unit length (24).



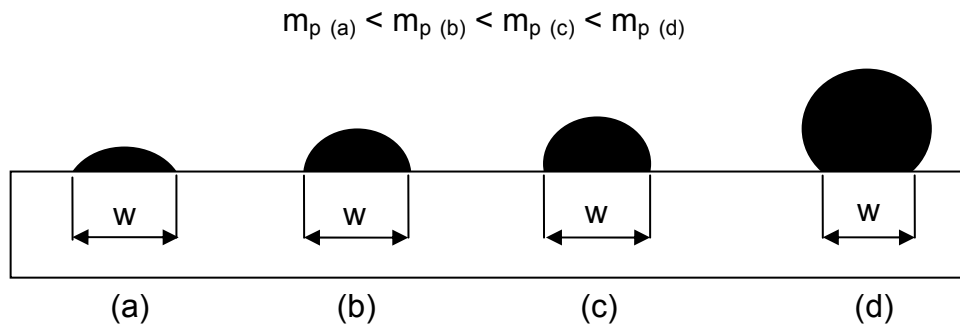


Figure 2.31: The change in the clad cross-section with an increase in the powder feed rate ( $m_p$ ) and a relatively fixed width determined by the laser beam diameter on the substrate surface (24).

## 2.11 The clad root angle or wetting angle

The clad root angle is an important characteristic of the clad layer describing the onset of possible inter-run porosity in the development of a coating.

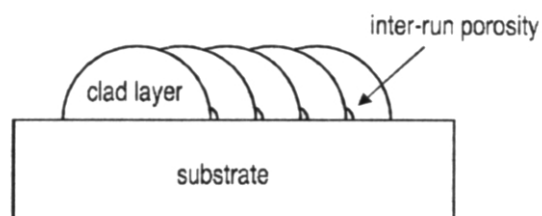


Figure 2.32: Inter-run porosity between adjacent clad layers forming a coating (10).

The root angle is required to be large enough to reduce the risk of inter-run porosity. It can be seen by considering Figure 2.29 that as the root angle becomes smaller than  $90^\circ$  the chances of inter run porosity increases.

**de Oliveira et al** mentions that the measurement of the root angle could cause significant data scatter and states that an assumption is often made that the cross-section of the clad layer lies in a circle. This allows the calculation of the root angle using equation 2.24 based on the clad height and width which are easier to measure and less susceptible to measurement errors (20).

$$\alpha_r = 180^\circ - 2 \cdot \arctan \left( \frac{2h}{w} \right) \quad (2.24)$$

## 2.12 Aspect ratio

The aspect ratio of a single pass clad layer and several other important clad properties are derived from the clad geometry. The aspect ratio is simply the ratio between the width and the height of the clad and is expressed as:

$$\text{Aspect ratio} = \left( \frac{w}{h} \right) \quad (2.25)$$

According to **Gedda** the aspect ratio should be bigger than five to avoid inter-run porosity between overlapping clad tracks/layers. (21).

## 2.13 Dilution

Another important clad quantity is dilution. According to **de Oliveira et al** dilution quantifies the relative amount of molten substrate material that has mixed with the material addition during the cladding process (20). There are three different methods to quantify dilution: geometrical dilution (2) (10); area ratio dilution (20), and metallurgical dilution (2).

In the first two cases a homogenous distribution of elements over the clad cross-section is assumed (10) and dilution can be easily calculated from the clad geometry using the following expressions:

$$Dilution (Geometrical) = \left( \frac{Z_{pd}}{h + Z_{pd}} \right) \quad (2.26)$$

$$Dilution (Area ratio) = \left( \frac{A_{below}}{A_{above} + A_{below}} \right) \quad (2.27)$$

Where  $A_{above}$  is the clad area above the substrate and  $A_{below}$  the area of clad that has penetrated beyond the substrate surface. The metallurgical method defines dilution according to composition.

$$Dilution (Metallurgical) = \left[ \frac{\rho_c \cdot (X_{c+s} - X_c)}{\rho_s \cdot (X_s - X_{c+s}) + \rho_c \cdot (X_{c+s} - X_c)} \right] \quad (2.28)$$

Where  $p_c$  is the density of the melted powder addition ( $\text{kg/m}^3$ ),  $p_s$  the density of the substrate material ( $\text{kg/m}^3$ ),  $X_{c+s}$  (wt%) the weight percentage of element X in the total clad area,  $X_c$  (wt%) the weight percentage of element X in the powder addition and  $X_s$  (wt%) is the weight percentage of element X in the substrate material (2).

For successful cladding there will always be some degree of dilution to ensure a good fusion/metallurgical bond. Dilution should however be kept to the minimum so as to retain the properties of the material addition (20).

## 2.14 Powder efficiency

Powder efficiency is one of the critical process outputs that, together with other variables such as the scanning velocity, determine the overall efficiency of the cladding process. Powder efficiency can simply be defined as the ratio of the amount of powder used in the development of the clad layer to the amount of powder delivered to the substrate.

$$\eta_{\text{powder}} = (100) \cdot \left( \frac{m_{p \text{ used}}}{m_{p \text{ delivered}}} \right) \quad (2.29)$$

The powder efficiency is generally determined by weighing the substrate before and after cladding. The difference in weight is assumed to be the amount of powder used in the formation of the clad layer ( $m_{p \text{ used}}$ ).

The mass of powder delivered ( $m_{p\ del}$ ) is obtained by multiplying the powder flow rate with the time that the laser was on during the development of the clad layer (25).

**Jin** states that the type of impact determines whether the particle adds to the development of the clad layer or not. **Jin** lists the various impact possibilities as being:

- *A solid particle-solid substrate surface* impact causing the particle to ricochet off the substrate surface;
- *A solid particle-liquid substrate surface* leading to particle catchment;
- *A liquid particle-solid substrate surface* leading to particle catchment and a rapid quench structure;
- *A liquid particle-liquid substrate surface* leading to catchment (25).

**Lin** further remarks that the collision of the powder particles on the substrate could be seen as the interaction between a spherical and plane surface with different surface temperatures. The particle impacting on the clad area is generally melted and trapped by the surface tension of the liquid film at the collision interface. **Lin** states that the maximum repelling force ( $F_r$ ) according to **Hertz's** theory for an elastic collision between a sphere and plane is given by the expression:

$$F_r = K \cdot r^2 \cdot V_r^{6/5} \quad (2.30)$$

Where  $V_r$  is the particle velocity,  $r$  is the particle radius and  $K$  a constant depending on the elastic properties of the material.

**Lin** further states that the adhesion force ( $F_{ad}$ ) on the melted substrate surface is proportional to its surface tension force, expressed as  $4\pi r\sigma$  ( $\sigma$  being the surface tension of the substrate material at its melting point) and that the ratio of  $F_{ad}/F_r$  can be defined as the adhesion parameter for particle bonding.

$$\frac{F_{ad}}{F_r} = \frac{4\pi\sigma}{K \cdot r^2 V_r^{6/5}} \quad (2.31)$$

Both the elastic coefficient and surface tension should be considered as temperature dependent properties and according to **Lin** both the elastic modulus and surface tension decreases with temperature.

**Lin** states that when  $F_{ad}/F_r > 1$  it implies that the powder is melted and sticks to the substrate surface due to surface tension and that the particle will rebound elastically when  $F_{ad}/F_r < 1$ . **Lin** further states that the solid surface adhesion force with different particle sizes has been studied by many researchers and estimations of the critical speed for elastic rebounding to escape from the solid surface has been made. **Lin** states that, for most surfaces, it can be seen that  $F_{ad}$  is proportional to  $1/r$  and for the ratio  $F_{ad}/F_r$ ,  $1/r^3$ , in the elastic rebounding region.

In conclusion **Lin** states that the possibility of a powder particle adhering to the substrate surface under a particular collision mechanism is dependent on the bonding temperature and can be increased by reducing the particle size and velocity (25). This statement is supported by the work of **Gedda** and **Schneider** in which they state that the amount of pre-heating experienced by a powder particle from when it exits the nozzle until it reaches the substrate surface is inversely proportional to particle size and particle velocity. Thus pre-heating would increase with a decrease in particle size and particle velocity (21) (10). Interesting to note was a calculation made by **Schneider** using an off- axis nozzle configuration that indicated no significant change in particle pre-heating with a change in the powder mass flow rate from 75-300 mg/s (10).

**de Oliveira et al** also remarked on the crucial role that particle velocity, which is mainly determined by the carrier gas flow rate and nozzle design, played in their investigation of the coaxial laser cladding process (20).

**de Oliveira et al** calculated the amount of laser power required to melt the substrate and powder respectively based on a model suggested by **Jouvard et al**. The results of their calculations were used to plot the laser power required to melt the substrate and powder as a function of the particle velocity. The powder used in their investigation was 19E Metco (size: 80  $\mu\text{m}$ ) on a C45 steel substrate. The powder feed rate and scanning velocity was 141.7 mg/s and 4.67 mm/s respectively. (Refer to Figure 2.33)

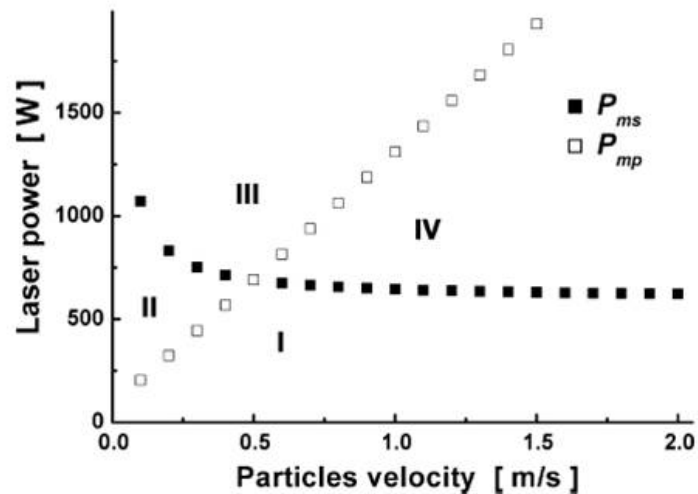


Figure 2.33: Calculated laser power required to melt the substrate ( $P_{ms}$ ) and the powder particles ( $P_{mp}$ ) as a function of the particle velocity for coaxial cladding. (26)

Figure 2.33 clearly indicates that the power required to heat the powder particle to its melting temperature ( $P_{mp}$ ) increases linearly with particle velocity. In addition it can be seen that the power required to melt the substrate ( $P_{ms}$ ) initially decreases significantly as particle velocity increases but starts to “stabilize” after a certain point. *de Oliveira et al* states that the intersection of the two curves forms four distinct areas in the processing window for coaxial cladding. Inside area I no cladding occurs, inside area II the substrate is not melted but it is possible to form a clad track without a good metallurgical bond between the clad layer and the substrate. *de Oliveira et al* states that the optimal cladding processing conditions lies somewhere in area III. area IV is characterized as an area with low powder efficiency where solid particles reaches the liquid surface with relatively high velocities, leading to solid particle-liquid surface interaction with a high repelling force (20).



Whether a particle with a given composition, size and shape reaches the substrate as a solid or a liquid thus generally depends on two factors namely, the path of the particle through the laser beam and the particle velocity. Depending on their temperature on arrival at the melt pool they either extract or add energy to the melt pool (10). If it is assumed that all particles exit the nozzle at the same velocity, and with the same initial temperature their different paths will determine their final temperature when they reach the melt pool (3). The variation in the laser power density along the powder particle path could also be considered.

## 2.15 The effect of process variables on the clad geometry and characteristics

Process variables	Height	Width	Dilution/ Penetration	Root Angle	Hardness
Laser power (P)	▲	▲	▲	–	▼
Scanning velocity ( $V_s$ )	▼	▼	▼	▲	▲
Powder feed rate	▲	▲	▼	▼	▲
Laser beam diameter	▲	▲*	▼*	–	▲*

Table 2.8: A summary of the effect of an increase in various process variables on the clad geometry and its properties (10) (20) (21) (1).

Table 2.8 summarizes the effect of an increase in various process variables on the geometry and properties of a developing clad layer. An increase is denoted by the symbol (▲) and a decrease by the symbol (▼).

Furthermore the symbols marked in red denote that the particular process variable is considered to have a significant effect on the geometry or properties of the clad layer compared to the other variables.

## 2.16 Microstructural development

### 2.16.1 The Al-Si binary system

**Toyserkani et al** reports that it is well known that the melt pool in laser cladding is not at equilibrium. Solidification of the melt pool can therefore not be qualitatively characterized by an equilibrium phase diagram. However an equilibrium phase diagram is still useful for interpreting the general metallurgical interactions that occurs during laser cladding (2).

**Makhlouf et al** in their investigation of the aluminium silicon eutectic reaction: Mechanisms and crystallography, remarks on the review of **Murray et al** on the Al-Si phase diagram under equilibrium cooling conditions. The Al-Si system is a simple binary eutectic system with limited solubility of aluminium in silicon and vice versa. There is only one invariant reaction to consider, namely:



Where L is the liquid phase,  $\alpha$  is predominantly aluminium and Si is silicon. The eutectic reaction occurs at a silicon concentration and temperature of 12.6 wt% and 577°C respectively.

Three different microstructures may develop upon solidification depending on the silicon concentration namely:

- Primary aluminium dendrites with Al-Si eutectic filling the inter-dendritic spaces in the case of hypo-eutectic alloys ( $\text{wt\%Si} < 12.6\text{wt\%}$ );
- At a silicon concentration of 12.6wt%, the eutectic level, the resultant microstructure consists entirely of Al-Si eutectic;
- In the case of hyper-eutectic alloys ( $\text{wt\%Si} > 12.6\text{wt\%}$ ) the microstructure consists of Al-Si eutectic with primary silicon crystals. The most commonly observed primary silicon morphologies are massive primary silicon, known as polygonal silicon and star-like primary silicon.

***Makhlouf et al*** states that typical eutectic structures in binary alloys generally form through the simultaneous growth of two phases from the liquid melt. The developing microstructure can therefore be classified according to two criteria:

- Lamellar versus fibrous morphology of the individual phases; and,
- Regular versus irregular growth of the individual phases.

As a rule of thumb the eutectic microstructure will tend to be fibrous if the volume fraction of the minor phase is less than 0.25%. Otherwise the microstructure tends to be lamellar. The typical Al-Si eutectic structure, even at a Si volume fraction below 0.25%, however tends to be closer to a lamellar

structure than a fibrous structure which is usually attributed to the strong anisotropy of growth of the silicon phase and the relatively low interfacial energy between silicon and aluminium.

The eutectic will exhibit a regular morphology if both phases in the eutectic are non-faceted. The resultant microstructure can thus be lamellar or fibrous with a high degree of regularity and periodicity. However if only one phase is faceted then the morphology is often irregular (27).

**Makhlouf et al** further remarks that the temperature of formation of primary aluminium and silicon as well as the temperature of the eutectic plateau is cooling rate dependent. Primary silicon undercools more than primary aluminium, hence the eutectic structure forms 10-12°C below the eutectic temperature without significant recalescence.

At higher cooling rates the Al-Si system behaves as though the eutectic point has shifted to a higher silicon concentration and the eutectic temperature is depressed (27). (Refer to Figure 2.34) This statement is supported by

**Douburg et al** which reported that for laser clad Al-12wt%Si the single Al-Si eutectic microstructure predicted by the binary phase diagram did not develop, instead the microstructure consisted of  $\alpha$ -aluminium dendrites and inter-dendritic Al-Si eutectic. **Douburg et al** attributed this change to the high solidification rates in laser material processing (28).

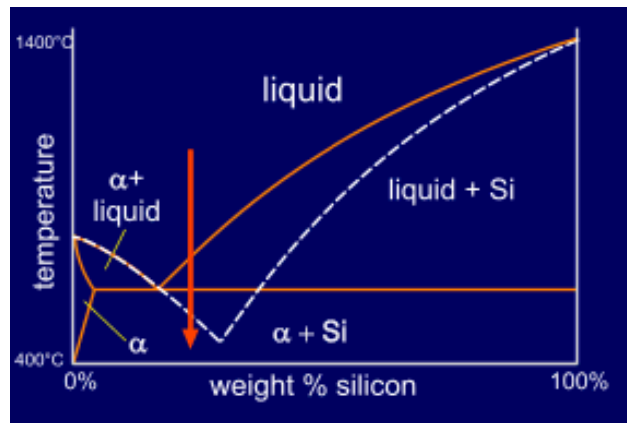


Figure 2.34: Undercooling due to a high solidification rate (29).

The effect of the solidification rate on the resultant microstructure is clearly illustrated in the micrographs of Al-12.6 wt%Si allowed to solidify at two different cooling rates. The microstructure of the slowly cooled Al-Si (Figure 2.35-a) consists of a eutectic structure with no primary aluminium dendrites visible. On the other hand in the micrograph of the rapidly cooled sample (Figure 2.35-b) a microstructure that consists of primary aluminium dendrites with inter-dendritic Al-Si eutectic is observed (27).

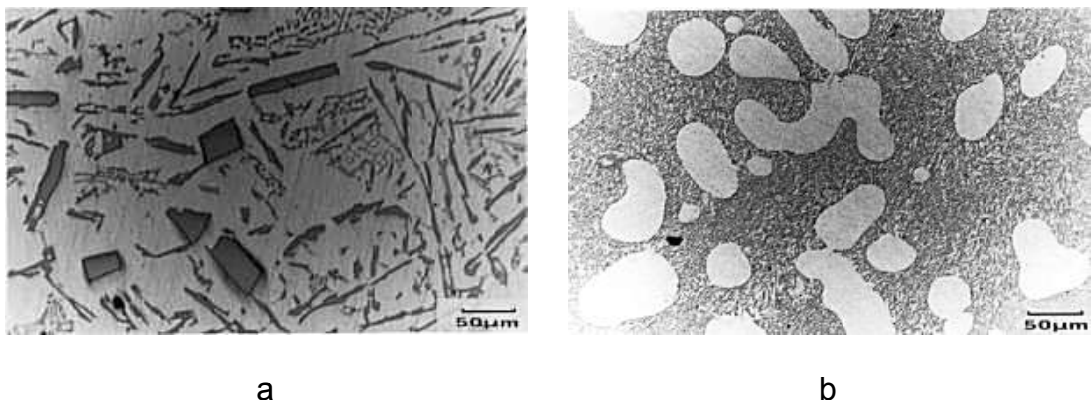


Figure 2.35: Change in microstructure due to a change in the solidification rate (29).

According to **Mahklouf et al** the depression of the eutectic temperature at higher cooling rates may be explained by considering the coupled region effect. The coupled region represents fields within the phase diagram where the two phases of the eutectic are arranged in such a way as to allow diffusion in the liquid to occur effectively at a duplex solid/ liquid front. The coupled region for the Al-Si system is asymmetric due to the fact that silicon, which is a non-metal with directed covalent bonds, tends to grow anisotropically into faceted crystals and hence requires a larger degree of undercooling than the isotropic aluminium phase for its growth. A hypothetical asymmetric phase diagram is shown in Figure 2.36 (27).

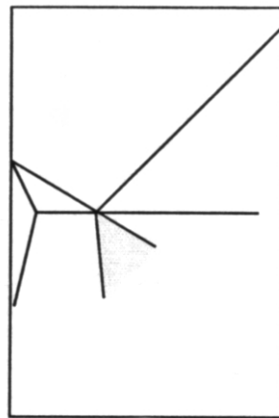


Figure 2.36: Coupled growth regions in an asymmetric hypothetical phase diagram (27).

**Uzan et al** in their investigation of the microstructure of rapidly solidified Al-Si alloys with compositions of 8, 12 and 16 wt% Si respectively states that previous research on eutectic metal systems have identified that:

A structure consisting of both primary and eutectic phases, or only the latter develops at a given undercooling condition depending on the fastest growing phase. *Uzan et al* states that, at a given undercooling condition, the silicon rich phase, which grows in a faceted manner, grows slower than the primary rich aluminium phase growing dendritically. *Uzan et al* also comments on a study by *Jacobson and Mckittrick* which reported that at relatively low undercooling of an alloy with a given composition dendritical growth was observed in which one of the phases grow rapidly and the other phase solidifies between dendrites whereas higher undercooling lead to cellular growth (30).

### **2.16.2 Factors influencing microstructural development**

Laser material processing generally involves a highly localized heat source, short interaction times and rapid solidification due to high heat removal by conduction into the bulk of the material or substrate. Heat removal tends to be highly directional, setting up large positive temperature gradients in the melt pool ahead of the solid/liquid interface (2). Solidification rates in laser material processing are generally in the order of  $10^6$  K/m (2), whereas conventional solidification rates are in the order of  $10^2$  K/s or less (30).

The effect of rapid solidification varies significantly from system to system.

However possible effects are:

- A decrease in the microstructural scale;
- Increased chemical homogeneity;
- Extension of solid solubility limits;
- The formation of metastable phases;
- The formation of metallic glasses (30).

**Toyserkani et al** states that the type of microstructure that develops upon solidification depends both on the cladding processing conditions and the material composition of the alloy addition and substrate. The cladding process conditions determine the temperature gradient ( $G$ ) and the velocity of the solid/liquid interface or solidification front ( $V_{sf}$ ) while the material composition determines the magnitude of the freezing range (2).

**Gremaud et al** also remarked on the importance of external and internal kinetic parameters in controlling the morphology of the re-solidified microstructure in laser surface re-melting of Al-Si alloys. External parameters include the process variables, for example energy density and scanning velocity; the substrate temperature; composition and atmosphere. Internal parameters on the other hand represent the kinetic response of the material and include factors such as the solidification velocity, degree of undercooling,



nucleation site density, nucleation rate, metastable phase selection options, microstructural scale and morphology (31).

The importance of these external parameters is also mentioned by **Mahklouf et al** who commented on a study by **Hellawell** in which the different forms of silicon in the Al-Si eutectic structure was investigated as a function of the temperature gradient, growth rate and material composition (27). It is therefore important to understand the effect that the main laser cladding process variables have on the composition of the clad layer, temperature gradient, solidification rate and degree of undercooling of the liquid melt.

### 2.16.3 The solidification front velocity and temperature gradient

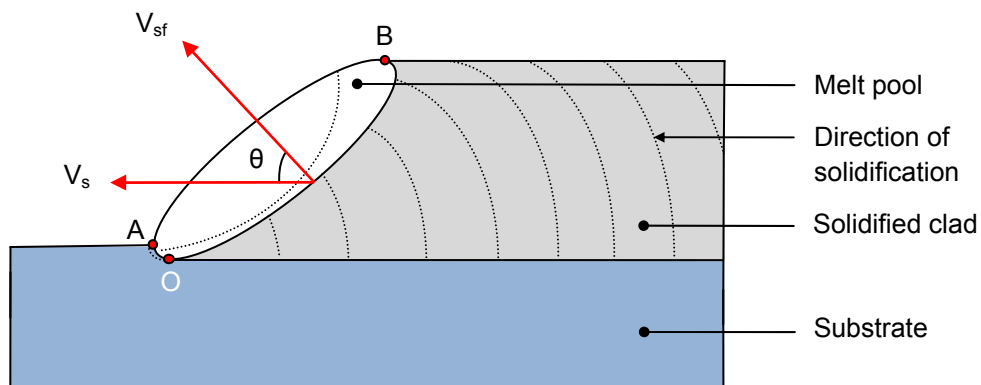


Figure 2.37: Schematic illustrating the relationship between  $V_s$  and  $V_{sf}$  (26) (31).

**Pei et al** states that, in laser cladding at a constant laser power, scanning velocity and powder feed rate, a steady state melt pool is created after the first few millimetres of the clad layer. If a longitudinal section through the

centreline of the clad layer is considered then the velocity of the solidification front ( $v_{sf}$ ) is related to the laser scanning velocity ( $v_s$ ) through the expression:

(2.33)

$$v_{sf} = v_s \cdot \cos \theta$$

Where,  $\theta$  is the angle between the vector representing the laser scanning velocity ( $v_s$ ) and the vector representing the velocity of the solidification front ( $v_{sf}$ ) at any point along and normal to the solidification front (26) (2) (31).  
(Refer to Figure 2.37)

Inspection of Figure 2.37 reveals that the solidification rate ( $v_{sf}$ ) varies from zero at the bottom of the melt pool (Point O), to a maximum approaching the scanning velocity ( $v_s$ ) at the top of the melt pool (Point B). (26)

**Toyserkani et al** states that an investigation by **Kurz et al** revealed that the temperature gradient could also be shown to be related to the laser scanning velocity. Figure 2.38 taken from the work of **Kurz et al** clearly illustrates this dependence (2).

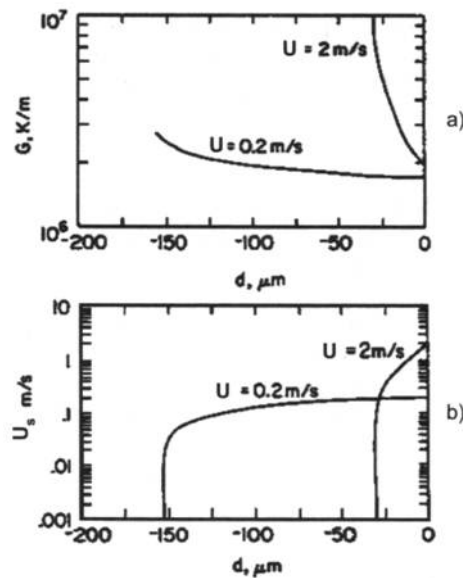


Figure 2.38: The calculated solidification conditions in laser surface re-melting at two different scanning velocities. Figure 2.38 (a) represents the change in the temperature gradient and Figure 2.38 (b) the change in the solidification rate with respect to the depth from the free surface ( $d$ ) (2).

#### 2.16.4 Reported microstructures of laser processed Al-Si alloys

*Pei et al* investigated the formation of Al-40Si functionally graded coatings (FGC) produced by one step laser cladding on a cast aluminium substrate. The microstructure of the Al-40Si FGC coating consisted of primary silicon crystals surrounded by  $\alpha$ -aluminium dendritic halos and branched aluminium-silicon eutectic adjacent to the halos. *Pei et al* observed that both the size and volume fraction of the silicon particles increased, from  $8.5 \mu\text{m}$  and 22.7% at the bottom to  $52 \mu\text{m}$  and 31.4% at the top of the clad layer respectively. The silicon particles also displayed a morphological transition from a polygonal shape at the bottom to an equiaxially five-branched shape near the top of the clad layer.

**Pei et al** remarks that silicon crystals with these five-fold geometries have been previously reported as a rare morphology that forms at slow cooling rates. In their investigation it was however often observed near the surface of the clad layer.

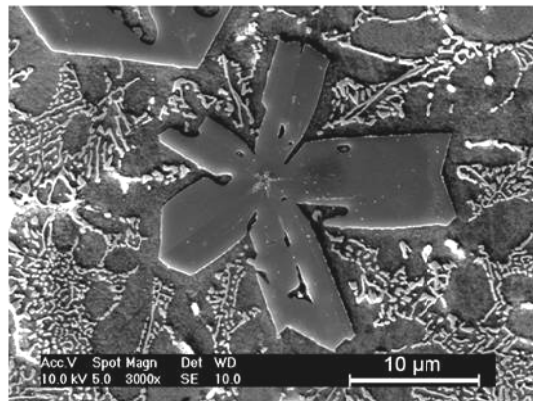


Figure 2.39: A SEM micrograph of a five-branched silicon crystal surrounded by  $\alpha$ -aluminium halos with inter-dendritic eutectic. (26)

The  $\alpha$ -aluminium halos and the eutectic structure did not however exhibit the same significant increase in size. **Pei et al** concluded that these observations suggest that the primary silicon particles nucleated from the liquid state rather than from the solid state precipitate.

Another interesting observation was a thin zone at the clad substrate interface that was free of silicon particles and consisted of  $\alpha$ -aluminium dendrites and Al-Si eutectic. **Pei et al** stated that this region could be beneficial in that it might be a region where thermal stresses could be relieved (26). The possible benefits of such a transition zone is highlighted by **de Deus et al** which remarked that the strong thermal gradients in laser

cladding coupled with the fact that the material addition and substrate often have different coefficients of thermal expansion leads to the generation of thermal stresses. *de Deus* et al states that since the yield stress of a material generally decrease with temperature, inelastic deformation would most likely take place imparting residual stresses in the material. These residual stresses are usually concentrated at the clad-substrate interface. Therefore, the clad-substrate interface is also the most likely location where defects such as pores or cracks would occur. (32)

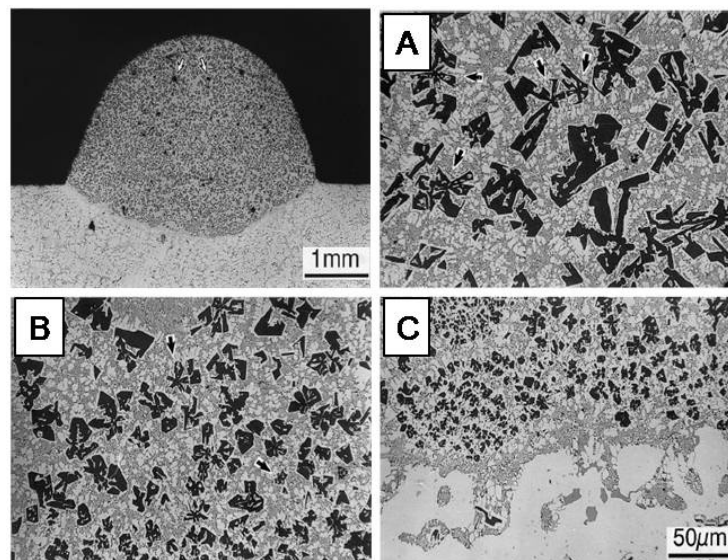


Figure 2.40: An optical micrograph of an Al-40wt%Si FGC produced at  $P = 3000$  W and  $v_s = 26.7$  mm/s. Micrographs A, B and C indicate the variation in both size and volume fraction of the silicon particles at the top (A), middle (B) and bottom (C) of the clad layer. (26)

According to *Pei et al* microstructural evolution during solidification of the melt pool occurs in the following sequence. The silicon particles nucleate from the liquid by heterogeneous mechanisms, growing into the surrounding undercooled melt. Subsequently aluminium solvent is rejected until the local concentration is sufficient to nucleate the  $\alpha$ -aluminium phase. The  $\alpha$ -

aluminium phase which appears in the form of halos surrounding the silicon particles arrest the growth of the silicon particles. Due to the growth of the  $\alpha$ -aluminium halos the silicon content of the remaining liquid phase increases to the extent that the eventual composition of the liquid phase lies in the coupled zone. This results in the co-operative growth mechanism between silicon and the  $\alpha$ -aluminium phase resulting in the formation of the eutectic phase in the latter stages of solidification (26). Several other authors have reported similar microstructures for laser processed hypereutectic alloys (28) (31).

**Gremaud et al** reported a variation in microstructure with the laser scanning velocity in their investigation of the microstructures of laser re-melted Al-Si alloys. For Al-26wt%Si the microstructure at scanning velocities between 5-8 mm/s consisted entirely out of fibrous eutectic. At scanning velocities higher than 8 mm/s the microstructure was similar to that described by **Pei et al** above. **Doubourg et al** agrees with **Pei et al** that the Si crystals seem to nucleate from the liquid rather than through solid state precipitation.

**Doubourg et al** also reports that as the laser scanning velocity increases the aerial density of the silicon particles increases, but without a significant increase in size (28).

**K G Watkins et al** commented on several investigations in their review of microstructure and corrosion properties of laser surface processed aluminium alloys. Of particular interest is the review of the investigations on aluminium silicon alloys discussed below:

**Hegge and de Hosson** in their investigation used a 1.5 kW CO<sub>2</sub> laser to melt the surface of Al-Si alloys containing 4, 7, 12 and 20wt% Si at scanning velocities between 1-250 mm.s<sup>-1</sup>. **Hegge et al** reported that the microstructures of the Al-Si alloys with a Si content of 4 & 7wt% were cellular at the bottom of the track and became dendritic and finally cellular dendritic moving towards the free surface. They also noted the formation of an interdendritic eutectic phase of Si plates in aluminium. At 12wt% Si the microstructure was completely eutectic at scan velocities of 5 mm.s<sup>-1</sup> or below, between 5-50 mm.s<sup>-1</sup> the structure changed from eutectic to dendritic. A cellular dendritic microstructure formed just below the surface and increased in depth by increasing the scanning velocity up to 200mm.s<sup>-1</sup>. The microstructure became cellular dendritic throughout the entire melt depth at scanning velocities higher than 200 mm.s<sup>-1</sup>. For Al-20wt%Si, **Hegge et al** observed that the re-solidified microstructure was dendritic at the bottom, became eutectic and finally cellular over the whole range of scanning velocities. In addition large portions of pure silicon were observed at the bottom of the melt pool.

**Pierantoni et al**, also using a 1.5 kW CO<sub>2</sub> laser showed that the re-solidified microstructure of Al-20wt%Si scanned at 100mm.s<sup>-1</sup> consisted of fine columnar grains of fine eutectic at the bottom, changing to α-aluminium dendrites and fibrous eutectic. They observed that the transition from eutectic to dendritic occurred when the local growth rate was greater than 70 mm.s<sup>-1</sup>. In addition the transition growth rate decreased with a decrease in a Si content (33).



## 3 Optimization of the experimental setup

### 3.1 Introduction

Chapter three describes the experimental test procedures used to establish the operating parameters for the laser cladding test platform and the main process variable test levels used for the experimental investigation of the coaxial laser cladding process.

Based on the literature review, the main process variables were identified as being: laser power ( $P$ ); laser beam scanning velocity ( $v_s$ ), and the powder mass flow rate ( $m_g$ ). Suitable test levels needed to be established for each of the above mentioned variables. In addition to the main process variables, the influence of several other parameters or variables that could possibly have a significant effect on the outcome of the experimental cladding tests had to be investigated and quantified. These include parameters and variables such as the nozzle stand-off distance and carrier gas volume flow rate.

The literature review highlighted the general trends and the experimental test procedures that follow aimed to quantify these trends for the experimental test platform used.

## 3.2 Test sample

### 3.2.1 Sample material composition

The substrate material used in this investigation was aluminium 1370-F. The composition of the substrate material was determined using a Spectro MAxX spectrometer. The results of the average composition by weight percentage are tabulated in Table 3.1:

% Si	% Fe	% Cu	% Mn	% Mg	% Cr	% Ni
0.048	0.147	0.0002	0.0018	0.0001	0.0008	0.0059
% Zn	% Ti	% B	% Ga	% V	% Al	
<0.0010	0.0019	0.0058	0.0074	0.0016	99.7	

Table 3.1 : Average wt% from the chemical composition test on the Al 1370-F substrate.

### 3.2.2 Sample geometry

Test samples, 150 mm long x 40 mm wide were cut from a 12 mm thick aluminium plate such that the rolling direction of the plate was perpendicular to the length of the sample.

### 3.2.3 Sample surface preparation

The surface of all test samples were wire brushed using a stainless steel wire brush prior to cladding to remove the oxide layer; reduce the reflectivity, and increase the surface roughness of the cladding surface. (Refer to Figure 3.1)



Figure 3.1: Surface reflectivity before and after wire brushing. Original test sample at the top, wire brushed sample below.

Each sample surface was prepared using the same two preparation steps to improve the repeatability of the resultant surface roughness. In the first step the surface was wire brushed in a circular motion to remove the hard, shiny surface produced by the rolling process during the manufacturing of the plate. In the second step, the surface was wire brushed with linear strokes, perpendicular to the cladding direction as indicated in Figure 3.2 below. Prior to each test, the samples were cleaned with acetone and a clean cotton cloth to remove any aluminium dust or dust particles on its surface.

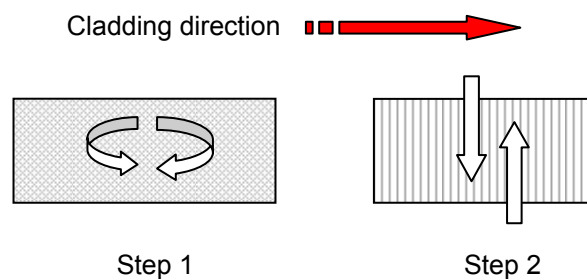


Figure 3.2: Sample surface preparation steps.

As stated in the literature review, surface roughness could have a significant effect on the amount of incident radiation absorbed by a material at a specific wavelength. In general the surface of a material becomes less reflective with an increase in its surface roughness. All the prepared test samples were considered rough since its arithmetical mean roughness (Ra) was greater than the wavelength of the laser. Radiation reflected from the sample surface would therefore be diffuse in nature.

#### **3.2.4 Evaluation of the sample surface roughness**

The test samples' were evaluated using a Mitutoyo SJ-201 surface roughness tester to determine the average arithmetical mean surface roughness (Ra) of the sample surface produced by wire brushing. The objective of the surface roughness tests was not to determine the roughness profile of the test sample surface as it is not possible to quantify the roughness profile of a surface by considering the arithmetical mean surface roughness alone.

However it is still considered useful to quantify the arithmetical mean surface roughness as it establishes the following:

- The effect of wire brushing and the possible error introduced due to surface roughness variation.
- A reference value that could provide other researchers working on similar material combinations with a point of reference when interpreting result variances.

#### **3.2.4.1 Sample surface preparation**

Ten samples were randomly selected from the batch of samples cut from the original plate and its surface prepared as described in section 3.2.3 for the evaluation of its arithmetical mean surface roughness.

#### **3.2.4.2 Calibration of the surface roughness tester**

The surface roughness tester was calibrated according to a DIN-standard calibration sequence, as specified by the manufacturer prior to any measurements to ensure measurement accuracy.

#### **3.2.4.3 Test procedure: Surface roughness evaluation**

The arithmetical mean surface roughness was evaluated according to the DIN standard for surface evaluation taken from the reference information supplied in users' manual of the SJ-201 surface roughness tester. Test settings are listed in Table 3.2.

Calibration condition	Default value
Parameter	Ra
Cut-off length	2.5 mm
Number of sampling lengths (n)	5
Evaluation length (l x n)	12.5 mm
Measurement range	Auto
Measured profile/filter	Pc50
Pre-travel/Post-travel length	ON

Table 3.2: Test settings used for arithmetic mean roughness (Ra) evaluation according to DIN standards.

With the PC50 filter selected, the traversing length was defined as being the evaluation length, pre-travel length and approach length.

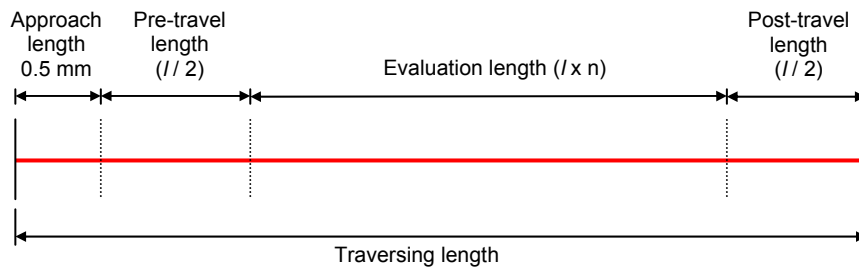


Figure 3.3: Sub-division of the traversing length of the detector

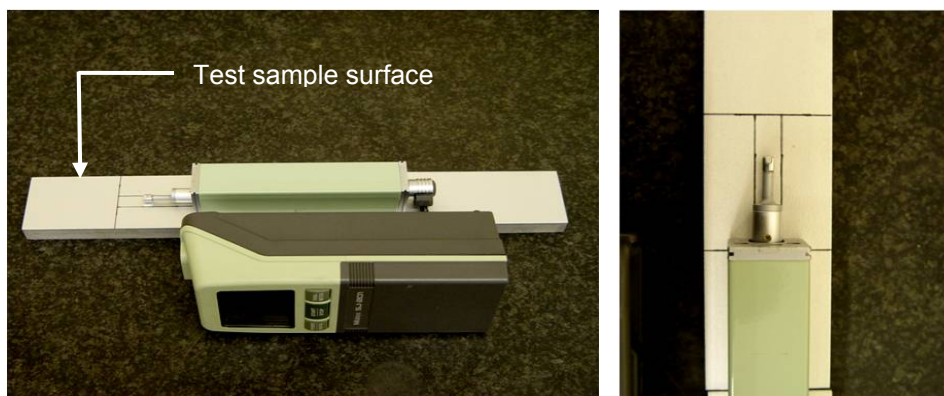


Figure 3.4: Test setup for evaluating the test sample Ra values

The test samples were only 40 mm wide, therefore the drive/detector unit was detached from its holding position below the tester and placed on the sample surface with the tester placed on the gauge block beside it.

Due to its length half the drive/detector unit rested on another sample. It was thus important that both samples had the same thickness and were flat to ensure that the detector was parallel to the measured surface, and that the styles mounted on the detector was in proper contact with the surface. Thus, prior to the preparation of the test surfaces the sample surface opposite the surface to be evaluated was machined to ensure that all samples had the same thickness and were flat.

#### 3.2.4.4 Test results: Surface roughness evaluation

The test results of the evaluation of the arithmetical mean surface roughness of the sample surface are tabulated in Table 3.3.

Sample Number	Arithmetical mean (Ra)
SR 001	4.37 $\mu\text{m}$
SR 002	5.29 $\mu\text{m}$
SR 003	3.70 $\mu\text{m}$
SR 004	3.89 $\mu\text{m}$
SR 005	4.63 $\mu\text{m}$
SR 006	4.48 $\mu\text{m}$
SR 007	4.42 $\mu\text{m}$
SR 008	4.18 $\mu\text{m}$

Table 3.3: Summary of the arithmetical mean surface roughness values.

### 3.3 Powder/alloy addition

The powder used for this investigation was gas atomized hyper-eutectic Al-20wt%Si (spherical particles) with a particle size ranging between 25-75  $\mu\text{m}$ . A micrograph of the spherical particles taken using a scanning electron microscope (SEM) is shown in Figure 3.5.

The microstructure of the powder particles varied but generally consisted either of a coarse Al-Si eutectic structure or an Al-Si eutectic structure with silicon crystals dispersed in it as can be seen in Figure 3.6.

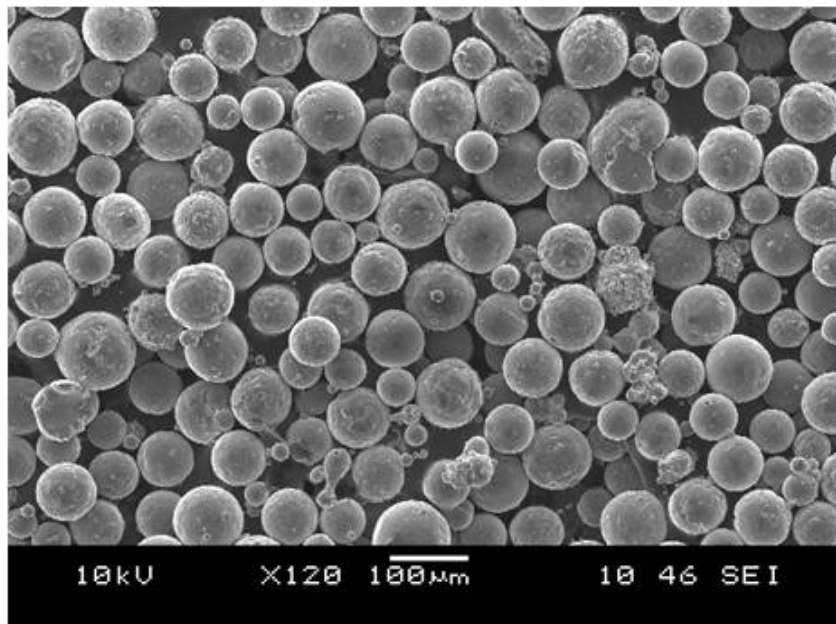


Figure 3.5: Gas atomized spherical Al-Si20wt% particles



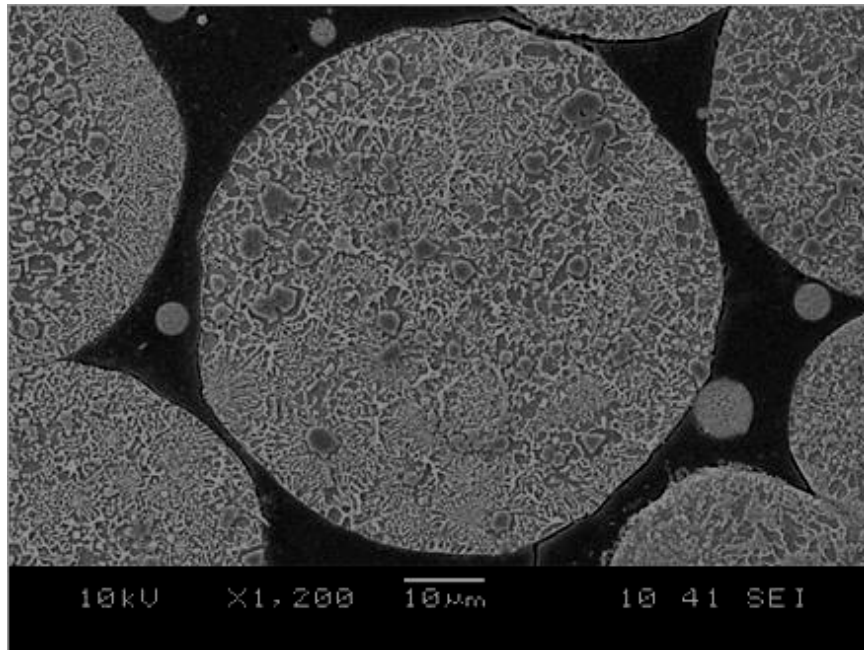


Figure 3.6: Microstructure of the Al-20wt%Si powder particles

## 3.4 Laser beam profiling

### 3.4.1 Introduction

Based on literature it was decided to use a laser beam diameter equal to 3 mm, measured on the sample surface, for this investigation. In order to establish the beam focus and experimental cladding position, as well as to gain some insight into the shape; intensity profile, and power density distribution of a propagating laser beam the laser beam was profiled.

Laser beam profiling was done using a Prometec laserscope UFF100 diagnostic unit and Prometec lasermeter. These units are specially designed for measuring and monitoring high power material processing lasers. Both focussed and unfocussed beams can be measured over a range of powers and wavelengths, in continuous and pulsed mode.

The laserscope UFF100 uses a short, inclined, hollow needle with a small pinhole in the side facing the laser beam mounted on a rotary head to scan the laser beam. The needle which is mounted perpendicular to the beam propagation axis scans the laser beam along the orbit of the pinhole as it rotates through the beam while also traversing the cross-section of the beam. Thus with each rotation of the needle the system is moved forward by a defined interval and in this manner the entire cross section of the beam is sampled. The laser beam enters the needle through the pinhole and is led via the needle towards the axis of rotation where it is received by a detector which digitalizes the signal.

This signal is temporarily stored by a 16-bit processor after which it is transferred through a standard serial interface to a personal computer for processing and analysis using PROLAS software from Prometec. (Refer to Figure 3.7)

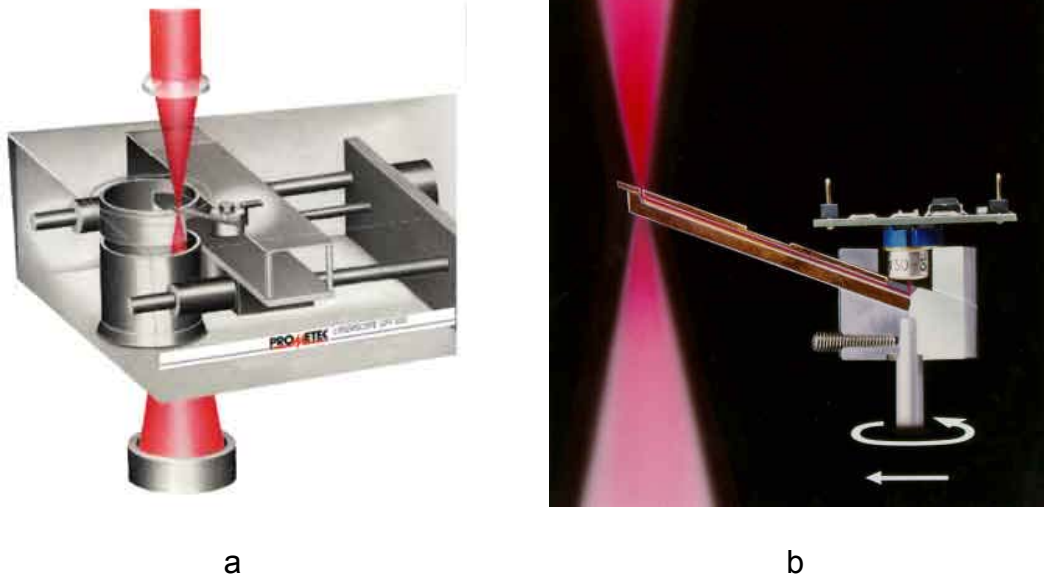


Figure 3.7: (a) Beam profile measurement of a focussed laser beam. (b) The working principle of the rotating hollow needle with detector on a feed slide. The smallest possible traversing step size is 12.5  $\mu\text{m}$ .

### 3.4.2 Objective: Laser beam profiling

- Determine the focus position of the laser beam relative to a pre-selected reference surface on the processing head;
- Establish the beam radius, intensity profile, and power density distribution of the laser beam at its focus position;
- Determine the position, relative to the pre-selected reference surface, where the beam diameter above the focus position is equal to 3 mm;
- Establish the intensity profile and power density distribution of the laser beam above the focus point where the beam diameter is equal to 3 mm.

### 3.4.3 Setup and test procedure: Laser beam profiling

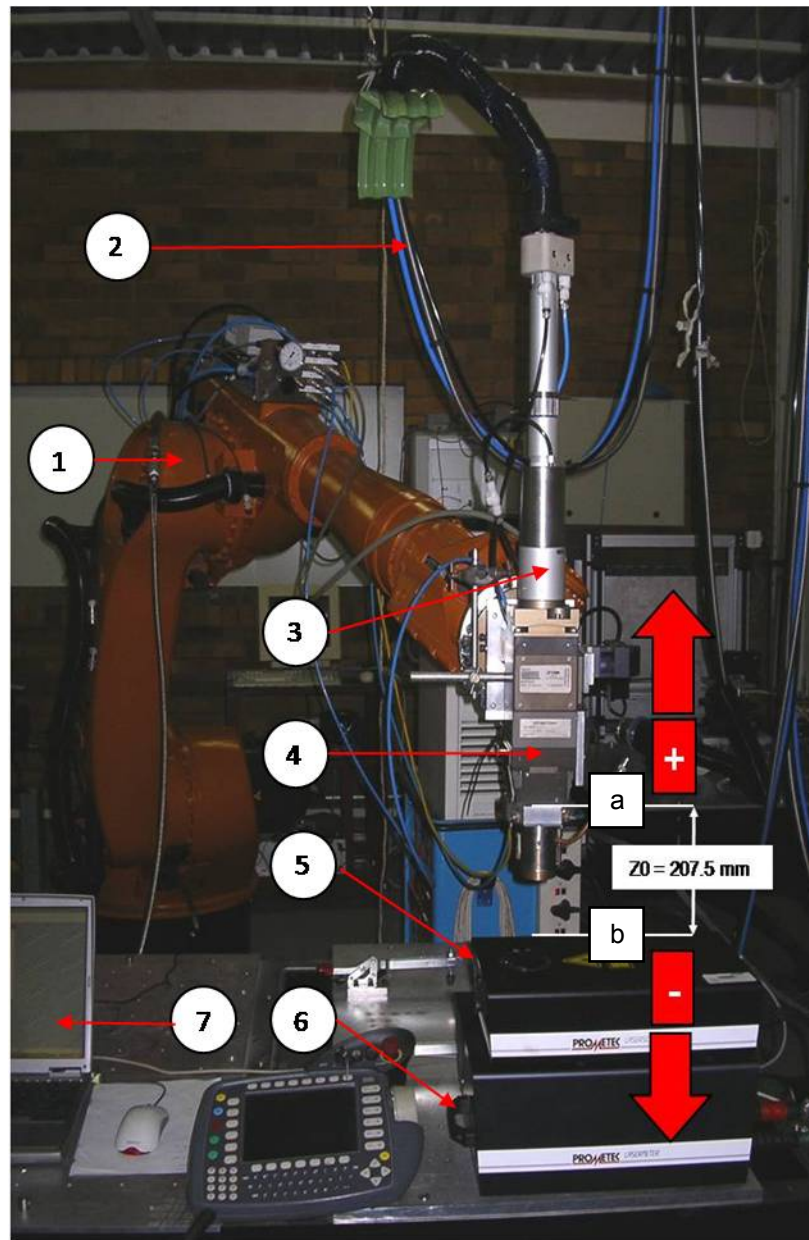


Figure 3.8: Laser beam profiling setup, indicating the reference plane (a) and the distance from it to the top surface (b) of the UFF100 laserscope. Also indicated is the sign convention used for the z-axis.

**Equipment used in the experimental test setup** (Refer to Figure 3.8):

1. A Kuka 6-axis robot to position the processing head.
2. A 0.4 mm multimode, step index fibre optic cable.
3. A collimator with a 200 mm collimating lens.
4. A Precitec YW50 processing head with 300 mm focussing lens.
5. A Prometec laserscope UFF100 with a 0.5 micron needle.
6. A Prometec lasermeter.
7. A laptop with Prometec PROLAS software
8. A height gauge vernier and 150 mm slide vernier (Not shown).

The UFF100 laserscope is placed directly above the lasermeter and aligned with each other such that the laser beam, not being diverted by the needle, is contained and dissipated within the lasermeter. The processing head is positioned above the UFF 100 laserscope with the optical axis of the processing head, which co-insides with the Z-axis, perpendicular to the top surface of the UFF 100 laserscope. This is done using the laser pointing diode as a reference for the actual laser beam, and positioning it relative to a thin circular perspex cover. The perspex cover fits in an opening above the rotating needle in the UFF100 laserscope indicating the measuring positions for focused and unfocussed beams. The processing head is thus positioned with respect to the X and Y-axis and it is only its position relative to the Z-axis that needs to be determined for the first scan.

The first scan is taken at the estimated focus position of the beam. The processing head is moved along the Z-axis so that the distance between the optical centre of the focussing lens and the needle of the laserscope is equal to the focal length of the focus lens which is 300 mm. Note that from previous investigations carried out by the National Laser Centre it is known that the needle is positioned  $\pm 7.5$  mm below the surface of the laserscope (Refer to Figure 3.9). Once the head is in position relative to all three axes the distance from the reference surface on the processing head to the laserscope is measured using a height gauge vernier. This distance was found to be 207.5 mm (Refer to Figure 3.8 ). Thus  $Z_0$ , at the estimated focus position is equal 215 mm, 207.5 mm plus 7.5 mm, allowing for the needle recess distance.

The radius of the laser beam at its waist/focus position was calculated to be  $\pm 0.3$  mm using equation 3.1. The optical centre of the of the focus lens was not marked on the processing head, thus the calculated beam focus was used to indicate whether or not the first scan was taken near the beam focus or whether the position of the first scan needed to be adjusted.

$$w_{or} = \frac{1}{2} \left( \frac{\phi_f \cdot f_f}{f_r} \right) \quad (3.1)$$

It is important to note that the Nd:YAG lasers spot size varies with average laser power, however in the case of a fibre delivered Nd:YAG laser such as was the case in this investigation the spot size remains the same irrespective of the average laser power.

The average laser power for each scan was 250 W, except for the scan at the working or cladding position for which the average laser power was increased to 500W.

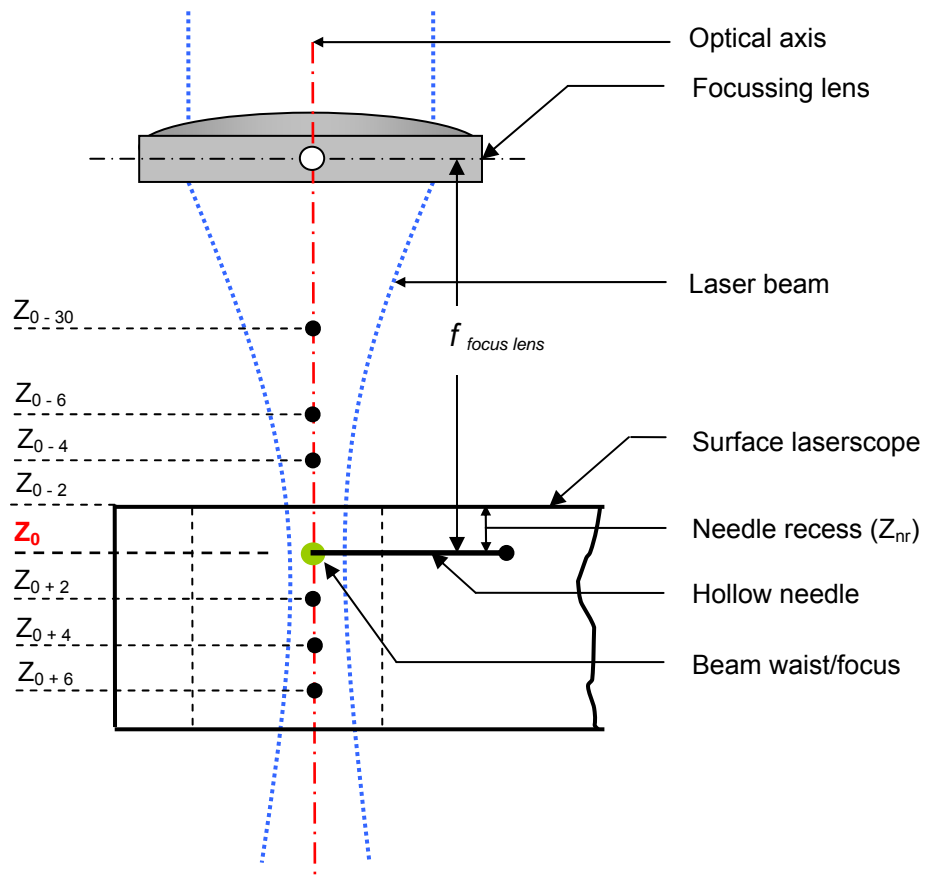


Figure 3.9: Schematic indicating the position the UFF100 needle recess and various scan positions.

The promotec software determines the laser beam focus position by considering several scans of the laser beam profile above and below its focus position. In addition to the first scan at the estimated focus position, three additional scans were carried out above and below the focus position in successive increments of 2 mm along the Z-axis (Refer to Figure 3.9).

These scans are combined to produce a caustic diagram. The caustic diagram is drawn by the software according to DIN ISO 11146.

### 3.4.4 Results: Laser beam profiling

The results from the laser beam profiling scans along the Z-axis are tabulated in Table 3.4.

		<p>1<sup>st</sup> Scan: <math>Z_0 = \text{Est. focus}</math></p> <table border="1"> <tr> <td><math>Z_0</math>:</td> <td>215 mm</td> </tr> <tr> <td><math>P_{\text{laser}}</math>:</td> <td>250W</td> </tr> <tr> <td><math>R</math> (86%):</td> <td>0.305 mm</td> </tr> <tr> <td><math>A</math> (86%):</td> <td><math>0.2920 \text{ mm}^2</math></td> </tr> <tr> <td><math>A_g</math> (86%):</td> <td><math>6.85 \times 10^4</math></td> </tr> </table>	$Z_0$ :	215 mm	$P_{\text{laser}}$ :	250W	$R$ (86%):	0.305 mm	$A$ (86%):	$0.2920 \text{ mm}^2$	$A_g$ (86%):	$6.85 \times 10^4$	
$Z_0$ :	215 mm												
$P_{\text{laser}}$ :	250W												
$R$ (86%):	0.305 mm												
$A$ (86%):	$0.2920 \text{ mm}^2$												
$A_g$ (86%):	$6.85 \times 10^4$												
		<p>2<sup>nd</sup> Scan: <math>Z_0 + 2 \text{ mm}</math></p> <table border="1"> <tr> <td><math>Z_2</math>:</td> <td>217 mm</td> </tr> <tr> <td><math>P_{\text{laser}}</math>:</td> <td>250 W</td> </tr> <tr> <td><math>R</math> (86%):</td> <td>0.2673 mm</td> </tr> <tr> <td><math>A</math> (86%):</td> <td><math>0.292 \text{ mm}^2</math></td> </tr> <tr> <td><math>A_g</math> (86%):</td> <td><math>7.47 \times 10^4</math></td> </tr> </table>	$Z_2$ :	217 mm	$P_{\text{laser}}$ :	250 W	$R$ (86%):	0.2673 mm	$A$ (86%):	$0.292 \text{ mm}^2$	$A_g$ (86%):	$7.47 \times 10^4$	
$Z_2$ :	217 mm												
$P_{\text{laser}}$ :	250 W												
$R$ (86%):	0.2673 mm												
$A$ (86%):	$0.292 \text{ mm}^2$												
$A_g$ (86%):	$7.47 \times 10^4$												
		<p>3<sup>rd</sup> Scan: <math>Z_0 + 4 \text{ mm}</math></p> <table border="1"> <tr> <td><math>Z_3</math>:</td> <td>219 mm</td> </tr> <tr> <td><math>P_{\text{laser}}</math>:</td> <td>250 W</td> </tr> <tr> <td><math>R</math> (86%):</td> <td>0.3382 mm</td> </tr> <tr> <td><math>A</math> (86%):</td> <td><math>0.328 \text{ mm}^2</math></td> </tr> <tr> <td><math>A_g</math> (86%):</td> <td><math>5.97 \times 10^4</math></td> </tr> </table>	$Z_3$ :	219 mm	$P_{\text{laser}}$ :	250 W	$R$ (86%):	0.3382 mm	$A$ (86%):	$0.328 \text{ mm}^2$	$A_g$ (86%):	$5.97 \times 10^4$	
$Z_3$ :	219 mm												
$P_{\text{laser}}$ :	250 W												
$R$ (86%):	0.3382 mm												
$A$ (86%):	$0.328 \text{ mm}^2$												
$A_g$ (86%):	$5.97 \times 10^4$												
		<p>4<sup>th</sup> Scan: <math>Z_0 + 6 \text{ mm}</math></p> <table border="1"> <tr> <td><math>Z_4</math>:</td> <td>221 mm</td> </tr> <tr> <td><math>P_{\text{laser}}</math>:</td> <td>250 W</td> </tr> <tr> <td><math>R</math> (86%):</td> <td>0.371 mm</td> </tr> <tr> <td><math>A</math> (86%):</td> <td><math>0.4318 \text{ mm}^2</math></td> </tr> <tr> <td><math>A_g</math> (86%):</td> <td><math>4.96 \times 10^4</math></td> </tr> </table>	$Z_4$ :	221 mm	$P_{\text{laser}}$ :	250 W	$R$ (86%):	0.371 mm	$A$ (86%):	$0.4318 \text{ mm}^2$	$A_g$ (86%):	$4.96 \times 10^4$	
$Z_4$ :	221 mm												
$P_{\text{laser}}$ :	250 W												
$R$ (86%):	0.371 mm												
$A$ (86%):	$0.4318 \text{ mm}^2$												
$A_g$ (86%):	$4.96 \times 10^4$												



Table continued

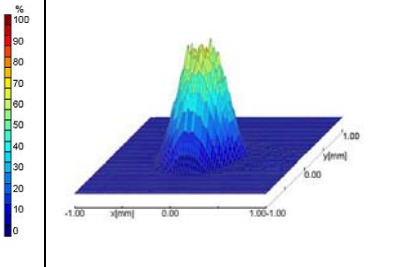
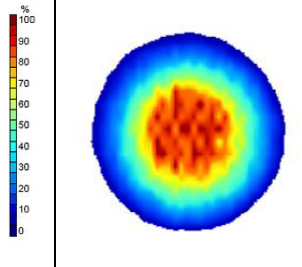
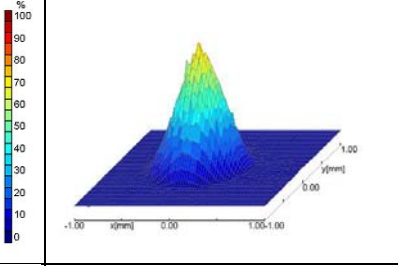
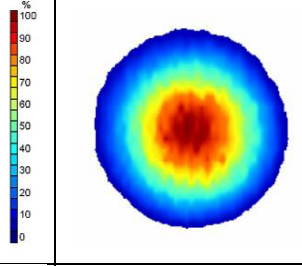
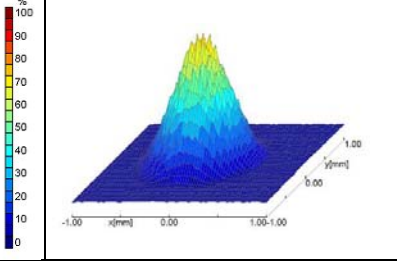
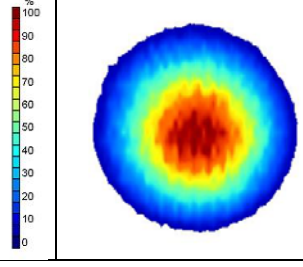
	5 <sup>th</sup> Scan: $Z_0 - 2$ mm		
	$Z_5$ :	213 mm	
	$P_{\text{laser}}$ :	250 W	
	$R$ (86%):	0.340 mm	
	$A$ (86%):	$0.3633 \text{ mm}^2$	
$Ag$	$5.83 \times 10^4$		
	6 <sup>th</sup> Scan: $Z_0 - 4$ mm		
	$Z_6$ :	211 mm	
	$P_{\text{laser}}$ :	250 W	
	$R$ (86%):	0.399 mm	
	$A$ (86%):	$0.5011 \text{ mm}^2$	
$Ag$	$4.41 \times 10^4$		
	7 <sup>th</sup> Scan: $Z_0 - 6$ mm		
	$Z_7$ :	209 mm	
	$P_{\text{laser}}$ :	250 W	
	$R$ (86%):	0.462 mm	
	$A$ (86%):	$0.6718 \text{ mm}^2$	
$Ag$	$3.29 \times 10^4$		

Table 3.4: Results from laser beam profiling tests.

#### 3.4.4.1 Caustic diagram

The laser beam focus position was determined from the caustic diagram using the Prometec software. The beam focus was determined to coincide with a point at a distance of 216.38 mm below the reference surface along the beam propagation axis or Z-axis. ( $Z_{w01} = Z_0 + 1.38 \text{ mm} = 216.38 \text{ mm}$ )

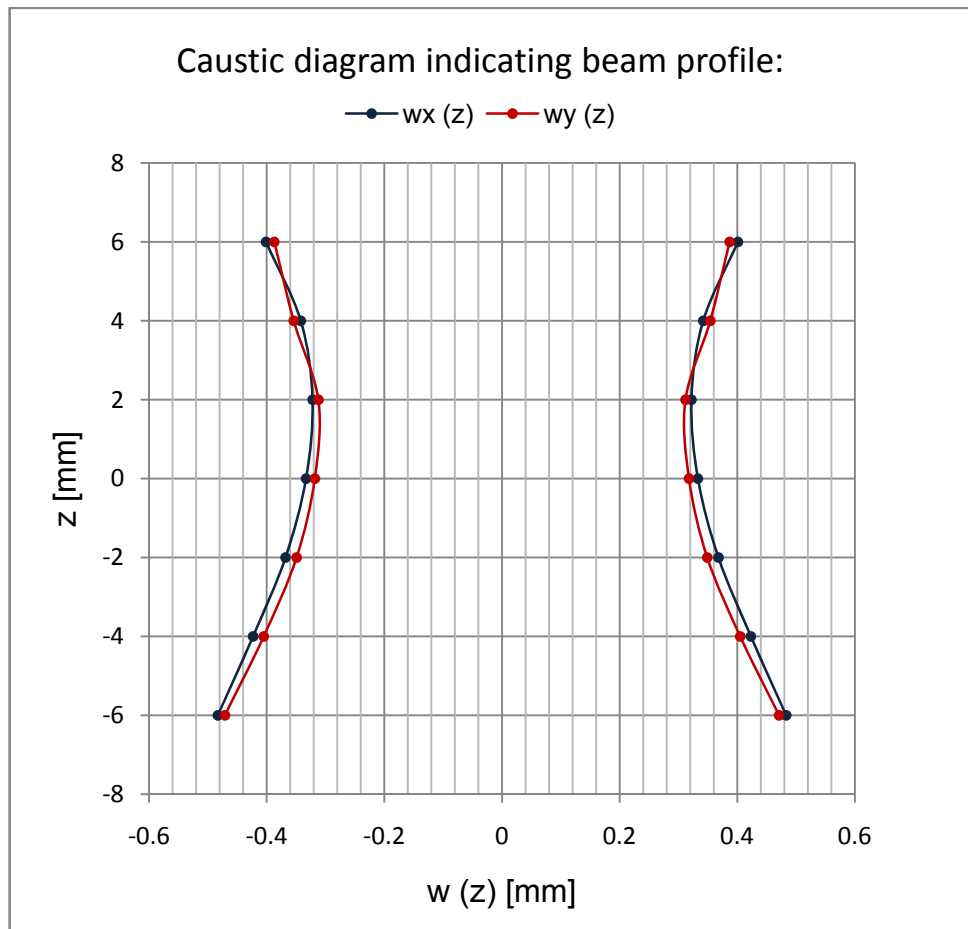


Figure 3.10: Caustic diagram indicating the beam profile or beam diameter with respect to each scanning position along the z-axis. ( $w$  = beam radius)

Subsequently, a scan at the beam focus position was carried out for documentation and in order to compare its intensity profile with the intensity profile at the experimental cladding position. The beam radius at its focus was found to be 0.29 mm which correlated well with the simple theoretical calculation made using equation 3.1. The experimental cladding position, with a beam radius of 1.51 mm, was determined to coincide with a point at a distance of 186.38 mm below the reference surface along the beam propagation axis or Z-axis.

### 3.4.4.2 Laser beam intensity profile and power density distribution

Table 3.5 compares the laser beam intensity profile and power density distribution of the beam focus and experimental cladding position.

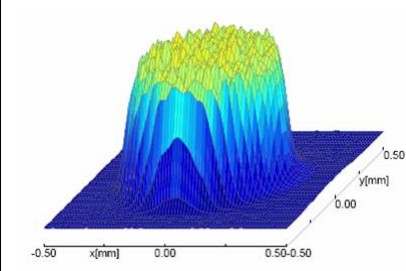
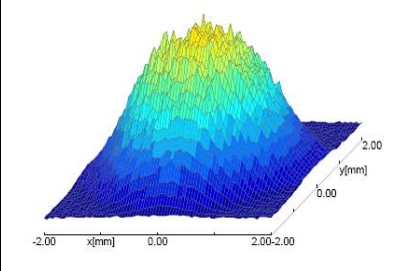
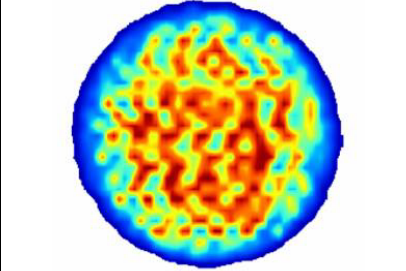
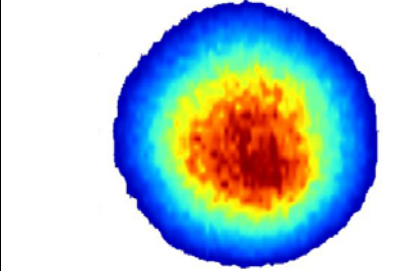
Scan at the beam focus: $Z_0 + 1.38$ mm		Scan at cladding position: $Z_{wo} - 30$ mm	
$Z_{wo}$ :	216.38 mm	$Z_{ECP}$ :	186.38 mm
$P_{laser}$ :	250 W	$P_{laser}$ :	500 W
$R_{(86\%)}$ :	0.29 mm	$R_{(86\%)}$ :	1.51 mm
$A_{(86\%)}$ :	0.2648 mm <sup>2</sup>	$A_{(86\%)}$ :	7.186 mm <sup>2</sup>
$Ag_{(86\%)}$ :	$7.5 \times 10^4$ W/cm <sup>2</sup>	$Ag_{(86\%)}$ :	$5.96 \times 10^4$ W/cm <sup>2</sup>
	 <p style="text-align: center;">a</p>		 <p style="text-align: center;">b</p>
	 <p style="text-align: center;">c</p>		 <p style="text-align: center;">d</p>

Table 3.5: Comparison of the laser beam intensity profile at its focus and at the experimental cladding position.

A clear difference was observed, considering Table 3.5 between the intensity profile of the laser beam at its focus and experimental cladding position when comparing the isometric projection of the three-dimensional power density distributions.

At the beam focus (Table 3.5-a) the intensity profile resembled a typical top-hat intensity profile generally associated with fibre delivered beams. At the experimental cladding position (Table 3.5-b) the laser beam intensity profile observed had a more gaussian-like shape.

From the contour displays it could further be seen that the power density distribution is much more uniform across the entire beam area at its focus (Table 3.5-c). At the experimental cladding position the highest power density lay in the centre of the beam area and decreased towards the periphery of the beam area (Table 3.5-d). In addition it could be seen that the power distribution was slightly off-centre but this may have been a result of reaching the limiting beam diameter that could be measured with the specific needle.

### **3.4.5 Discussion: Laser beam profile**

The results from the laser beam profiling tests revealed the following important points:

- The laser beam focus position was found to coincide with a point at a distance of 216.38 mm below the reference surface along the beam propagation axis or Z-axis.
- At its focus position the beam radius was found to be 0.29 mm and exhibited a typical top-hat intensity profile with a relatively uniform power density distribution over the entire beam area.

- The experimental cladding position above the beam focus where the beam radius was 1.5 mm was found to coincide with a point at a distance of 186.33 mm below the reference surface along the beam propagation axis or Z-axis.
- At the experimental cladding position the intensity profile had a gaussian-like shape and the majority of the laser power was concentrated in the centre of the beam area.

### **3.5 Determining the main process variables test levels**

#### **3.5.1 Introduction**

Through the literature review, it was established that the main process variables that define the laser cladding processing window are laser power ( $P$ ), laser scanning velocity ( $v_s$ ) and the powder mass flow rate ( $m_g$ ). It was however not known what the various test level settings should be for each of the main process variables. Therefore several tests were carried out to determine suitable test level settings, as described in sections 3.5.2 to 3.5.7.

#### **3.5.2 Objective: Variable test level tests**

To determine the various test level settings for the variables: laser power ( $P$ ); laser scanning velocity ( $v_g$ ), and the powder feed rate ( $m_p$ ) which would be used in the experimental cladding test matrix.

### 3.5.3 Experimental test setup: Establishing the variable test levels

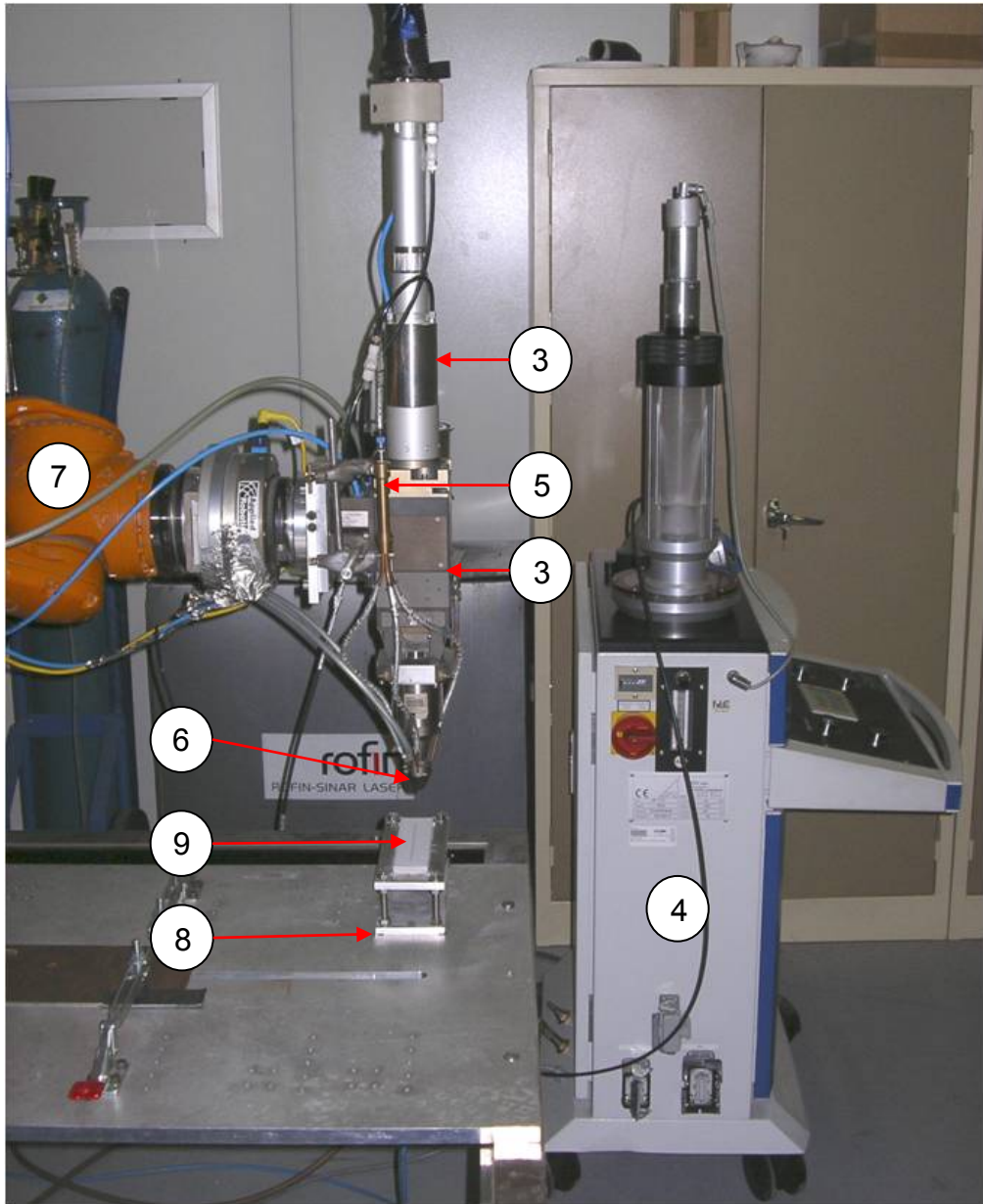


Figure 3.11: Cladding setup to determine the various process variable test level settings.

**Test equipment used in the experimental test setup (Refer to Figure 3.11)**

1. A 4.4 kW, Rofin Sinar DY44 Nd:YAG laser source.
2. A 0.4 mm multimode step index fibre.
3. An YW50 Precitec processing head.
4. A GTV PF 2/2 powder feed unit.
5. A three way powder splitter attached to the processing head.
6. A discontinuous or three way coaxial.
7. A Kuka 6 axis robot.
8. An aluminium specimen holder.
9. Al 1370-F aluminium specimens, 150 mm long x 40 mm wide x 12 mm thick.
10. Al-20wt%Si, spherical particles, 25-75  $\mu\text{m}$ .

The laser source used for this investigation was a Rofin Sinar DY44, 4.4 kW, diode pumped Nd:YAG laser with a principal wavelength of 1064 nm. The laser beam was transported by means of a 0.4 mm multimode, step index fibre optic cable. The focal length of the collimation and focus lenses were 200 and 300 mm respectively. The distance between the focus lens and the specimen surface was such that the resultant beam diameter on the specimen surface was 3 mm. The angle of incidence of the laser beam relative to the substrate surface was  $90^\circ$ . Laser beam movement was provided by a 6-axis Kuka robot on which the processing head was mounted while The specimen remained stationary.

The powder delivery system consisted of a GTV PF 2/2 powder feed unit using argon as the carrier gas. (No additional shielding gas was used.) The Al-20wt%Si powder was transported from the powder feed unit through anti-static tubing to the coaxial nozzle via the powder splitter. A three way coaxial nozzle with an apex angle of  $\pm 70^\circ$  was used. The diameter of the three individual nozzles was 2 mm. The nozzle stand-off distance was kept constant at 12 mm.

The Al 1370-F specimens were placed in a purpose made specimen holder (Refer to Figure 3.12) which was clamped to the work table surface. The specimen holder not only located each specimen correctly but minimized the heat loss through other surfaces in contact with the specimen. The bottom surface of the specimen had minimal contact with the specimen holder and it was raised  $\pm 50$  mm from the work table surface.

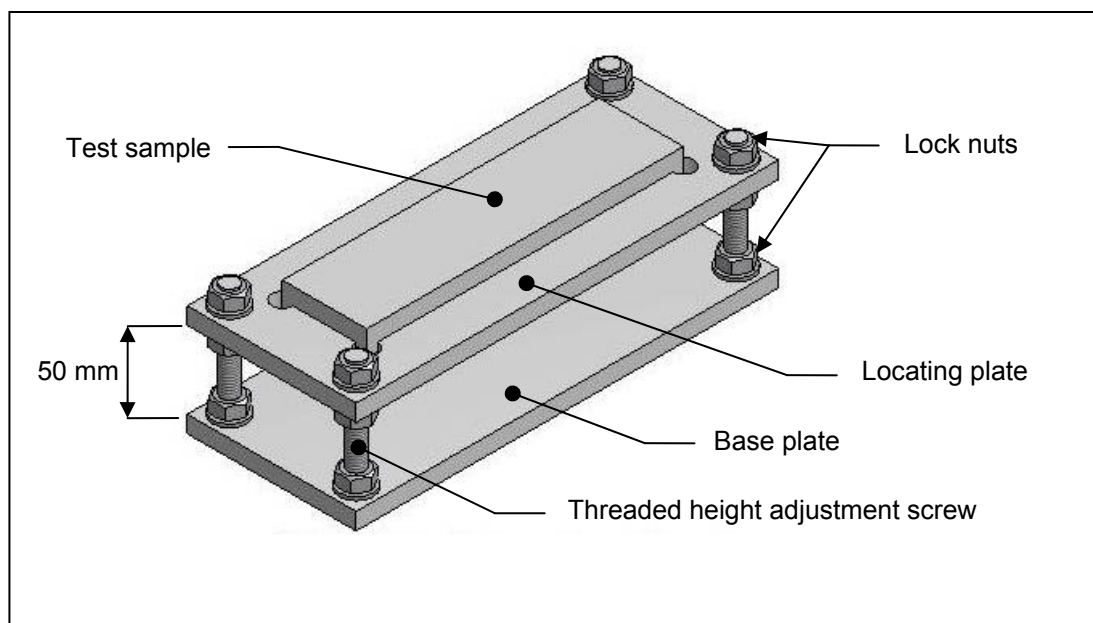


Figure 3.12: Test sample holder.



Prior to testing, a robot working sequence, consisting of several points in space was programmed with respect to a marked sample placed in the sample holder. The markings represented the start and end position of the single pass clad layer on the sample surface.

The working sequence shown in Figure 3.13 consisted of five points in space. Point (o) represents the home position of the robot. From point (o) to point (a), point to point interpolation movement was programmed and again from point (d) to point (o). However, from points (a) to (d) linear interpolation movement was programmed to ensure smooth jerk-free motion across the sample surface.

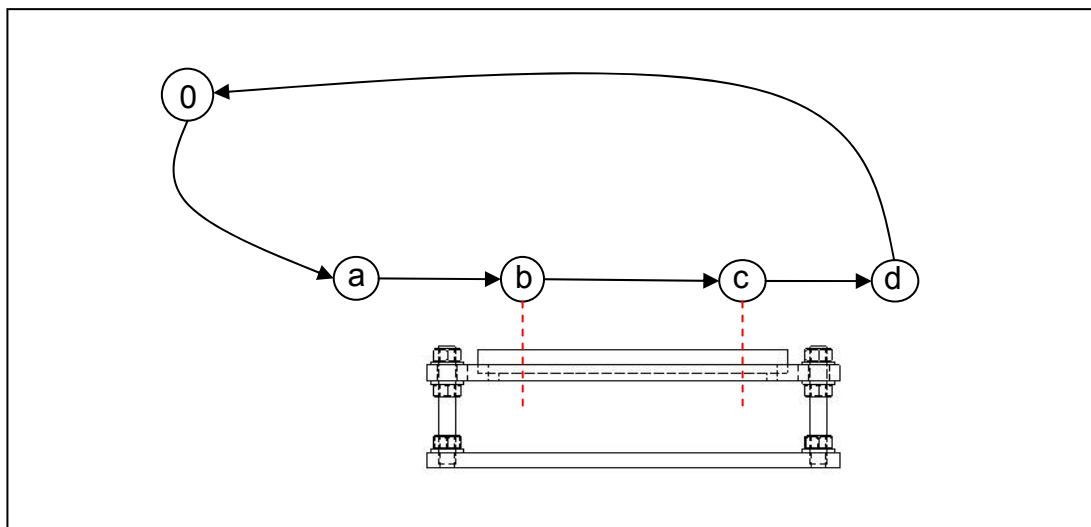


Figure 3.13: Robot working sequence.

### **3.5.4 Experimental test procedure: Establishing the variable test levels**

A test sample was placed in the sample holder, with the robot in its home position, and the various test levels set. (The carrier gas flow rate was kept constant at 1.5 l/min.) Next the programmed robot sequence was started. At point (a) the powder feed unit was manually switched on and at point (b) the laser was automatically switched on, signalling the start of the single pass clad layer. The laser was switched off at point (c), the end of the single pass clad layer. The powder feed unit was switched off at point (d) before the robot returned to its home position again at point (o).

### **3.5.5 Experimental test matrix: Establishing the variable test levels**

Based on literature, three laser power ( $P$ ) test levels were selected namely 2000, 2500 and 3000 W. The optimum laser scanning velocity was to be determined at each of the laser power set points through visual inspection, considering substrate wettability. In this case substrate wettability refers to the ability of the laser to create a very shallow melt pool on the surface of the test sample.

The first step was to determine the laser scanning velocity ( $v_s$ ) boundary conditions,  $v_{s1}$  and  $v_{s3}$  at  $P_1 = 2500$  W and  $P_3 = 3000$  W respectively. The upper scanning velocity limit ( $v_{s3}$ ) was assumed to correspond to a scanning velocity that just started to melt the substrate surface at the upper test limit for the laser power ( $P_3$ ).

Similarly it was assumed that the lower scanning velocity limit ( $v_{s1}$ ) could be determined at the lower test limit for laser power ( $P_1$ ). With the aid of published data six different scanning velocity test level settings were selected namely: 6, 9, 12, 15 and 18 mm/s.

However the initial tests indicated that this type of approach, which was previously successfully used for a mild steel substrate, was not suitable for the highly reflective aluminium substrate.

At a laser power and scanning velocity of 2000 W and 6 mm/s respectively the test sample surface showed no effect after being scanned with the laser. At a higher laser power and the same scanning velocity of 3000 W and 6 mm/s respectively the laser initially did not couple with the sample surface. However, as the sample surface temperature increased the laser suddenly coupled with the sample surface only to cause a serious back reflection resulting in the laser source shutting down. It was therefore decided to discontinue testing without powder being added to the melt pool.

The inability to determine suitable laser scanning velocity test levels at the pre-determined laser power test levels using the substrate wettability approach prompted an unexpected change in the approach to establish the process variable test levels. Due to experimental constraints, a pragmatic approach was adopted. After each test, the single pass clad layer on the sample surface was inspected and the test level settings adjusted.

The adjustment in the test level settings was based on the known influence of a change in the variable settings on the clad geometry which had been established during the literature review. The various random test level settings that were explored are tabulated in Table 3.6.

Nr	P (W)	$v_s$ (mm/s)	$N_{pfd}$ (rpm)	$v_g$ (l/min)
ST 001	2000	6	N/A	1.5
ST 002	3000	6	N/A	1.5
ST 003	2000	6	1.0	1.5
ST 004	2500	6	0.5	1.5
ST 005	2500	6	1.0	1.5
ST 006	2500	6	1.5	1.5
ST 007	3000	6	1.0	1.5
ST 008	3500	6	0.5	1.5
ST 009	3500	6	1.0	1.5
ST 010	3500	6	1.5	1.5
ST 011	3500	6	2.0	1.5
ST 012	3500	6	2.5	1.5
ST 013	3500	6	3.0	1.5
ST 014	3500	10	1.0	1.5
ST 015	3500	10	1.5	1.5
ST 016	3500	3	1.0	1.5
ST 017	2750	6	0.5	1.5
ST 018	2750	6	1.0	1.5
ST 019	2750	6	1.5	1.5
ST 020	2750	6	2.0	1.5
ST 021	2750	14	1.5	1.5
ST 022	2750	6	1.0	1.5
ST 023	2750	10	1.0	1.5
ST 024	3500	12	1.5	1.5
ST 025	3500	3	0.5	1.5
ST 026	3500	14	2.0	1.5
ST 027	3500	16	2.5	1.5

Table 3.6: Random test variable levels tested during the setup tests.

### 3.5.6 Test results: Establishing the variable test levels

The results from the experimental test matrix for establishing the main process variable test levels (Table 3.6) are tabulated in Table 3.7.







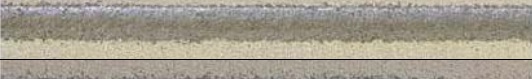










Sample Nr	H (mm)	W (mm)	Aspect ratio	Visual appearance of the clad layer
ST 001	n/a	n/a	n/a	n/a
ST 002	n/a	n/a	n/a	
ST 003	0.82	1.20	1.46	
ST 004	0.37	1.65	4.45	
ST 005	0.72	1.55	2.15	
ST 006	0.94	1.83	1.94	
ST 007	0.60	2.16	3.60	
ST 008	0.29	3.06	10.56	
ST 009	0.58	2.71	4.67	
ST 010	0.82	2.55	3.11	
ST 011	1.06	2.53	2.39	
ST 012	1.25	2.85	2.28	
ST 013	1.41	2.98	2.12	
ST 014	0.39	2.75	7.05	
ST 015	0.52	2.38	4.57	
ST 016	1.00	2.98	2.98	
ST 017	0.33	2.06	6.24	
ST 018	0.66	1.75	2.65	

Table continued










Sample Nr	H (mm)	W (mm)	Aspect ratio	Visual appearance of the clad layer
ST 019	0.93	1.82	1.95	
ST 020	1.23	2.02	1.64	
ST 021	0.47	1.37	2.92	
ST 022	0.84	1.69	2.01	
ST 023	0.41	1.65	4.02	
ST 024	0.42	2.38	5.65	
ST 025	0.54	3.02	5.60	
ST 026	0.47	2.77	5.89	
ST 027	0.55	2.06	3.75	

Table 3.7: Tabulated results from the setup test matrix.

Considering the visual appearance of the single pass clad layer on the test sample surface in Table 3.7 it can be seen that when the laser power was reduced to 2500 W the surface of the clad layer became increasingly irregular and the amount of powder adhering to the sample surface but not contributing to the actual build-up of the clad layer increased. Similarly, when the powder feed rate was increased the amount of powder adhering to the surface but not contributing to the actual build-up of the clad layer increased. Interestingly the clad layer surface did however seem to become more regular with an increase in the powder feed rate at the lower power level test settings. Based on this evidence a lower laser power test limit of 2750 W was selected.

An upper laser power limit of 3500 W was selected simply to keep the upper limit within an acceptable level from the maximum power output of the laser.

Again based on the visual appearance of the clad layer surface it was found that a low laser scanning velocity at a particular laser power and powder feed rate produced the best clads. A lower test limit for the laser scanning velocity was selected based on the believe that a scanning velocity below 5 mm/s would make an already expensive process economically less viable.

Therefore, a lower test limit of 5 mm/s was selected for the lower laser scanning velocity test limit. An upper test limit for the laser scanning velocity of 11 m/s was selected by considering the reduction in the clad width with an increase in the laser scanning velocity, especially when considering the lower power test levels.

The lower limit for the powder feed rate was selected by considering the height of the clad layer at the lower laser power test limit and upper scanning velocity test limit. Reducing the powder feed rate below 0.5 rpm would have resulted in a very thin clad layer which would have increased the risk of a flashback should the clad layer become discontinuous. Therefore a lower test limit of 0.5 rpm was selected for the powder feed rate. The upper test limit for the powder feed rate was selected by considering the clad height at the upper laser power and lower laser scanning velocity test limits. Increasing the powder feed rate beyond 2.0 rpm resulted in a clad layer with a relatively

small aspect ratio which increases the potential risk of inter-run porosity.

Therefore an upper powder feed rate test limit of 2.0 rpm was selected.

### 3.5.7 Discussion: Process variable test levels

Based on the results of the setup test matrix the following variable test level settings were selected for the final cladding test matrix in section 3.10.5.

Laser power (P)	P <sub>1</sub>	2750 W
	P <sub>2</sub>	3000 W
	P <sub>3</sub>	3250 W
	P <sub>4</sub>	3500 W
Laser scanning velocity (v <sub>s</sub> )	v <sub>s1</sub>	5 mm/s
	v <sub>s2</sub>	7 mm/s
	v <sub>s3</sub>	9 mm/s
	v <sub>s4</sub>	11 mm/s
Powder feed rate (N <sub>pdf</sub> )	N <sub>1</sub>	0.5 rpm
	N <sub>2</sub>	1.0 rpm
	N <sub>3</sub>	1.5 rpm
	N <sub>4</sub>	2.0 rpm

Table 3.8: Main process variable test level settings established based on the results of the setup test matrix.



## 3.6 Analysis of the coaxial nozzle

### 3.6.1 Introduction

A simplified visual analysis method was used for the cold stream analysis of the powder stream from a three-way coaxial nozzle. The process variables: powder mass flow rate ( $m_p$ ) and the carrier gas volume flow rate ( $v_g$ ) were evaluated to determine their effect on the powder stream produced.

The results from the cold stream visual analysis were used to determine several process parameters associated with the experimental cladding test setup.

### 3.6.2 Objective: Coaxial nozzle tests

- To determine the half apex,  $\beta_1$  or  $\beta_2$  of the nozzle.
- To determine the effect of the process variables,  $m_p$  and  $v_g$  on the position of the powder stream focus relative to the nozzle tip.
- To determine the effect of the process variables,  $m_p$  and  $v_g$  on the core diameter of the powder stream at its focus.

### 3.6.3 Experimental test setup: Coaxial nozzle tests

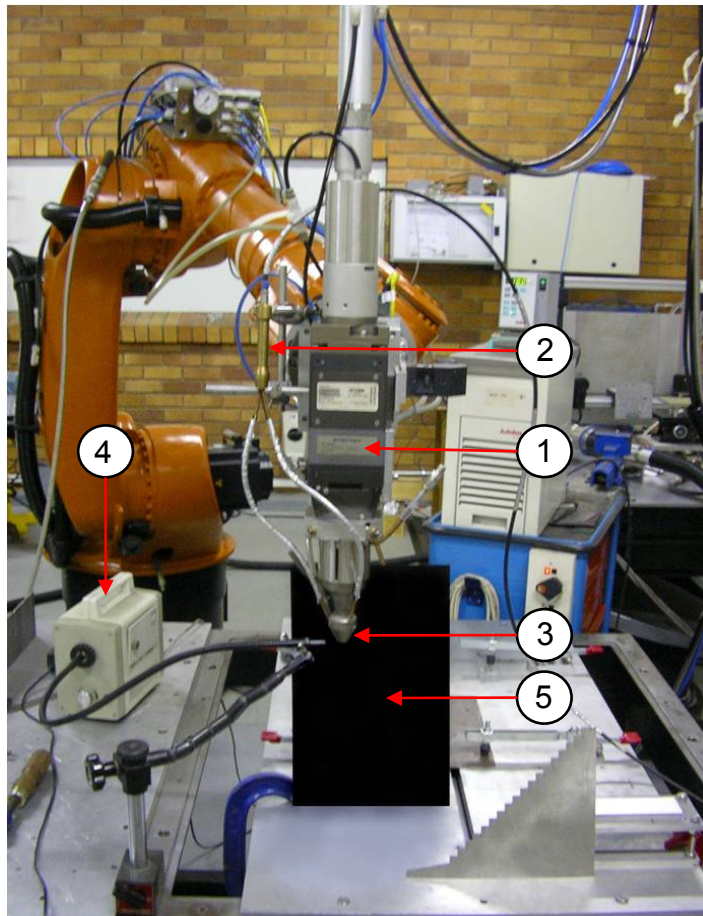


Figure 3.14: Experimental test setup for the cold stream analysis of the powder flow from a coaxial nozzle.

#### Test equipment used in the experimental test setup (Refer to Figure 3.14)

1. An YW50 Precitec processing head for mounting the powder splitter and three-way coaxial nozzle.
2. A three-way powder splitter.
3. A three-way coaxial nozzle.
4. A focussed light source.
5. Black background.

6. GTV PF 2/2 powder feed unit with argon as carrier gas.
7. Digital camera, visual analysis software.

The coaxial nozzle (mounted on the processing head) is positioned such that its work axis was perpendicular to the work surface and with the nozzle  $\pm 200$  mm away from the work table surface. A black background was placed behind the coaxial nozzle to remove the background noise from the images and to increase image contrast. A point light source was used to illuminate the cold powder stream. Digital images of the cold powder stream were taken using a high resolution digital camera. Ideally the position of the camera should be fixed. However during this investigation its position was not fixed. The Al-20wt%Si powder was supplied by a GTV PF 2/2 powder feed unit via anti-static tubing through the powder splitter to the three-way nozzle.

At the beginning of the test sequence the nozzle shoulder diameter, indicated in Figure 3.16, was measured using a vernier and found to be 34.8 mm. The nozzle shoulder diameter served as a reference dimension for determining the scale of the digital images during the visual analysis of the powder stream.

#### **3.6.4 Experimental test procedure: Coaxial nozzle tests**

The first step was to set the powder feed rate by setting the rotational speed of the powder feed disc. Once the powder feeder was switched on, the carrier gas flow rate could be set by adjusting the gas flow rate meter.

With both process variables set the powder was allowed to flow through the nozzle for  $\pm 15$  seconds before at least two digital images were taken of the illuminated powder stream from the coaxial nozzle. These images were saved and analyzed using visual analysis software.

### 3.6.5 Experimental test matrix: Coaxial nozzle tests

The effect of the powder mass flow rate ( $m_p$ ), represented by the rotational speed of the powder feed disc ( $N_{pfd}$ ), was evaluated at four different levels namely: 0.5, 1, 1.5 and 2 rpm respectively. The effect of the carrier gas volume flow rate ( $v_g$ ) was evaluated at three different levels namely: 2, 3 and 4 l/min at each of the powder mass flow rate test levels respectively. A total of 24 images were taken, two at each test level combination.

Test sequence:	$N_{pfd}$ (rpm):	$v_g$ (l/min)		
1	0.5	2	3	4
2	1.0	2	3	4
3	1.5	2	3	4
4	2.0	2	3	4

Table 3.9: Experimental test matrix for the visual analysis tests of the coaxial nozzle.

### 3.6.6 Test results: Coaxial nozzle tests

#### 3.6.6.1 Variation in the cold stream powder profile

Figure 3.15 shows the digital images taken of the variation in the cold stream powder profile from the three-way coaxial nozzle with a change in the powder feed rate (represented by the rotational speed of the powder disc,  $N_{pfd}$ ) and the carrier gas volume flow rate.

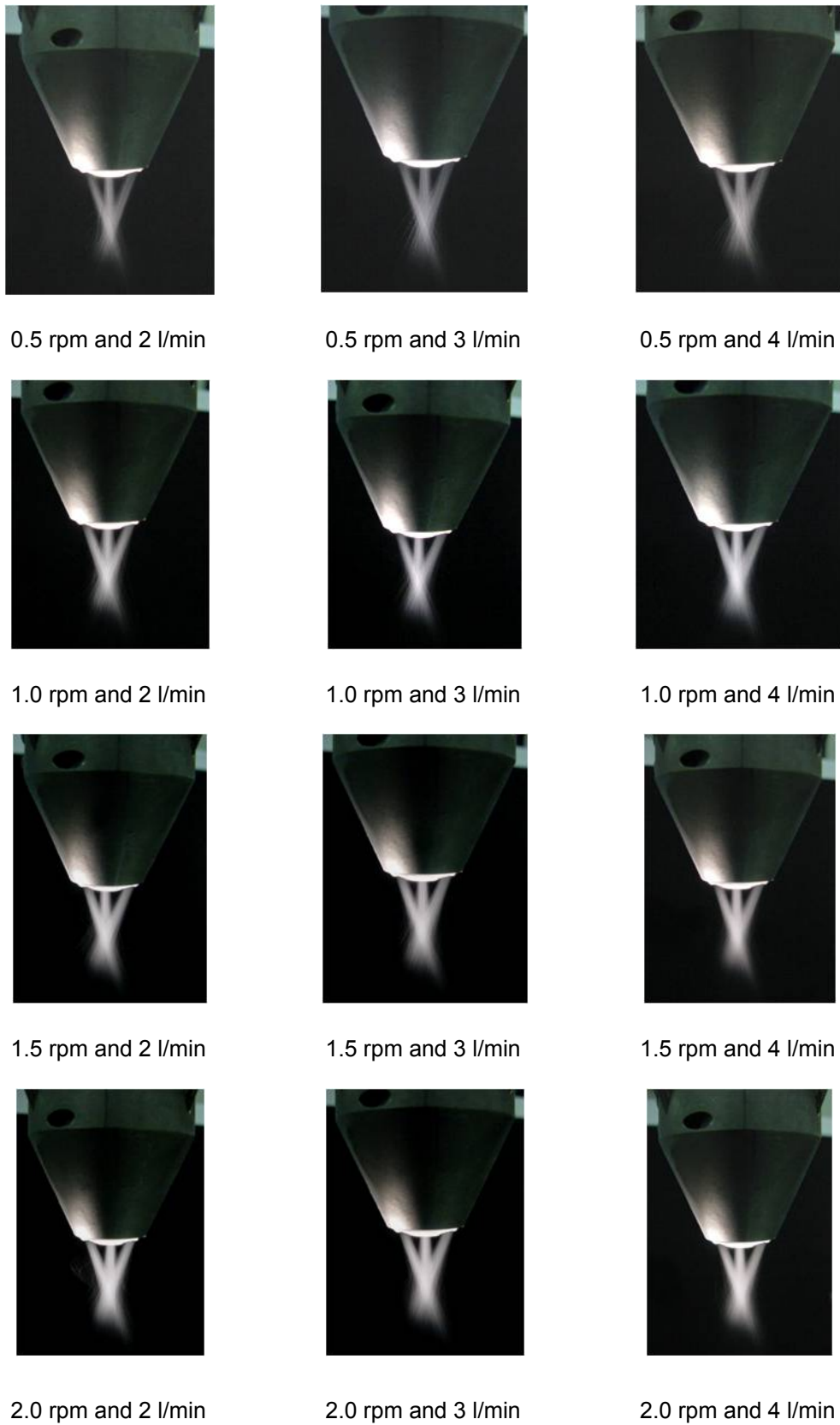


Figure 3.15: The variation in the powder stream profile with a change in the powder feed rate and carrier gas flow rate.

### 3.6.6.2 Visual analysis: Cold stream powder profile

In order to realize the objectives of the visual analysis of the coaxial nozzle several measurements were taken from the digital images. These measurements include: (Refer to Figure 3.16)

1. The distance from the nozzle tip to the powder stream focus ( $Z_{pf}$ );
2. The diameter of the powder stream at its focus ( $\varnothing_{pf}$ );
3. The diameter of the powder stream 10.5 mm from the nozzle tip ( $\varnothing_{ps\ 10.5}$ );
4. The distance between the nozzle tip and the position where the individual powder streams start to interfere with each other ( $Z_{int}$ );
5. The nozzle half apex angle ( $\beta_1$  and  $\beta_2$ ).

The scale of each digital image was different. To calibrate the measurement scale of the image analysis software (IAS) the nozzle reference diameter was measured using the image analysis software. The measured value was then set equal to the known reference nozzle diameter that was previously measured and found to be 34.8 mm. The image analysis software automatically adjusts its scale for subsequent measurements.

The resultant measurements for the different powder feed rate level settings at a carrier gas flow rate of 2 l/min are tabulated in Table 3.10.

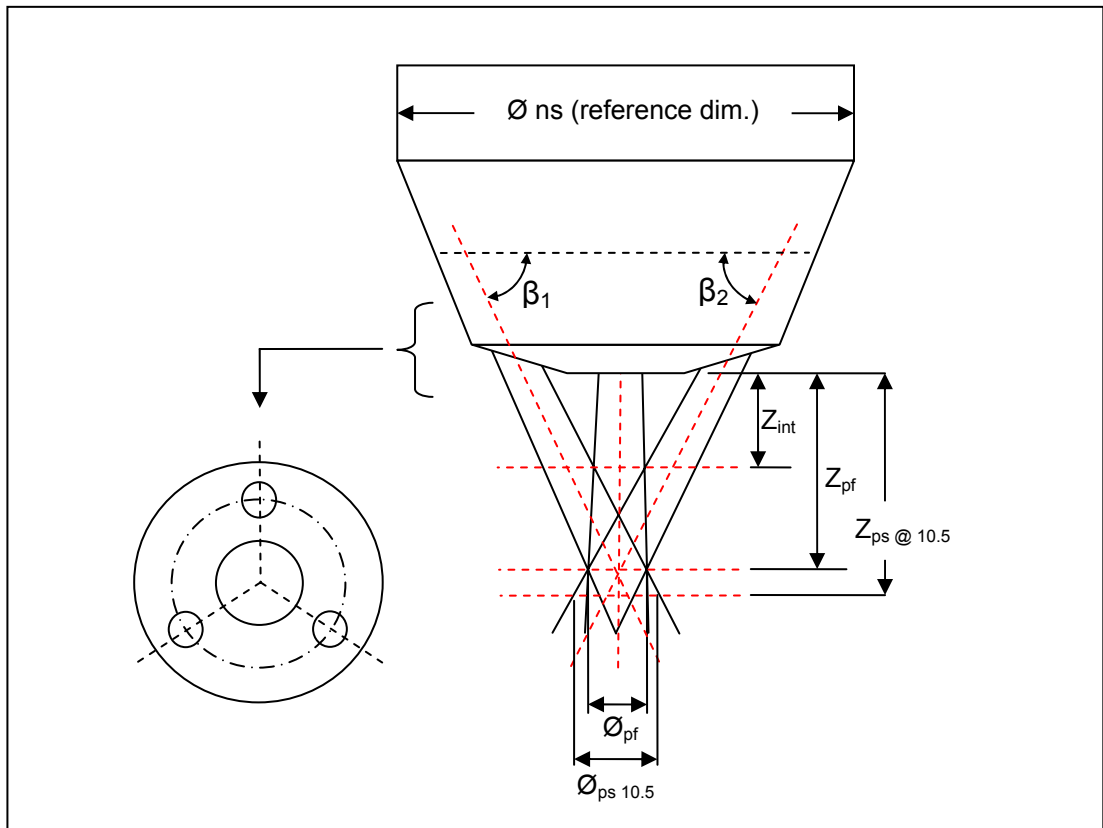


Figure 3.16: Measurements taken from the digital images for the visual analysis of the coaxial nozzle

Image Nr	$m_p$	$v_g$	$Z_{pf}$	$\varnothing_{pf}$	$\varnothing_{pf @ 10.5}$	$\beta_1$	$\beta_2$	$Z_{int}$
I	0.5	2	10.51	3.34	3.63	70.59	69.96	6.58
II	0.5	2	10.35	3.06	3.57	71.57	69.33	6.38
		AVG <sub>0.5</sub>	10.43	3.20	3.60	71.08	69.65	6.48
I	1.0	2	10.15	4.07	4.15	70.20	70.82	6.07
II	1.0	2	-	-	-	-	-	-
		AVG <sub>1.0</sub>	10.15	4.07	4.15	70.20	70.82	6.07
I	1.5	2	10.31	4.39	4.53	71.20	70.56	5.41
II	1.5	2	10.10	4.53	4.53	70.35	70.91	5.62
		AVG <sub>1.5</sub>	10.21	4.46	4.53	70.78	70.74	5.52
I	2.0	2	9.92	4.66	4.81	71.57	70.17	4.81
II	2.0	2	9.91	4.46	4.84	72.00	71.57	5.05
		AVG <sub>2.0</sub>	9.92	4.56	4.83	71.79	71.27	4.93

Table 3.10: Tabulated measurement results from the visual analysis of the coaxial nozzle.

### 3.6.7 Discussion: Cold stream powder profile

Based on the visual analysis of the powder stream from a three-way coaxial nozzle under cold stream flow conditions and based on the findings of the literature review an experimental stand-off distance ( $Z_{ns}$ ) of 10.5 mm was selected for the final experimental test matrix setup in section 3.10.5.

Based on literature the highest powder efficiency is achieved when the distance between the nozzle tip and the substrate surface equals the distance between the nozzle tip and the powder stream focus. Through the literature review it was also established that the highest powder efficiency is achieved when the ratio of the powder stream diameter to the laser beam diameter, measured on the substrate surface, equals a one to one ratio. Therefore, although the estimated powder stream focus diameter was always bigger than the laser beam diameter on the substrate surface, it was still the minimum powder stream diameter achievable with the nozzle used. In addition to the effect of the nozzle stand-off distance on the powder efficiency of the cladding process two other considerations are worth mentioning. Firstly, it was the researcher's opinion that a three-way coaxial nozzle should be used with a stand-off distance that is slightly larger than the distance between the powder stream focus from the nozzle tip to allow the three individual powder streams to form a consolidated powder stream. Thus since the distance between the nozzle tip and the powder stream focus was 10.43 mm at a powder feed rate of 0.5 rpm, 10.5 mm was considered to be a suitable stand-off distance. Secondly reducing the nozzle stand-off distance



to below 10.5 mm would increase the risk of powder particles ricocheting of the substrate surface damaging the nozzle.

Several other observations were made regarding the general trends associated with a change in the powder mass flow and carrier gas volume flow rate on the powder stream.

- The diameter of the powder stream at its focus increased with an increase in the powder mass flow rate at a constant gas flow rate.
- The distance between the nozzle tip and the powder stream focus position decreased with an increase in the powder mass flow rate at a constant gas flow rate.
- The half apex angle of the nozzle remained virtually constant as expected.

The first two observations seemed logical since individual powder stream divergence increased with an increases in the powder feed rate from 0.5-2.0 rpm. In addition an increase in the core powder focus diameter was observed with an increase in the carrier gas flow rate at a constant mass flow rate.

Based on the literature review and the observations made during the visual analysis tests, it was thus expected that at a constant laser power and scanning velocity the powder efficiency would decrease as the ratio of the

powder stream focus diameter to the laser beam spot diameter on the substrate surface increased.

### **3.7 Determining the optimum gas flow rate ( $v_g$ )**

#### **3.7.1 Introduction**

The total amount of test variable combinations in a four-variable, four-level, full factorial design is 128 tests. Reducing the amount of test variables to three significantly reduces the amount of variable combinations to be tested, from 128 to 64 tests. Therefore it was decided to evaluate the effect of the carrier gas flow rate prior to testing the final cladding test matrix as reported in section 3.10.5 in order to estimate an optimum carrier gas flow rate.

#### **3.7.2 Objective: Optimization of the gas flow rate**

To establish an experimental optimum gas flow rate for producing single pass clad layers on an aluminium substrate using Al-20wt%Si powder and a three-way coaxial nozzle.

#### **3.7.3 Experimental test setup: Optimization of the carrier gas flow rate**

See experimental test setup in section 3.5.3.

#### **3.7.4 Experimental test procedure: Optimization of the carrier gas flow rate**

See experimental test procedure in section 3.5.4.

### 3.7.5 Test matrix: Optimization of the carrier gas flow rate

The test matrix used to optimize and determine the effect of the carrier gas volume flow rate on the geometry of the single pass clad layer is tabulated in Table 3.11.

Sample nr	Std order	Run order	Power (W)	$v_s$ ( mm/s)	$m_p$ (rpm)	$v_g$ (l/min)
GFR 001	5	1	3125	9	1.25	3
GFR 002	8	2	3500	9	1.25	3
GFR 003	7	3	3500	9	1.25	2
GFR 004	2	4	2750	9	1.25	3
GFR 005	4	5	3125	9	1.25	2
GFR 006	3	6	2750	9	1.25	4
GFR 007	9	7	3500	9	1.25	4
GFR 008	1	8	2750	9	1.25	2
GFR 009	6	9	3125	9	1.25	4

Table 3.11: Experimental test matrix for determining the optimum carrier gas volume flow rate ( $v_g$ ).

Based on the results of the experimental test matrix in section 3.5.6 it was established that a carrier gas volume flow rate of  $\pm 1.5$  l/min would be suitable for the experimental investigation of the coaxial laser cladding process. At 1.5 l/min the powder stream profile appeared steady and consistent; the profile of the single pass clad layer on the substrate did not indicate that the gas-powder stream exerted excessive force on it and the apparent surface roughness of the clad layer was acceptable.

However the lowest marked gas flow rate setting on the gas flow meter was 2 l/min and therefore 2 l/min was chosen as the lower boundary test level for the experimental test matrix in Table 3.11 with two additional test level settings of 3 and 4 l/min respectively.

The main process variable test level settings were selected based on the outcome of the test matrix in section 3.5.6. The laser scanning velocity and powder feed rate were fixed at an average test level of 9 mm/s and 1.25 rpm respectively. To allow for the possible effect that an increase in the carrier gas flow rate might have on the interpretation of the results, three different laser power levels were selected namely: 2750 W, 3125 W and 3500 W respectively.

### 3.7.6 Test results: Carrier gas flow rate tests

Test results from the experimental test matrix re-ordered according to laser power and increasing carrier gas flow rate for clarity.





Sample Nr	P (W)	$v_s$ (mm/s)	$m_p$ (rpm)	$v_g$ (l/min)	Visual appearance
GFR 008	2750	9	1.25	2	
GFR 004	2750	9	1.25	3	
GFR 006	2750	9	1.25	4	
GFR 005	3125	9	1.25	2	
GFR 001	3125	9	1.25	3	

Table continued





Sample Nr	P (W)	$v_s$ (mm/s)	$m_p$ (rpm)	$v_g$ (l/min)	Visual appearance
GFR 009	3125	9	1.25	4	
GFR 003	3500	9	1.25	2	
GFR 002	3500	9	1.25	3	
GFR 007	3500	9	1.25	4	

Table 3.12: Tabulated test results from the experimental test matrix indicating the depression of the clad centre when considering the clad profile on the substrate surface.

### 3.7.7 Discussion: Optimization of the carrier gas flow rate

Visual analysis of the single pass clad layer profile on the test sample surface clearly indicated the adverse effect of increasing the carrier gas volume flow rate beyond 2 l/min over the entire range of laser power settings.

Increasing the gas flow rate resulted in an increase in the degree to which the melt pool centre was depressed, resulting in a significant increase in the acuteness of the clad root angle or wetting angle. An increase in the acuteness of the clad root angle increases the risk of inter-run porosity impacting negatively on coating quality. In addition the undulations in the coating layer would require additional machining to correct.

The depression of the clad centre was very evident even at a gas flow rate of 3 l/min. It was also observed that the depression of the clad centre generally increased with an increase in the laser power at constant powder feed rates.

## **3.8 Analysis of the GTV PF 2/2 powder feeder**

### **3.8.1 Introduction**

The GTV PF 2/2 powder feed unit is based on the principle of volumetric feed rate control. The volume of powder delivered to the substrate is dependent on the geometry of the annular groove in the powder feed disc, the shape of the spreader unit, the material addition, its size, and the rotational speed of the disc.

Therefore, in order to calculate the powder efficiency the amount of powder delivered in grams/second needs to be determined for each rotational speed setting of the powder disc. This would also ensure that the results could be transferred to other investigations using different powder delivery systems not based on volumetric feed rate control.

### **3.8.2 Objective: Investigation of the powder feed unit**

- To determine the relationship between the powder disc speed in revolutions per minute and the powder mass flow rate in grams per second.
- To determine the consistency of powder delivery.

### 3.8.3 Experimental test setup: Investigation of the powder feed unit

Test equipment used in the experimental test setup (Refer to Figure 3.17)

1. An YW50 Precitec processing head.
2. A GTV PF 2/2 powder feed unit.
3. A three-way powder splitter.
4. Nozzle height and alignment adaptor.
5. A discontinuous or three way coaxial.
6. A conically shaped test beaker.
7. Laboratory scale.

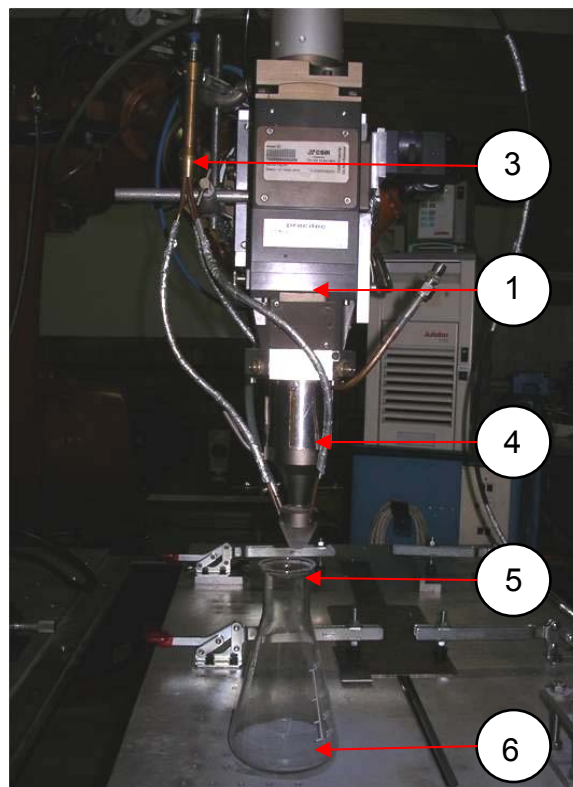


Figure 3.17: Experimental test setup for determining the relationship between the powder disc speed and the powder mass flow rate in grams/second.

The same cladding setup, as would be used for the final cladding test matrix in section 3.10.5, was used for determining the relationship between the powder disc speed and the powder mass flow rate to ensure that all system losses were considered.

The powder delivery system consisted of a GTV PF 2/2 powder feed unit using argon as the carrier gas. The Al-20wt%Si powder was transported from the powder feed unit through anti-static tubing to the three-way coaxial nozzle via the powder splitter. A conical test beaker was placed on the work table surface below the coaxial nozzle. The coaxial nozzle mounted on the processing head was positioned  $\pm 10$  mm above and slightly off-centre relative to the opening of the test beaker.

#### **3.8.4 Experimental test procedure: Investigation of the powder feed unit**

The test beaker was placed on the scale prior to each test and the scale reset to zero. A piece of paper was placed above the opening of the test beaker (to block any powder from entering the test beaker) before it was placed on the work table under the coaxial nozzle. The next step was to set the powder disc speed and switch on the powder feed unit. After the powder feed unit was switched on the carrier gas flow rate was set to 2 l/min, and the powder flow was allowed to stabilize for  $\pm 10$  seconds after which the paper was swiftly removed from above the opening of the test beaker and replaced again after 300 seconds had lapsed.



Afterwards the test beaker was weighed and the results tabulated before repeating the test sequence again with the next set of test parameters.

### **3.8.5 Experimental test matrix: Investigation of the powder feed unit**

Three variables were considered for this investigation. The inlet carrier gas pressure, the rotational speed of the powder feed disc ( $N_{\text{pfd}}$ ) and the volume flow rate of the carrier gas ( $v_g$ ).

The inlet carrier gas pressure was fixed at the recommended pressure specified by the manufacturer. In addition the manufacturer states that a change in the carrier gas volume flow rate does not affect the powder mass flow rate. In principle the researcher agrees with this statement but care must be exercised when powder delivery occurs over long distances and at low gas flow rates. In such a situation the researcher felt that fluctuations in powder delivery might exist. The only variable that remained to be evaluated to determine the powder mass flow rate was the rotational speed of the powder feed disc.

The powder mass flow rate was determined for four different rotational speed settings of the powder feed disc, selected based on the visual results of the experimental test matrix in section 3.5.6. Four identical test sequences, in which each of the rotational speed settings were evaluated were carried out resulting in a total of 16 tests. Five minutes was deemed a suitable period for

powder catchment to reduce the sensitivity of the test to errors associated with such low mass flow rates.

Test sequence	Test run	$N_{\text{pfd}}$ (rpm)	$v_g$ (l/min)	t (s)
A	1	0.50	2	300
	2	1.00	2	300
	3	1.50	2	300
	4	2.00	2	300
B	5	1.50	2	300
	6	1.00	2	300
	7	2.00	2	300
	8	0.50	2	300
C	9	1.50	2	300
	10	2.00	2	300
	11	0.50	2	300
	12	1.00	2	300
D	13	2.00	2	300
	14	1.50	2	300
	15	1.00	2	300
	16	0.50	2	300

Table 3.13: Test matrix indicating the test settings used to determine the powder mass flow rate at various powder disc speeds and the consistency of powder delivery.

### 3.8.6 Test results: Investigation of the powder feed unit

The relationship between the rotational speed of the powder disc ( $N_{pds}$ ) and the powder mass delivered in 300s for the four test sequences is illustrated in Figure 3.18.

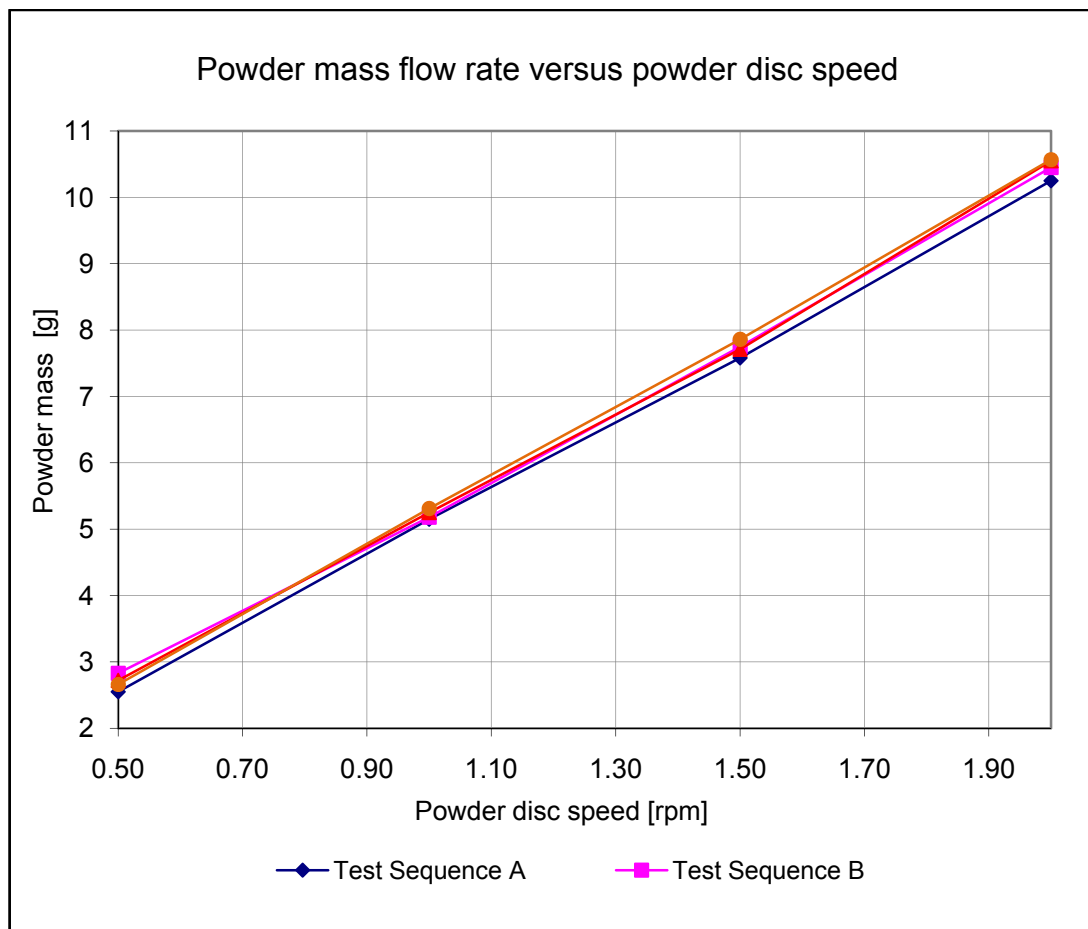


Figure 3.18: Graph representing the powder mass flow rate versus the powder disc rotational speed for each of the test sequences.

The input data to the graphical representation of the test results above are tabulated below in Table 3.14, organized according to powder disc rotational speed.

Sequence	$N_{pfd}$ (rpm)	$\dot{v}_g$ (l/min)	t (s)	$m_{seq}$ (g)
A	0.5	2	300	2.9968
	1.0	2	300	5.5968
	1.5	2	300	8.0268
	2.0	2	300	10.6968
B	0.5	2	300	3.2768
	1.0	2	300	5.6268
	1.5	2	300	8.1968
	2.0	2	300	10.8968
C	0.5	2	300	3.1668
	1.0	2	300	5.6968
	1.5	2	300	8.1568
	2.0	2	300	10.9968
D	0.5	2	300	3.1068
	1.0	2	300	5.7568
	1.5	2	300	8.3068
	2.0	2	300	11.0168

Table 3.14: Test results from the four test sequences indicating the mass of powder caught in the test beaker in 300 seconds.

### 3.8.6.1 Calculating the mass flow rate for each powder feed disc speed

The average experimental powder mass delivered in 300 seconds for each of the powder disc rotational speed test levels was calculated using equation

3.2.

$$m_{avg\ n} = \frac{\sum(m_{seq\ An} + m_{seq\ Bn} + m_{seq\ Cn} + m_{seq\ Dn})}{4} \quad (3.2)$$

The average experimental powder mass flow rate in grams per second for each of the powder disc rotational speed test levels was calculated by substituting the average experimental powder mass delivered calculated using equation 3.2 into equation 3.3.

(3.3)

$$\dot{m}_{avg n} = \frac{m_{avg} n}{300}$$

### 3.8.6.2 Tabulated calculation results

$N_{pfd}$ (rpm)	$m_{avg}$ (g)	$\dot{m}_{avg}$ (g/s)	$\dot{m}_{avg}$ (g/min)
0.50	3.1367	10.456E <sup>-03</sup>	0.627
1.00	5.6697	18.899E <sup>-03</sup>	1.134
1.50	8.1717	27.239E <sup>-03</sup>	1.634
2.00	10.9017	36.339E <sup>-03</sup>	2.180

Table 3.15: Tabulated calculation results for the mass of powder delivered per 300 seconds and powder mass flow rate per second for each test level setting of the powder disc speed.

### 3.8.6.3 Determining the consistency of powder delivery

The test sequences in Figure 3.18 were statistically analysed to determine if there was a significant difference between the results of the four test sequences. Both the slope and the intercept values of the individual test sequences were compared.

No statistically significant difference was found between the slopes of the four test sequences. Equal slopes indicated a constant change in the powder mass delivered in-between successive increments of the powder feed disc rotational speed. However when the intercept values for the test sequences were considered, it was found that the four test sequences could not be considered to be the same. There were no statistically significant differences

in the values of the differences between the average intercept value and the intercept values for test sequence B, C and D.

However, statistically the intercept for test sequence A was significantly lower than the average intercept value for all test sequences. A variation in the intercept value indicated that the powder mass delivered at each of the powder feed disc rotational speed settings were not always constant when comparing the four test sequences.

If test sequence A is ignored and it is assumed there was some initial error involved in the first test sequence it could be assumed that powder delivery is consistent.

### **3.8.7 Discussion: Investigation of the powder feed unit**

Prior to testing the test matrix several methods of powder catchment were tested. The most effective method of powder catchment was considered the solution that resulted in the most powder caught in 300 seconds, measured in grams.

A major drawback of the powder catchment method used was the loss of a small percentage of powder aerated during the process thereby escaping containment. It was perceived that powder escaping containment would have a negative effect on the accuracy of the powder efficiency calculations yielding higher than expected powder efficiencies for the process. The error

introduced was difficult to determine but irrespective of the error introduced the mass flow rate results are still valid when used to determine the influence of the main process variables on the level of variation in the geometry of the developing clad layer and the level of variation in the powder efficiency.

## **3.9 Alignment of the coaxial nozzle**

### **3.9.1 Introduction**

The Precitec YW50 processing head used for this investigation is generally used as a laser welding head but due to its modular nature it could easily be adapted for coaxial laser cladding. For coaxial laser cladding a nozzle, height and alignment adaptor, shown in Figure 3.19, was fitted to the bottom of the processing head. Since it is an adjustable adaptor, alignment between the laser beam propagation axis and the nozzle work axis needs to be verified from time to time.

If the nozzle is not properly aligned with the laser beam, the resultant clad layer will appear asymmetrical about its centre when considering a clad cross-section. This is due to the powder stream that is not being injected into the centre of the melt pool or due to a variation in the individual powder stream-beam interaction times

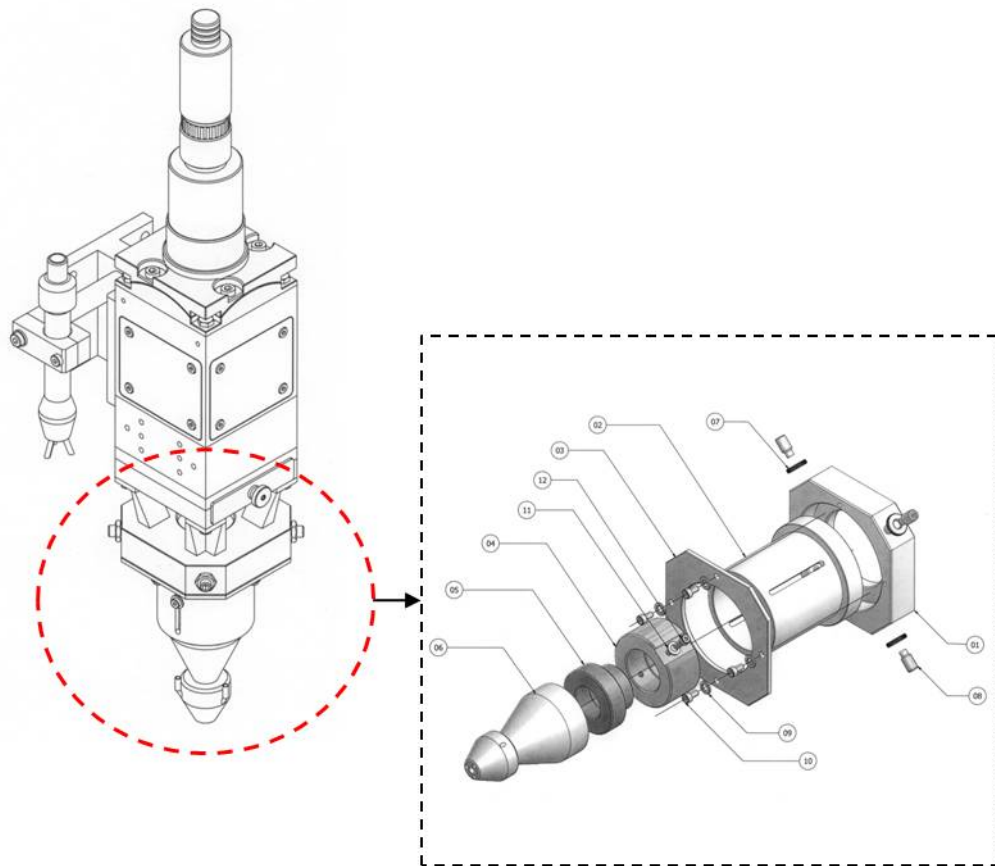


Figure 3.19: Nozzle height and alignment adaptor fitted to the bottom of the processing head.

Therefore, a simple visual inspection method was devised to confirm alignment between the nozzle and the laser beam (Refer to section 3.9.3). In addition the symmetry of the clad layer about its centre on the sample surface was inspected for confirmation. Ideally the symmetry of the clad cross-section would be considered but due to time constraints this was not possible.



### 3.9.2 Objective: Alignment verification tests

The principle objective of the alignment procedure was to align the nozzle work axis with the laser beam work axis, ensuring that they are concentric with each other. However in addition to the alignment procedure it was also investigated whether the test jig could be used to confirm the nozzle stand-off distance.

### 3.9.3 Experimental test setup: Alignment verification tests

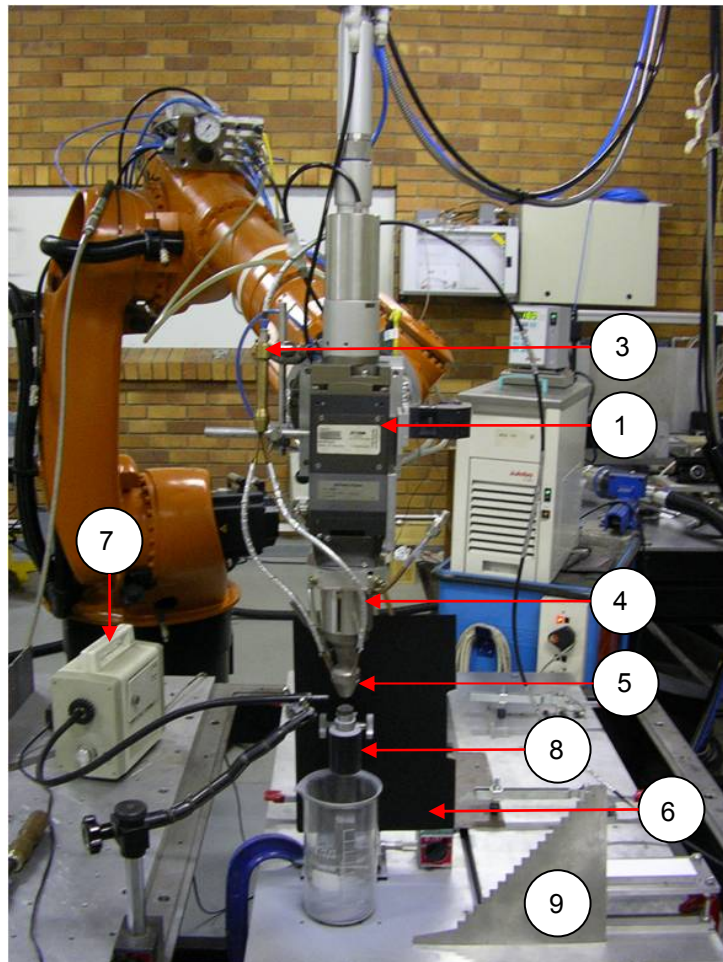


Figure 3.20: Alignment verification test setup.

**Test equipment used in the experimental test setup (Refer to Figure 3.20)**

1. An YW50 Precitec processing head.
2. GTV PF 2/2 powder feed unit with argon as carrier gas.
3. A three-way powder splitter.
4. A nozzle height and alignment adaptor.
5. A three-way coaxial nozzle.
6. A black background.
7. A focussed light source.
8. A three-axis alignment test jig.
9. Laser cut gauge plate.
10. Digital camera, visual analysis software.

The three-axis alignment test jig was clamped to the work table surface where after the coaxial nozzle was positioned over the test jig, using the robot. At this stage the coaxial nozzle was only roughly aligned with the centre of a test target placed in the test jig (Figure 3.21-5) and positioned such that the coaxial nozzle tip was  $\pm 15$  mm above the test target surface.

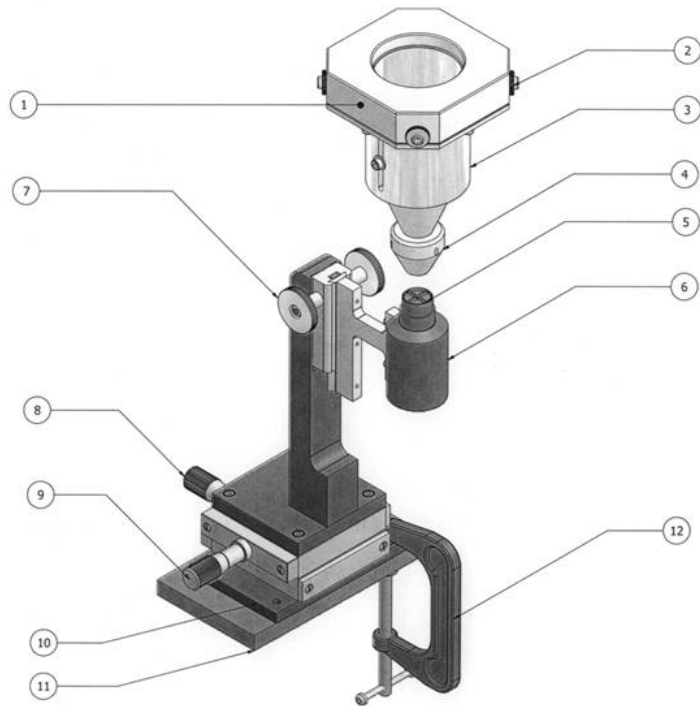


Figure 3.21: Illustrates the three-axis alignment test jig clamped to the work surface with the coaxial nozzle and nozzle height and alignment adaptor positioned over the test target.

Once the coaxial nozzle was roughly positioned, the laser pointing diode was used to finally align the laser beam propagation axis with the test target centre. (By aligning the test target centre with the beam propagation axis, the alignment test jig was also automatically aligned with the beam propagation axis.) During the final alignment process the processing head remained stationary. The X and Y-axis of the test jig was moved into position by adjusting the X and Y-micrometer dials (Figure 3.21-8 and 9). The achievable positioning accuracy was 0.002 mm.

Once the beam propagation axis, represented by the pointing diode, was aligned with the test target centre the X and Y-axis of the alignment test jig was locked into position and the test target replaced with an alignment test nozzle. The alignment test nozzle (Figure 3.22) has a conical face and an  $\varnothing$  4 mm opening in its centre.

Finally the nozzle stand-off distance was adjusted to 10.5 mm by turning the Z-axis adjustment knob (Figure 3.21- 7). The distance between the nozzle tip and the alignment test nozzle was measured using a custom laser cut gauge plate.

#### **3.9.4 Experimental alignment verification procedure**

The experimental alignment verification procedure was carried out at a fixed gas flow rate of 2 l/min, the experimental optimum gas flow rate as determined during the experimental gas flow rate tests in section 3.7. The powder feed rate was set to 1 rpm. It was considered that a lower powder feed rate would simplify the verification of the alignment between the coaxial nozzle work axis and the alignment test jig work axis. (It was previously experimentally shown in section 3.6 that an increase in the powder feed rate results in an increase in the core powder focus diameter.) In addition it was assumed a powder feed rate of 1 rpm might result in a better test resolution than 0.5 rpm.

The first step in the alignment procedure was to set the powder feed rate by setting the rotational speed of the powder disc to 1 rpm after which the powder feed unit was switched on. Once the powder feed unit was switched on the carrier gas volume flow rate was set to 2 l/min.

Using a focussed light source to illuminate the powder particles the cold powder stream from the coaxial nozzle entering the conical test nozzle opening was visually examined from various directions. The alignment of the coaxial nozzle was adjusted by adjusting four grub screws on the height and alignment adaptor attached to the processing head (Figure 3.21-2). In this manner the coaxial nozzle work axis was aligned with the test jig work axis, which was previously aligned with the beam propagation axis.

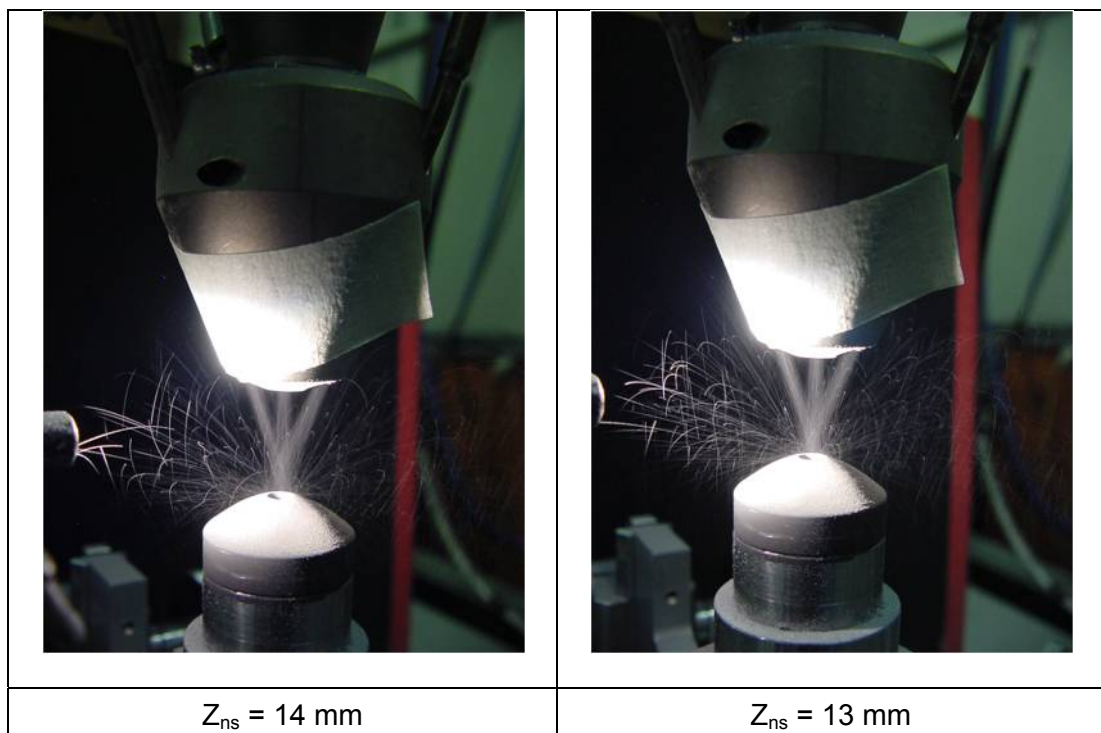


Figure 3.22: Visual inspection of the alignment between the coaxial nozzle work axis and the alignment test jig work axis (centre of the conical nozzle) representing the beam propagation axis

### 3.9.5 Experimental nozzle stand-off distance verification procedure

Upon completion of the alignment verification procedure an experimental test procedure was carried out using exactly the same setup to verify the findings regarding the optimum nozzle stand-off distance reached during the nozzle investigation in section 3.6.

To simulate various nozzle stand-off distances the Z-axis of the alignment test jig was simply adjusted up or down. Four different nozzle stand-off distances were investigated namely: 14, 13, 12 and 11 mm using a constant powder feed rate and gas flow rate of 1 rpm and 2 l/min respectively. At each of the simulated nozzle stand-off settings three digital images were taken with a high resolution digital camera for analysis. Selected images representing each nozzle stand-off distance is tabulated in Table 3.16.



*Table continues*

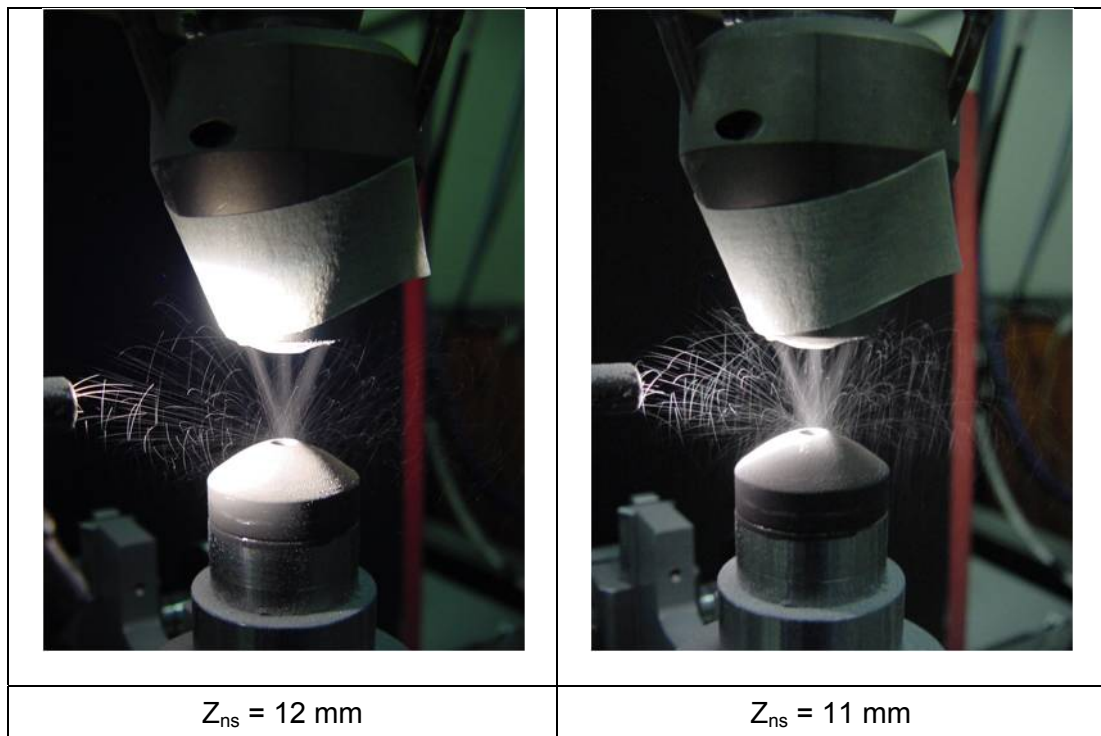


Table 3.16: Tabulated results from the experimental test procedure to verify the nozzle stand-off distance.

Based on the images in Table 3.16 a clear difference in the amount of powder ricocheting off the conical nozzle could be seen. The general trend seemed to be when comparing the images taken at a nozzle stand-off distance of 14 and 11 mm that the amount of powder ricocheting off the conical nozzle increased with a decrease in the nozzle stand-off distance. It is reasonable to assume that an increase in powder particles ricocheting off the nozzle surface indicated that less powder were entering the 4 mm opening suggesting that the powder stream was de-focussed. This is somewhat misleading and can mainly be attributed to the position of the light source when the digital image was taken. It was not always possible to illuminate all the powder particles effectively with a single light source.

During the visual inspection it was found that an important factor to consider was the angle at which the particles were deflected from the conical surface. Consider the conical surface of the alignment test nozzle in Figure 3.23 with three powder streams impacting on its surface.

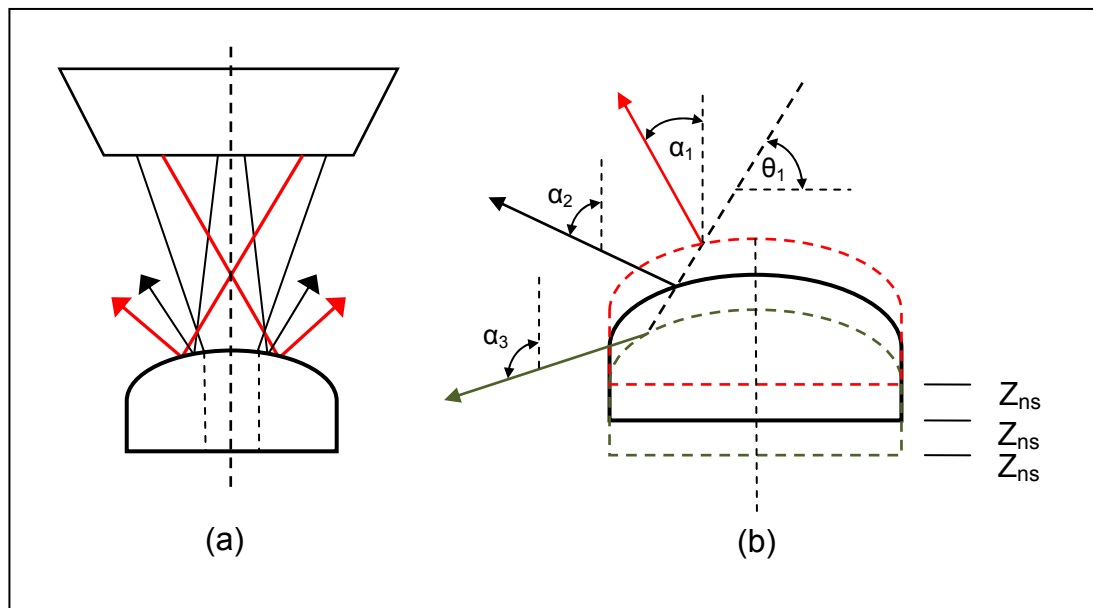


Figure 3.23: (a) Powder streams from a three-way coaxial nozzle impacting on a conical surface. (b) Schematic illustrating the change in the deflection angle of a powder particle with a change in the nozzle stand-off distance.

Figure 3.23 Consider Figure 3.23 (b) where a single powder particle impacts on a conical surface. It is shown that if the nozzle stand-off distance is increased from  $Z_{ns1}$  to  $Z_{ns3}$  the powder particle impact point tends to shift further away from the centre of the conical surface and therefore the deflection angle ( $\alpha$ ), off the conical surface, increases.



Therefore by considering both the change in the angle of deflection from the conical surface and the increase in the amount of powder particles ricocheting off the conical surface the estimated optimum nozzle stand-off distance was confirmed.

### 3.9.6 Experimental alignment verification test matrix

To confirm the alignment between the coaxial nozzle work axis and the laser beam propagation axis a couple of random single pass clad layers were made on test samples with the variable settings listed in Table 3.17:

Nr	P (W)	$v_s$ (mm/s)	$N_{pfd}$ (rpm)	$v_g$ (l/min)	$Z_{ns}$ (mm)
CT 001	3500	12	1.5	1.5	12
CT 002	3500	12	1.5	1.5	11
CT 003	3500	10	1.5	1.5	11
CT 004	3500	10	1.5	1.5	12
CT 005	3500	10	1.5	1.5	12
CT 006	3500	10	1.5	1.5	10
CT 007	3500	10	1	1.5	11
CT 008	3500	10	1	1.5	12
CT 009	3500	10	2	1.5	12

Table 3.17: Variable settings for random tests to confirm alignment.

### 3.9.7 Test results: Experimental alignment verification tests

The results from the experimental alignment verification test matrix are tabulated in Table 3.18.










Sample Nr	Surface inspection	
CT 001		
CT 002		
CT 003		
CT 004		
CT 005		
CT 006		
CT 007		
CT 008		
CT 009		

Table 3.18: Test results from the alignment verification tests.

### 3.9.8 Discussion: Experimental alignment verification tests

The alignment between the laser beam propagation axis/work axis and the nozzle work axis was confirmed through the visual inspection of the single pass clad layers on the substrate. Visual inspection confirmed that the profile of the clad layer was symmetrical about its centre which is a good indication that the laser beam and nozzle is aligned. This is especially true when considering samples CT001 to CT004 and CT009.

## **3.10 Cladding test matrix**

### **3.10.1 Introduction**

The final setup of the experimental cladding platform and the full factorial design cladding test matrix is the culmination of all the test results in the previous sections of chapter three. The results from the final cladding test matrix are discussed in chapter four.

### **3.10.2 Objective of the final experimental cladding test matrix**

The primary objective of the final experimental cladding test matrix was to determine the relationship between the main process variables: laser power (P); laser scanning velocity ( $v_s$ ); and the powder feed rate ( $m_g$ ), and the geometry of the single pass clad layer that developed on the test sample surface.

The secondary objective was to determine the relationship between the main process variables and clad characteristics such as the powder efficiency, vickers microhardness profile, microstructure and the defect population.

### **3.10.3 Experimental test setup**

The laser source used for this investigation was a Rofin Sinar DY44, 4.4 kW diode pumped Nd:YAG laser with a principle wavelength of 1064 nm. The laser beam was transported by means of a 0.4 mm multimode, step index fibre optic cable. The focal length of the collimation and focus lenses was 200 and 300 mm respectively.

The distance between the focus lens and the specimen surface was such that the resultant beam diameter on the specimen surface was 3 mm.

The angle of incidence of the laser beam relative to the substrate surface was 90°. Laser beam movement was provided by a 6-axis Kuka robot on which the processing head was mounted. (The test sample remained stationary)

The powder delivery system consisted of a GTV PF 2/2 powder feed unit using argon as the carrier gas. (No additional shielding gas was used) The Al-20wt%Si powder was transported from the powder feed unit through anti-static tubing to the coaxial nozzle via the powder splitter. A three-way coaxial nozzle with an apex angle of  $\pm 70^\circ$  was used. The diameter of the three individual nozzles was 2 mm. The nozzle stand-off distance was kept constant at 10.5 mm.

The Al 1370-F specimens were placed in a purpose-made specimen holder which was clamped to the work table surface. The specimen holder not only located each specimen correctly but minimized the heat loss through other surfaces in contact with the specimen. The bottom surface of the specimen had minimal contact with the specimen holder and it was raised  $\pm 50$  mm from the work table surface.

(Refer to Figure 3.11 in section 3.5.3 for further information regarding the test equipment used.)

### 3.10.4 Experimental test procedure

Exactly the same experimental test procedure was followed as what was described in section 3.5.4. However in addition to the normal test procedure the mass of each sample was recorded before and after cladding to determine the precise amount of powder used in forming the clad layer on the sample surface.

### 3.10.5 Final experimental test matrix

Run order	Std order	Sample Nr	P (W)	$v_s$ (mm/s)	$N_{pfd}$ (rpm)	$v_g$ (l/min)
36	1	C 001	3250	5	2	1.5
18	2	C 002	3000	5	1	1.5
38	3	C 003	3250	7	1	1.5
10	4	C 004	2750	9	1	1.5
47	5	C 005	3250	11	1.5	1.5
52	6	C 006	3500	5	2	1.5
43	7	C 007	3250	9	1.5	1.5
27	8	C 008	3000	9	1.5	1.5
57	9	C 009	3500	9	0.5	1.5
7	10	C 010	2750	7	1.5	1.5
33	11	C 011	3250	5	0.5	1.5
8	12	C 012	2750	7	2	1.5
63	13	C 013	3500	11	1.5	1.5
61	14	C 014	3500	11	0.5	1.5
31	15	C 015	3000	11	1.5	1.5
64	16	C 016	3500	11	2	1.5
5	17	C 017	2750	7	0.5	1.5
62	18	C 018	3500	11	1	1.5
53	19	C 019	3500	7	0.5	1.5
3	20	C 020	2750	5	1.5	1.5
39	21	C 021	3250	7	1.5	1.5
25	22	C 022	3000	9	0.5	1.5
44	23	C 023	3250	9	2	1.5
56	24	C 024	3500	7	2	1.5
17	25	C 025	3000	5	0.5	1.5
58	26	C 026	3500	9	1	1.5

Table continued

Run order	Std order	Sample Nr	P (W)	$v_s$ (mm/s)	$N_{pfd}$ (rpm)	$v_g$ (l/min)
15	27	C 027	2750	11	1.5	1.5
41	28	C 028	3250	9	0.5	1.5
1	29	C 029	2750	5	0.5	1.5
26	30	C 030	3000	9	1	1.5
48	31	C 031	3250	11	2	1.5
13	32	C 032	2750	11	0.5	1.5
35	33	C 033	3250	5	1.5	1.5
24	34	C 034	3000	7	2	1.5
34	35	C 035	3250	5	1	1.5
9	36	C 036	2750	9	0.5	1.5
51	37	C 037	3500	5	1.5	1.5
4	38	C 038	2750	5	2	1.5
46	39	C 039	3250	11	1	1.5
32	40	C 040	3000	11	2	1.5
2	41	C 041	2750	5	1	1.5
20	42	C 042	3000	5	2	1.5
42	43	C 043	3250	9	1	1.5
28	44	C 044	3000	9	2	1.5
29	45	C 045	3000	11	0.5	1.5
6	46	C 046	2750	7	1	1.5
23	47	C 047	3000	7	1.5	1.5
49	48	C 048	3500	5	0.5	1.5
55	49	C 049	3500	7	1.5	1.5
45	50	C 050	3250	11	0.5	1.5
30	51	C 051	3000	11	1	1.5
22	52	C 052	3000	7	1	1.5
11	53	C 053	2750	9	1.5	1.5
50	54	C 054	3500	5	1	1.5
19	55	C 055	3000	5	1.5	1.5
60	56	C 056	3500	9	2	1.5
16	57	C 057	2750	11	2	1.5
37	58	C 058	3250	7	0.5	1.5
40	59	C 059	3250	7	2	1.5
59	60	C 060	3500	9	1.5	1.5
12	61	C 061	2750	9	2	1.5
54	62	C 062	3500	7	1	1.5
21	63	C 063	3000	7	0.5	1.5
14	64	C 064	2750	11	1	1.5

Table 3.19: Main process variable test levels for the final experimental cladding test matrix.

## 4 Laser cladding process response

### 4.1 Introduction

In this chapter the process response to a change in the main process variables; laser power ( $P$ ); laser scanning velocity ( $v_s$ ) and the powder feed rate ( $m_g$ ) is discussed by considering the results from the statistical analysis of the final cladding test matrix.

The process response in this case specifically refers to the resultant clad geometry and clad characteristics such as dilution; Vickers microvickers hardness; microstructure, and the defect population of the clad layer. The process efficiency was measured by considering the variation in the powder efficiency.

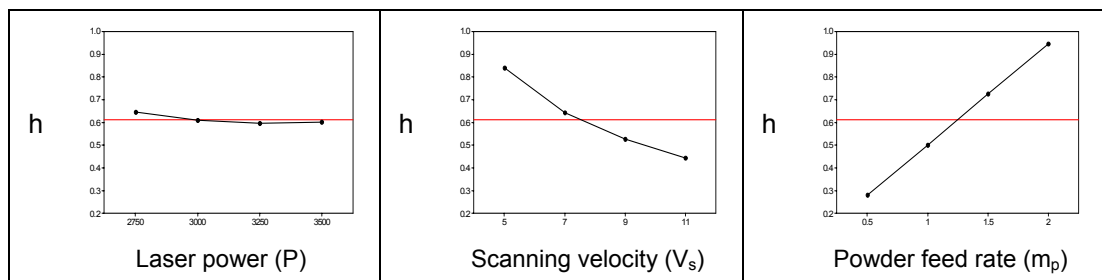
The statistical analysis of the process response values highlights the most influential process variables that affected a specific clad characteristic or property and the order of their importance (From the most influential to the least influential). In addition the process response means, considering each clad characteristic/property separately, to a change in each of the process variable test level settings is also summarised for easy interpretation of the process response.

## 4.2 The effect of the main process variables on the clad geometry

### 4.2.1 Clad height (h)

An analysis of the mean process response indicated that the most significant process variable affecting the clad height was the powder feed rate, followed by the laser scanning velocity. A change in laser power had little or no effect on the height of the clad layer.

Mean clad height at the four test level settings for: P;  $v_s$ , and  $m_p$



Variable	Level 1	$\Delta_{2-1}$	Level 2	$\Delta_{3-2}$	Level 3	$\Delta_{4-3}$	Level 4
P	0.6461	0.0365	0.6096	0.0133	0.5963	-0.0043	0.6006
$v_s$	0.8385	-0.1956	0.6429	-0.1161	0.5268	-0.0838	0.4430
$m_g$	0.2796	0.2212	0.5008	0.2254	0.7262	0.2197	0.9459

Table 4.1: The mean clad height for each process variable test level.

Considering Table 4.1, several observations were made regarding the general effect that a change in the main process variable test levels had on the height of a single pass clad layer:

- The height of the clad layer increased linearly with an increase in the powder feed rate. The increase could be directly attributed to an



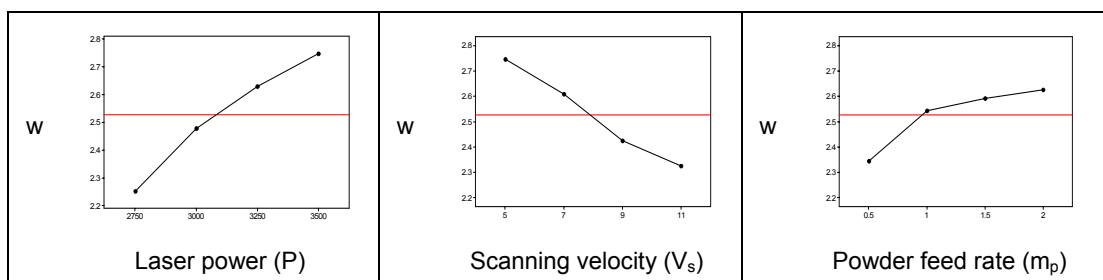
increase in the amount of powder delivered per unit length with an increase in the powder feed rate.

- The height of the clad layer decreased with an increase in the laser scanning velocity. The decrease could be attributed to a decrease in the amount of powder delivered per unit length with an increase in the laser scanning velocity.
- Laser power had no significant effect on the height of the clad layer.

#### 4.2.2 Clad width (w)

All three main process variables influenced the width of the clad layer. A change in laser power seemed to have the most significant effect on the width of the clad layer, followed by the laser scanning velocity and powder feed rate.

Mean clad width at the four test level settings for: P; v<sub>s</sub>, and m<sub>p</sub>



Variable	Level 1	$\Delta_{2-1}$	Level 2	$\Delta_{3-2}$	Level 3	$\Delta_{4-3}$	Level 4
P	2.2519	0.2262	2.4781	0.1500	2.6281	0.1194	2.7475
v <sub>s</sub>	2.7475	-0.1387	2.6088	-0.1838	2.4250	-0.1006	2.3244
m <sub>g</sub>	2.3438	0.1993	2.5431	0.0488	2.5919	0.035	2.6269

Table 4.2: The mean clad width for each process variable test level.

Considering Table 4.2, several observations were made regarding the general effect that a change in the main process variable test levels had on the width of a single pass clad layer:

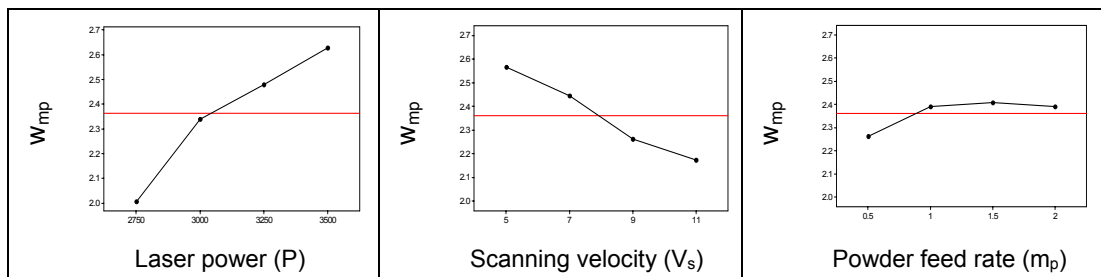
- The width of the clad layer increased almost linearly with an increase in laser power. An increase in laser power results in a direct increase in the energy input into the substrate material leading to an increase in the width of the melt pool on the substrate surface.
- An increase in the laser scanning velocity had the inverse effect on the clad width when compared to laser power. The width of the clad layer decreased almost linearly with an increase in the laser scanning velocity. The decrease in the clad width could be attributed to a reduction in the interaction time between the laser and the substrate, and thus also the energy input per unit length.
- The width of the clad layer increased with an increase in the powder feed rate. However, only the mean clad width between test level one and two in Table 4.2 increased significantly. The increase in the width of the clad layer with a increase in the powder feed rate is only likely to occur if the powder particles were already melted upon impact on the un-melted substrate, allowing the melt pool to spread laterally beyond the general melt-substrate interface defined by the diameter of the laser beam on the substrate surface. Inspection of the clad cross-sections revealed that when the clad layer spread too far

beyond the melt-substrate interface the ends of the clad layer often did not form a proper metallurgical bond with the substrate.

#### 4.2.3 Width of the melt pool ( $w_{mp}$ )

As expected, a change in laser power had the most significant influence on the width of the melt pool, followed by the laser scanning velocity. A change in the powder feed rate had little or no effect on the width of the melt pool, except between levels one and two.

Mean width of the melt pool at the four test level settings for:  $P$ ;  $v_s$ , and  $m_p$



Variable	Level 1	$\Delta_{2-1}$	Level 2	$\Delta_{3-2}$	Level 3	$\Delta_{4-3}$	Level 4
P	2.005	0.333	2.338	0.141	2.479	0.149	2.628
$v_s$	2.568	-0.122	2.446	-0.183	2.263	-0.089	2.174
$m_g$	2.262	0.129	2.391	0.017	2.408	-0.018	2.390

Table 4.3: The mean width of the melt pool for each process variable test level.

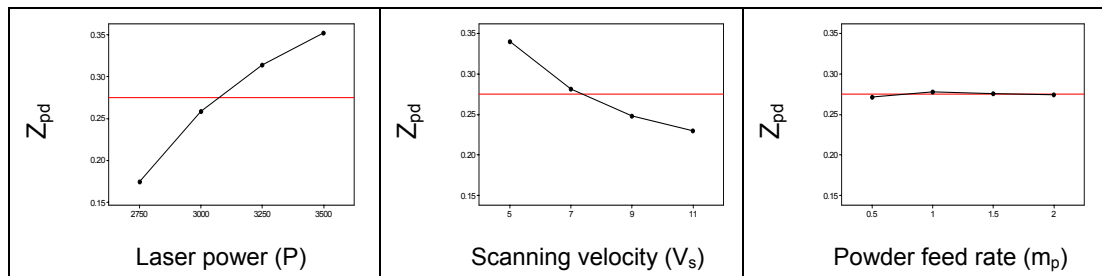
Considering Table 4.3, several observations were made regarding the general effect that a change in the main process variable test levels had on the width of a single pass clad layer:

- The width of the melt pool increased with an increase in the laser power.
- An increase in the laser scanning velocity caused a decrease in the width of the melt pool.
- An increase in the powder feed rate had no significant effect on the width of the melt pool.

#### 4.2.4 Alloy penetration depth ( $Z_{pd}$ )

The depth of alloy penetration was mainly dependent on laser power and to a lesser extent on the laser scanning velocity. The powder feed rate had no significant effect on the depth of alloy penetration.

Mean alloy penetration depth at the four test level settings for:  $P$ ;  $v_s$ , and  $m_p$



Variable	Level 1	$\Delta_{2-1}$	Level 2	$\Delta_{3-2}$	Level 3	$\Delta_{4-3}$	Level 4
P	0.1747	0.0842	0.2589	0.0548	0.3137	0.0388	0.3525
$v_s$	0.3404	-0.0593	0.2811	-0.0327	0.2484	-0.0184	0.2300
$m_g$	0.2718	0.0061	0.2779	-0.0020	0.2759	-0.0016	0.2743

Table 4.4: The mean depth of alloy penetration for each process variable test level.

Considering Table 4.4, several observations were made regarding the general effect that a change in the main process variable test levels had on the depth of alloy penetration into the substrate material:

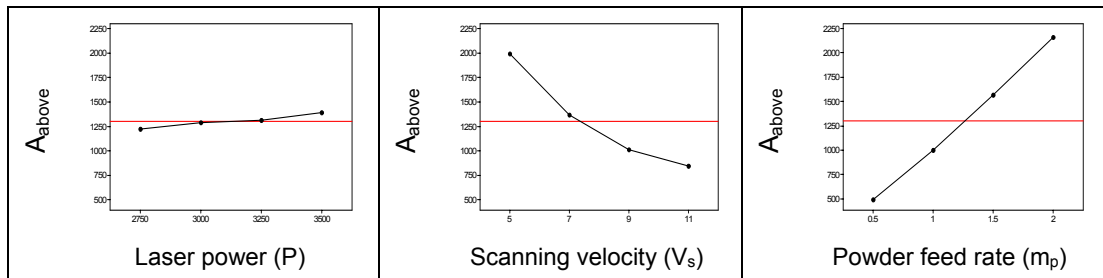
- The depth of alloy penetration increased with an increase in laser power. The increase could be attributed to an increase in the energy supplied to, and absorbed by the substrate material.
- The depth of alloy penetration decreased with an increase in the laser scanning velocity due to a reduction in the interaction time between the laser beam and the substrate surface.
- A change in the powder feed rate had little or no effect on the depth of alloy penetration. This was an interesting observation since **Schneider** reported that laser power attenuation increases linearly with an increase in the powder feed rate (10). Based on **Schneider's** statement, an increase in the powder feed rate was therefore expected to result in a decrease in the depth of alloy penetration, generally due to an increase in the shadowing effect of the powder particles whereby the substrate is shielded from direct laser radiation. However this was not the case, which could be explained by considering another statement made by **Schneider** which stated that depending on the temperature of the powder particles upon arrival at the melt pool, they can either add or extract energy from the melt pool. Therefore it could be assumed, that for this investigation, either an increase in the powder feed rate had a negligible effect on laser power

attenuation, or possibly, that the powder particles added energy to the melt pool which reduced the overall effect of an increase in the powder feed rate on the net energy supplied to the melt pool.

**4.2.5 Clad area above the substrate surface ( $A_{above}$ )**

The most significant process variable affecting the clad area above the substrate was the powder feed rate followed by the laser scanning velocity. A change in laser power had little or no effect on clad area above the substrate.

Mean clad  $A_{above}$  the substrate at the four test level settings for: P;  $v_s$ , and  $m_p$



Variable	Level 1	$\Delta_{2-1}$	Level 2	$\Delta_{3-2}$	Level 3	$\Delta_{4-3}$	Level 4
P	1222	64	1286	29	1315	77	1392
$v_s$	1992	-627	1365	-350	1015	-172	843
$m_g$	489.8	507.8	997.6	571.4	1569	590	2159

Table 4.5: The mean clad area above the substrate for each process variable test level.

Considering Table 4.5, several observations were made regarding the general effect that a change in the main process variable test levels had on the clad area above the substrate surface:

- The clad area above the substrate surface increased linearly with an increase in the powder feed rate. The increase could again be attributed directly to an increase in the amount of powder delivered per unit length with an increase in the powder feed rate.
- The clad area above the substrate decreased with an increase in the laser scanning velocity. The decrease could be attributed to less powder being delivered per unit length with an increase in the laser scanning velocity.
- Laser power had no significant effect on the clad area above the substrate. It is worth noting a statement made by *de Oliveira* which suggests that if the velocity of the powder particles is selected such that the difference between the power required to melt the substrate and the particles respectively is small it is very difficult to determine the dependence of the clad area above the substrate on an increase in laser power (34). Considering the small difference between the melting points of the substrate material and the powder addition it is possible that this was also the case for this investigation. The lateral spread of the clad layer beyond the melt substrate interface did seem to suggest that it could be possible that the powder particles were melted upon impact on the substrate, for the whole range of power levels tested. It is however difficult to predict the path of the powder particles, through the laser beam, responsible for the lateral spread and whether the temperature rise experienced by these particles were representative of the temperature rise experienced by the majority of

the powder particles in the powder stream. Another important consideration not taken into account due to the constraints of the investigation was the critical importance of the powder particle velocity on the temperature rise and final temperature of the powder particles upon impact on the substrate.

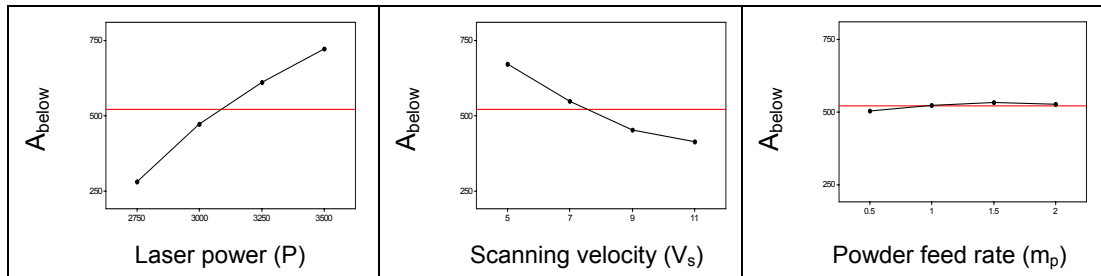
It was observed that the clad height and area above the substrate responded similarly to a change in the main process variable test levels. The correlation coefficient between the clad height and area above the substrate, measuring the strength of the linear relationship between two clad properties, was calculated to be 0.981.

#### **4.2.6 Clad area below the substrate surface ( $A_{\text{below}}$ )**

The clad area below the substrate was mainly dependent on the laser power and to a lesser extent on the laser scanning velocity. The powder feed rate had no significant effect on the clad area below the substrate surface.



Mean clad  $A_{\text{below}}$  the substrate at the four test level settings for:  $P$ ;  $v_s$ , and  $m_p$



Variable	Level 1	$\Delta_{2-1}$	Level 2	$\Delta_{3-2}$	Level 3	$\Delta_{4-3}$	Level 4
P	279.8	191.5	471.3	139.2	610.5	112.2	722.7
$v_s$	671.5	-123.6	547.9	-96.5	451.4	-37.9	413.5
$m_g$	502.8	19.5	522.3	10.6	532.9	-6.6	526.3

Table 4.6: The mean clad area below the substrate for each process variable test level.

Considering Table 4.6, several observations were made regarding the general effect that a change in the main process variable test levels had on the clad area below the substrate surface:

- The clad area below the substrate surface increased with an increase in laser power.
- The clad area below the substrate surface decreased with an increase in the laser scanning velocity.
- A change in powder feed rate had little or no effect on the clad area below the substrate surface.

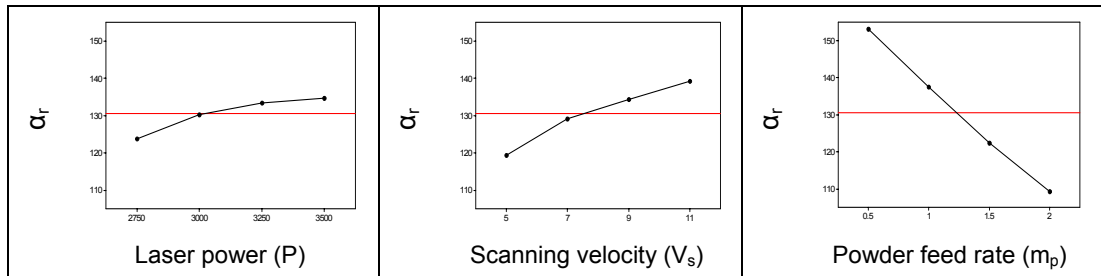
Similar trends were observed, considering the effect that the main process variables had on both the depth of alloy penetration and the clad area below the substrate. The correlation coefficient, between the depth of alloy penetration and clad area below the substrate, was calculated to be 0.987.

#### **4.2.7 The clad root angle ( $\alpha_r$ )**

The clad root angle was both measured, and calculated using equation 2.24. A correlation between the measured and calculated results revealed a strong correlation, with a correlation coefficient of 0.935. It was however the opinion of the researcher that the calculated results were not as prone to error, owing to the subjective nature of the measurements. Therefore the discussion on the clad root angle is based on the calculated results rather than the measured values.

The most significant process variable affecting the clad root angle was the powder feed rate, followed by the laser scanning velocity. A change in the laser power test level had little or no effect on the clad root angle.

Mean calculated root angle at the four test level settings for: P;  $v_s$ , and  $m_p$



Variable	Level 1	$\Delta_{2-1}$	Level 2	$\Delta_{3-2}$	Level 3	$\Delta_{4-3}$	Level 4
P	123.79	6.44	130.23	3.17	133.40	1.31	134.71
$v_s$	119.37	9.77	129.14	5.27	134.41	4.8	139.21
$m_g$	153.13	-15.69	137.44	-15.14	122.30	-13.03	109.27

Table 4.7: The mean root angle for each process variable test level.

Considering Table 4.7, several observations were made regarding the general effect that a change in the main process variable test levels had on the calculated root angle of the clad layer:

- The clad root angle became more acute with an increase in the powder feed rate. The increase in the acuteness of the clad angle is strongly related to the effect that an increase in the powder feed rate had on the height of the clad layer and it's comparatively much smaller influence on the clad width.
- An increase in the laser scanning velocity resulted in a decrease in the acuteness of the clad root angle. The decrease in the acuteness of the clad root angle is similarly related to a decrease in the height of the clad layer with an increase in the laser scanning velocity. However, unlike the effect of a change in the powder feed rate, an increase in

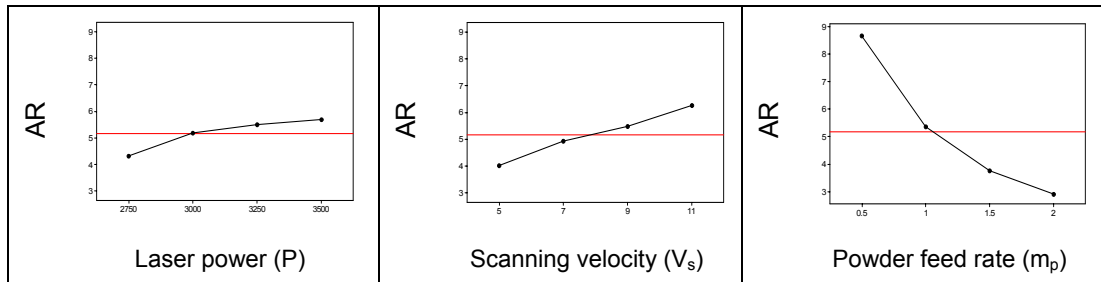
the scanning velocity also had a significant influence on the clad width, which would explain why the powder feed rate had a more significant influence on the clad root angle. It must be noted that a much larger change in the width of the clad layer was required to have a similar effect as a change in the clad height on the clad root angle. This is clearly evident when considering that the total change in the clad height and width for the complete range of laser scanning velocities tested was 0.3955 and 0.4231 respectively.

- A change in the laser power did cause a reduction in the acuteness of the clad root angle but was less significant compared to the effect that a change in the powder feed rate or laser scanning velocity had on the clad root angle.

#### **4.2.8 The clad aspect ratio (AR)**

All three process variables influenced the aspect ratio of the clad layer. The powder feed rate seemed to have the most significant effect, followed by the laser scanning velocity and laser power.

Mean calculated aspect ratio at the four test level settings for: P;  $v_s$ , and  $m_p$



Variable	Level 1	$\Delta_{2-1}$	Level 2	$\Delta_{3-2}$	Level 3	$\Delta_{4-3}$	Level 4
P	4.311	0.866	5.177	0.333	5.510	0.183	5.693
$v_s$	4.008	0.914	4.922	0.566	5.488	0.786	6.274
$m_g$	8.684	-3.332	5.352	-1.590	3.762	-0.869	2.893

Table 4.8: The mean clad aspect ratio for each process variable test level.

Considering Table 4.8, several observations were made regarding the general effect that a change in the main process variable test levels had on the aspect ratio of the clad layer:

- The clad aspect ratio decreased with an increase in the powder feed rate. A change in the powder feed rate resulted in a more significant change in the clad height than the clad width. The total change in the clad height and width over the complete range of powder feed rates tested was 0.67 and 0.28 mm respectively.
- The clad aspect ratio increased with an increase in the laser scanning velocity. As previously stated, an increase in the laser scanning velocity resulted in a decrease in both the clad height and clad width. Therefore it can also be concluded that the effect of the laser scanning

velocity on the clad height was comparatively more significant than its effect on the clad width.

- The clad aspect ratio increased with an increase in laser power. It has been shown previously that an increase in laser power caused an increase in the clad width while it had little or no effect on the clad height.

The relationship between the clad root angle and the aspect ratio could be described by a cubic function as shown in the fitted line plot in Figure 4.1.

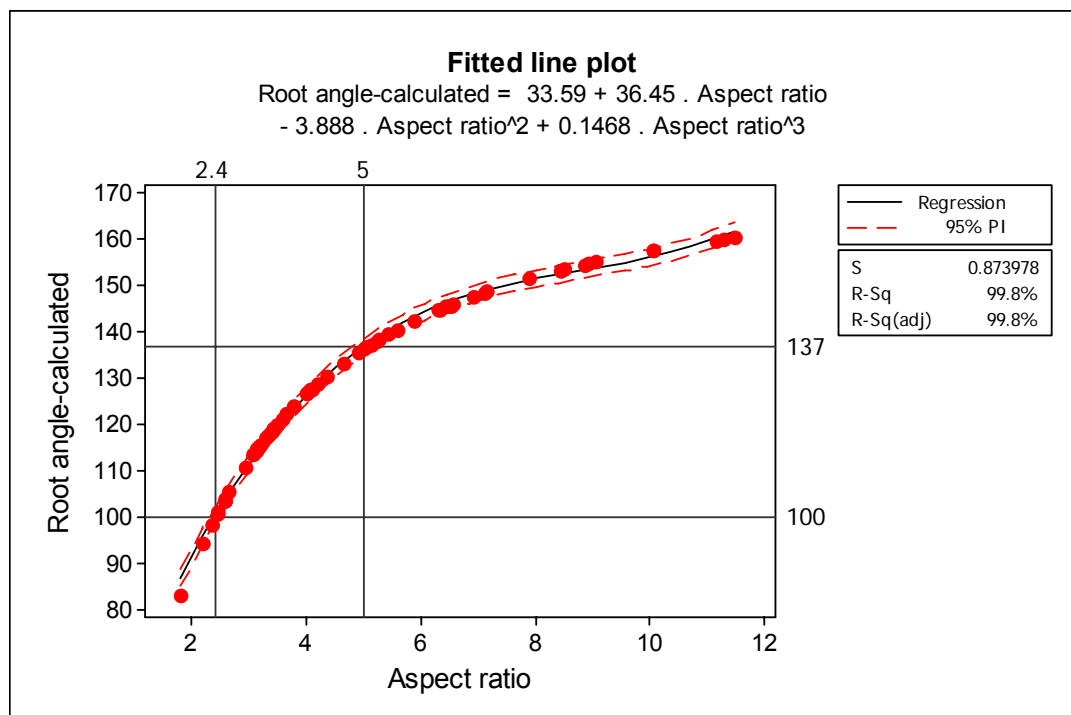


Figure 4.1: Relationship between the calculated clad root angle and aspect ratio.

**Gedda** suggested that in order to avoid inter-run porosity the aspect ratio should be larger than five (21). Therefore, considering Figure 4.1 the root angle should not be smaller than 137 degrees. **de Oliveira** remarked on a study by **Felda et al** which suggested that, in order to avoid inter-run porosity the root angle should not be smaller than  $100^\circ$  (34), which would suggest that an aspect ratio as small as 2.4 would still be acceptable.

### **4.3 The effect of the main process variables on clad characteristics**

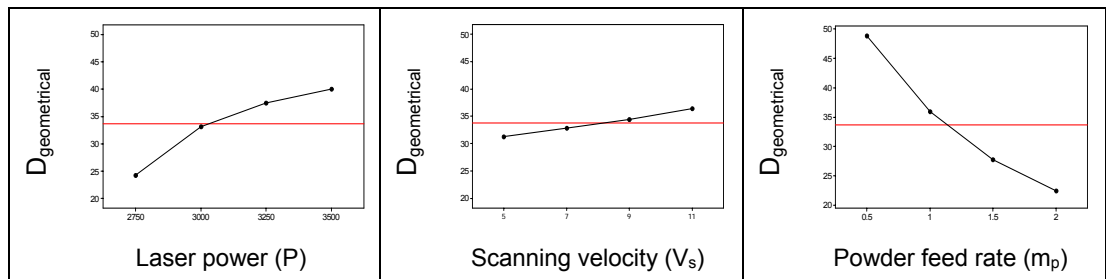
#### **4.3.1 Dilution**

The dilution of the Al-20wt%Si material addition by the Al-1370 F substrate material was determined using both the geometrical and area ratio calculation methods described in section 2.12 of the literature review. Both these methods assume a homogenous distribution of the alloying elements across the clad cross-section. **Uzan et al**, in the literature review remarked that high solidification rates leads to increased chemical homogeneity.

A correlation between the geometrical and area ratio dilution test methods revealed a strong correlation between the two methods with a correlation coefficient of 0.995. The high correlation coefficient suggested that either test method could be used to establish the effect that a change in the main process variable test levels had on the dilution of the clad layer.

All three main process variables influenced the dilution of the clad layer. The powder feed rate had the most significant effect, followed by the laser power and laser scanning velocity. The effect of a change in the laser scanning velocity on dilution, was not as significant, when compared to the powder feed rate and laser power.

Mean geometrical dilution at the four test level settings for: P;  $v_s$ , and  $m_p$



Variable	Level 1	$\Delta_{2-1}$	Level 2	$\Delta_{3-2}$	Level 3	$\Delta_{4-3}$	Level 4
P	24.23	8.96	33.19	4.33	37.52	2.49	40.01
$v_s$	31.30	1.51	32.81	1.62	34.43	1.97	36.40
$m_g$	48.82	-12.91	35.91	-8.17	27.74	-5.26	22.48

Table 4.9: The mean dilution (Geometrical test method) for each process variable test level.

Mean area ratio dilution at the four test level settings for: P; $v_s$ , and $m_p$							
	Variable level						
Variable	Level 1	$\Delta_{2-1}$	Level 2	$\Delta_{3-2}$	Level 3	$\Delta_{4-3}$	Level 4
P	23.04	8.52	31.56	5.03	36.59	2.15	38.74
$v_s$	28.37	3.36	31.73	2.29	34.02	1.79	35.81
$m_g$	49.80	-14.87	34.93	-9.32	25.61	-6.02	19.59

Table 4.10: The mean dilution (Area ratio test method) for each process variable test level.



Considering Table 4.9 and Table 4.10, several observations were made regarding the general effect that a change in the main process variable test levels had on the dilution of the clad layer:

- Dilution decreased with an increase in the powder feed rate. It was previously shown that a change in the powder feed rate did not significantly decrease the depth of alloy penetration in the substrate material. Therefore, it could be assumed that the increase in the clad area above the substrate surface, rather than a reduction in the depth of alloy penetration caused the reduction in the dilution of the clad layer.
- Dilution increased with an increase in the laser power. This seemed only logical as both the depth of penetration, and the clad area below the substrate surface increased with an increase in laser power while it had no significant effect on the clad height or the clad area above the substrate.
- Dilution unexpectedly increased, although only slightly, with an increase in the laser scanning velocity. This unexpected observation was attributed to the ratio of change between the clad area above and below the substrate. The contour plot in Figure 4.2 clearly indicated the dependence of dilution on the ratio of change between the clad area above and below the substrate with a change in the main process variables. The clad area below the substrate is generally an indication of the amount of the substrate material that has mixed with the material addition. Therefore, high dilution of the clad layer is

associated with a steep increase in the clad area below the substrate with a negligible increase in the clad area above the substrate. When compared it could be seen that clad area above the substrate decreased more significantly than the clad area below the substrate which resulted in the unexpected increase in dilution with an increase in the laser scanning. This statement is further supported by the decrease in the clad area below the substrate with an increase in the laser scanning velocity, as shown in Figure 4.3. This observation merely highlighted the possibility that the effect of a process variable on a specific clad characteristic/property could be influenced by the range of test levels selected for the main process variables, relative to each other.

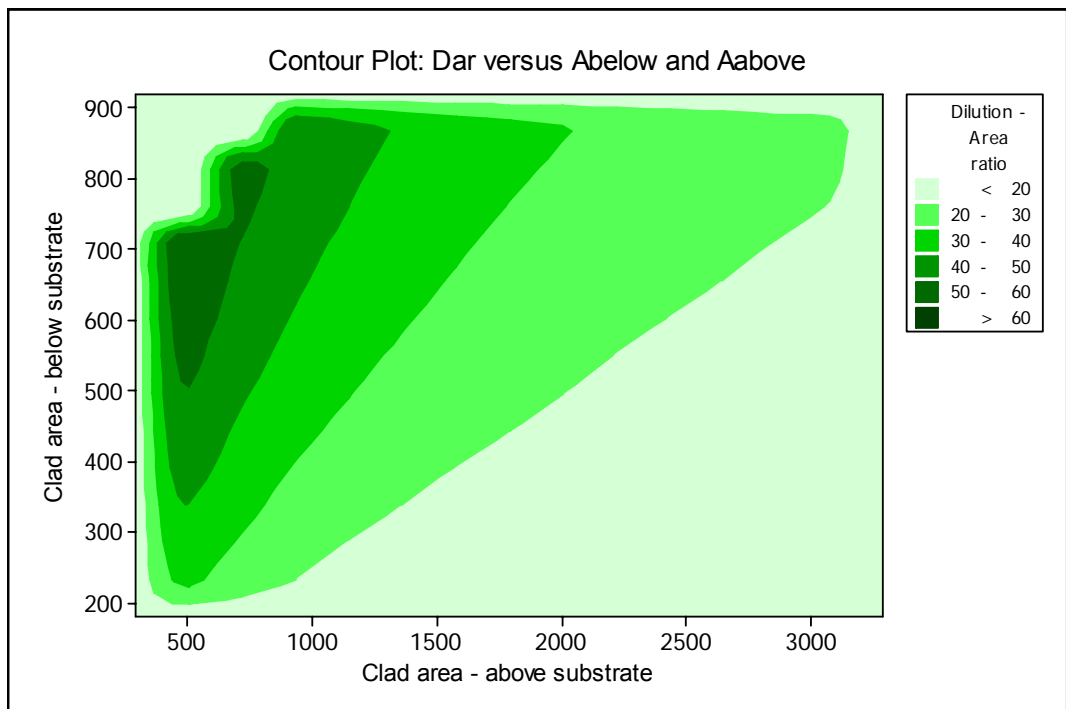


Figure 4.2: Contour plot indicating the dependence of dilution on the relationship between the change in the clad area above and below the substrate at the various test levels.

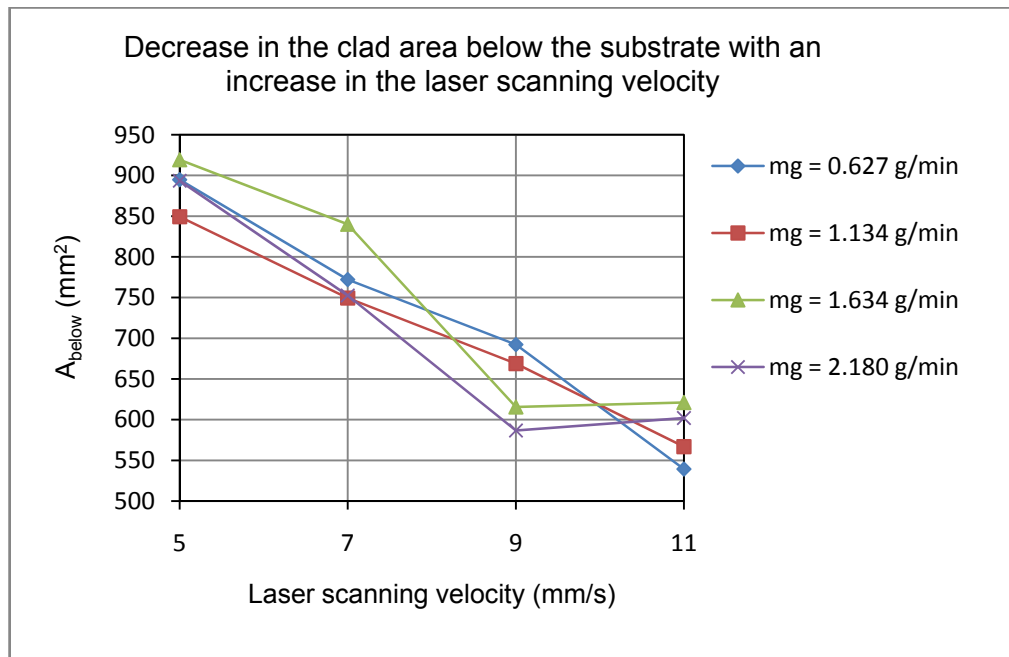
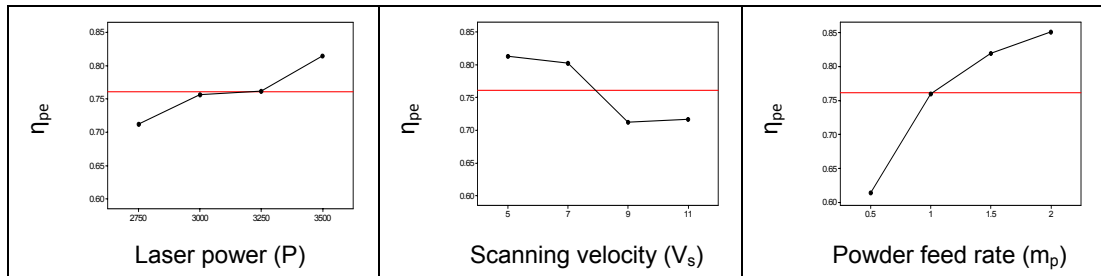


Figure 4.3: Decrease in the clad area below the substrate with an increase in the laser scanning velocity.

#### 4.3.2 Powder efficiency ( $\eta_{pe}$ )

All three process variables had an influence on the powder efficiency of the cladding process. The powder feed rate had the most significant influence on powder efficiency, followed by the laser scanning velocity and laser power.

Mean powder efficiency at the four test level settings for: P;  $v_s$ , and  $m_p$ 

Variable	Level 1	$\Delta_{2-1}$	Level 2	$\Delta_{3-2}$	Level 3	$\Delta_{4-3}$	Level 4
P	71.19	4.44	75.63	0.50	76.13	5.37	81.50
$v_s$	81.25	-1.00	80.25	-9.00	71.25	0.44	71.69
$m_g$	61.38	14.62	76.00	5.94	81.94	3.19	85.13

Table 4.11: The mean powder efficiency for each process variable test level.

Considering Table 4.11, several observations were made regarding the general effect that a change in the main process variable test levels had on the powder efficiency of the cladding process:

- Powder efficiency decreased with an increase in the laser scanning velocity. However, only the change in the powder efficiency between levels two and three were statistically significant. The most important contributing factor seemed to be the decrease in the width of melt pool on the substrate surface with an increase in the laser scanning velocity. The decrease in the width of the melt pool decreased the possibility of powder catchment due to an increase in less favourable impact conditions (Liquid particle-solid substrate) or un-favourable impact conditions (Solid particle-solid substrate).

- Powder efficiency increased with an increase in laser power. The increase could be attributed to both an increase in the width of the melt pool on the substrate surface, and an assumed increase in the powder particle temperature upon arrival at the melt pool/substrate surface. The increased width of the melt pool and powder particle temperature increased the possibility of powder catchment due to favourable impact conditions (Solid particle- liquid substrate; liquid particle-liquid substrate or liquid particle-solid substrate).
- Powder efficiency increased with an increase in the powder feed rate. It was an unexpected observation since it was expected that the powder efficiency would decrease with an increase in the powder feed rate for the cladding setup used. In his investigation of a simple model for powder catchment in coaxial laser cladding, *Lin* showed that powder efficiency increases with an increase in the powder feed rate. However in *Lin's* investigation the ratio of the powder stream diameter ( $d_p$ ) to the diameter of the laser beam ( $d_l$ ) on the substrate surface was well below 1 (25). Based on the visual analysis of the cold stream powder flow from the three-way nozzle the ratio ( $d_p/d_l$ ) was estimated to be  $\pm 1.2$  and  $\pm 1.6$  at the lowest and highest powder feed rate test level respectively. Possible explanations for this unexpected observation might be found by considering the concentration distribution of the consolidated powder stream and the effect of laser beam interaction on cold stream flow conditions from the coaxial nozzle.

#### 4.4 Vickers microhardness

The microhardness profile of the clad cross-section was evaluated according to test standard, ASTM E 384-99<sup>e1</sup>, for the determining the micro indentation hardness of materials.

Hardness measurements were made using a Future Tech FM-700 automatic hardness tester. A 25 g test load was selected with a 15 s dwell time. A low test load was selected in order to optimize the amount of indentations in the hardness profile, considering the large variation in clad heights observed, ranging from a maximum of 1.35 mm to a minimum of 0.183 mm. In addition a low test load reduced the plastic deformation at the edges of the indentation, thus improving measurement accuracy especially when considering that the average hardness of the substrate was only  $\pm 24.63$  HV.

The hardness profile of the clad layer consisted of several indentations along the centre of the clad cross-section, forming a vertical line, stretching from the top edge of the clad layer into the substrate. The position of the indentations on the clad cross-section is shown in Figure 4.4. The first indentation was made at 0.1 mm from the top edge of the clad layer and the distance between indentations was 0.15 mm.

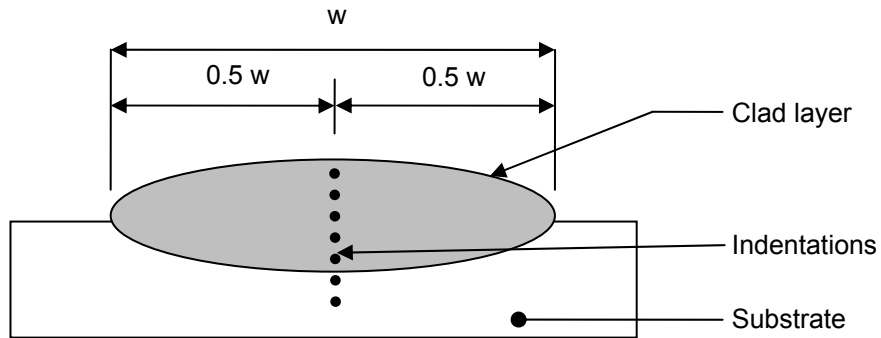


Figure 4.4: Position of indentations on the clad cross-section making up the hardness profile of the clad layer.

The typical observed hardness profile of an Al-20wt%Si clad layer on an Al-1370-F substrate is shown in Figure 4.5.

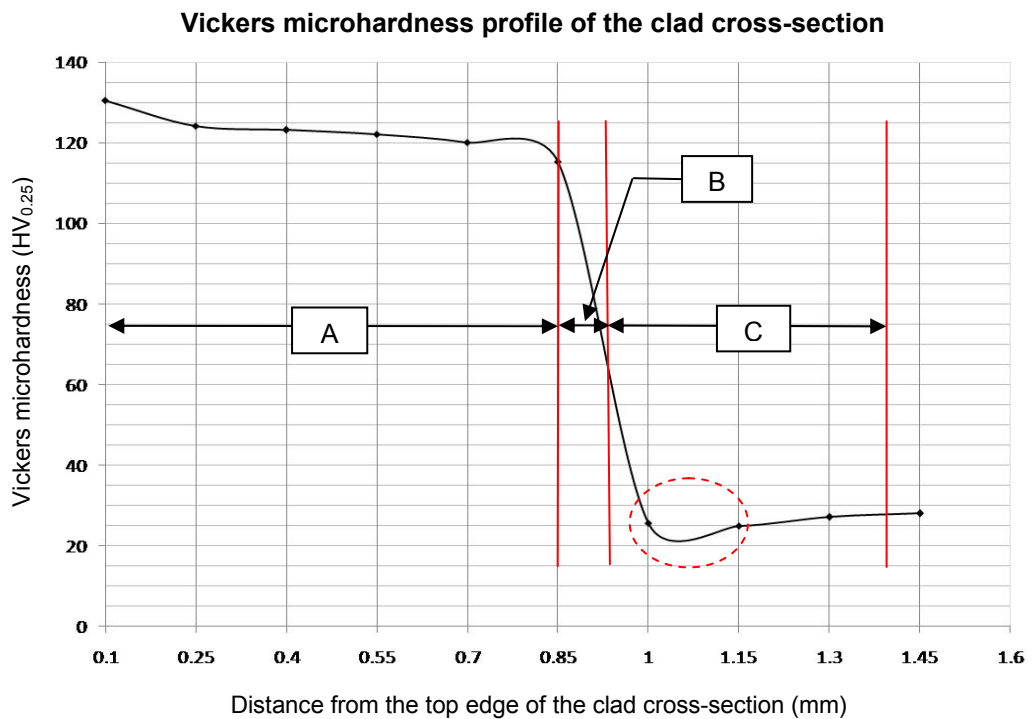


Figure 4.5: Typical Vickers microhardness profile observed.

Considering Figure 4.5, three distinct hardness regions were distinguishable. Region, A, represents the hardness profile of the clad layer. Region, B, represents the sharp decrease in the microhardness at the interface between the clad layer and the substrate. Region, C, represents the hardness profile of the substrate. A small dip in the substrate hardness just below the clad substrate interface was generally observed, but the depth over which it was observed and the change in hardness was not significant enough to identify the heat affected zone just below the clad layer.

The variation in clad height made it difficult to compare the hardness profiles of the various test samples. Therefore, specific hardness values were selected for comparison, namely:

- The maximum microhardness within the clad layer ( $HV_{\max}$ );
- The minimum microhardness within the clad layer ( $HV_{\min}$ );

#### **4.4.1 Statistical analysis of Vickers microhardness tests**

Considering the three main process variables, the powder feed rate had the most significant effect on the hardness of the clad layer followed by laser power. The laser scanning velocity had little or no effect on the hardness of the clad layer.



#### 4.4.1.1 Maximum microhardness ( $HV_{max}$ )

Table 4.12 indicates the variation in the maximum microhardness with a change in the main process variable test levels and the strength of each variables influence.

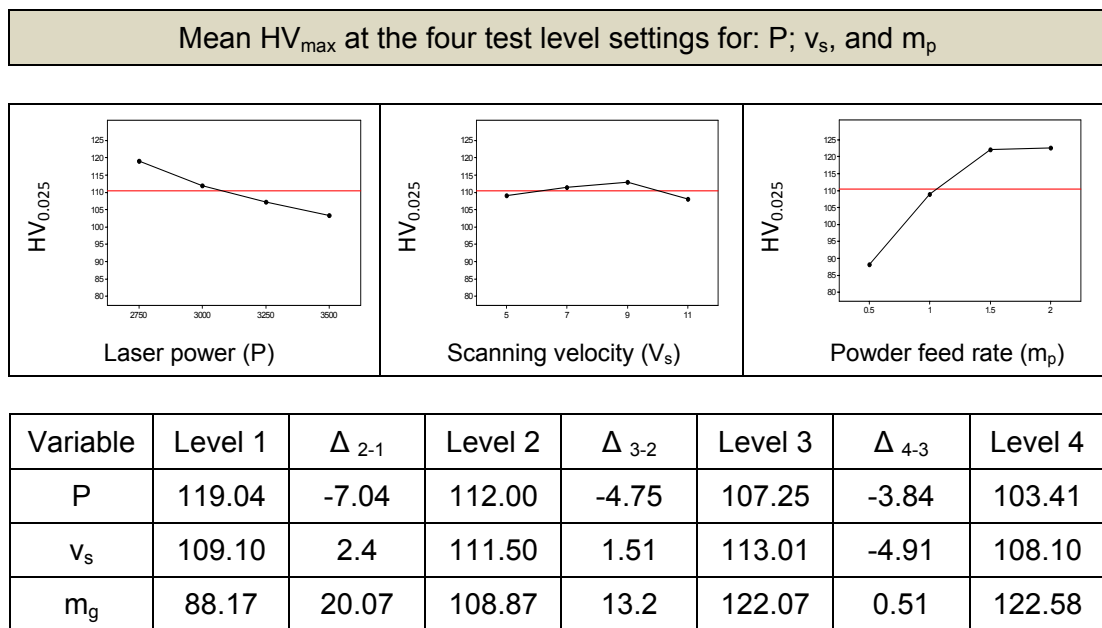


Table 4.12: The change in the mean, maximum microhardness of the clad cross-section.

- The maximum hardness of the clad layer increased with an increase in the powder feed rate, from 88.17  $HV_{0.025}$  to 122.584  $HV_{0.025}$  at a powder feed rate of 0.627 and 2.18 g/min respectively. A total change of 34.414  $HV_{0.025}$  in the mean, maximum hardness. Only the change between test levels one and two, and, two and three was significant considering Table 4.12.
- An increase in laser power resulted in a decrease in the maximum hardness of the clad layer, from 119.037  $HV_{0.025}$  to 103.406  $HV_{0.025}$  at

a laser power of 2750 and 3500 W respectively. A total change of 15.577 HV<sub>0.025</sub> in the mean maximum hardness.

- A change in the laser scanning velocity had no significant effect on the maximum hardness of the clad layer. A total change of only 5.09 HV<sub>0.025</sub> in the mean maximum hardness was observed.

An analysis of the position of the maximum hardness indentation showed that 76.57% of the indentations were located within a distance of 0.25 mm from the top edge of the clad cross-section (See Figure 4.6). However, if it was assumed that a 5% difference between the 1<sup>st</sup> indentation and the maximum hardness indentation is negligible, 78.13% of the maximum hardness indentations were located within 0.1 mm from the top edge of the clad cross-section.

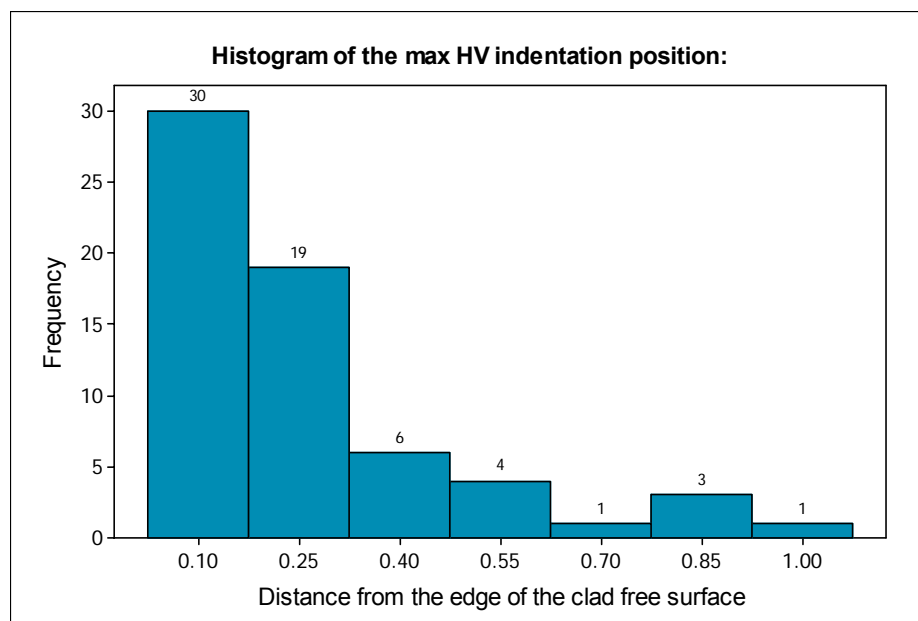


Figure 4.6: Histogram representing the number of maximum microhardness indentations relative to their position from the edge of the free surface of the clad cross-section.

An interesting observation could be made when considering the relationship between dilution and the maximum clad hardness with a change in the powder feed rate and laser power.

In section 4.3.1 it was shown that dilution decreased with an increase in the powder feed rate. The maximum clad hardness on the other hand increased with an increase in the powder feed rate. A similar, inverse relationship between dilution and the maximum clad hardness was also observed with a change in laser power. An increase in laser power resulted in an increase in dilution and decrease in the maximum clad hardness respectively.

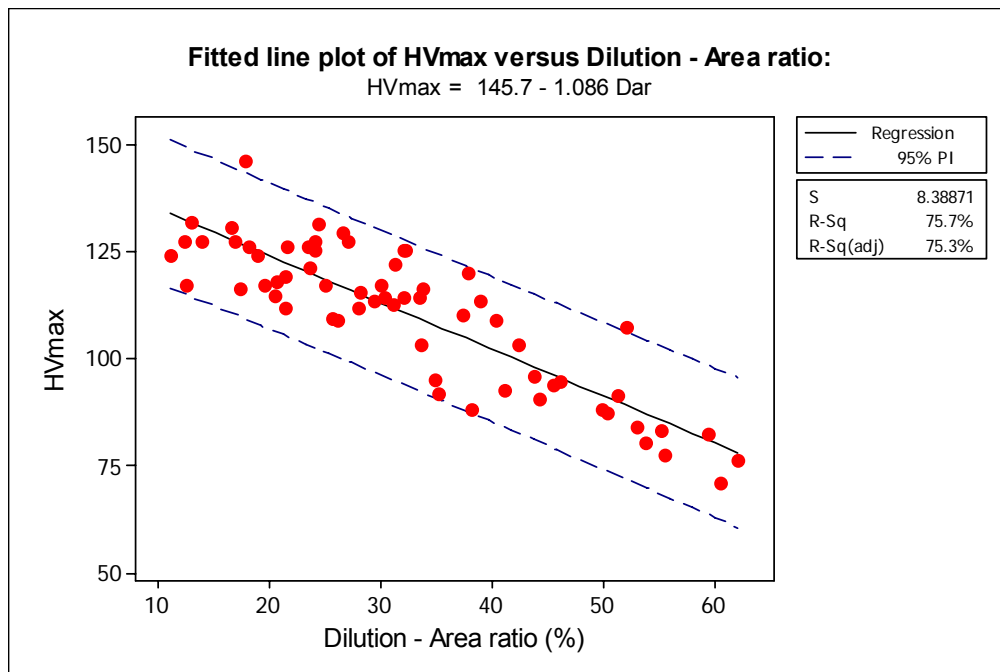


Figure 4.7: Fitted line plot indicating the relationship between HVmax and dilution.

A fitted line plot with 0.95 predicted confidence interval levels indicated a possible linear relationship between the maximum clad hardness and dilution (Refer to Figure 4.7). The maximum clad hardness decreased linearly with an increase in dilution. The decrease could be attributed to a reduction in the silicon concentration of the clad layer. Although dilution of the clad layer seemed to be the most important factor that influenced the maximum hardness of the clad layer it cannot account for the total change in the maximum clad hardness. Dilution has to be considered in conjunction with other solidification factors such as the solidification rate and temperature gradient which could affect the type of microstructure that develop upon solidification.

#### **4.4.1.2 Minimum microhardness ( $HV_{min}$ )**

The minimum clad microhardness in all cases was observed just above the clad-substrate interface. A similar linear trend between dilution and the minimum clad hardness was observed as previously mentioned existed between dilution and the maximum hardness of the clad layer. Interestingly, the linear trend between dilution and the maximum clad hardness seemed to be stronger than the linear relationship between dilution and the minimum clad hardness. The correlation coefficient between the maximum clad hardness and dilution and the minimum clad hardness and dilution was -0.87 and -0.783 respectively.

Table 4.13 indicates the variation in the minimum microhardness with a change in the main process variable test levels and the strength of each variables influence.

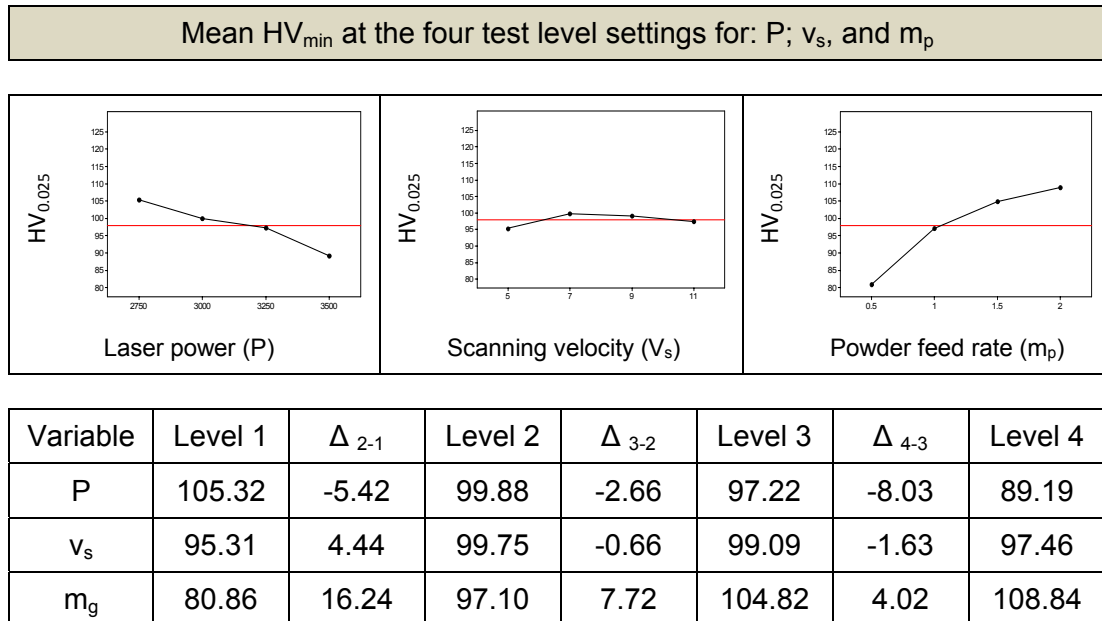


Table 4.13: The change in the mean, minimum hardness of the clad cross-section.

- The minimum hardness of the clad layer increased with an increase in the powder feed rate from 80.862  $HV_{0.025}$  to 108.841  $HV_{0.025}$  at a powder feed rate of 0.627 and 2.18 g/min respectively. A total change of 27.979  $HV_{0.025}$  in the mean minimum hardness of the clad layer.
- An increase in laser power resulted in a decrease in the minimum hardness of the clad layer, from 105.318  $HV_{0.025}$  to 89.194  $HV_{0.025}$  at a laser power of 2750 and 3500 W respectively. A total change of 16.186  $HV_{0.025}$  in the mean, minimum hardness of the clad layer.

- The laser scanning velocity had no significant effect on the minimum hardness of the clad layer. A change of only 4.445 HV<sub>0.025</sub> in the mean minimum hardness was observed.

## **4.5 Microstructural development**

### **4.5.1 Introduction**

The primary objective of this investigation was not to characterize the microstructural development of the clad layer. Microstructural development however is a fundamental part of any materials processing investigation. It was therefore considered necessary to at least provide a basic overview of the clad microstructure that developed and the variation thereof; treating the clad layer as a simple binary Al-Si alloy.

It could be expected that impurities in the substrate material such as iron, even trace amounts, would affect the development of the resulting microstructure and possibly cause the formation of inter-metallic compounds. However the formation of inter-metallic compounds, and any other material combination not described by a simple Al-Si binary phase diagram was considered to fall outside the scope of this investigation.

### **4.5.2 General microstructures observed**

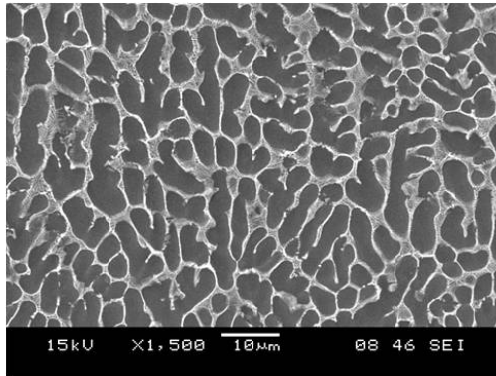
As previously mentioned the powder material addition used was an Al-20wt%Si alloy and the substrate material commercially pure Al 1370-F. The liquidus temperature for an Al-Si alloy with 20wt% silicon concentration is

$\pm 948$  K ( $675^{\circ}\text{C}$ ), which is only  $\pm 16$  K higher than the melting point of commercially pure aluminium. Based on a simple, equilibrium Al-Si phase diagram the solidification microstructure should generally consist of Al-Si eutectic with primary silicon crystals distributed within the eutectic structure.

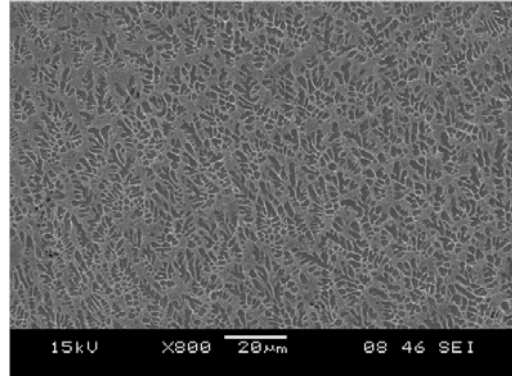
However, in addition to the hyper-eutectic microstructure predicted by the equilibrium Al-Si phase diagram, two other types of microstructure and variations thereof developed upon solidification. The observed microstructures (Refer to Figure 4.8) were divided into five different categories, with microstructures consisting of a:

- $\alpha$ -Al cellular structure with inter-dendritic Al-Si eutectic (a);
- $\alpha$ -Al quasi-dendritical structure with inter-dendritic Al-Si eutectic (b);
- $\alpha$ -Al columnar dendritic structure with inter-dendritic Al-Si eutectic (c);
- Al-Si eutectic structure and (d),
- Al-Si eutectic structure with primary silicon crystals surrounded by  $\alpha$  – Al halos (e).

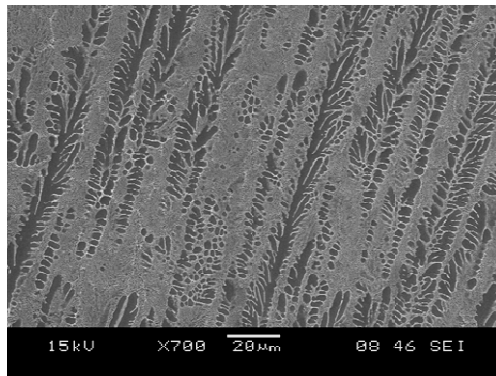
The deviation from the predicted equilibrium microstructure was attributed to both the effect of dilution on the composition of the melt pool and to the high solidification rates associated with laser cladding. An increase in dilution has a direct influence on the silicon concentration in the melt pool and therefore also on its solidification microstructure. The effects of high solidification rates were discussed during the literature review (Refer to section 2.15.1).



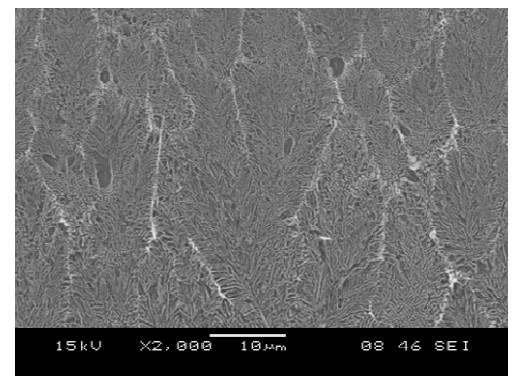
(a)  $\alpha$ -Al cellular structure with inter-dendritic Al-Si eutectic



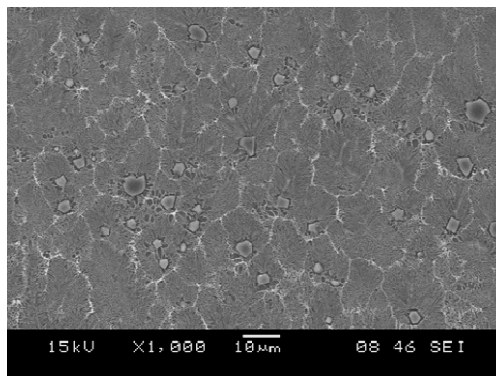
(b)  $\alpha$ -Al quasi-dendritic structure with inter-dendritic Al-Si eutectic



(c)  $\alpha$ -Al columnar dendritic structure with inter-dendritic Al-Si eutectic



(d) Al-Si eutectic



(e) Al-Si eutectic structure with Si-crystals surrounded by  $\alpha$ -Al halos

Figure 4.8: SEM micrographs of the five main types of microstructures observed.



In addition to the microstructures mentioned above, a very thin featureless zone was observed at the clad-substrate interface, shown in Figure 4.9 below.

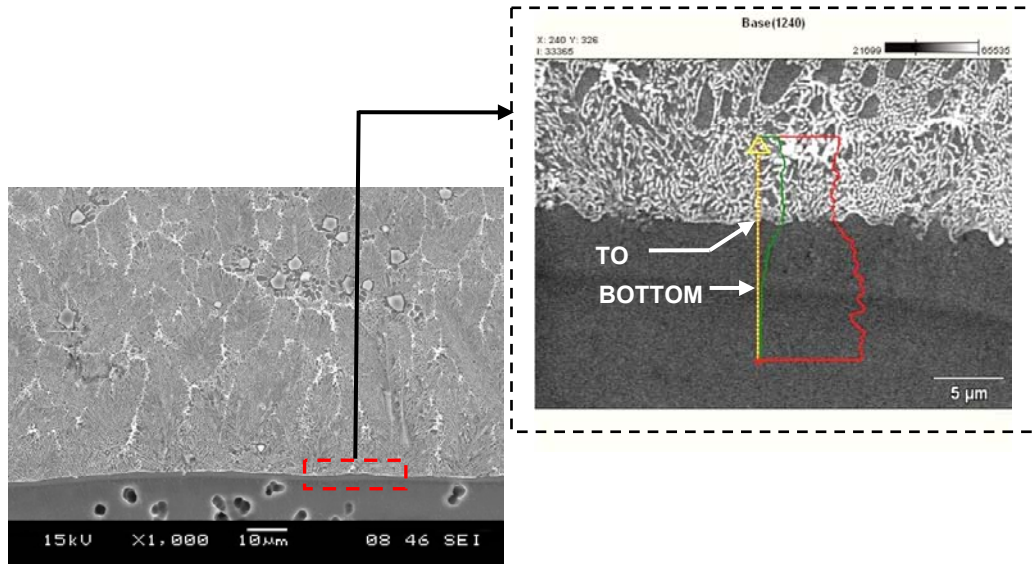


Figure 4.9: Featureless, transitional zone at the bottom of clad layer at the clad-substrate interface

A line scan, to determine the compositional variation across the transitional zone was carried out using a scanning electron microscope (Refer to Figure 4.9). The line scan indicated that the silicon concentration of the transitional zone decreased gradually, from a concentration similar to that of the clad layer at the top, to a negligible concentration similar to that of the substrate at the bottom. A typical variation in the aluminium and silicon concentration level across the transitional zone is indicated by the red and green lines respectively. The thickness of the transitional zone varied from sample to sample. The overall range of thicknesses observed ranged from 1-10  $\mu\text{m}$ .

### 4.5.3 General phases observed

The main phases observed were: primary aluminium (Figure 4.10.1 and 4); Al-Si eutectic (Figure 4.10.2), and primary silicon (Figure 4.10.3)

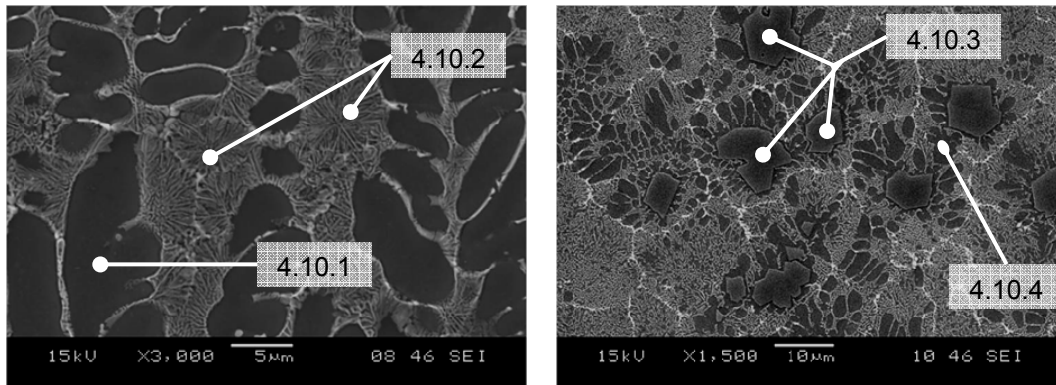


Figure 4.10: SEM micrographs of the main phases observed.

### 4.5.4 Microstructural scale and variation

The microstructure of the single pass clad layer is a function of its composition; the temperature gradient across the solid/liquid interface ( $G$ ), and the velocity of the solidification front ( $V_{sf}$ ) (35) (36) (37). It was established during the literature review that the solidification front varies from a minimum at the bottom of the clad layer to a maximum, approaching the speed of the laser scanning velocity, near the top of the clad layer (26). The temperature gradient on the other hand decreases from a maximum near the bottom of the melt pool to a minimum near the surface of the clad layer (2).

**Kumar et al** states that the cooling rate,  $\dot{T} = V_{sf} \cdot G$ , determines the scale of the resulting microstructure, while the ratio,  $G/V_{sf}$ , determines the form of the microstructure (37). Therefore, a variation in both the solidification rate and temperature gradient, across the clad height, results in a variation in the solidification conditions throughout the clad melt pool and therefore also its microstructure upon solidification.

Inspection of the various clad cross-sections revealed both a refinement in the microstructure, from the bottom to the top of the clad cross-section, as well as a variation in the type of microstructure itself. The refinement in the clad microstructure was directly attributed to an increase in the solidification rate from the bottom to the top of the clad layer. (For the purpose of this investigation the type of microstructure refers to the different microstructures noted in Figure 4.8).

Note that only the clad microstructure along the centreline of the clad cross-section was considered. This was done to simplify the microstructural analysis of the clad cross-section, which can be difficult due to a variation in the local solidification conditions throughout the melt pool as mentioned above.

Although all samples showed an increase in their microstructural scale, moving from the top to the bottom of the clad cross-section less than 10% of the samples exhibited a uniform type of microstructure over the entire clad cross-section. The microstructure of the majority of the samples varied between the top and bottom of the clad cross-section.

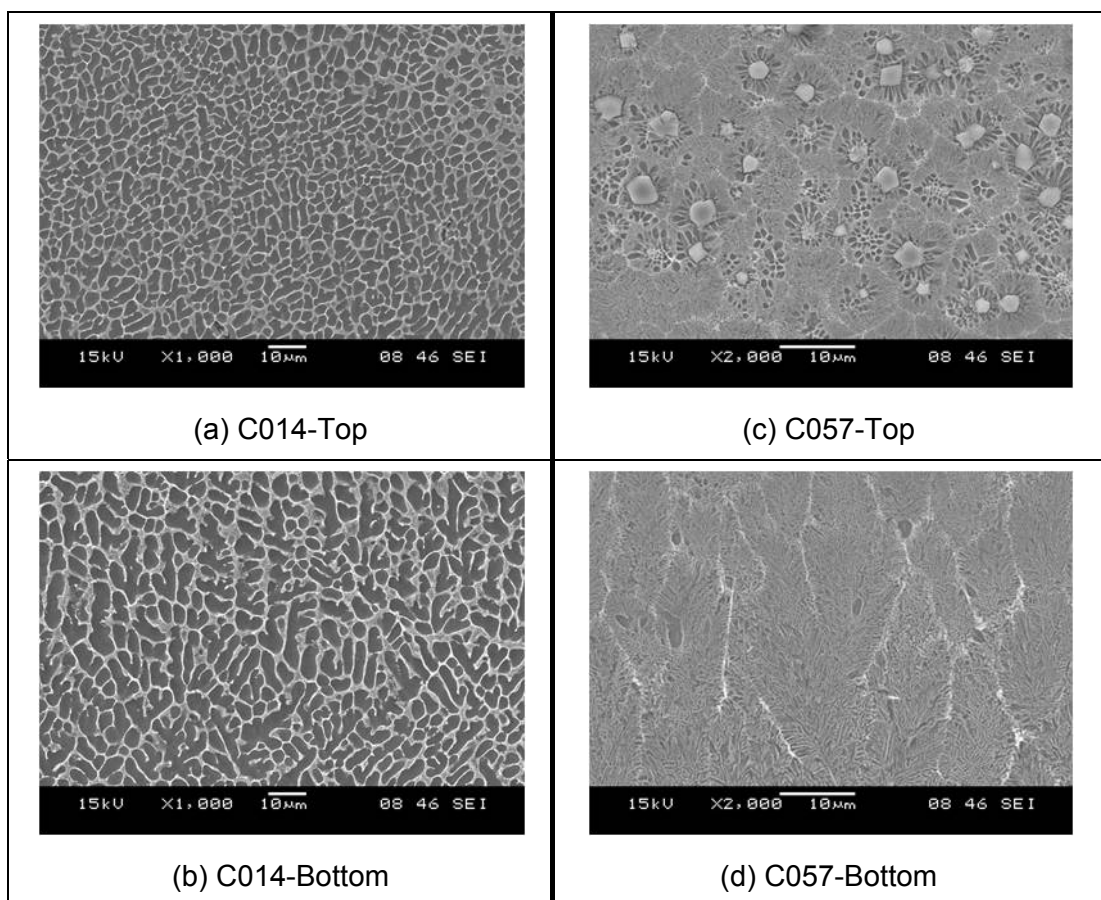


Table 4.14: SEM micrographs of sample C014 ( $P= 3500$  W,  $v_s = 11$  mm/s and  $m_g = 0.627$  g/min [ $D_{ar} = 60.57\%$ ]) and sample C057 ( $P= 2750$  W,  $v_s = 11$  mm/s and  $m_g = 2.18$  g/min [ $D_{ar} = 13.87\%$ ]) indicating a typical reduction in the microstructural scale, and variation in the type of microstructure, respectively.

An analysis of the variation in the clad microstructure at the bottom of the clad layer revealed that 37.5% of the samples had a columnar dendritic structure with inter-dendritic eutectic; 32.8% of the samples had a Al-Si

eutectic structure; 17.2% of the samples had quasi-dendritical structure (not quite columnar dendritic but also not cellular) with inter-dendritic Al-Si eutectic; 6.3% had a cellular structure with inter-dendritic Al-Si eutectic, and a further 6.3% had an Al-Si eutectic structure with Si-crystals surrounded by  $\alpha$ -Al halos.

The variation in the clad microstructure at the top of the clad layer revealed that 48.4% of the samples had a quasi-dendritical structure with inter-dendritic Al-Si eutectic; 31.25% had an Al-Si eutectic structure with Si-crystals surrounded by  $\alpha$ -Al halos; 12.5% had a cellular structure with inter-dendritic Al-Si eutectic; 6.3% had a columnar dendritic structure with inter-dendritic eutectic; and only 1.5% had an Al-Si eutectic structure.

Considering the variation in the type of microstructure, moving from the bottom to the top of the clad cross-section, the microstructure of the majority of the clad layers either changed from having a columnar dendritic structure to a quasi-dendritical structure; or from a eutectic structure to a microstructure consisting of Al-Si eutectic with Si-crystals and  $\alpha$ -Al halos.

Of the three main process variables, the powder feed rate had the most significant effect on the clad microstructure, followed by laser power and laser scanning velocity. Laser power had a more significant effect on the clad microstructure at the top of the clad layer than at the bottom of the clad layer. The strong influence of the powder feed rate seemed to indicate that dilution

was the predominant factor influencing the type of microstructure that developed upon solidification. The weak influence of the laser scanning velocity could possibly be attributed to the small range of scanning velocities tested.

Consider the purely illustrative microstructural sequence shown in Figure 4.11.

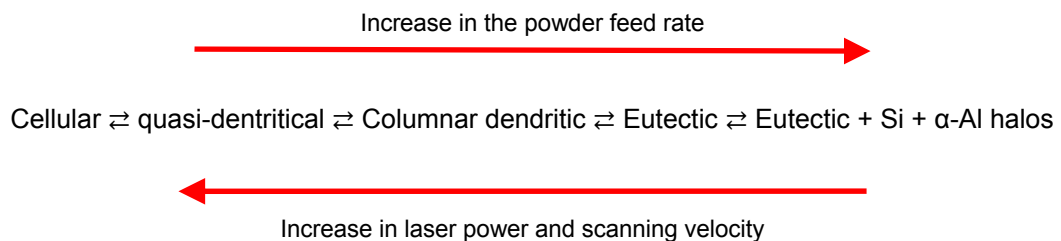


Figure 4.11: Influence of an increase in the main process variables test level on the clad microstructure.

It was observed that an increase in the powder feed rate caused a change in the type of microstructure, in the direction, left to right in the microstructural sequence. An increase in both laser power and the laser scanning velocity had the inverse affect, causing a change in the direction, right to left, in the sequence.

#### 4.5.5 Variation in the size and volume fraction of the silicon particles

In general, both the number and volume fraction of the silicon particles increased from the bottom to the top of the clad layer, considering the clad cross-section. This observation corresponds with the observations made by

**Pei et al** in their investigation of functionally graded coatings using Al-40wt%Si mentioned in the literature review. The silicon particles however did not display a similar morphological transition from a polygonal shape at the bottom to an equiaxially five branched shape near the top as observed by **Pei et al**. A change however was observed in the number of sides of the polygonal silicon particles, increasing from the bottom to the top.

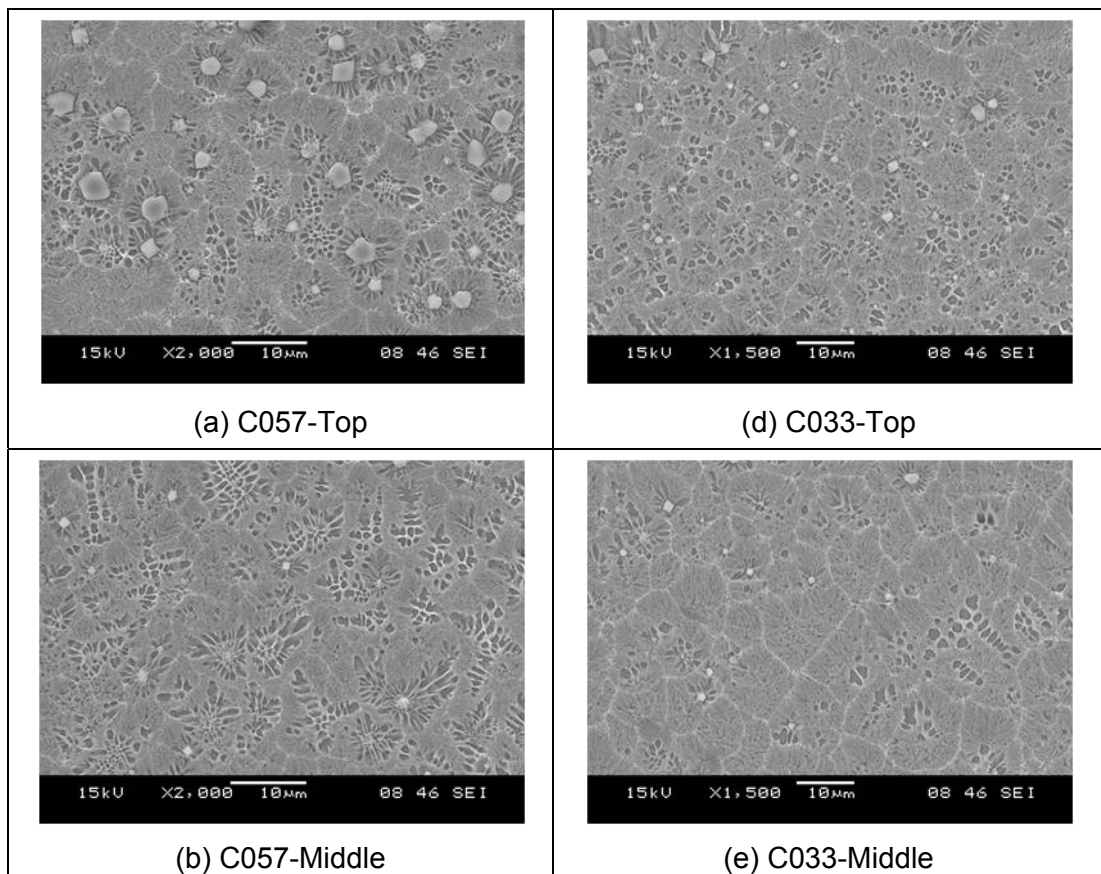


Table continued

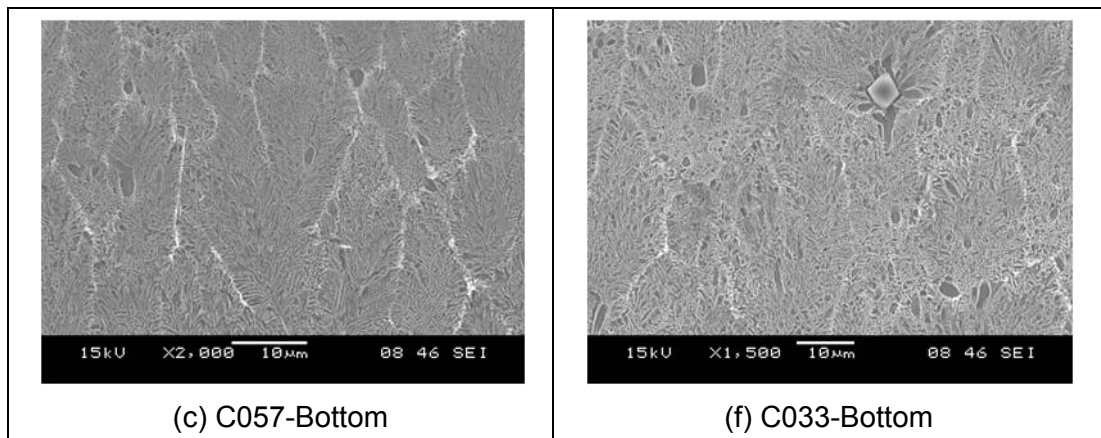


Table 4.15: SEM micrographs indicating a general increase in both the volume fraction and size of the Si particles, from the bottom of the clad layer to the top of the clad layer. Sample C057 was processed at  $P = 2750$  W,  $v_s = 11$  mm/s and  $m_g = 2.18$  g/min ( $D_{ar} = 13.87\%$ ). Sample C033 was processed at  $P = 3250$ ,  $v_s = 5$  mm/s and  $m_g = 1.634$  g/min ( $D_{ar} = 25.56\%$ ).

#### 4.5.6 Solidification rate

It is well established that the solidification rate is mainly defined by the laser scanning velocity. However, it could also be shown that the solidification rate, at the bottom of the clad layer, is coupled to the clad height.

In this investigation the laser power was suddenly switched off at the end of the single pass clad layer while powder feeding continued. The sudden removal of the heat input source dramatically increased the solidification rate and temperature gradient experienced by the melt pool. It was assumed that this sudden change would firstly provide some insight into the shape of the solidification front; and secondly the influence that an increase in the solidification rate had on the clad microstructure. The advantage was that a change in microstructure could be directly related to the solidification rate without having to consider the influence of dilution.



To investigate the assumption made above, several longitudinal cross-sections were cut through the centreline, and end of six single pass clad layers for comparison.

Consider the SEM micrograph in Figure 4.12 of a longitudinal cross-section. The red dashed line separates the “steady-state” (Area A) and the rapidly solidified (Area B) melt pool area at the end of the single pass clad layer. It was assumed that this boundary, highlighted by a sudden refinement in the clad microstructure, could be considered to represent the shape of the solidification front

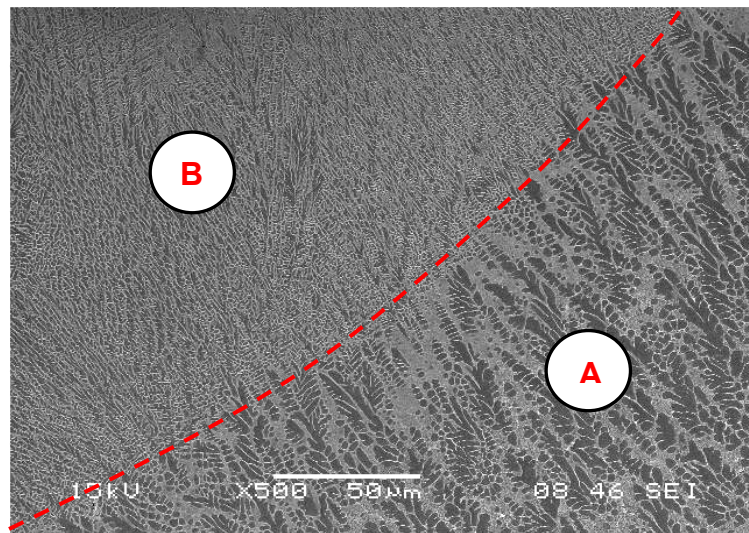


Figure 4.12: Microstructural transition / scale variation on either side of the solidification front. Sample C029 processed at  $P = 2750 \text{ W}$ ,  $v_s = 5 \text{ mm/s}$  and  $m_p = 0.627 \text{ g/min}$  ( $D_{ar} = 37.34\%$ ).

Based on the assumption above the test samples were analysed according to Figure 4.13. The results are tabulated in Table 4.16.

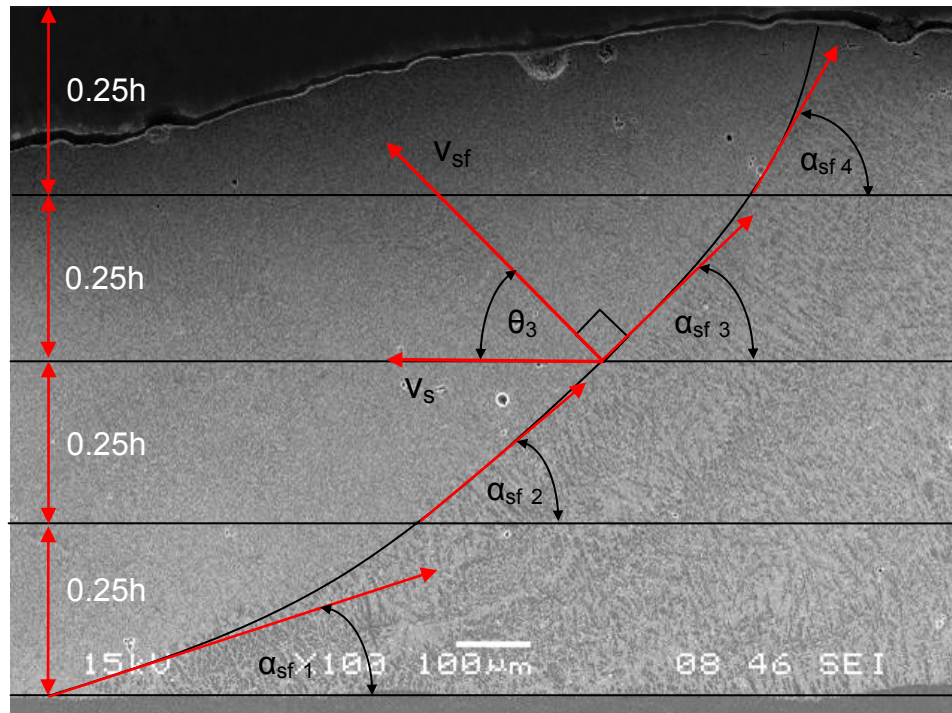


Figure 4.13: Measurements to determine the variation in both the solidification front angle and the velocity of the solidification front across the height of the longitudinal clad cross-section (Where  $\theta_3 = 90^\circ - \alpha_3$ ).

Sample nr	h	$\theta_1$	$v_{sf 1}$	$\theta_2$	$v_{sf 2}$	$\theta_3$	$v_{sf 3}$	$\theta_4$	$v_{sf 4}$
C016	0.691	66.22	4.435	53.9	6.481	34.87	9.025	24.81	9.985
C014	0.220	76.59	2.551	55.83	6.178	49.94	7.079	42.33	8.132
C006	1.25	65.2	2.097	45.68	3.493	30.12	4.325	13.57	4.860
C038	1.35	67.55	1.909	44.34	3.576	22.98	4.603	18.7	4.736
C029	0.363	68.57	1.827	57.67	2.637	51.15	3.136	37.35	3.974
C057	0.710	72.3	3.344	55.71	6.197	49.59	7.131	36.08	8.890

Table 4.16: Tabulated measurement results of the variation in the solidification front angle.

Inspection of the SEM micrographs revealed that the variation in the solidification front angle ( $\alpha_{sf}$ ) at the bottom of the clad layer could be related to the clad height. With an increase in the clad height the angle between the solidification front and the substrate ( $\alpha_{sf}$ ) increased. An increase in  $\alpha_{sf}$  resulted in an increase in the velocity of the solidification front at the bottom of the clad layer compared to a clad layer processed at the same laser power and scanning velocity but at a lower powder feed rate. The difference in the overall variation of  $\alpha_{sf}$  seemed to remain fairly similar with an increase in the clad height.

#### 4.5.7 Solidification direction

According to **Mohanthy et al** the average growth direction during solidification is approximately perpendicular to the solid/liquid interface and aligned with the heat flow direction. In addition it is also affected by the preferential crystallographic growth direction of the material (38). **de Oliveira** states that the grain growth orientation of cubic metals coincides with the heat flow direction and that the morphology of the microstructure resembles the heat flow orientation in the melt.

**de Oliveira** further states that in regions where the heat is directionally extracted the grains will tend to grow in elongated shapes while in regions of iso-directional heat extraction it tends to form equiaxial grains (34).

Similar trends, as described by both *Mohanthy et al* and *de Oliveira*, were observed in the clad layers. Considering the longitudinal cross-section in Figure 4.14 it can be seen how the dendrites orientated themselves in the direction of heat flow, almost perpendicular to the solid/liquid interface.

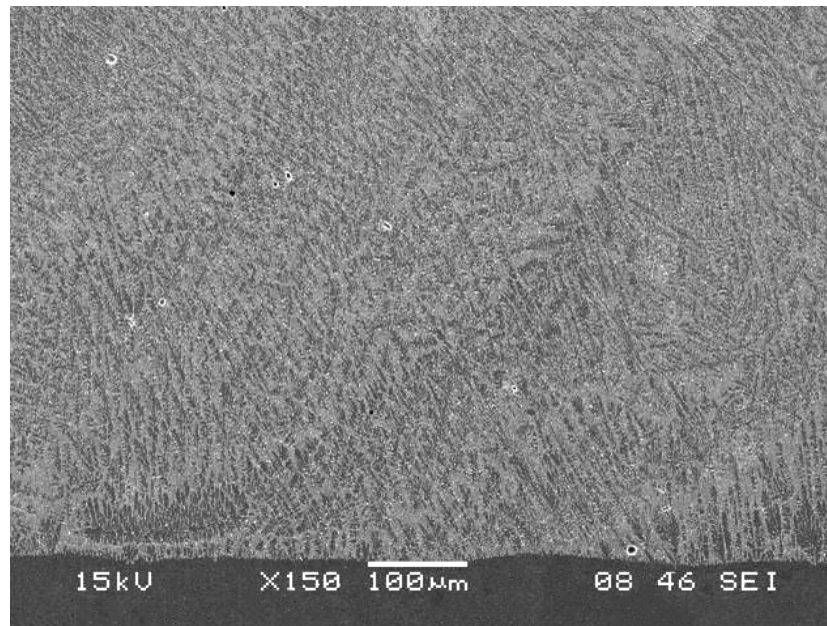


Figure 4.14: Variation in the dendrite growth direction across the clad height.

Considering a normal clad cross-section, examples of both directionally, and iso-directional heat extraction could be seen. Iso-directional heat extraction (Refer to Table 4.17) was most often observed near the centre and top of the clad cross-section, while directional heat extraction (Refer to Table 4.17) was best observed at the bottom of the clad layer.

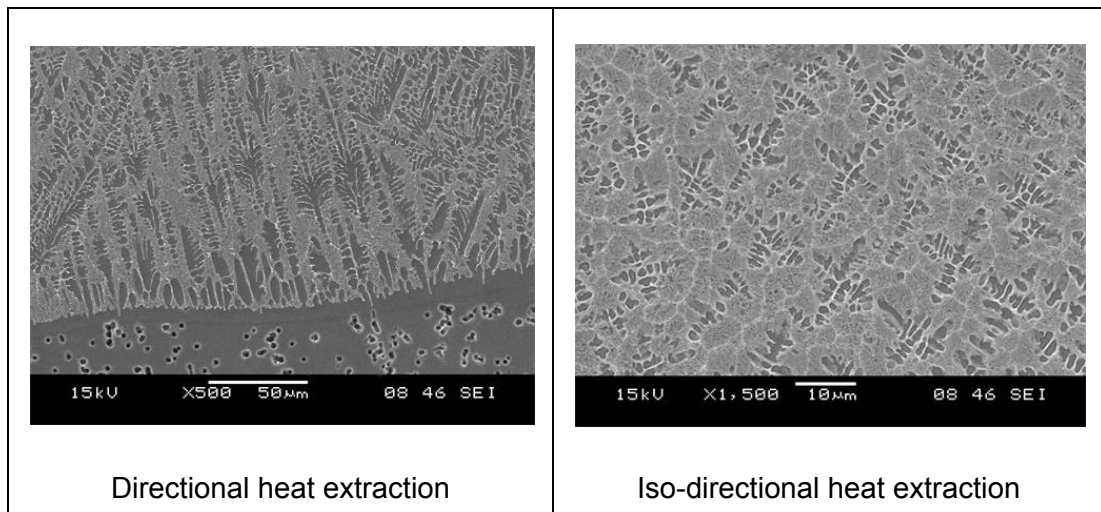


Table 4.17: Examples of the influence of directional and iso-directional heat extraction on the shape of the dendritic structure.

In addition to a variation in the growth direction of the dendritic structure across the clad height, banding was observed when considering the longitudinal cross-sections. The shape/orientation of the banding lines seemed to be similar to that of the solidification front. Banding is often observed in studies where the laser source is operated in pulsed mode. However, for continuous operation a likely explanation for the banding structure seemed to be one that is based on a statement made by **de Oliveira**, which states that the direction of the maximum temperature gradient changes continuously due to the continuous movement of the heat source. Crystals therefore continuously attempt to preserve their favourable growth direction and thus the crystal growth direction essentially becomes a function of the position of the solidification front.

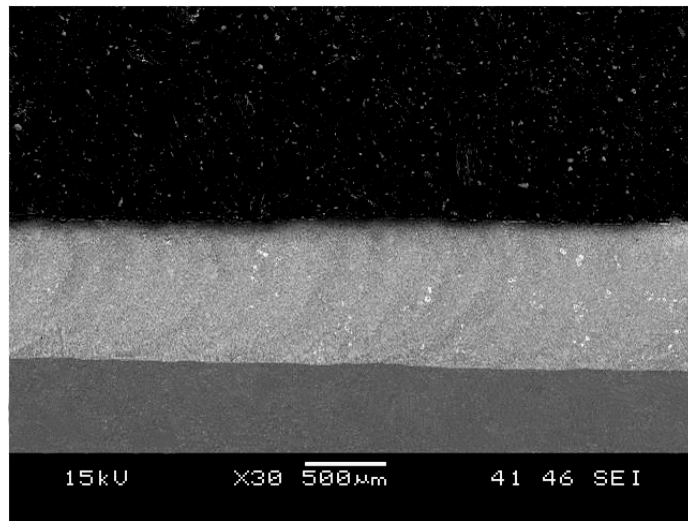


Figure 4.15: Banding observed in a longitudinal section through the centreline of the clad layer.

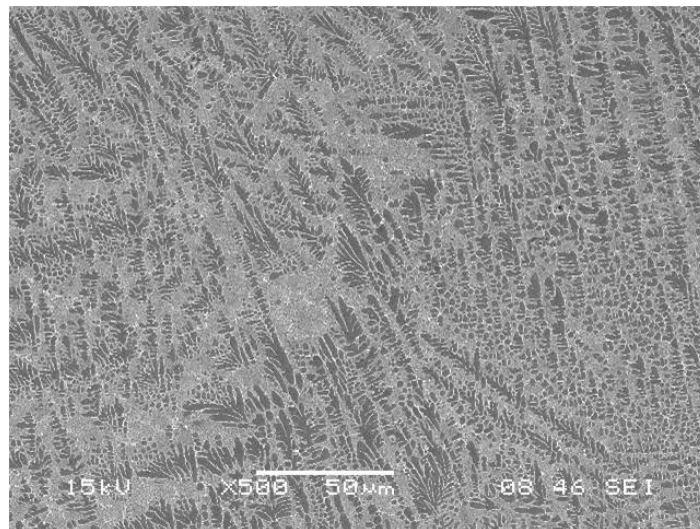


Figure 4.16: Change in the growth orientation of the dendritic structure, re-orientating itself towards the moving laser beam

#### 4.5.8 Relationship between microstructure, hardness and clad characteristics

It follows that if a definite relationship can be found between the Vickers microhardness of the clad layer and its microstructure, then the variation in the clad microstructure can be related to the main process variables by considering the variation in the microhardness with a change in the main process variables.

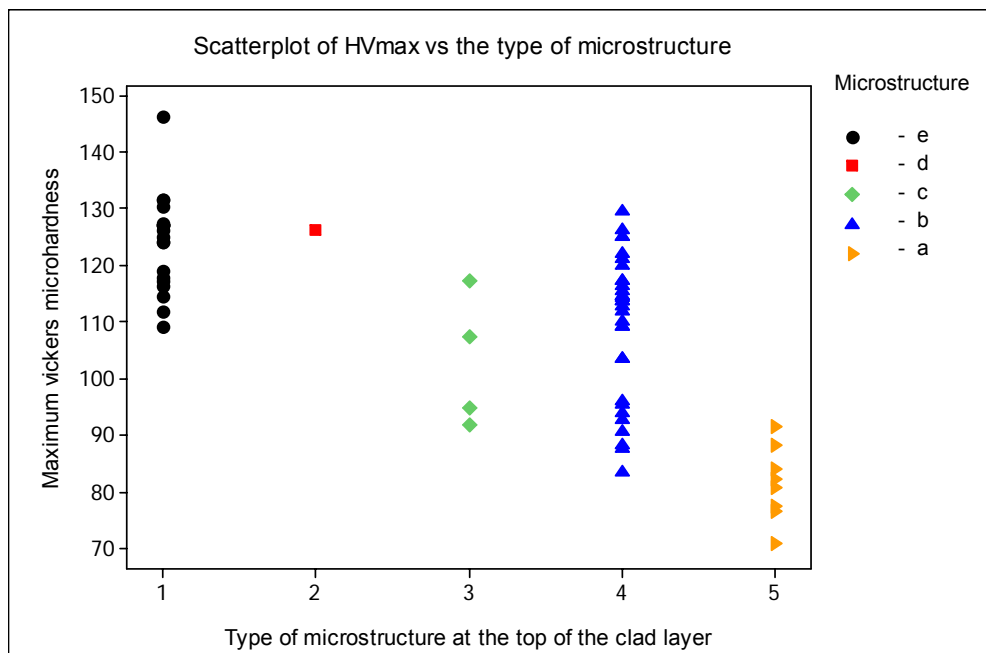


Figure 4.17: Relationship between the maximum microhardness of the clad cross-section and the type of microstructure that developed upon solidification. (The legend key relates the type of microstructure to that shown Figure 4.8)

Considering the scatter-plot of the maximum microhardness versus the type of microstructure it could be seen that a general relationship does exist between the microhardness of the clad layer and the type of microstructure that developed upon solidification. The relationship however is too weak to

derive a definite relationship between the main process variables and the type of microstructure that developed upon solidification.

In terms of a microstructural hardness scale the hardest microstructure was one consisting of Al-Si eutectic with silicon particles and  $\alpha$ -Al halos (Type 1 in Figure 4.17) and became softer as the microstructure changed to a eutectic, columnar dendritic, quasi-dendritic and finally a cellular structure with interdendritic Al-Si eutectic (Type 5 in Figure 4.17) which was the softest microstructure observed.

#### **4.6 Defect population**

*Ion* in his description of the laser cladding process states that the most common defects found in laser cladding are cracks; distortion; porosity, and a lack of fusion (1).

The investigation revealed that there were no cracks in the clad layer and no distortion of the substrate occurred. However the majority of the single pass clad layers contained some form of defect within the clad layer itself or near the surface of the clad layer. Defects near the surface of the clad layer are not critical as it is likely to be removed by subsequent machining processes that reduce the undulations that naturally exist in a laser clad coatings owing to the overlapping of single pass clad layers.



Defects were assumed to be caused mainly by particle entrapment in the liquid melt pool towards the latter stages of solidification or by incomplete melting of the powder particles. Incomplete melting of the powder particles was especially evident near the surface of the clad layer, which is to be expected. Table 4.18 shows the major types of defects observed.

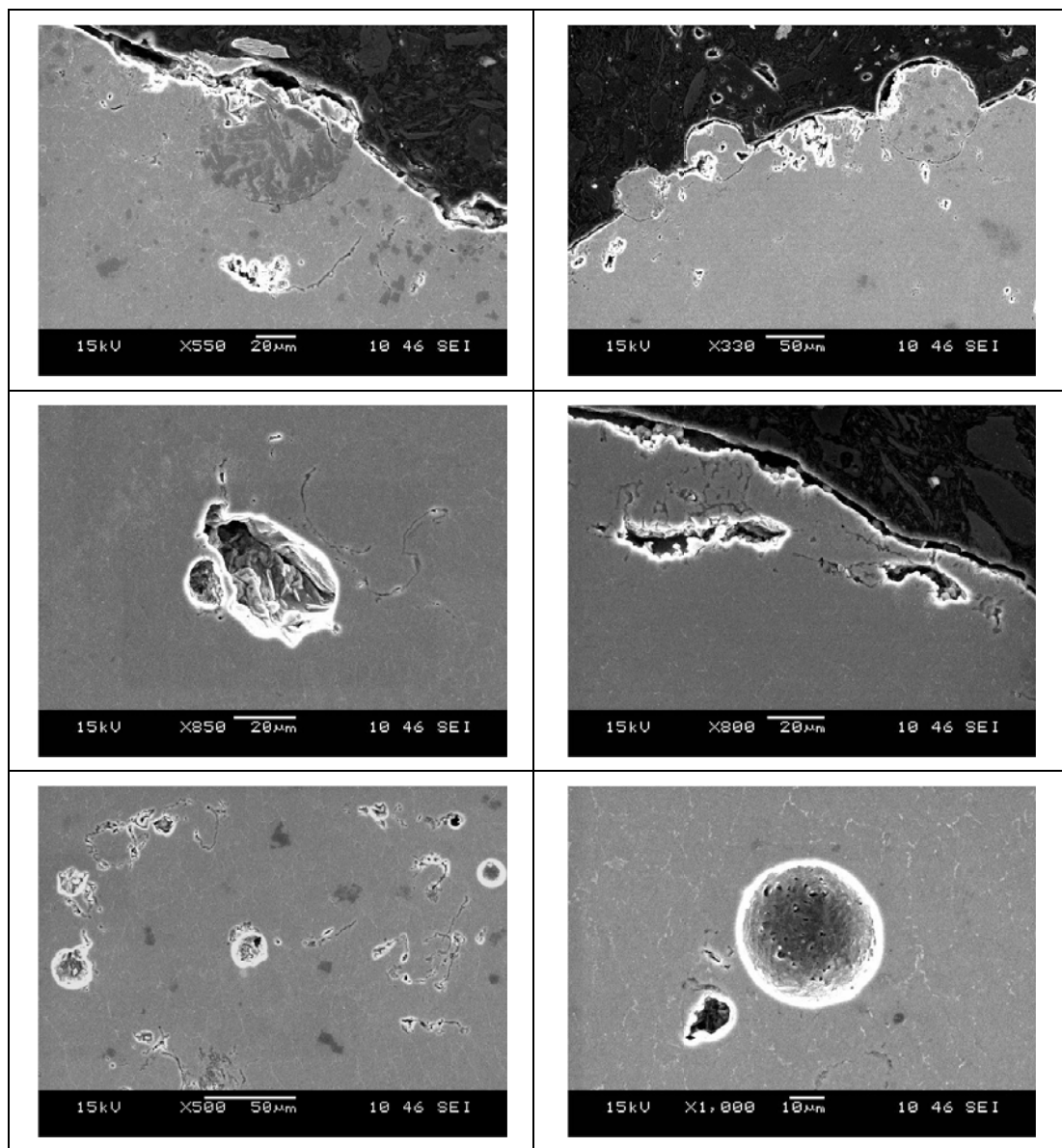


Table 4.18: Some of the typical defects observed in the clad layers from the experimental test matrix.

Inspection of the clad cross-sections revealed that when the clad layer spread too far beyond the melt-substrate interface the ends of the clad layer often did not form a proper metallurgical bond with the substrate. A typical example is shown in Figure 4.18. These un-bonded areas either formed part of the clad layer or became separate “islands” with a very weak, often mechanical bond with the clad layer.

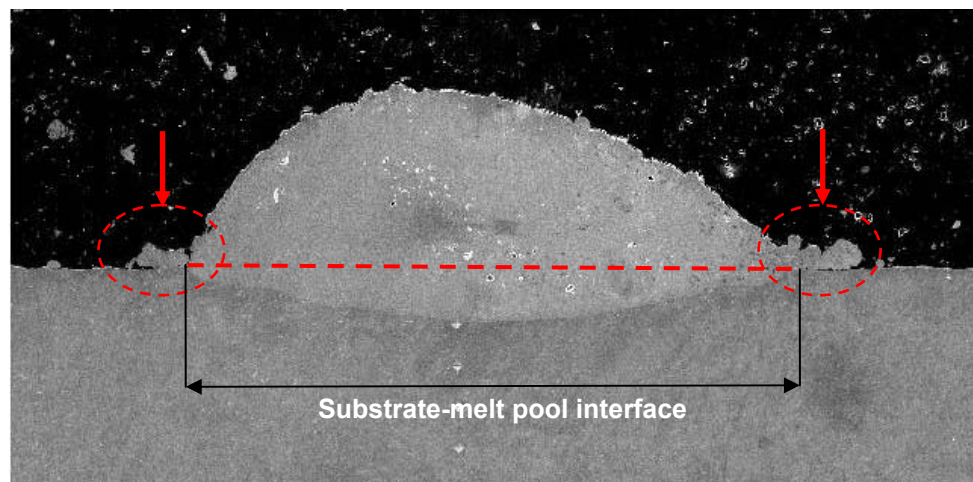


Figure 4.18: Powder particles adhering to the substrate surface at the root of the clad layer, not actually forming part of the clad layer itself (Areas indicated by the red arrows).

In approximately five cases, where the clad height was more than  $\pm 0.8$  mm and the clad layer spread beyond the melt-substrate interface, a “false” build up of the clad layer was observed. A typical false build up defect is shown in Figure 4.19.

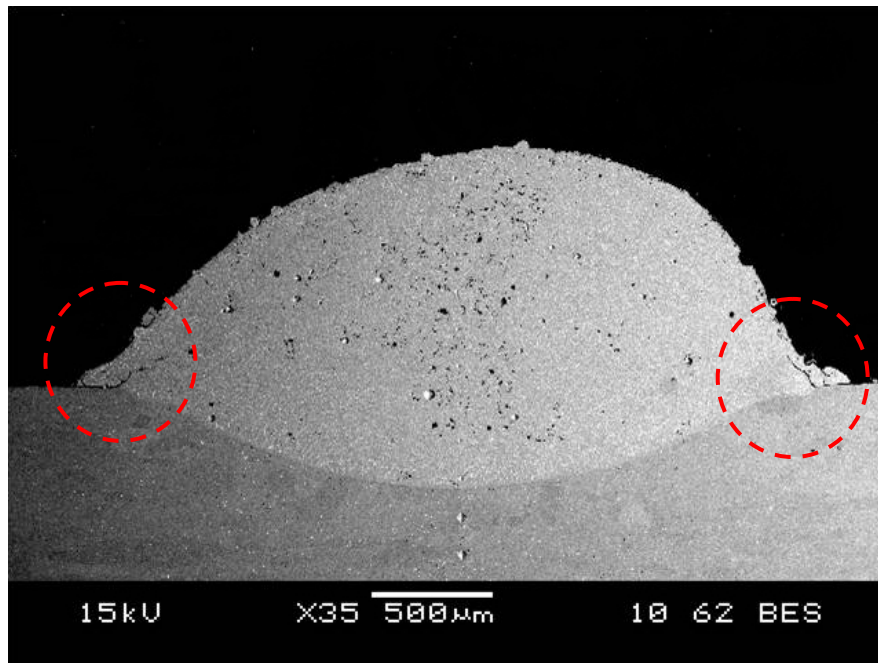


Figure 4.19: False build-up defect at the sides of the clad cross-section.

Considering the general influence of the main process parameters on the size of the defect population it was found that the defect population increased with an increase in the powder feed rate, however only the increase between level one and two were significant. There was a slight increase in the defect population with an increase in the laser scanning velocity. No definite relationship existed between laser power and the size of the defect population, which seemed to vary randomly between test levels.

## 4.7 Combined process variables

Several authors have mentioned or used combined process variables to describe or define a laser cladding processing window. The most widely used combined process parameters are  $CP_1$  and  $CP_2$  (Refer to Table 4.19) or a variation thereof.

In his investigation of the coaxial laser cladding process **de Oliveira** pointed out that from a practical point of view it could be useful if a correlation between an individual clad characteristic and a combined process parameter could be found. According to **de Oliveira** these combined process parameters are usually found by trial and error, considering the statistical relationship between a specific process variable and a clad characteristic such as the clad height for instance (34). Table 4.19 contains a summary of the combined process parameters that **de Oliveira** found, correlated strongly with an individual clad geometry or characteristics.

Q	Combined process variables (CP)		R	a	b
h (mm)	$CP_1$	$\dot{m}_p/v_s$	0.97	0.164	0.023
w (mm)	$CP_2$	$P/\sqrt{v_s}$	0.95	0.947	0.002
$A_{above}$ (mm <sup>2</sup> )	$CP_3$	$(\dot{m}_g \cdot \sqrt{P})/v_s$	0.99	-0.2782	0.0019
$A_{below}$ (mm <sup>2</sup> )	$CP_4$	$P/\sqrt[3]{(\dot{m}_g \cdot v_s)}$	0.95	-0.3269	0.0073
$A_r$ (°)	$CP_5$	$v_s/\dot{m}_g$	0.90	55.0	961
Dilution	$CP_6$	$\sqrt{(P \cdot v_s)/\dot{m}_g}$	0.92	-19.3	8.5
$\eta_{pe}$ (%)	$CP_7$	$P \cdot \sqrt{\dot{m}_g/v_s}$	0.91	14.2	0.0043

Table 4.19: Correlation between combined process parameters and individual clad characteristics. Where: R is the correlation coefficient, a and b are constants in the linear relation:  $Q = a + b \cdot CP$  (34).

A correlation between the combined process parameters in Table 4.19 and the results from the final cladding test matrix was carried out to determine whether a similarly high correlation coefficient existed between the same individual clad geometries or characteristics and the combined process parameters mentioned by *de Oliveira*. If the correlation coefficients differed significantly it was considered whether the highest correlation was found between the same combined process parameter and clad geometry or characteristic. It was assumed that if a similarly strong correlation existed between a certain individual clad geometry or characteristic and a combined process parameter couple, then the cladding process behaved similarly to a change in the main process variables. In addition it means that general trends could be transferred between investigations.

The results of the correlation between the final test matrix and the combined process parameters in Table 4.19, are tabulated in Table 4.20.

	h	w	A <sub>above</sub>	A <sub>below</sub>	$\alpha_r$	D <sub>ar</sub>	$\eta_{pe}$	AR
CP <sub>1</sub>	0.989	0.562	0.993	0.327	-0.936	-0.762	0.659	-0.830
CP <sub>2</sub>	0.397	0.793	0.513	0.862	-0.225	0.041	0.398	-0.182
CP <sub>3</sub>	0.978	0.611	0.996	0.399	-0.911	-0.725	0.672	-0.813
CP <sub>4</sub>	-0.422	0.262	-0.304	0.558	0.566	0.735	-0.251	0.604
CP <sub>5</sub>	-0.858	-0.602	-0.823	-0.283	0.860	0.810	-0.781	0.932
CP <sub>6</sub>	-0.914	-0.498	-0.868	-0.166	0.928	0.891	-0.718	0.963
CP <sub>7</sub>	-0.887	-0.382	-0.825	-0.038	0.924	0.926	-0.644	0.962
CP <sub>8</sub>	-0.851	-0.488	-0.801	-0.158	0.875	0.871	-0.715	0.958

Table 4.20: Results of the correlation between the final test matrix results and known combined process parameters.

A comparison of the results indicated that only the correlation coefficient-combined process parameter couple for the clad height and the area above the substrate correlated strongly with the results reported by *de Oliveira*.

It is the opinion of the researcher that although certain general trends seem to be universal, such as the clad height for instance, the strength of the correlation between these trends depend on several factors that cannot be compensated for by considering only the main process variables. Some of these factors are research platform specific, such as the laser used; its wavelength, and spatial distribution; the focal length of the focusing lens which affects the power density distribution of the laser beam and the interaction area between the laser beam and powder stream; the nozzle design used and its specific reaction to changes in the flow rate of the shielding and carrier gasses for example and other factors that arise due to variations in the material properties or platform setup.

Therefore it is the researcher's opinion that, yes, combined process variables is useful for describing the cladding process and for providing a general idea of the location of the cladding processing window. The processing window however is specific to a particular cladding platform setup; material combination and material properties. It is thus very evident that each prospective laser cladding job-shop should consider that it would be required to do its own material coating qualification for its particular set-up and material combination.

## 5 Final conclusions and future work

### 5.1 Introduction

The primary objective of this investigation was to determine the relationship between a change in the main process variables and the geometry and characteristics of a single pass clad layer. The secondary objective was to determine whether such an evaluation could indicate a suitable processing window for the application of an Al-Si clad layer on an aluminium substrate using an Nd:YAG laser. The primary objective was satisfied, considering the results discussed in chapter four. The secondary objective was only partially met, since it is believed that further work is required to refine the cladding platform setup and therefore also the boundaries of the main process variables. The sections that follow discuss the overall findings of the investigation, its shortcomings and future research that would contribute to the understanding of the laser cladding process.

### 5.2 The process response

In general the process responded similarly that reported by other investigations of the laser cladding process, summarised in table 2.8, section 2.15 of the literature review. However, two notable differences were observed. The first being the effect that an increase in the laser scanning velocity had on the level of dilution and the second being the effect that an increase in the powder feed rate had on the powder efficiency of the process.

The first deviation was dealt with in chapter four and the second is discussed in section 5.2.6.

Table 5.1 summarises the effect of an increase in the test level of the main process variables: laser power ( $P$ ); laser scanning velocity ( $v_s$ ), and powder feed rate ( $m_g$ ) on the geometry and characteristics of the resultant single pass clad layer. An increase is denoted by the symbol ( $\blacktriangle$ ); a decrease by the symbol ( $\blacktriangledown$ ), and in the case where a process variable exhibited no significant effect it is noted as: ( $\leftrightarrow$ ). In addition the symbols are marked from one to three to denote their order of significance. One indicating that it was the most significant variable influencing a specific clad geometry or characteristic and three being the least significant.

Process response	Main process variables		
	$P$	$v_s$	$m_g$
<b>Clad geometry/characteristics</b>			
Clad height ( $h$ )	$\leftrightarrow$	$\blacktriangledown_2$	$\blacktriangle_1$
Clad width ( $w$ )	$\blacktriangle_1$	$\blacktriangledown_2$	$\blacktriangle_3$
Width of the melt pool ( $w_{mp}$ )	$\blacktriangle_1$	$\blacktriangledown_2$	$\leftrightarrow$
Alloy penetration depth ( $z_{pd}$ )	$\blacktriangle_1$	$\blacktriangledown_2$	$\leftrightarrow$
Clad area above substrate ( $A_{above}$ )	$\leftrightarrow$	$\blacktriangledown_2$	$\blacktriangle_1$
Clad area below the substrate ( $A_{below}$ )	$\blacktriangle_1$	$\blacktriangledown_2$	$\leftrightarrow$
Clad root angle ( $\alpha_r$ )	$\leftrightarrow$	$\blacktriangle_2$	$\blacktriangledown_1$
Clad aspect ratio ( $w/h$ )	$\blacktriangle_3$	$\blacktriangle_2$	$\blacktriangledown_1$
Dilution	$\blacktriangle_2$	$\blacktriangle_3^*$	$\blacktriangledown_1$
Powder efficiency ( $\eta_{pe}$ )	$\blacktriangle_3$	$\blacktriangledown_2$	$\blacktriangle_1^*$



Table continued

Process response	Main process variables		
	P	$v_s$	$m_g$
<b>Vickers microhardness</b>			
Maximum Vickers microhardness ( $HV_{max}$ )	▼ <sub>2</sub>	↔	▲ <sub>1</sub>
Minimum Vickers microhardness ( $HV_{min}$ )	▼ <sub>2</sub>	↔	▲ <sub>1</sub>
<b>Defect population</b>			
Amount of visible defects	↔	▲ <sub>2</sub>	▲ <sub>1</sub>

Table 5.1: Summary of the observed effect of an increase in the test level of the main process variables on the clad geometry and characteristics.

### 5.2.1 Clad height (h)

The clad height is a function of the powder feed rate and laser scanning velocity when operating in a cladding regime where the powder particles are already melted or partially melted upon arrival at the melt pool or substrate.

The clad height correlated well with the combined process parameter CP1 ( $\dot{m}_p/v_s$ ) which describes the amount of powder delivered per unit mm of the clad layer. Figure 5.1 indicates the relationship between the clad height and CP1. The blue lines in Figure 5.1 indicate the 95% predicted confidence intervals. The relationship between the clad height (h) and the combined process variable CP1 is given by the expression:  $h = 0.08464 + (3.104) \cdot CP1$

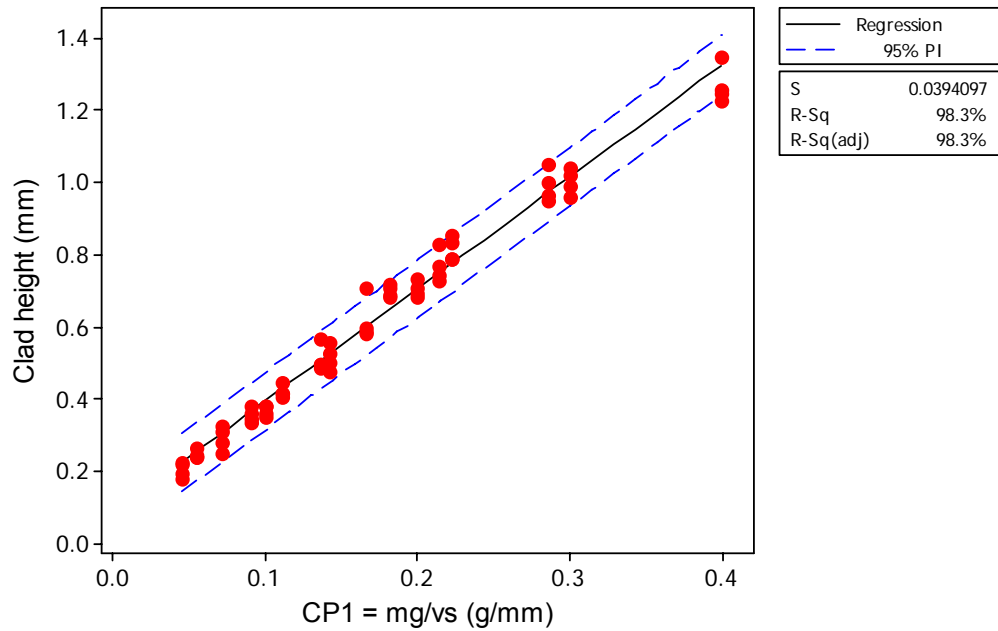


Figure 5.1: Relationship between the clad height and the combined process parameter CP1.

### 5.2.2 Clad width (w)

The clad width is pre-dominantly a function of laser power and the laser scanning velocity although it was also observed that the clad width was influenced by the powder feed rate. The increase in the width of the clad layer with an increase in the powder feed rate was considered not to be a true reflection of its real influence and attributed to the cladding platform setup that was not completely optimized. The explanation for this statement could be found in section 5.2.8. It was therefore to be expected that the correlation between the combined process parameter CP2 ( $P/\sqrt{v_s}$ ) and the clad width (w) would be weaker than that observed by *de Oliveira*. The correlation coefficient was found to be only 0.79 compared to 0.95 quoted by *de Oliveira*.

The correlation coefficient could still be further improved by adjusting the influence of the laser scanning velocity in CP2. Improving the correlation between CP2 and the clad width and deriving an expression for it would however serve little purpose as it would still contain the error introduced by the cladding platform setup that was not completely optimized.

### 5.2.3 The clad aspect ratio (AR)

The clad aspect ratio is often referred to when considering a suitable relationship between the clad width and height that would allow individual clad layers to be successfully overlapped without any defects. This is mainly due to the relationship between the clad root angle and aspect ratio. **Error! Reference source not found.** in chapter four indicated that the clad root angle increased with an increase in the clad aspect ratio thus reducing the possibility of inter-run porosity.

However, contrary to the statement made by **Gedda** which suggested that the clad aspect ratio should be larger than five to prevent inter-run porosity, the investigation established that the clad aspect ratio could be as small as 2.4 and still produce a clad layer with a large enough clad root angle to prevent inter-run porosity. The validity of this statement is based on a remark made by **de Oliveira** in which he commented on a study by **Felde et al** which suggested that the clad root angle should not be smaller than  $100^\circ$  to prevent inter-run porosity.

It was interesting to note that the level of dilution generally increased with an increase in the clad aspect ratio, as shown by Figure 5.2, which indicates the relationship between the clad root angle; dilution, and aspect ratio of the clad layer. This suggests that the clad aspect ratio should only be used as a general guideline but more importantly that a suitable clad layer should be selected such that the clad root angle is large enough to prevent inter-run porosity with a suitably low level of dilution to ensure that the coating fulfils its intended service requirements.

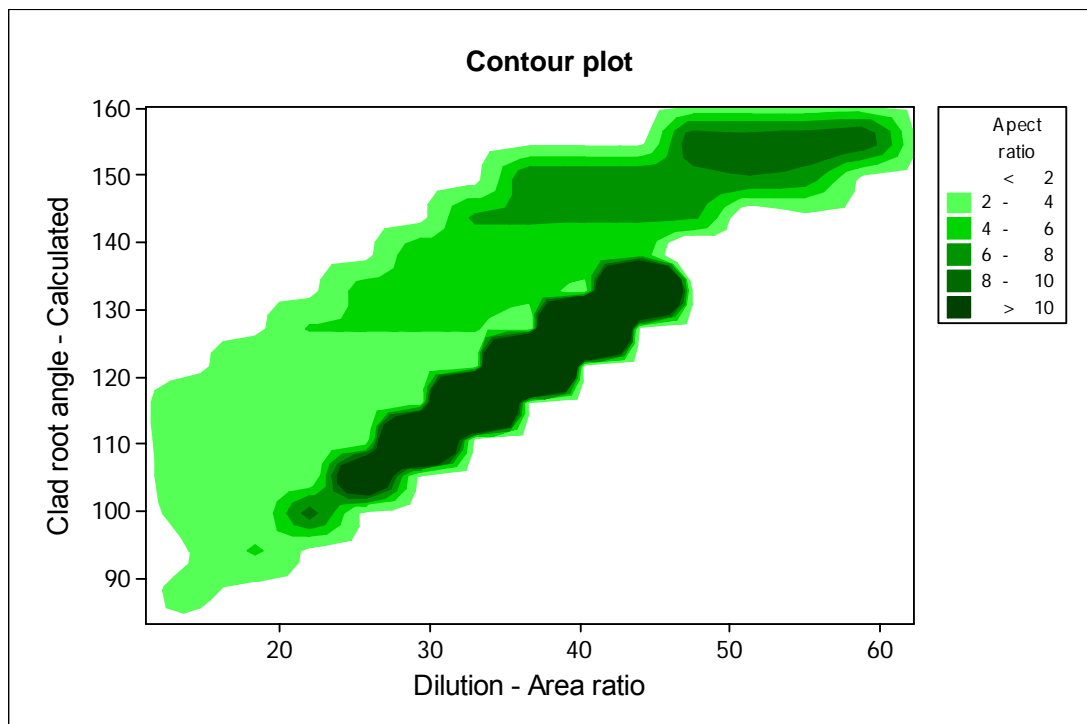


Figure 5.2: Contour plot indicating the relationship between the clad characteristics: dilution; the calculated clad root angle, and the clad aspect ratio.

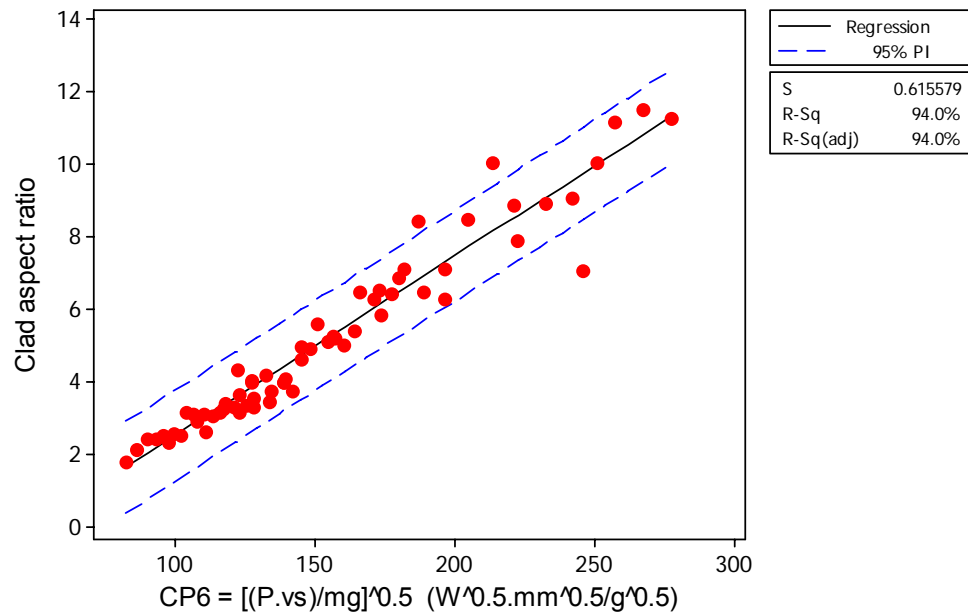


Figure 5.3: Relationship between the clad aspect ratio and the combined process parameter CP6.

Figure 5.3 indicates the relationship between the clad aspect ratio and the combined process parameter CP6 ( $\sqrt{(P \cdot v_s) / \dot{m}_g}$ ). The blue lines indicate the 95% predicted confidence intervals. The relationship between the clad aspect ratio (AR) and CP6 is given by the expression:  $AR = -2.473 + (0.04967) \cdot CP6$ .

#### 5.2.4 Alloy penetration depth ( $Z_{pd}$ )

The depth of alloy penetration indicates the amount of substrate material that has mixed with the material/alloy addition. It is thus an important parameter considering the optimization of the service properties of the clad layer. The depth of alloy penetration was found to be mainly a function of the process variables laser power and laser scanning velocity. **de Oliveira** mentions that

previous investigations have found that the depth of alloy penetration into the substrate increases linearly with an increase in laser power and that it is inversely proportional to the square root of the laser scanning velocity (34).

This suggests that a strong correlation should exist between the combined process parameter CP2 ( $P/\sqrt{v_s}$ ) and the depth of alloy penetration. Upon investigation it was found that the correlation coefficient was 0.866 but could be improved to 0.933 by considering the depth of alloy penetration to be inversely proportional to the cubed root of the laser scanning velocity. Figure 5.4 indicates the relationship between the depth of alloy penetration and the modified combined process parameter CP2\* ( $P/\sqrt[3]{v_s}$ ). The blue lines indicate the 95% predicted confidence intervals. The relationship between the depth of alloy penetration ( $Z_{pd}$ ) and CP2\* is given by the expression:

$$Z_{pd} = - 0.2868 +(0.000353).CP2^*.$$

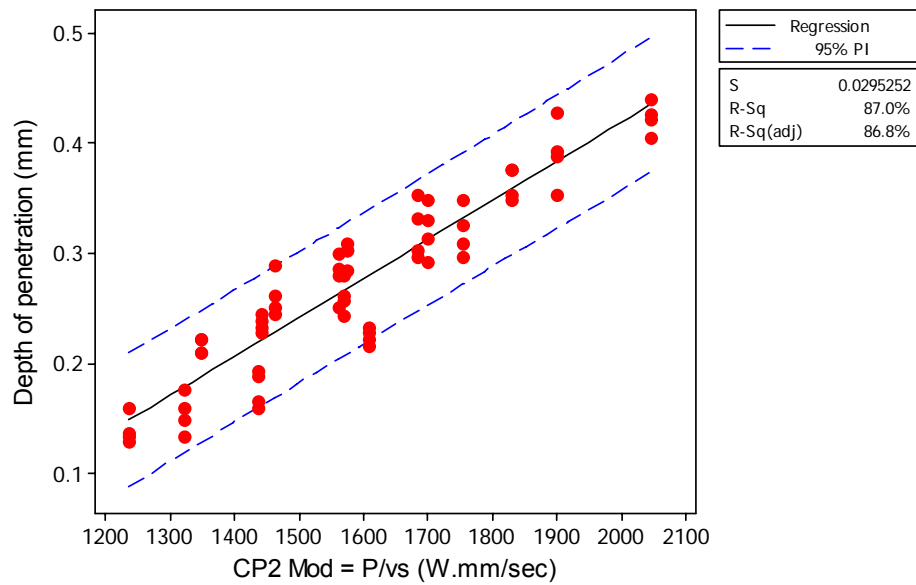


Figure 5.4: Relationship between the depth of alloy penetration and the modified combined process parameter CP2\*.

The shape of the clad area below the substrate surface bears some resemblance to the shape of the laser beam intensity profile as illustrated in Figure 5.5, similarly to what is generally observed in laser heat treatment. The power density distribution in Figure 5.5 clearly indicates that the majority of the laser energy is located in the centre of the laser spot and thus it is only reasonable to expect that the maximum depth of alloy penetration would coincide with the centre of the laser spot as indicated by the clad cross-section in Figure 5.5.

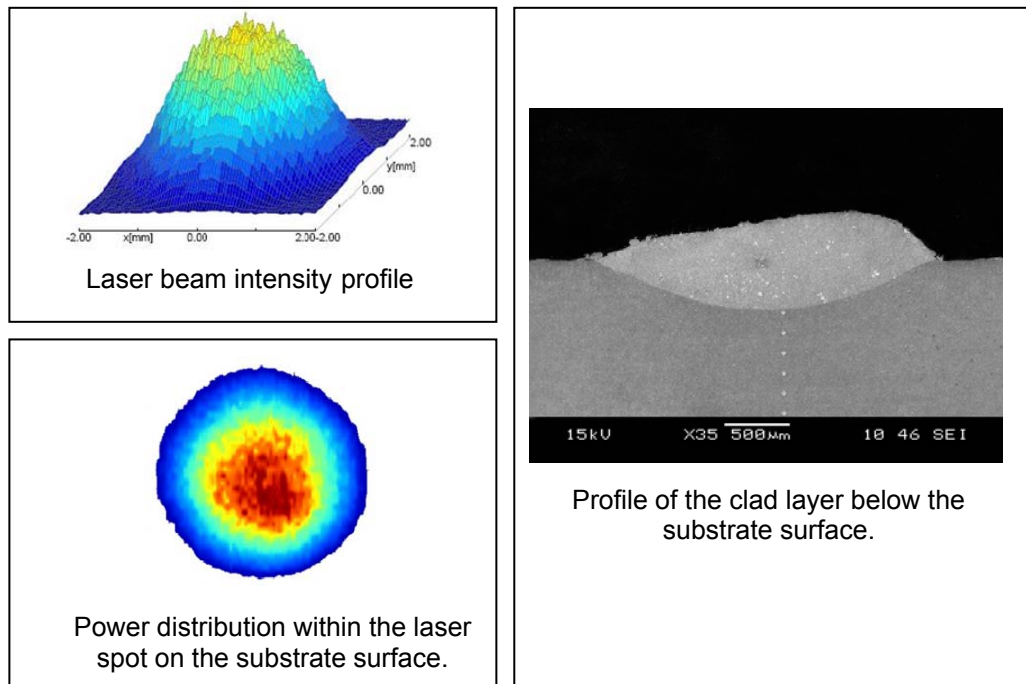


Figure 5.5: SEM micrograph indicating the resemblance between the laser beam intensity profile and the profile of the clad area below the substrate.

The resemblance between the shape of the clad area below the substrate surface and the intensity profile of the laser beam illustrates the potential benefit of working with a uniform intensity profile such as the top-hat intensity profile, generally observed at the newly formed beam waist radius after focusing.

When working with a uniform intensity profile or uniform power density distribution, it would be reasonable to assume that the depth of alloy penetration could be reduced by reducing the laser power without reducing the width of the melt pool on the substrate surface as significantly as would be the case when working with a non-uniform intensity profile. It would also be possible to create a wider melt pool on the substrate surface at the same



power level thereby increasing the favourable impact conditions for powder particles.

### 5.2.5 Dilution

Dilution levels varied between 10.9-62.2% when considering the area ratio method of calculating dilution. It is considerably higher than the 5% quoted by *Ion* as being the typical dilution level for laser cladding. *de Oliveira* in his investigation of the coaxial laser cladding process however suggest that a single pass clad layer should be selected with a dilution level between 10-30% to form a thick, pore free coating by overlapping individual clad layers. He further remarked that the final level of dilution of the coating could be expected to be lower due to a part of the beam energy that would be consumed to melt the clad layer being overlapped.

The investigation indicated that the powder feed rate had the most significant effect on the level of dilution followed by laser power and the laser scanning velocity. It therefore seems reasonable to increase the powder feed rate in order to reduce dilution.

It is however not very practical, since by increasing the powder feed rate the aspect ratio of the clad layer is reduced, which means that clad root angle becomes more acute and therefore the risk of inter-run porosity is increased. It is the researcher's opinion that it would be more beneficial to consider the depth of alloy penetration and how it could be reduced as a means of

reducing dilution. This would allow the formation of clad layers with a higher aspect ratio at similar or lower dilution levels that can be achieved by changing the powder feed rate. The depth of alloy penetration can be reduced by either decreasing the laser power or by increasing the laser scanning velocity. However, if the depth of alloy penetration could not be reduced without reducing the width of the melt pool significantly it should be considered how the power density distribution could be changed so as to reduce the peak power density in the centre of the laser spot.

The dilution of the clad layer correlated well with the combined process parameter CP6 ( $\sqrt{(P \cdot v_s) / \dot{m}_g}$ ). Figure 5.6 indicates the relationship between area ratio dilution and CP6. The blue lines in Figure 5.6 indicate the 95% predicted confidence intervals. The relationship between the area ratio dilution ( $D_{ar}$ ) and CP6 is given by the expression:  $D_{ar} = -9.113 + 0.03753 \cdot CP6$ .

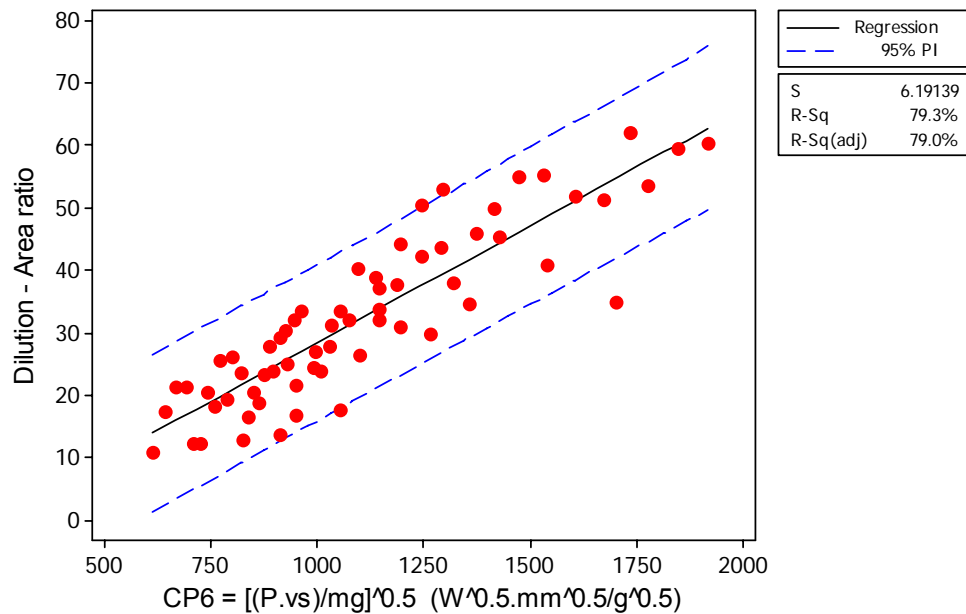


Figure 5.6: Relationship between the level of dilution and the combined process parameter CP6.

### 5.2.6 Powder efficiency ( $\eta_{pe}$ )

The powder efficiency of the cladding process is a measure of the efficiency with which the powder consumable/material addition is used within the development of the clad layer. Powder efficiencies ranging from between 37-96% were observed. However, as previously mentioned in chapter three these values are higher than the true values owing to the method used to determine the relationship between the powder disc speed of the volumetric powder feed unit and the powder feed rate in g/sec. Therefore the powder efficiency values should only be considered for indicating general trends and for comparative purposes.

The most significant variable influencing the powder efficiency of the process was found to be the powder feed rate, followed by the laser scanning velocity and laser power. The strong influence of the powder feed rate on the powder efficiency of the process deviates from reported literature which generally suggests that the laser scanning velocity followed by laser power is the most significant variables affecting powder efficiency.

**de Oliveira** reported a correlation coefficient of 0.91 between the combined process parameter CP7 ( $P \cdot \sqrt{\dot{m}_g/v_s}$ ) and the powder efficiency of the process. He also reported a similarly high correlation coefficient between powder efficiency and CP6 which suggested that a strong relationship exists between the powder efficiency of the process and the width of the clad track. **de Oliveira** states that this correlation supports the assumptions made by powder catchment models which suggest that both solid-liquid and liquid-liquid powder/substrate interactions lead to particle catchment (34). Our investigation did suggest that the powder efficiency increased with an increase in the width of the melt pool on the substrate surface, however, the correlation coefficient between the width of the clad layer and powder efficiency was found to be only 0.66 due to the strong influence of the powder feed rate.

Remarks made by both **Toyserkani et al** and **Lin** support the statement made by **de Oliveira**. Both **Toyserkani et al** and **Lin** remarked that the powder efficiency of the coaxial laser cladding process is related to the ratio

of the diameter of the melt pool to the diameter of the powder stream on the substrate surface. Based on the visual analysis of the cold stream powder flow from the three-way coaxial nozzle used in this investigation the ratio of the powder stream to laser beam diameter on the substrate surface was estimated to be  $\pm 1.2$  and  $\pm 1.61$  at the lowest and highest powder feed rate settings respectively. The ratios mentioned above are in fact lower than the actual ratios since the width of the melt pool on the substrate surface varied between 0.96-2.90 mm over the whole range of tests carried out. Therefore it was expected that powder efficiency would decrease with an increase in the powder feed rate due to an increase in un-favourable impact conditions such as solid-solid and liquid-solid powder/substrate interactions.

Further investigation revealed no suitable explanation for the deviation from literature. However a few points worth considering will be discussed in brief. Firstly, the visual analysis of the powder stream was carried out under cold stream flow conditions. This does not indicate the effect of the laser beam or temperature on the resultant powder stream profile. Secondly the effect of the substrate and the angle of injection were not considered. Figure 5.7 indicates the three powder streams from the three-way nozzle; its injection direction, and the projected elliptical profile of each powder stream on the substrate surface. The common area bound by all three elliptical profiles represent the consolidated powder stream and the circle formed by the red dashed line the melt pool on the substrate surface. When considering each individual diverging powder stream in Figure 5.7 it is reasonable to assume

that even if the powder particles are not directly injected into the melt pool it could still be transported into the melt zone through the interaction with the other two powder streams that tends to redirect the particles of the powder stream in question. This is also true for particles ricocheting off the cold substrate surface.

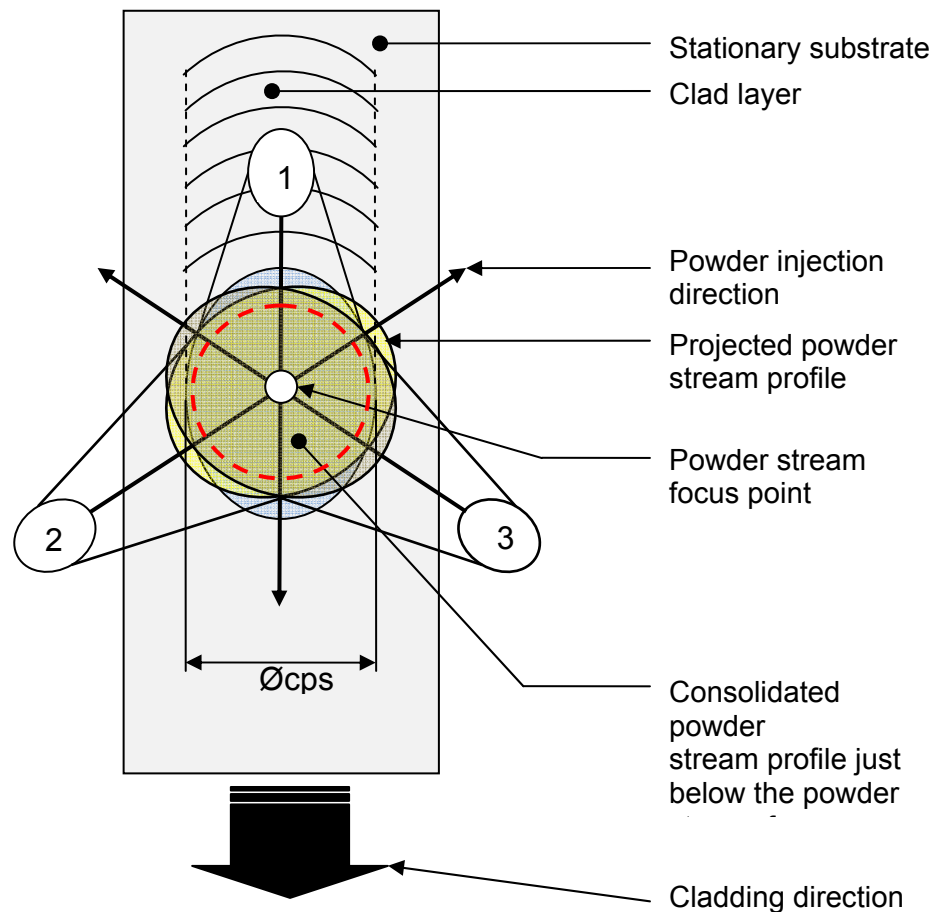


Figure 5.7: The three powder streams from the three-way coaxial nozzle impacting on the substrate surface.

Thirdly it is well noted in literature that the concentration distribution of the powder particles within the powder stream is Gaussian of nature. This can be seen by considering the modified pictures in Figure 5.8, taken from the cold stream visual analysis tests, which indicate the variation in the powder particle concentration within the powder stream by considering the variation in the luminescence of the powder stream. The pink area represents the area of peak powder concentration in the powder stream.

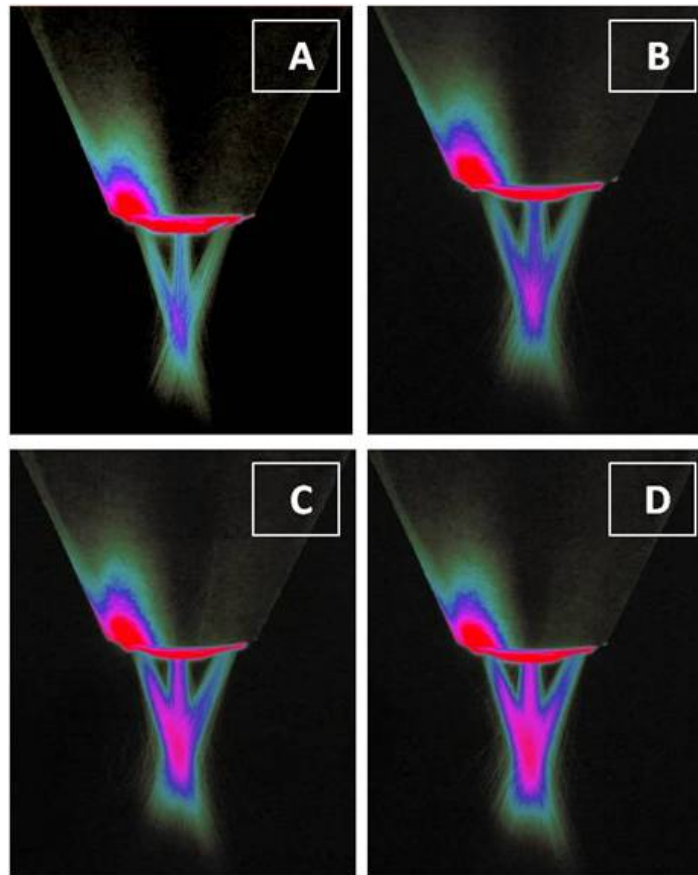


Figure 5.8: The change in the powder concentration of the powder stream with an increase in the powder feed rate under cold stream flow conditions. The powder mass flow rate in A = 0.627 g/min; B = 1.134 g/min; C = 1.634 g/min, and D = 2.180 g/min.

### **5.2.7 Vickers microhardness and microstructure of the clad layer**

The Vickers microhardness of the clad layer increased with an increase in the powder feed rate and decreased with an increase in laser power. The laser scanning velocity had no significant influence on the hardness of the clad layer.

The strong influence of the powder feed rate and laser power on the hardness profile of the clad cross-section suggested that dilution and therefore the composition of the melt pool upon solidification was the main contributing factor responsible for the difference in the hardness of the clad cross-sections, between samples.

Upon inspection a relatively strong inverse relationship was found between the maximum hardness of the clad layer and dilution. This relationship and the expression describing it is shown in Figure 5.9.



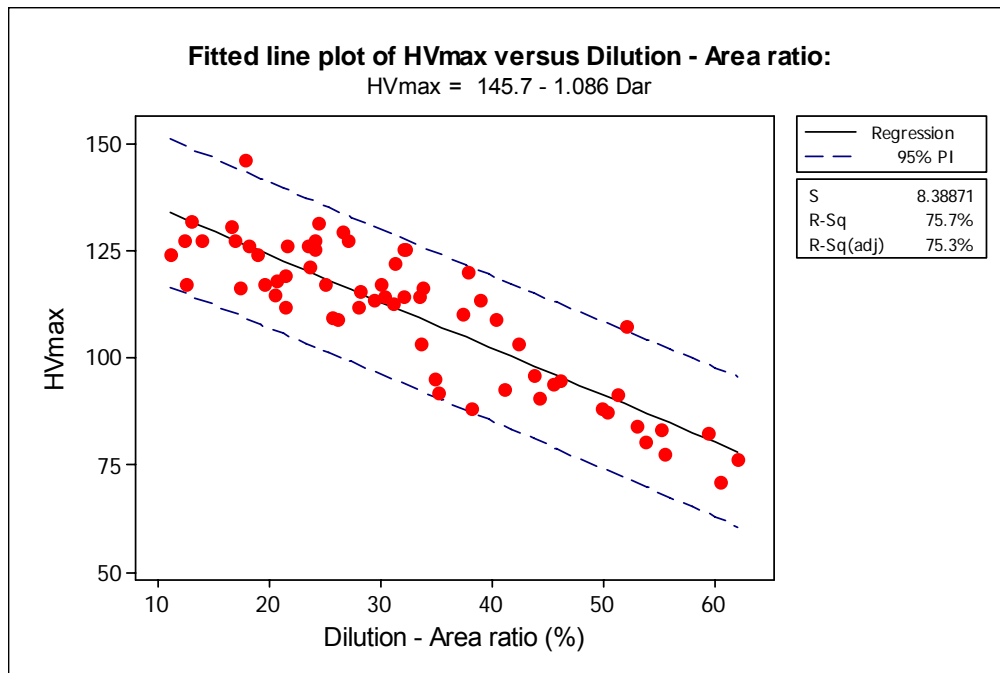


Figure 5.9: Relationship between the maximum hardness and dilution of the clad layer.

When considering the clad cross-section the maximum hardness was generally found near the top edge of the clad cross-section and the minimum hardness at the bottom, just above the clad-substrate interface. The variation in hardness of each clad cross-section were attributed to a variation in both the solidification rate and temperature gradient across the clad height which resulted in a variation in the solidification conditions throughout the melt pool and therefore also the microstructure of the clad cross-section upon solidification.

The solidification rate is related to the velocity of the solidification front ( $v_{sf}$ ) which in turn is related to the laser scanning velocity ( $v_s$ ) through the expression  $v_{sf} = v_s \cdot \cos\theta$ . Inspection of the relationship between the solidification front and the laser scanning velocity revealed that the

solidification rate varies from zero at the bottom of the melt pool to a maximum approaching the laser scanning velocity at the top of the melt pool.

The influence of the increase in the velocity of the solidification front from the bottom to the top of the clad layer was observed as a refinement in the clad microstructure from the bottom to the top of the clad cross-section. The temperature gradient on the other hand is known to decrease from a maximum near the bottom of the melt pool to a minimum near the surface of the clad layer. However how the temperature gradient is related to the main process variables is not specifically known.

In addition to a refinement in the microstructure microstructural changes was also observed within the clad cross-section. Considering the variation in the type of microstructure, moving from the bottom to the top of the clad cross-section the microstructure of the clad cross-section generally changed from a columnar dendritic structure to a quasi-dendritic structure or from a eutectic structure to a microstructure consisting of Al-Si eutectic with Si-crystals surrounded by alpha aluminium halos.

An illustrative microstructural scale, shown in Figure 5.10, was constructed to indicate the variation in the clad microstructure with a change in the main process variables.

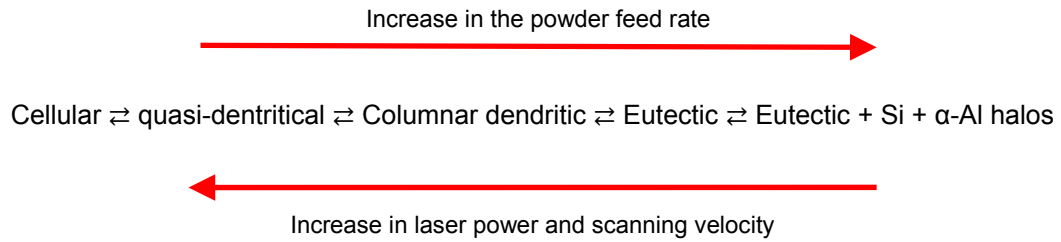


Figure 5.10: Influence of an increase in the main process variables test level on the clad microstructure

It was observed that an increase in the powder feed rate caused a change in the type of microstructure, in the direction, left to right in the microstructural sequence. An increase in both laser power and the laser scanning velocity had the inverse affect, causing a change in the direction, right to left, in the sequence. The microstructural scale interestingly also represents the hardness scale. An alpha aluminium cellular microstructure with interdendritic Al-Si eutectic was found to be the softest while a microstructure consisting of Al-Si eutectic with silicon crystals dispersed in the eutectic structure and surrounded by alpha aluminium was found to be the hardest. The maximum hardness scale varied between 65.68-146.4 HV<sub>0.025</sub>.

Considering the observations made regarding the microstructure of the clad cross-section and the Vickers microhardness it was considered that if a relationship could be found between the Vickers microhardness and the type of microstructure then the microstructure could be related to the process variables through the relationship found between the Vickers microhardness

and the main process variables without having to consider the influence of each variable that effect the clad microstructure.

The advantage would then be that the microstructure of the clad layer could be tailored to the requirements of the coating by having gained a better understanding of the influence of the main process variables on its formation. Further inspection however could only reveal a general relationship between the clad microstructure and the Vickers microhardness of the clad layer and therefore no definite connection could be made between the clad microstructure and the main process variables.

#### **5.2.8 General observations regarding the shape of the clad cross-section**

*Toyserkani et al* stated that the balance between interfacial free energies govern the shape of the clad cross-section. *Gedda* on the other hand stated that the effect of surface tension gradients is negligible compared to the effect of the laser beam diameter on the substrate. *Gedda* stated that the laser beam diameter on the substrate effectively fixes the width of the melt-substrate interface which means that the clad cross-section cannot spread laterally and that the shape of the clad cross section will thus assume a shape which forms a part of a circle intersected by a chord of more or less fixed width represented by the melt-substrate interface.

Generally the clad cross-section did behave similarly to **Gedda's** description of its behaviour. Our investigation however also showed that the clad cross-section is not always bound by the melt-substrate interface and it is possible for the clad cross-section to spread laterally beyond the melt-substrate interface. The lateral spread of the clad layer could be attributed to the ratio of the powder stream diameter to the diameter of the laser beam/melt pool on the substrate that increased with an increase in the powder feed rate, from  $\pm 1.2$ -1.61 at the lowest and highest powder feed rate respectively. A graphical representation of this increase is shown in Figure 5.11. This lateral spread would however only occur when operating in a cladding regime were the powder particles are melted or partially melted, impacting on a hot, but solid substrate.

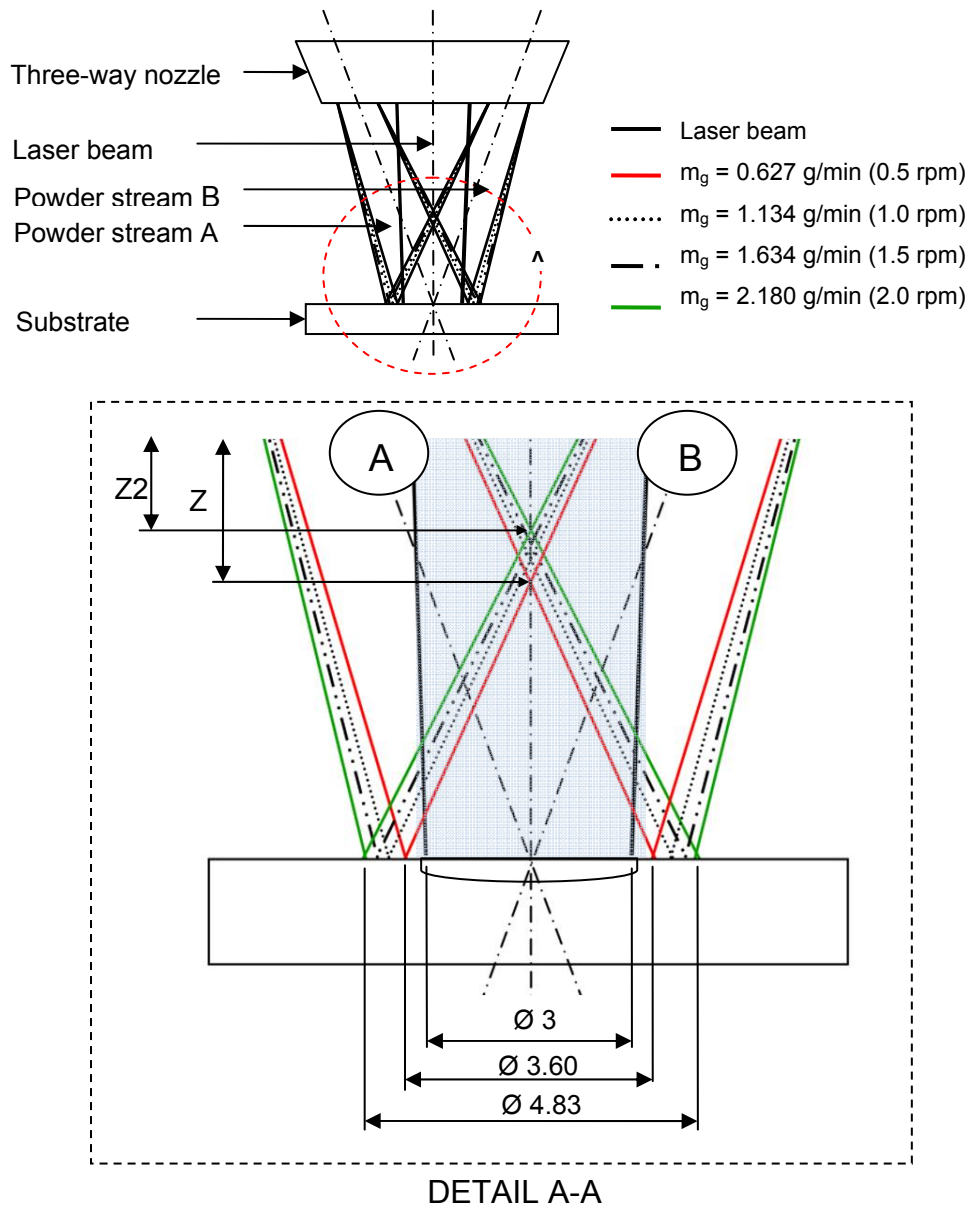


Figure 5.11: Increase in the ratio between the powder stream diameter to the laser beam diameter on the substrate surface with an increase in the powder mass flow rate.

The investigation also indicated that when the clad cross-section spread beyond the melt-substrate interface the bond between the clad layer and the substrate changed from a fusion bond to one that resembles a forge bond, generally associated with the impact of high speed particles with a solid substrate. According to **Steen**, these forge like bonds are much less resistant to thermal and impact shock when compared to fusion bonds (7). A typical example of where the clad cross-section has spread beyond the melt substrate interface is shown in Figure 5.12.

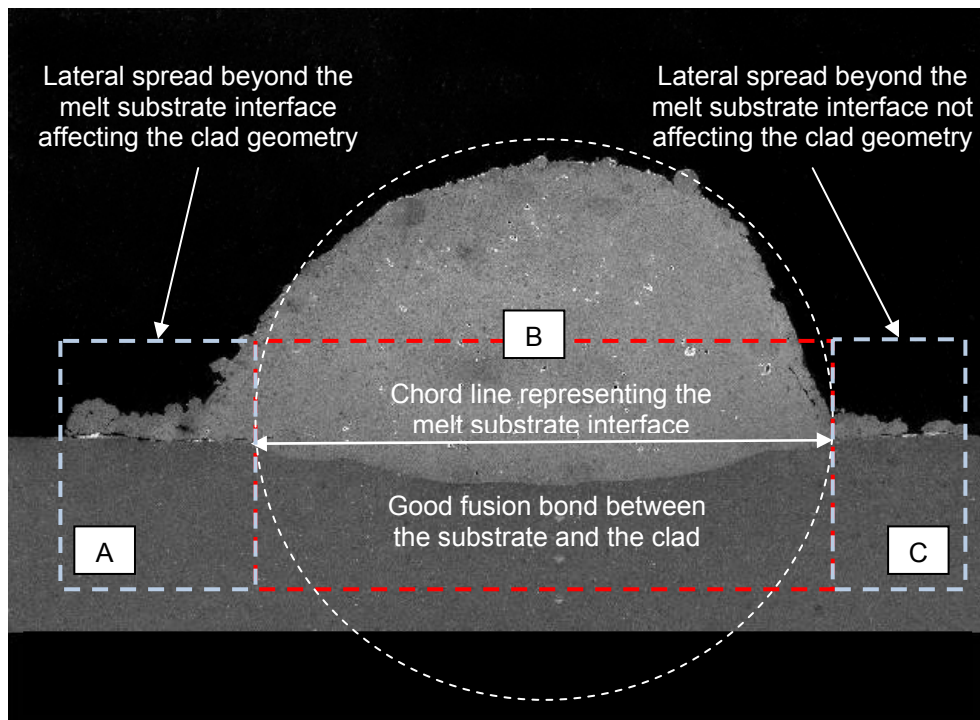


Figure 5.12: Lateral spread of the clad layer beyond the melt substrate interface.

Owing to the poor bond between the clad layer and the substrate when the clad cross-section spreads beyond the melt-substrate interface it is only reasonable to suggest that the consolidated powder stream diameter should never exceed the diameter of the laser beam on the substrate surface to ensure that the powder particles are injected directly into the melt pool.

### **5.3 Processing window**

The investigation could suggest a probable processing window for the application of an Al-Si coating on an aluminium substrate using an Nd:YAG laser. It is however the belief of the researcher that several improvements could still be made to refine the cladding platform setup that would affect the response of the process and the test level boundaries of the main process variables before a suitable process window could be defined. It is also believed that a second processing window exists at higher scanning velocities and powder feed rates. The concern would however be the quality of the clad layer at these high scanning velocities and powder feed rates.



## 5.4 Future work

The investigation of the coaxial laser cladding process raised several questions which could form the basis for future investigations of the laser cladding process. Some of these questions are summarised below:

1. The investigation was carried out above the laser beam focus.  
Generally research is carried out below the powder focus. The reason given in literature for working below the laser beam focus position however only states that increasing the distance between the work piece and the optics helps to protect the optics from damage. Quick inspection of Figure 5.13 reveals that for our specific set-up the powder stream-laser beam interaction area was considerably larger than what would have been the case if the work was carried out below the focus position, however interaction between the powder stream and nozzle moved closer to the nozzle tip as well and this decreases with an increase in the powder feed rate could pose a potential problem. The question however becomes considering the interaction area and the time that the powder particles spent under the laser beam are there any advantages or disadvantages to working above or below the laser beam focus position?

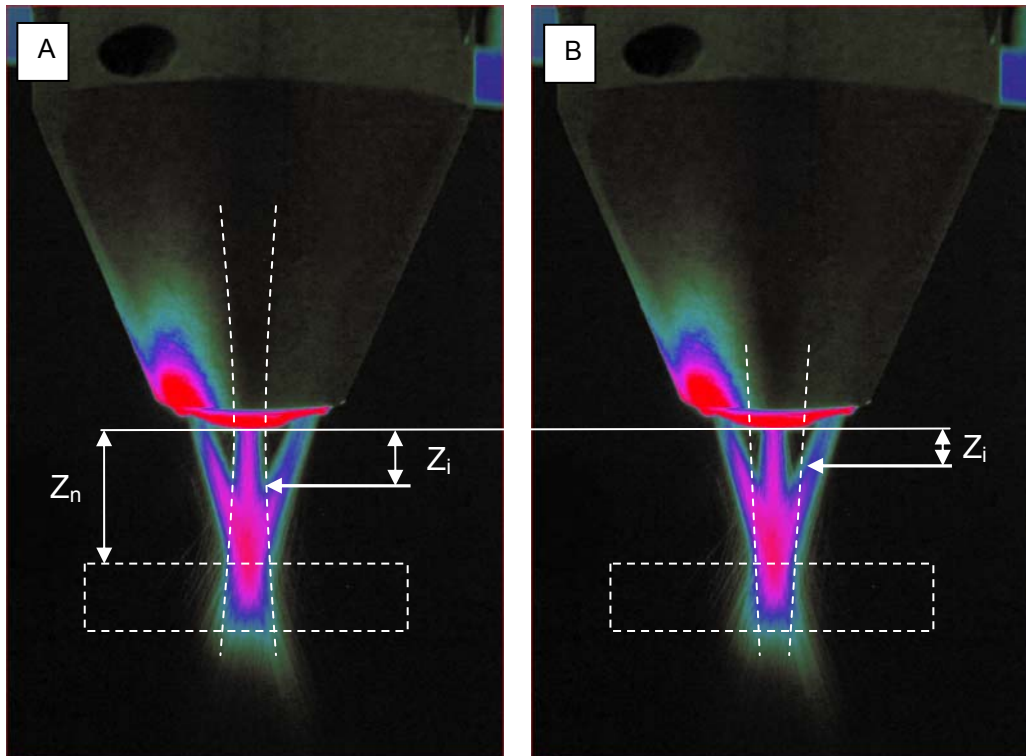


Figure 5.13 (A) Working below the beam focus. (B) Working above the beam focus

2. What effect does the laser beam have on the cold stream powder profile and is the cold stream powder flow profile analysis representative of actual flow conditions during cladding or is it misleading?
3. What does the powder concentration distribution of the consolidated powder stream look like and what is the effect of an increase in both the carrier gas flow rate and powder feed rate on the powder stream concentration profile?
4. What does the temperature distribution within the powder stream look like?
5. Does the level of the test variables in relation to each other have a significant influence on the effect that a process variable have on a specific clad geometry or characteristic?

## REFERENCE LIST

1. Ion, J C. 2005. *Laser processing of engineering materials*. Elsevier Butterworth-Heinemann: Oxford.
2. Toyserkani, E; Khajepour, A; Corbin, S. 2005. *Laser cladding*. CRC Press LLC: Florida.
3. Yunchang, F et al. 2002. A theoretical model for laser and powder particles interaction during laser cladding. *Journal of Materials Processing Technology* Vol.128, Issues 1-3. pp 106-112. Viewed 26 May 2006.  
<<http://www.sciencedirect.com/>>
4. Ready, J F (ed.). 2001. *LIA handbook of laser material processing*. Laser Institute of America: Florida.
5. Gengel, Y A. 1998. *Heat transfer: A practical approach*. International Ed. McGraw-Hill: Boston.
6. Bergstrom, D. 2005. The absorptance of metallic alloys to Nd:YAG and Nd:YLF laser light. Lulea University of Technology: Sweden. Viewed 15 October 2006.  
<http://www.epubl.ltu.se/1402-1757/2005/89/LTU-LIC-0589-SE.pdf>
7. Steen, W M. 2003. *Laser material processing*. 3<sup>rd</sup> ed. Springer-Verlag: London
8. Bergstrom, D et al. 2005. The absorptance of metallic alloys to Nd:YAG and Nd:YLF laser light: Mathematical modeling of laser absorption mechanisms in metals: A review. Lulea University of Technology: Sweden. Viewed 15 October 2006.  
<http://www.epubl.ltu.se/1402-1757/2005/89/LTU-LIC-0589-SE.pdf>

9. Bergstrom, D et al. 2005. The absorptance of metallic alloys to Nd:YAG and Nd:YLF laser light: The absorptance of non-ferrous alloys to Nd:YAG and Nd:YLF laser light. Lulea University of Technology: Sweden. Viewed 15 October 2006.  
<http://www.epubl.ltu.se/1402-1757/2005/89/LTU-LIC-0589-SE.pdf>
10. Schneider, M. 1998. *Laser cladding with powder* (Ph.D Thesis). University of Twente: Enschede-The Netherlands.
11. VLOC. Viewed 10 May 2006  
<http://www.vloc.com/PDFs/YAGBrochure.pdf>
12. Koechner, W; Bass, M. 2003. *Solid state lasers: A graduate text*. Springer-Verlag: New York.
13. Rofin-Sinar. 2000. *Introduction to industrial laser material processing*. Rofin-Sinar:Hamburg.
14. Olympus. Viewed 17 June 2007  
<http://www.java.magnet.fsu.edu/olympus/micd/curriculum/lightandcolor/index.html>
15. GSI Lumonics. Technical Tips: Number one. Viewed 12 June 2006  
<http://www.gsig.com>
16. Sulzer Metco. *Powder feeders using rotating disc technology*. Sulzer Metco: Switzerland.
17. GSI Lumonics. Technical Tips: Number five. Viewed 12 June 2006  
<http://www.gsig.com>
18. Weisheit, A et al. 2001. Powder injection: The key to reconditioning and generating components using laser cladding. ILT Fraunhofer: Germany. Viewed 23 July 2006  
<http://www.ilt.fraunhofer.de/ilt/pdf/eng/paper1232.pdf>

19. Salehi, D. 2005. *Sensing and control of Nd:YAG laser cladding process* (Ph. D Thesis). Swinburne University of Technology: Australia. Viewed 18 August 2006.  
<http://adt.lib.swin.edu.au/public/adt-VSWT20050915.142812/index.html>
20. de Oliveira, U et al. 2005. Analysis of coaxial laser cladding processing conditions. *Surface and Coatings Technology* Vol.197, Issues 2-3. pp 127-136  
<<http://www.sciencedirect.com/>>
21. Gedda, H. 2000. Laser surface cladding: A literature review. Lulea University of Technology: Sweden. Viewed 3 November 2006.  
<http://www.epubl.luth.se/1402-1536/2000/07/index-en.html>
22. Alabama Lasers. Viewed 6 September 2006.  
<http://www.alspi.com/wirefeed.htm>
23. Trumpf. 2006. *Laser deposition: Optimizing and repairing surfaces*. Trumpf: Germany.
24. Gedda, H. 2004. Laser cladding: An experimental and theoretical investigation. Lulea University of Technology: Sweden. Viewed 3 November 2006.  
<http://www.epubl.ltu.se/1402-1544/2004/41/index.html>
25. Lin, J. 1999. A simple model of powder catchment in coaxial laser cladding. *Optics & Laser Technology* Vol.31, Issue 3. pp 233-238.  
<<http://www.sciencedirect.com/>>
26. Pei, Y T. 2000. Functionally graded materials produced by laser cladding. *Acta Materialia* Vol.48, Issue 10. pp 2617-2624  
<<http://www.sciencedirect.com/>>

27. Makhlof, M M. 2001. The aluminium-silicon eutectic reaction: Mechanisms and crystallography. *Journal of Light Metals* Vol.1, Issue 4. pp 199-218  
<<http://www.sciencedirect.com/>>
28. Dubourg, L. 2005. Laser cladding of MMC coatings on aluminium substrate: Influence of composition and microstructure on mechanical properties. *Wear* Vol.258, Issues 11-12. pp 1745-1754  
<<http://www.sciencedirect.com/>>
29. University of South Hampton, 17 November 1997. Viewed 20 May 2007.  
<http://www.soton.ac.uk/~pasr1/index.htm>
30. Uzun, O et al. 2000. Production and structure fo rapidly solidified Al-Si alloys. *Turkish Journal of Phys* Vol.25. pp 455-466.  
<http://www.journals.tubitak.gov.tr/physics/issues/fiz-01-25-5/fiz-25-5-10-0010-7.pdf>
31. Gremaud, M et al. 1996. The development of nucleation controlled microstructures during laser treatment of Al-Si alloys. *Acta Materialia* Vol.44, Issue7. Pp 2669-2681.  
<<http://www.sciencedirect.com/>>
32. De Deus, A M et al. 1996. 'Two dimensional thermo-mechanical finite element model for laser cladding'. Proceedings of ICALEO '96, 15<sup>th</sup> International Congress on Applications of Lasers & Electro-Optics, 14-17 October 1996. Detroit, Michigan, USA.  
<http://www.eecs.umich.edu/~dedeus/claim/lcaleo96paper.pdf>.
33. Watkins, K G. 1997. Microstructure and corrosion properties of laser surface processed aluminium alloys: A review. *Materials Science and Engineering: A* Vol.231, Issues 1-2. pp 55-61.  
<<http://www.sciencedirect.com/>>

34. De Oliveira, U. 2007. *Laser treatment of alloys: Processing, microstructures and structural properties* (Ph.D Thesis). Rijksuniversiteit Groningen:Groningen.
35. Fearon, E. 2004. 'Optimisation of layer height control in direct laser deposition'. Proceedings of the ICALEO '04, 23<sup>rd</sup> International Congress on Applications of Lasers & Electro-Optics, 4-7 October 2004. San Francisco, California, USA.  
<http://www.lasers.org.uk/paperstore/fabrication4.pdf>.
36. Jones, H. 2005. Some effects of solidification kinetics on microstructure formation in aluminium-base alloys. *Materials Science and Engineering: A* Vol.413-414. pp 165-173.  
<<http://www.sciencedirect.com/>>
37. Kumar, S et al. 2007. Development of a theoretical process map for laser cladding using a two-dimensional conduction heat transfer model. *Computational Materials Science*. In press.  
<<http://www.sciencedirect.com/>>
38. Mohanthy, P et al. 1998. Solidification behavior and microstructural evolution during laser beam-material interaction. *Metallurgical and Materials Transactions B* Vol.29, Number 6. pp 1269-1279  
<<http://www.igentaconnect.com/>>

# APPENDIX A

## **Clad geometry and characteristics**



## Tabulated measurements: Clad geometry and characteristics

Measurements taken from the single pass clad layer cross-section and clad characteristics such as the clad aspect ratio; calculated root angle, and the geometrical and area ratio dilution is tabulated in Table A1 and A2.

Sample Nr	h (mm)	w (mm)	$W_{mp}$ (mm)	$Z_{ap}$ (mm)	$A_{above}$ (mm <sup>2</sup> )	$A_{below}$ (mm <sup>2</sup> )
C001	1.230	2.980	2.77	0.429	3212.87	875.32
C002	0.709	3.070	2.64	0.326	1567.89	612.55
C003	0.480	2.680	2.51	0.349	979.97	663.87
C004	0.417	2.180	2.02	0.160	621.03	293.80
C005	0.486	2.490	2.37	0.263	950.00	485.40
C006	1.250	3.040	2.68	0.427	3285.27	893.61
C007	0.589	2.400	2.27	0.280	1172.11	532.61
C008	0.600	2.260	2.05	0.234	1174.37	437.01
C009	0.240	2.410	2.41	0.354	419.99	692.37
C010	0.829	2.530	2.27	0.189	1616.81	321.03
C011	0.383	2.640	2.64	0.389	789.18	804.78
C012	1.050	2.440	2.23	0.194	2013.63	282.47
C013	0.497	2.500	2.50	0.309	1016.79	621.01
C014	0.220	2.480	2.48	0.285	351.19	539.38
C015	0.497	2.440	2.27	0.211	975.35	353.85
C016	0.691	2.750	2.57	0.303	1548.50	601.96
C017	0.326	2.050	2.05	0.160	472.07	252.44
C018	0.360	2.570	2.50	0.303	679.47	566.77
C019	0.314	2.780	2.78	0.377	618.00	772.08
C020	1.040	2.650	2.23	0.223	2386.92	338.33
C021	0.743	2.700	2.58	0.331	1641.88	684.17
C022	0.240	2.140	2.10	0.240	361.78	393.02
C023	0.789	2.610	2.42	0.286	1758.63	555.64
C024	0.966	2.990	2.54	0.354	2429.64	752.73
C025	0.383	2.510	2.51	0.297	718.56	573.04
C026	0.406	2.610	2.53	0.333	858.84	668.82
C027	0.571	2.150	1.92	0.137	948.97	204.86
C028	0.265	2.400	2.20	0.251	439.41	463.93
C029	0.363	2.360	2.28	0.233	646.65	385.29
C030	0.446	2.420	2.26	0.246	903.84	409.08
C031	0.720	2.500	2.38	0.246	1626.78	525.59
C032	0.227	1.610	0.96	0.130	332.32	179.99
C033	0.960	3.020	2.72	0.393	2370.07	813.84
C034	1.000	2.550	2.48	0.257	2172.48	482.67
C035	0.697	2.800	2.69	0.354	1653.84	722.56

*Table continued*

Sample Nr	h (mm)	w (mm)	W <sub>mp</sub> (mm)	Z <sub>ap</sub> (mm)	A <sub>above</sub> (mm <sup>2</sup> )	A <sub>below</sub> (mm <sup>2</sup> )
C036	0.246	1.940	1.82	0.177	348.58	243.34
C037	0.994	2.890	2.89	0.440	2594.51	919.19
C038	1.350	2.400	2.25	0.229	3122.48	385.69
C039	0.380	2.460	2.42	0.290	669.21	574.25
C040	0.686	2.280	2.21	0.211	1322.67	364.71
C041	0.737	2.420	2.23	0.217	1474.76	380.63
C042	1.260	2.720	2.48	0.349	3215.75	676.35
C043	0.420	2.650	2.55	0.300	622.06	457.28
C044	0.834	2.650	2.25	0.229	1730.97	403.40
C045	0.183	2.040	2.04	0.223	290.46	338.36
C046	0.558	2.230	1.91	0.167	927.76	293.13
C047	0.771	2.630	2.47	0.280	1672.31	512.73
C048	0.354	2.980	2.84	0.423	789.03	894.73
C049	0.731	2.970	2.90	0.377	1774.47	839.99
C050	0.194	2.230	2.23	0.251	293.82	432.98
C051	0.337	2.400	2.22	0.223	617.39	380.81
C052	0.503	2.510	2.42	0.263	997.70	502.16
C053	0.708	2.520	2.01	0.135	1125.72	227.62
C054	0.686	2.860	2.63	0.406	1671.50	849.36
C055	1.020	2.620	2.60	0.309	2379.00	619.10
C056	0.789	2.650	2.65	0.297	1759.46	586.61
C057	0.710	2.240	1.66	0.135	1326.09	213.50
C058	0.251	2.520	2.44	0.314	484.53	598.24
C059	0.953	2.970	2.48	0.293	2381.32	577.41
C060	0.583	2.700	2.47	0.303	1299.05	615.50
C061	0.857	2.260	2.19	0.149	1642.92	242.40
C062	0.528	2.780	2.67	0.349	1174.81	749.51
C063	0.284	2.410	2.41	0.244	482.00	481.43
C064	0.349	2.050	2.05	0.160	541.64	232.63

Table A1

Sample Nr	Average measured $\alpha_r$ (°)	Calculated $\alpha_r$ (°)	AR	D <sub>geometrical</sub> (%)	D <sub>area ratio</sub> (%)
C001	124.94	100.92	2.42	25.86	21.41
C002	135.65	130.42	4.33	31.50	28.09
C003	151.36	140.58	5.58	42.10	40.39
C004	150.11	138.13	5.23	27.73	32.12
C005	145.20	137.35	5.12	35.11	33.82
C006	117.51	101.13	2.43	25.46	21.38
C007	131.67	127.71	4.07	32.22	31.24
C008	134.02	124.07	3.77	28.06	27.12
C009	147.98	157.47	10.04	59.60	62.24
C010	125.16	113.52	3.05	18.57	16.57
C011	146.98	147.64	6.89	50.39	50.49
C012	118.00	98.57	2.32	15.59	12.30
C013	141.30	136.63	5.03	38.34	37.92
C014	161.71	159.88	11.27	56.44	60.57
C015	143.13	135.67	4.91	29.80	26.62
C016	141.69	126.64	3.98	30.48	27.99
C017	152.23	144.71	6.29	32.92	34.84
C018	154.95	148.70	7.14	45.70	45.48
C019	160.22	154.54	8.85	54.56	55.54
C020	120.47	103.74	2.55	17.66	12.41
C021	130.06	122.35	3.63	30.82	29.41
C022	131.62	154.72	8.92	50.00	52.07
C023	133.95	117.69	3.31	26.60	24.01
C024	132.77	114.26	3.10	26.82	23.65
C025	148.24	146.06	6.55	43.68	44.37
C026	146.48	145.44	6.43	45.06	43.78
C027	139.42	124.05	3.77	19.35	17.75
C028	152.92	155.09	9.06	48.64	51.36
C029	148.90	145.80	6.50	39.09	37.34
C030	145.37	139.53	5.43	35.55	31.16
C031	139.89	120.12	3.47	25.47	24.42
C032	7.09	154.73	148.50	36.41	35.13
C033	3.15	128.49	115.11	29.05	25.56
C034	2.55	119.66	103.78	20.45	18.18
C035	4.02	131.52	127.07	33.68	30.41
C036	7.89	152.32	151.54	41.84	41.11
C037	2.91	124.37	110.95	30.68	26.16
C038	1.78	99.77	83.27	14.50	10.99
C039	6.47	151.18	145.66	43.28	46.18
C040	3.32	128.73	117.92	23.52	21.61
C041	3.28	130.42	117.31	22.75	20.51
C042	2.16	106.62	94.37	21.69	17.38
C043	6.31	148.31	144.82	41.67	42.37
C044	3.18	133.91	115.62	21.54	18.90
C045	11.15	153.94	159.66	54.93	53.81
C046	4.00	140.30	126.83	23.03	24.01
C047	3.41	130.43	119.23	26.64	23.47
C048	8.42	157.81	153.27	54.44	53.14
C049	4.06	135.95	127.58	34.03	32.13
C050	11.49	163.11	160.26	56.40	59.57
C051	7.12	155.00	148.63	39.82	38.15
C052	4.99	145.14	136.32	34.33	33.48
C053	3.56	135.15	121.34	16.01	16.82

*Table continued*

Sample Nr	Average measured $\alpha_r$ (°)	Calculated $\alpha_r$ (°)	AR	D <sub>geometrical</sub> (%)	D <sub>area ratio</sub> (%)
C054	4.17	132.36	128.74	37.18	33.69
C055	2.57	114.93	104.19	23.25	20.65
C056	3.36	130.10	118.45	27.35	25.00
C057	3.15	129.42	115.26	15.98	13.87
C058	10.04	152.87	157.47	55.58	55.25
C059	3.12	126.55	114.62	23.52	19.52
C060	4.63	144.06	133.29	34.20	32.15
C061	2.64	126.99	105.65	14.81	12.86
C062	5.27	143.53	138.40	39.79	38.95
C063	8.49	155.08	153.48	46.21	49.97
C064	5.87	146.49	142.39	31.43	30.05

Table A2

## APPENDIX B

**Calculation method and results for determining the powder  
efficiency of the cladding process**

## Calculation method: Powder efficiency of the cladding process

The powder efficiency of the laser cladding process is defined as the ratio of the mass of powder used in the development of the clad layer to the total mass of powder delivered to the substrate. The powder efficiency of the cladding process can thus be calculated using equation 1.

$$\eta_{\text{powder efficiency}} = (100) \cdot \left( \frac{m_{p \text{ used}}}{m_{p \text{ delivered}}} \right) \quad (1)$$

The total mass of the powder used in the development of the single pass clad layer ( $m_{p \text{ used}}$ ) was calculated using equation 2. The total mass of the powder used in the development of clad layer is thus simply the difference in the mass of the test sample prior to ( $m_1$ ) and after cladding ( $m_2$ ).

$$m_{p \text{ used}} = m_2 - m_1 \quad (2)$$

The total mass of powder delivered to the substrate ( $m_{p \text{ delivered}}$ ) was calculated using equation 3. In equation 3 the powder mass flow rate ( $m_p$ ) is multiplied by length of the clad layer ( $l_{\text{clad layer}}$ ) and divided by the laser scanning velocity ( $v_s$ ).

(3)

$$m_{p \text{ delivered}} = \dot{m}_p \cdot \left( \frac{l_{\text{clad layer}}}{v_s} \right)$$

The input data used to calculate the powder efficiency of the coaxial laser cladding process as well as the calculation results are tabulated in Table B1.

Sample Nr	m <sub>1</sub> (g)	m <sub>2</sub> (g)	m <sub>p used</sub> (g)	(l <sub>cl</sub> /v <sub>s</sub> ) (s)	m <sub>p delivered</sub> (g)	η <sub>pe</sub> (%)
C001	196.617	197.265	0.648	20.000	0.726783	89.19
C002	195.887	196.208	0.321	20.000	0.377950	85.00
C003	195.537	195.773	0.236	14.286	0.269964	87.51
C004	195.877	196.034	0.157	11.111	0.209972	74.89
C005	194.787	194.950	0.163	9.091	0.247629	65.93
C006	194.767	195.388	0.621	20.000	0.726783	85.48
C007	195.747	195.967	0.220	11.111	0.302657	72.77
C008	196.297	196.556	0.259	11.111	0.302657	85.66
C009	196.387	196.444	0.057	11.111	0.116176	49.28
C010	194.797	195.085	0.288	14.286	0.389131	74.08
C011	195.357	195.528	0.171	20.000	0.209117	81.89
C012	195.087	195.553	0.466	14.286	0.519131	89.81
C013	196.017	196.241	0.224	9.091	0.247629	90.56
C014	195.557	195.633	0.076	9.091	0.095053	80.22
C015	196.507	196.716	0.209	9.091	0.247629	84.50
C016	195.667	195.983	0.316	9.091	0.330356	95.73
C017	195.987	196.103	0.116	14.286	0.149369	77.83
C018	196.327	196.471	0.144	9.091	0.171795	83.97
C019	196.147	196.270	0.123	14.286	0.149369	82.51
C020	195.337	195.833	0.496	20.000	0.544783	91.09
C021	196.477	196.8190	0.3422	14.286	0.3891	87.95
C022	194.947	195.011	0.064	11.111	0.116176	55.30
C023	194.917	195.273	0.356	11.111	0.403769	88.23
C024	195.267	195.724	0.457	14.286	0.519131	88.08
C025	196.567	196.707	0.140	20.000	0.209117	67.07
C026	196.767	196.917	0.150	11.111	0.209972	71.56
C027	194.777	194.956	0.179	9.091	0.247629	72.39
C028	196.437	196.506	0.069	11.111	0.116176	59.61

*Table continued*

Sample Nr	$m_1$ (g)	$m_2$ (g)	$m_{p \text{ used}}$ (g)	$(l_{cl}/v_s)$ (s)	$m_{p \text{ delivered}}$ (g)	$\eta_{pe}$ (%)
C029	196.127	196.259	0.132	20.000	0.209117	63.24
C030	196.237	196.378	0.141	11.111	0.209972	67.27
C031	196.367	196.648	0.281	9.091	0.330356	85.14
C032	196.207	196.251	0.044	9.091	0.095053	46.55
C033	196.277	196.759	0.482	20.000	0.544783	88.52
C034	196.257	196.702	0.445	14.286	0.519131	85.77
C035	196.667	196.965	0.298	20.000	0.377950	78.91
C036	195.907	195.950	0.043	11.111	0.116176	37.23
C037	195.347	195.821	0.474	20.000	0.544783	87.05
C038	195.847	196.455	0.608	20.000	0.726783	83.69
C039	196.077	196.198	0.121	9.091	0.171795	70.58
C040	195.507	195.746	0.239	9.091	0.330356	72.42
C041	195.737	196.029	0.292	20.000	0.377950	77.33
C042	195.477	196.108	0.631	20.000	0.726783	86.86
C043	195.097	195.244	0.147	11.111	0.209972	70.13
C044	195.757	196.095	0.338	11.111	0.403769	83.77
C045	196.087	196.133	0.046	9.091	0.095053	48.66
C046	196.287	196.467	0.180	14.286	0.269964	66.77
C047	194.987	195.318	0.331	14.286	0.389131	85.13
C048	195.497	195.637	0.140	20.000	0.209117	67.07
C049	189.707	190.025	0.318	14.286	0.389131	81.78
C050	195.887	195.927	0.040	9.091	0.095053	42.34
C051	196.247	196.377	0.130	9.091	0.171795	75.82
C052	196.227	196.446	0.219	14.286	0.269964	81.21
C053	195.817	196.042	0.225	11.111	0.302657	74.42
C054	194.977	195.294	0.317	20.000	0.377950	83.94
C055	189.767	190.227	0.460	20.000	0.544783	84.48
C056	195.817	196.167	0.350	11.111	0.403769	86.75
C057	195.717	195.968	0.251	9.091	0.330356	76.05
C058	196.437	196.529	0.092	14.286	0.149369	61.76
C059	196.507	196.954	0.447	14.286	0.519131	86.15
C060	196.137	196.392	0.255	11.111	0.302657	84.34
C061	194.757	195.075	0.318	11.111	0.403769	78.82
C062	196.227	196.456	0.229	14.286	0.269964	84.92
C063	194.497	194.588	0.091	14.286	0.149369	61.09
C064	195.817	195.911	0.094	9.091	0.171795	54.86

Table B1



# APPENDIX C

## **Vickers microhardness**

## Vickers microhardness of the clad cross-section

The results from the Vickers microhardness tests are summarized in Table C1.

Sample Nr	HV <sub>max clad cross-section</sub>	HV <sub>min clad cross-section</sub>	HV <sub>min substrate</sub>	HV <sub>max indentation position</sub>	HV <sub>1st Indentation</sub>	%HV <sub>difference 1st and max indentation HV</sub>
C 001	111.83	106.70	24.04	3.0	107.54	3.84
C 002	115.41	101.92	24.65	3.0	101.92	11.69
C 003	109.20	95.37	24.65	1.0	109.20	0.00
C 004	125.20	113.56	24.56	1.0	125.20	0.00
C 005	116.35	103.52	25.02	2.0	116.33	0.02
C 006	119.19	108.34	24.83	3.0	114.48	3.95
C 007	122.14	111.75	25.30	4.0	111.75	8.51
C 008	127.34	110.04	24.56	2.0	125.20	1.68
C 009	76.53	72.22	25.12	1.0	76.53	0.00
C 010	130.60	115.35	24.92	1.0	130.60	0.00
C 011	87.54	80.15	24.27	1.0	87.54	0.00
C 012	127.34	115.14	23.77	1.0	127.34	0.00
C 013	120.15	97.43	24.20	1.0	120.15	0.00
C 014	70.88	65.86	24.64	3.0	65.86	7.08
C 015	129.54	119.16	25.02	1.0	129.54	0.00
C 016	111.80	101.19	24.38	2.0	101.19	9.49
C 017	95.33	93.31	24.39	1.0	95.33	0.00
C 018	93.98	84.58	22.84	2.0	87.56	6.83
C 019	77.52	75.55	23.93	2.0	75.55	2.54
C 020	117.28	76.07	22.84	6.0	111.83	4.65
C 021	113.61	108.36	24.21	2.0	113.61	0.00
C 022	107.54	82.33	24.48	1.0	107.54	0.00
C 023	127.31	105.85	25.39	2.0	126.30	0.79
C 024	121.22	101.17	25.41	1.0	121.22	0.00
C 025	90.68	84.56	23.76	2.0	84.58	6.73
C 026	96.03	90.86	24.66	1.0	96.03	0.00
C 027	146.40	116.30	25.32	1.0	146.40	0.00
C 028	91.40	80.69	25.22	2.0	80.69	11.72
C 029	110.12	94.00	24.28	1.0	110.12	0.00
C 030	112.70	100.43	25.30	3.0	112.70	0.00
C 031	131.70	113.53	24.92	1.0	131.70	0.00
C 032	91.98	88.76	24.94	1.0	91.98	0.00
C 033	109.25	101.19	24.84	3.0	109.22	0.03
C 034	126.30	120.12	24.65	6.0	124.21	1.65
C 035	114.48	103.45	25.20	2.0	92.63	19.09
C 036	92.63	90.04	24.83	2.0	90.04	2.80
C 037	109.22	79.52	23.42	2.0	101.92	6.68

*Table continued*

Sample Nr	HV <sub>max clad</sub> cross-section	HV <sub>min clad</sub> cross-section	HV <sub>min</sub> substrate	HV <sub>max</sub> indentation position	HV <sub>1st</sub> Indentation	%HV <sub>difference 1st</sub> and max indentation HV
C 038	124.21	107.52	25.01	5.0	119.26	3.99
C 039	94.73	85.17	25.03	1.0	94.73	0.00
C 040	126.23	110.01	24.03	4.0	124.14	1.66
C 041	114.56	95.31	25.85	1.0	114.56	0.00
C 042	116.33	105.11	24.66	7.0	105.11	9.64
C 043	103.50	94.00	23.34	2.0	98.18	5.14
C 044	124.24	114.51	23.85	1.0	124.24	0.00
C 045	80.62	76.02	24.46	1.0	80.62	0.00
C 046	125.20	106.73	24.92	1.0	125.20	0.00
C 047	126.26	113.50	24.36	1.0	126.26	0.00
C 048	84.01	79.10	24.72	4.0	84.01	0.00
C 049	114.48	98.90	24.84	2.0	102.73	10.26
C 050	82.33	78.58	26.20	2.0	78.58	4.55
C 051	88.24	85.19	22.93	2.0	88.19	0.06
C 052	114.42	93.96	25.21	2.0	112.68	1.52
C 053	127.34	112.68	24.64	1.0	127.34	0.00
C 054	103.45	95.33	25.12	4.0	102.70	0.72
C 055	118.02	106.65	24.73	1.0	118.02	0.00
C 056	117.25	73.63	23.86	2.0	110.94	5.38
C 057	127.38	123.17	24.85	1.0	127.38	0.00
C 058	83.42	78.02	25.50	1.0	83.42	0.00
C 059	117.25	109.20	24.02	6.0	116.33	0.78
C 060	125.20	106.65	24.91	1.0	125.20	0.00
C 061	131.77	126.26	24.39	1.0	131.77	0.00
C 062	113.59	96.77	24.94	1.0	113.59	0.00
C 063	88.19	74.60	24.84	1.0	88.19	0.00
C 064	117.25	110.89	26.37	2.0	110.92	5.40

Table C1

# APPENDIX D

## **Combined process variables**

## Combined process variables

The calculated combined process variables, used to investigate whether a strong correlation could be found between an individual clad geometry or characteristic and a combined process variable, are tabulated in Table D1.

Sample Nr	CP1	CP2	CP3	CP4	CP5	CP6	CP7
C 001	0.400000	1453.44	16.1245	1508.52	2.5000	90.139	2055.48
C 002	0.200000	1341.64	10.9545	1754.41	5.0000	122.474	1341.64
C 003	0.142857	1228.38	8.1441	1698.96	7.0000	150.831	1228.38
C 004	0.111111	916.67	5.8267	1322.06	9.0000	157.321	916.67
C 005	0.136364	979.91	6.3474	1276.60	7.3333	154.380	1200.14
C 006	0.400000	1565.25	16.7332	1624.56	2.5000	93.541	2213.59
C 007	0.166667	1083.33	7.7579	1364.91	6.0000	139.642	1326.81
C 008	0.166667	1000.00	7.4536	1259.92	6.0000	134.164	1224.74
C 009	0.055556	1166.67	4.6481	2119.97	18.0000	250.998	824.96
C 010	0.214286	1039.40	9.1752	1255.85	4.6667	113.284	1273.00
C 011	0.100000	1453.44	8.0623	2394.62	10.0000	180.278	1027.74
C 012	0.285714	1039.40	10.5946	1141.01	3.5000	98.107	1469.94
C 013	0.136364	1055.29	6.5870	1374.80	7.3333	160.208	1292.46
C 014	0.045455	1055.29	3.8030	1982.81	22.0000	277.489	746.20
C 015	0.136364	904.53	6.0984	1178.40	7.3333	148.324	1107.82
C 016	0.181818	1055.29	7.6060	1249.09	5.5000	138.744	1492.41
C 017	0.071429	1039.40	5.2973	1811.24	14.0000	196.214	734.97
C 018	0.090909	1055.29	5.3783	1573.76	11.0000	196.214	1055.29
C 019	0.071429	1322.88	5.9761	2305.22	14.0000	221.359	935.41
C 020	0.300000	1229.84	12.8452	1404.90	3.3333	95.743	1506.24
C 021	0.214286	1228.38	9.9745	1484.18	4.6667	123.153	1504.46
C 022	0.055556	1000.00	4.3033	1817.12	18.0000	232.379	707.11
C 023	0.222222	1083.33	8.9581	1240.11	4.5000	120.934	1532.06
C 024	0.285714	1322.88	11.9523	1452.20	3.5000	110.680	1870.83
C 025	0.100000	1341.64	7.7460	2210.42	10.0000	173.205	948.68
C 026	0.111111	1166.67	6.5734	1682.62	9.0000	177.482	1166.67
C 027	0.136364	829.16	5.8387	1080.20	7.3333	142.009	1015.50
C 028	0.055556	1083.33	4.4790	1968.55	18.0000	241.868	766.03
C 029	0.100000	1229.84	7.4162	2026.22	10.0000	165.831	869.63
C 030	0.111111	1000.00	6.0858	1442.25	9.0000	164.317	1000.00
C 031	0.181818	979.91	7.3293	1159.87	5.5000	133.697	1385.80
C 032	0.045455	829.16	3.3710	1557.92	22.0000	245.967	586.30
C 033	0.300000	1453.44	13.9642	1660.34	3.3333	104.083	1780.10
C 034	0.285714	1133.89	11.0657	1244.74	3.5000	102.470	1603.57
C 035	0.200000	1453.44	11.4018	1900.61	5.0000	127.475	1453.44
C 036	0.055556	916.67	4.1201	1665.69	18.0000	222.486	648.18
C 037	0.300000	1565.25	14.4914	1788.06	3.3333	108.012	1917.03

*Table continued*

Sample Nr	CP1	CP2	CP3	CP4	CP5	CP6	CP7
C 038	0.400000	1229.84	14.8324	1276.44	2.5000	82.916	1739.25
C 039	0.090909	979.91	5.1826	1461.34	11.0000	189.077	979.91
C 040	0.181818	904.53	7.0418	1070.65	5.5000	128.452	1279.20
C 041	0.200000	1229.84	10.4881	1608.21	5.0000	117.260	1229.84
C 042	0.400000	1341.64	15.4919	1392.48	2.5000	86.603	1897.37
C 043	0.111111	1083.33	6.3343	1562.44	9.0000	171.026	1083.33
C 044	0.222222	1000.00	8.6066	1144.71	4.5000	116.190	1414.21
C 045	0.045455	904.53	3.5209	1699.55	22.0000	256.905	639.60
C 046	0.142857	1039.40	7.4915	1437.58	7.0000	138.744	1039.40
C 047	0.214286	1133.89	9.5831	1370.01	4.6667	118.322	1388.73
C 048	0.100000	1565.25	8.3666	2578.82	10.0000	187.083	1106.80
C 049	0.214286	1322.88	10.3510	1598.35	4.6667	127.802	1620.19
C 050	0.045455	979.91	3.6647	1841.18	22.0000	267.395	692.90
C 051	0.090909	904.53	4.9793	1348.93	11.0000	181.659	904.53
C 052	0.142857	1133.89	7.8246	1568.27	7.0000	144.914	1133.89
C 053	0.166667	916.67	7.1362	1154.93	6.0000	128.452	1122.68
C 054	0.200000	1565.25	11.8322	2046.81	5.0000	132.288	1565.25
C 055	0.300000	1341.64	13.4164	1532.62	3.3333	100.000	1643.17
C 056	0.222222	1166.67	9.2962	1335.50	4.5000	125.499	1649.92
C 057	0.181818	829.16	6.7420	981.43	5.5000	122.984	1172.60
C 058	0.071429	1228.38	5.7588	2140.56	14.0000	213.307	868.60
C 059	0.285714	1228.38	11.5175	1348.47	3.5000	106.654	1737.20
C 060	0.166667	1166.67	8.0508	1469.91	6.0000	144.914	1428.87
C 061	0.222222	916.67	8.2402	1049.32	4.5000	111.243	1296.36
C 062	0.142857	1322.88	8.4515	1829.65	7.0000	156.525	1322.88
C 063	0.071429	1133.89	5.5328	1975.90	14.0000	204.939	801.78
C 064	0.090909	829.16	4.7673	1236.52	11.0000	173.925	829.16

Table D1

# APPENDIX E

## **Sample preparation for metallurgical examination**

## **E1: Sectioning**

The test samples were sectioned using a LECO wet-abrasive cut-off machine. It is important the correct cut-off wheel is selected for sectioning since it affects the amount of deformation and plainness of the surface obtained after sectioning. Selecting the wrong cut-off wheel could also lead to heat build-up in the cutting zone causing burns that alter the microstructure of the material under investigation. The main considerations when selecting a cut-off wheel is the hardness and ductility of the material.

For this investigation a 56UNI, Struers cut-off wheel with SiC abrasive and a Bakelite bond was selected. It is suitable for cutting soft, non-ferrous materials with a hardness range of between 30-280 HV. The Vickers hardness of the aluminium 1370-F substrate is estimated to range between 20-30 HV, while that of the single pass clad layer is estimated to range between 70-140 HV.

In order to obtain a representative sample for metallographic examination the single pass clad layer was cross-sectioned in the centre of the clad layer, perpendicular to the length of the clad layer. Sectioning produced four cross-sections. Each cross-section was marked with the same reference number or sample number as the original test sample for identification. In addition two arrows were drawn facing the reference line (Shown in Figure E1) to identify the cross-sectional surfaces that were to be used for metallographic



examination after sectioning. Only sections B and C in Figure 2E were used for metallographic examination of the clad cross-section.

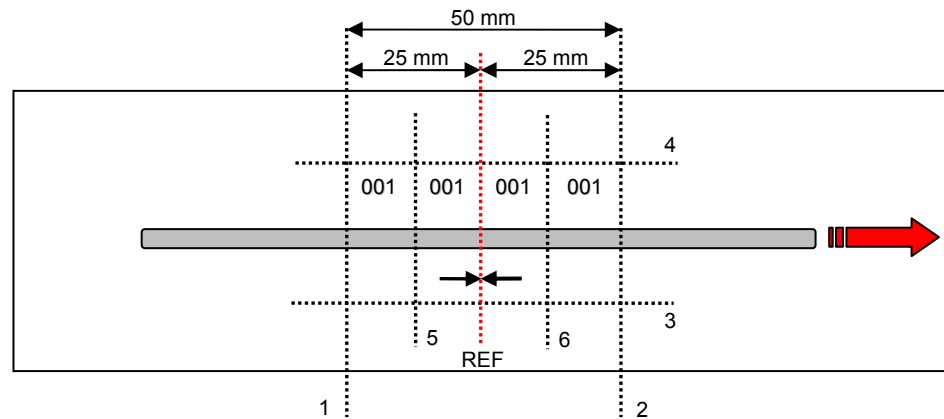


Figure 1E: Layout of the cutting lines, numbered one to six, for cross-sectioning the single pass clad layer.

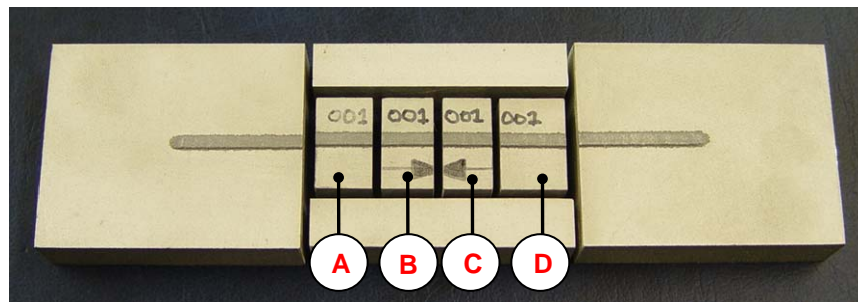


Figure 2E: Clad cross-sections produced after sectioning.

## E2: Grinding and polishing

The purpose of grinding is to successively reduce the amount of deformation brought about by sectioning. Each grinding step removes previous deformation but also introduces deformation of its own. The depth and scale of deformation however decreases with each successive preparation step.

The first step in the grinding sequence also referred to as rough/plain grinding, starts with the finest grit size that will produce a flat surface and remove the effects of sectioning. 200 Grit SiC paper is generally used for the first plain grinding step for most materials. It was however soon realized during subsequent grinding that the use of 200 grit SiC paper resulted in a substantial amount of SiC particles being embedded in the soft substrate material. Once embedded these particles became extremely difficult to remove. In addition these particles often became a source of contamination during later preparation stages or came loose during one of the polishing steps resulting in deep scratches.

After several grinding tests it was found that using 800 grit SiC paper for the first grinding step resulted in virtually no SiC particles being embedded in the aluminium substrate material. Thus 800 grit SiC paper was selected for the first grinding step and 1200 grit for fine grinding. The outcome of these tests ultimately resulted in the polishing procedure designated method AI-01, summarized below.

**Method number: AI-01**

Mounting material: Lucite

Mounting size: 25 mm

Disc size: 250 mm

### Grinding steps

Preparation step	RG	IG
Disc surface	NA	NA
Abrasive material	800 SiC paper	1200 Sic paper
Lubricant	water	water
Speed (rpm)	-	-
Force (N)	-	-
Sample rotation	stationary	stationary
Time (min)	1	1

(RG-Rough grinding; IG-Intermediate grinding)

### Polishing steps

Preparation step	1P	FP
Disc surface	Red felt (virgin wool)	Wool
Abrasive material	6 $\mu\text{m}$ – diamond paste	1 $\mu\text{m}$ – diamond paste
Lubricant	Diamond extender	Diamond extender
Speed (rpm)	-	-
Force (N)	-	-
Sample rotation	stationary	stationary
Time (min)	3	1

(1P-1<sup>st</sup> Polishing step; FP-Final polishing)

Preparation method AI-01 often produced over-polished samples due to the time required to remove deformation from the fine grinding step or possibly due to cloth resilience. Over-polishing resulted in rounded edges and relief at the clad substrate interface due to the hardness variation between the substrate and the clad layer.

Initially it was felt that the mounting material might have an influence and thus samples mounted in three different mounting media lucite, bakelite and dialyl phalate was tested and compared using the same preparation method, AI-01. Although the ease of sample preparation improved using bakelite and dialyl phalate it did not decrease the polishing times significantly.

In an effort to reduce polishing times it was decided to use a mounting media that is more suitable for soft materials and had a higher material removal rate. A Struers product called Polyfast was selected. Polyfast is a phenolic resin with carbon filler. In addition to its good edge retention and relatively high removal rate it also has the added advantage that it could be used directly in the scanning electron microscope due to its good conductive properties. Polyfast not only decreased polishing times but also improved the results between successive preparation steps reducing edge rounding and relief at the clad-substrate interface.

Deformation from the last fine grinding stage however still remained a problem when moving on to the polishing steps. Several preparation procedures recommended by Struers for soft non-ferrous metals were considered to overcome this problem. The first of which was method number 1620 for very soft aluminium and aluminium alloys. Method number 1620 consists of three grinding stages: rough; intermediate, and fine grinding using 800; 1200, and 4000 grit SiC paper respectively. Fine grinding using 4000 grit SiC paper however resulted in a significant amount of very fine SiC

particles being embedded in the substrate. Subsequently another method, method number 1477 was considered which is also recommended for very soft aluminium and aluminium alloys. Method number 1477 starts with a rough grind step using 320 grit SiC paper which was determined to be too coarse by previous grinding tests. Method number 1477 however used a different fine grinding step using a MD-Largo disc with DiaPro Allegro /Largo from Struers. It was thus decided to modify method number 1477 based on the knowledge gained from testing previous preparation methods. Combining the best preparation steps from each method resulted in a new preparation method, method AI-02.

### **Method: AI-02**

Mounting material: Polyfast

Mounting size: 25 mm

Disc size: 250 mm

### **Grinding steps**

Preparation steps	RG	IG	FG
Disc surface	NA	NA	MD - Largo
Abrasive material	800 SiC paper	1200 Sic paper	DiaPro Allegro/Largo
Lubricant	water	water	Diamond extender
Speed (rpm)	-	-	-
Force (N)	-	-	-
Sample rotation	stationary	stationary	stationary
Time (min)	1	1	2

(RG- Rough grinding; IG-Intermediate grinding, FG-Fine grinding)

### Polishing steps

Preparation steps	P1	PF
Disc surface	MD - Mol	OP - Chem
Abrasive material	DiaPro Mol	OP – S, 0.04 µm
Lubricant	Diamond extender	-
Speed (rpm)	-	-
Force (N)	-	-
Sample rotation	stationary	stationary
Time (min)	2	1

(1P-1<sup>st</sup> Polishing step; FP-Final polishing)

### E3: Etching

Several etchants were tested to determine whether it could be used to reveal the clad microstructure and heat affected zone. The composition of the etchants that were tested is listed below.

#### Etchant E3-1

100 ml                      Distilled water  
5, 10 and 20 g          Sodium hydroxide

Three different variations of etchant E3-1 was tested with varying amounts of sodium hydroxide as listed above. Etchant E3-1 revealed the clad microstructure but failed to reveal the heat affected zone

**Etchant E3-2 (Keller's reagent)**

190 ml	Distilled water
3 ml	Hydrochloric acid (32%)
5 ml	Nitric acid (65%)
1 ml	Hydrofluoric acid (40%)

Etchant E3-2 also revealed the clad microstructure but failed to reveal the heat affected zone. The hazardous nature of Keller's reagent made it less suitable than etchant E3-1 and E3-3 especially when considering it did not reveal the heat affected zone below the clad layer.

**Etchant E3-3**

60 ml	Distilled water
10g	Sodium hydroxide
5 g	Potassium ferricyanide

Etchant E3-3 revealed the clad microstructure but failed to reveal the heat affected zone. Etchant E3-3 however produced the best results when considering the microstructure of the clad layer. Etchant E3-3 therefore was the preferred etchant for sample preparation.